



**HAL**  
open science

# Shear-induced diffusion of road minerals within the tire tread : A solid flow modeling using a soft multibody approach

Kévin Daigne

► **To cite this version:**

Kévin Daigne. Shear-induced diffusion of road minerals within the tire tread : A solid flow modeling using a soft multibody approach. Mechanics [physics]. INSA de Lyon, 2024. English. NNT : 2024ISAL0046 . tel-04691459v2

**HAL Id: tel-04691459**

**<https://theses.hal.science/tel-04691459v2>**

Submitted on 10 Jan 2025

**HAL** is a multi-disciplinary open access archive for the deposit and dissemination of scientific research documents, whether they are published or not. The documents may come from teaching and research institutions in France or abroad, or from public or private research centers.

L'archive ouverte pluridisciplinaire **HAL**, est destinée au dépôt et à la diffusion de documents scientifiques de niveau recherche, publiés ou non, émanant des établissements d'enseignement et de recherche français ou étrangers, des laboratoires publics ou privés.



N° d'ordre NNT :2024ISAL0046

**THESE de DOCTORAT DE L'INSA LYON,  
membre de l'Université de Lyon**

**Ecole Doctorale N° 162**

Mécanique, Énergétique, Génie Civil et Acoustique (MÉGA)

**Spécialité/discipline de doctorat :**  
Génie Mécanique

Soutenue publiquement le 24/05/2024, par :

**Kévin Daigne**

---

**Shear-induced diffusion of road minerals  
within the tire tread: a solid flow modeling  
using a soft multibody approach**

---

Devant le jury composé de :

AZEMA	Emilien	Professeur, HDR	Univ. de Montpellier	Examineur
DIANI	Julie	Directeur de recherche CNRS	École polytechnique	Rapporteuse
MAGNIER	Vincent	Maître de conférences, HDR	Polytech Lille	Rapporteur
FILLOT	Nicolas	Professeur, HDR	INSA Lyon	Directeur de thèse
MOLLON	Guilhem	Maître de conférences, HDR	INSA Lyon	Co-directeur
DESCARTES	Sylvie	Ingénieur de recherche, HDR	INSA Lyon	Invitée/Co-directrice
J. D. GROSJEAN	Romain	Ingénieur	Michelin	Invité





Référence : TH1103\_DAIGNE Kévin

L'INSA Lyon a mis en place une procédure de contrôle systématique via un outil de détection de similitudes (logiciel Compilatio). Après le dépôt du manuscrit de thèse, celui-ci est analysé par l'outil. Pour tout taux de similarité supérieur à 10%, le manuscrit est vérifié par l'équipe de FEDORA. Il s'agit notamment d'exclure les auto-citations, à condition qu'elles soient correctement référencées avec citation expresse dans le manuscrit.

Par ce document, il est attesté que ce manuscrit, dans la forme communiquée par la personne doctorante à l'INSA Lyon, satisfait aux exigences de l'Établissement concernant le taux maximal de similitude admissible.

**INSA LYON**

Campus LyonTech La Doua  
20, avenue Albert Einstein - 69621 Villeurbanne cedex - France  
Tél. +33 (0)4 72 43 83 83 - Fax +33 (0)4 72 43 85 00  
[www.insa-lyon.fr](http://www.insa-lyon.fr)





## Département FEDORA - INSA Lyon - Ecoles Doctorales

SIGLE	ECOLE DOCTORALE	NOM ET COORDONNEES DU RESPONSABLE
ED 206 CHIMIE	<b>CHIMIE DE LYON</b> <a href="https://www.edchimie-lyon.fr">https://www.edchimie-lyon.fr</a> Sec. : Renée EL MELHEM Bât. Blaise PASCAL, 3e étage <a href="mailto:secretariat@edchimie-lyon.fr">secretariat@edchimie-lyon.fr</a>	<b>M. Stéphane DANIELE</b> C2P2-CPE LYON-UMR 5265 Bâtiment F308, BP 2077 43 Boulevard du 11 novembre 1918 69616 Villeurbanne <a href="mailto:directeur@edchimie-lyon.fr">directeur@edchimie-lyon.fr</a>
ED 341 E2M2	<b>ÉVOLUTION, ÉCOSYSTÈME, MICROBIOLOGIE, MODÉLISATION</b> <a href="http://e2m2.universite-lyon.fr">http://e2m2.universite-lyon.fr</a> Sec. : Bénédicte LANZA Bât. Atrium, UCB Lyon 1 Tél : 04.72.44.83.62 <a href="mailto:secretariat.e2m2@univ-lyon1.fr">secretariat.e2m2@univ-lyon1.fr</a>	<b>Mme Sandrine CHARLES</b> Université Claude Bernard Lyon 1 UFR Biosciences Bâtiment Mendel 43, boulevard du 11 Novembre 1918 69622 Villeurbanne CEDEX <a href="mailto:e2m2.codir@listes.univ-lyon1.fr">e2m2.codir@listes.univ-lyon1.fr</a>
ED 205 EDISS	<b>INTERDISCIPLINAIRE SCIENCES-SANTÉ</b> <a href="http://ediss.universite-lyon.fr">http://ediss.universite-lyon.fr</a> Sec. : Bénédicte LANZA Bât. Atrium, UCB Lyon 1 Tél : 04.72.44.83.62 <a href="mailto:secretariat.ediss@univ-lyon1.fr">secretariat.ediss@univ-lyon1.fr</a>	<b>Mme Sylvie RICARD-BLUM</b> Laboratoire ICBMS - UMR 5246 CNRS - Université Lyon 1 Bâtiment Raulin - 2ème étage Nord 43 Boulevard du 11 novembre 1918 69622 Villeurbanne Cedex Tél : +33(0)4 72 44 82 32 <a href="mailto:sylvie.ricard-blum@univ-lyon1.fr">sylvie.ricard-blum@univ-lyon1.fr</a>
ED 34 EDML	<b>MATÉRIAUX DE LYON</b> <a href="http://ed34.universite-lyon.fr">http://ed34.universite-lyon.fr</a> Sec. : Yann DE ORDENANA Tél : 04.72.18.62.44 <a href="mailto:yann.de-ordenana@ec-lyon.fr">yann.de-ordenana@ec-lyon.fr</a>	<b>M. Stéphane BENAYOUN</b> Ecole Centrale de Lyon Laboratoire LTDS 36 avenue Guy de Collongue 69134 Ecully CEDEX Tél : 04.72.18.64.37 <a href="mailto:stephane.benayoun@ec-lyon.fr">stephane.benayoun@ec-lyon.fr</a>
ED 160 EEA	<b>ÉLECTRONIQUE, ÉLECTROTECHNIQUE, AUTOMATIQUE</b> <a href="https://edeea.universite-lyon.fr">https://edeea.universite-lyon.fr</a> Sec. : Philomène TRECOURT Bâtiment Direction INSA Lyon Tél : 04.72.43.71.70 <a href="mailto:secretariat.edeea@insa-lyon.fr">secretariat.edeea@insa-lyon.fr</a>	<b>M. Philippe DELACHARTRE</b> INSA LYON Laboratoire CREATIS Bâtiment Blaise Pascal, 7 avenue Jean Capelle 69621 Villeurbanne CEDEX Tél : 04.72.43.88.63 <a href="mailto:philippe.delachartre@insa-lyon.fr">philippe.delachartre@insa-lyon.fr</a>
ED 512 INFOMATHS	<b>INFORMATIQUE ET MATHÉMATIQUES</b> <a href="http://edinfomaths.universite-lyon.fr">http://edinfomaths.universite-lyon.fr</a> Sec. : Renée EL MELHEM Bât. Blaise PASCAL, 3e étage Tél : 04.72.43.80.46 <a href="mailto:infomaths@univ-lyon1.fr">infomaths@univ-lyon1.fr</a>	<b>M. Hamamache KHEDDOUCI</b> Université Claude Bernard Lyon 1 Bât. Nautibus 43, Boulevard du 11 novembre 1918 69 622 Villeurbanne Cedex France Tél : 04.72.44.83.69 <a href="mailto:direction.infomaths@listes.univ-lyon1.fr">direction.infomaths@listes.univ-lyon1.fr</a>
ED 162 MEGA	<b>MÉCANIQUE, ÉNERGÉTIQUE, GÉNIE CIVIL, ACOUSTIQUE</b> <a href="http://edmega.universite-lyon.fr">http://edmega.universite-lyon.fr</a> Sec. : Philomène TRECOURT Tél : 04.72.43.71.70 Bâtiment Direction INSA Lyon <a href="mailto:mega@insa-lyon.fr">mega@insa-lyon.fr</a>	<b>M. Etienne PARIZET</b> INSA Lyon Laboratoire LVA Bâtiment St. Exupéry 25 bis av. Jean Capelle 69621 Villeurbanne CEDEX <a href="mailto:etienne.parizet@insa-lyon.fr">etienne.parizet@insa-lyon.fr</a>
ED 483 ScSo	<b>ScSo<sup>1</sup></b> <a href="https://edsciencessociales.universite-lyon.fr">https://edsciencessociales.universite-lyon.fr</a> Sec. : Mélina FAVETON Tél : 04.78.69.77.79 <a href="mailto:melina.faveton@univ-lyon2.fr">melina.faveton@univ-lyon2.fr</a>	<b>M. Bruno MILLY (INSA : J.Y. TOUSSAINT)</b> Univ. Lyon 2 Campus Berges du Rhône 18, quai Claude Bernard 69365 LYON CEDEX 07 Bureau BEL 319 <a href="mailto:bruno.milly@univ-lyon2.fr">bruno.milly@univ-lyon2.fr</a>

1. ScSo : Histoire, Géographie, Aménagement, Urbanisme, Archéologie, Science politique, Sociologie, Anthropologie



# Contents

<b>Résumé</b>	<b>11</b>
<b>Résumé étendu</b>	<b>13</b>
<b>Abstract</b>	<b>27</b>
<b>General introduction</b>	<b>29</b>
<b>1 State of the art and strategy</b>	<b>31</b>
1 Rubber-like materials . . . . .	31
1.1 From tree to automobile . . . . .	31
1.2 Manufacturing . . . . .	33
1.3 Properties . . . . .	37
2 Tire properties . . . . .	41
2.1 Structure . . . . .	41
2.2 Friction . . . . .	42
2.3 Wear . . . . .	47
3 Tribological framework . . . . .	49
3.1 Context . . . . .	49
3.2 Third body . . . . .	51
3.3 Tribological circuit . . . . .	51
4 Hertzian framework . . . . .	52
4.1 Static contact . . . . .	52
4.2 Rolling contact . . . . .	54
5 Friction modeling . . . . .	55
5.1 Analytical . . . . .	55
5.2 Numerical . . . . .	58
6 Wear modeling . . . . .	64
6.1 Analytical . . . . .	65
6.2 Numerical . . . . .	65
7 Objectives . . . . .	68
7.1 Observations . . . . .	68
7.2 Strategy . . . . .	71
<b>2 Framework</b>	<b>73</b>
1 Experimental set-up . . . . .	73
1.1 Tribometer . . . . .	73
1.2 Specimen . . . . .	73
1.3 Observations . . . . .	74
1.4 Minerals . . . . .	74
1.5 Surface topography . . . . .	75
2 Diffusion framework . . . . .	77

2.1	Stochastic view . . . . .	77
2.2	Deterministic view . . . . .	78
2.3	From stochastic to deterministic . . . . .	79
2.4	Shear-induced diffusion . . . . .	80
3	Numerical method . . . . .	81
3.1	Overview . . . . .	81
3.2	Spatial discretization . . . . .	86
3.3	Temporal discretization . . . . .	89
3.4	Contacts . . . . .	90
4	Diffusion model . . . . .	92
4.1	Overview . . . . .	92
4.2	Descriptors . . . . .	99
4.3	List of performed simulations . . . . .	102
<b>3</b>	<b>Rubber characterization</b>	<b>109</b>
1	State of the art . . . . .	109
1.1	Unicity of the solution . . . . .	109
1.2	Indentation method . . . . .	110
1.3	Numerical approach . . . . .	111
2	Method . . . . .	113
2.1	Experimental set-up . . . . .	113
2.2	Indentation model . . . . .	114
3	Numerical results . . . . .	118
3.1	Kinematics . . . . .	118
3.2	Load-depth curves . . . . .	120
4	Reverse analysis . . . . .	122
4.1	General method . . . . .	122
4.2	Experimental results . . . . .	124
4.3	Reverse analysis results . . . . .	126
	Conclusion . . . . .	128
<b>4</b>	<b>Mixing mechanisms</b>	<b>131</b>
1	Intake . . . . .	131
1.1	Plowing . . . . .	131
1.2	Abrasion . . . . .	134
1.3	Fracture . . . . .	135
2	Diffusion . . . . .	137
2.1	Overview . . . . .	137
2.2	Green-Kubo framework . . . . .	138
2.3	Mechanisms . . . . .	141
2.4	Orientation . . . . .	142
3	Long time scales . . . . .	143
4	Transient diffusion . . . . .	145
4.1	Direct jamming . . . . .	145
4.2	Delayed jamming . . . . .	148
5	Experimental observations . . . . .	151
5.1	Surfaces . . . . .	151
5.2	Longitudinal section . . . . .	152
	Conclusion . . . . .	154

<b>5</b>	<b>Steady-state diffusion</b>	<b>157</b>
1	Numerical parameters	157
1.1	Sliding velocity	157
1.2	Interfacial layer thickness	161
1.3	Rubber particle size	163
2	External parameters	165
2.1	Contact pressure	165
2.2	Roughness	167
2.3	Mineral fraction	168
2.4	Mineral size	171
3	Rubber properties	174
3.1	Rubber stiffness	174
3.2	Rubber cohesion	177
	Conclusion	180
	<b>General conclusion</b>	<b>183</b>
	<b>Perspectives</b>	<b>185</b>
	<b>Appendices</b>	<b>189</b>
	<b>Appendix A Green-Kubo validation</b>	<b>191</b>
	<b>Appendix B Snapshots</b>	<b>195</b>
1	Direct jamming	195
2	Delayed jamming	196
2.1	Interfacial layer thickness in a delayed jamming case	196
2.2	Friction between rocky materials	197
2.3	Friction between rock and rubber materials	198
3	Steady-state diffusion	199
3.1	Numerical parameters	199
3.2	External parameters	202
3.3	Material parameters	207
	<b>Appendix C Mean square displacement</b>	<b>209</b>
1	Direct jamming	209
2	Delayed jamming	209
2.1	Interfacial layer thickness in a delayed jamming case	209
2.2	Friction between rocky materials	210
2.3	Friction between rock and rubber materials	210
3	Steady-state diffusion	210
3.1	Numerical parameters	210
3.2	External parameters	212
3.3	Material parameters	214
	<b>Appendix D Velocity autocorrelation function</b>	<b>217</b>
1	Numerical parameters	217
1.1	Sliding velocity	217
1.2	Interfacial layer thickness	217
1.3	Rubber particle size	218
2	External parameters	218
2.1	Contact pressure	218
2.2	Roughness (high-pass filter)	218



2.3	Roughness (low-pass filter)	218
2.4	Mineral fraction	219
2.5	Mineral size	219
3	Material parameters	219
3.1	Rubber stiffness	219
3.2	Rubber cohesion	219
<b>List of Figures</b>		<b>241</b>
<b>List of Tables</b>		<b>243</b>
<b>List of Algorithms</b>		<b>245</b>

# Résumé

Il peut être observé par des coupes longitudinales d'une bande de roulement de pneumatique, que les minéraux de la route y pénètrent dans l'extrême surface. L'objectif de ce travail est, pour une configuration expérimentale de référence, d'étudier expérimentalement et numériquement le processus menant à cette pénétration. Ce travail s'est articulé autour de trois grands axes.

Le premier a été de proposer une méthode de caractérisation du matériau composé de caoutchouc, adaptée au modèle numérique utilisé par la suite. Pour ce faire, une analyse inverse d'un essai d'indentation a été réalisée. Le modèle numérique considère le matériau comme étant composé d'une multitude de corps discrets et déformables. Les paramètres à identifier sont la rigidité et la cohésion entre chaque corps discret. L'étude a montré que la cinématique obtenue est proche de ce qui est mesuré expérimentalement. Un critère de convergence pour l'analyse inverse a été défini, qui se base sur la dureté et la profondeur résiduelle. Il a été montré que l'effet de la rigidité peut être découplé de celui de la cohésion. La dépendance de ces derniers au critère de convergence étant monotone, la solution obtenue est unique.

Un modèle numérique pour étudier la pénétration puis migration des minéraux a ensuite été réalisé. Il consiste à cisailer une couche de minéraux déposée sur la surface d'un matériau composé de caoutchouc, modélisé comme un ensemble de corps discrets et déformables. Il a tout d'abord été montré que les phénomènes initiaux de pénétration des minéraux dans la matière, sont différents de ceux observés à plus long terme. Notamment, trois modes de pénétration ont pu être définis, qui sont le labourage, l'abrasion et la fracturation. Ces modes modifient la vitesse à laquelle les minéraux pénètrent à l'intérieur du matériau.

Lorsque les minéraux sont suffisamment incorporés au matériau, ils forment ce qui sera appelé une couche mixée. Les minéraux migrent de plus en plus profondément, du fait de contacts répétés entre agglomérats de minéraux, causés par leurs vitesses relatives (caractérisées par le taux de cisaillement). Il est notamment montré que ces contacts conduisent à une évolution stochastique de la position d'un minéral. Si l'ensemble des minéraux est considéré, le comportement devient déterministe et suit une évolution proche de ce qui est attendu pour un processus diffusif. Ce dernier point permet ainsi d'utiliser les outils liés à la diffusion, et notamment d'évaluer un coefficient de diffusion via la fluctuation de vitesse transverse et sa persistance. Il est ainsi montré que ces deux paramètres dépendent fortement de phénomènes plastiques locaux, qui dans le modèle actuel sont pilotés par la cohésion.



# Résumé étendu

## Introduction

Les pneumatiques sont utilisés dans un grand nombre de domaines, de l'industrie automobile, en passant par le génie civil et jusqu'à l'aéronautique. Le pneumatique est un matériau composite constitué de différentes couches empilées, chacune ayant des propriétés spécifiques. Le caoutchouc est au cœur de sa composition. Pour améliorer les propriétés (mécaniques, chimiques, etc.), d'autres constituants sont ajoutés. Le matériau final sera désigné ci-après par le terme mélange ou gomme. Une coupe longitudinale de la bande de roulement permet de mettre en évidence des minéraux de la route qui ont pénétré en profondeur dans la matière. Un exemple est montré fig. 1, où la zone noire correspond à la gomme et la zone claire aux minéraux.

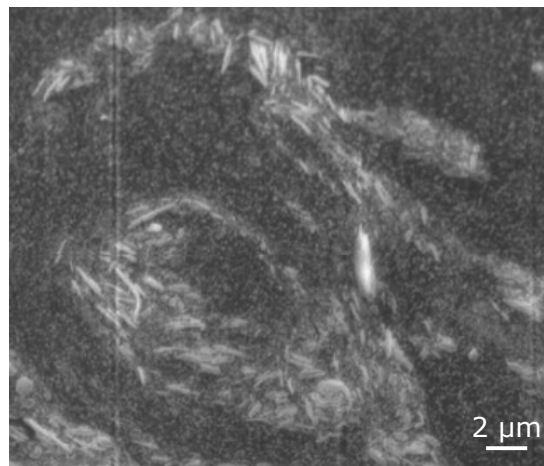


Figure 1: Image MEB (microscope électronique à balayage) avec un contraste correspondant au numéro atomique (Z-contrast) pour une coupe longitudinale d'une éprouvette après un essai d'usure; la direction de glissement est horizontale

Cette image suggère la présence d'un flux de minéraux à l'intérieur de la gomme, ce qui peut paraître surprenant de prime abord pour un matériau solide. De plus, si l'on observe des particules d'usure provenant d'un pneumatique, on peut distinguer de multiples inclusions minérales [Kreider et al., 2010]. Dans le contexte de ce travail, la compréhension des mécanismes mis en jeu nécessite de faire appel à trois disciplines majeures.

- La première est celle de l'étude des polymères et des élastomères. Ces matériaux ont des propriétés spécifiques, qui dépendent par exemple du temps, de la température ou même de l'amplitude de la déformation. Bien que ces effets aient été largement étudiés à l'échelle macroscopique, il reste encore beaucoup d'inconnus à l'échelle du contact.
- La seconde est celle de la tribologie. On sait aujourd'hui que la vision idéalisée de deux corps en contact, qui se réduisent à un coefficient de frottement, a de nombreuses limites.

En réalité, ces corps sont séparés par une couche interfaciale appelée troisième corps. Cette couche possède des propriétés distinctes des corps en contact, ce qui permet par exemple d'expliquer la dépendance du coefficient de frottement à l'humidité. Un autre point important est la notion de circuit tribologique. Elle consiste à dresser un bilan des flux de matières au sein du contact. Cette notion est particulièrement pertinente dans le cas présent, où un flux de minéraux est observé.

- La troisième est celle du mélange mécanique. Le fait que deux corps en cisaillement puissent former un mélange complexe est bien documenté. Cependant, comme indiqué ultérieurement, ce processus peut en réalité englober de nombreux phénomènes différents. En particulier, la migration d'un milieu dans un autre peut entrer dans la catégorie de ce qui est connu sous le nom de diffusion. La diffusion est un processus spécifique et de nature stochastique. Par conséquent, un processus de mélange mécanique ne peut être qualifié de diffusif que s'il répond à certaines caractéristiques.

L'objectif de ce travail est de réunir ces trois disciplines pour comprendre la migration des minéraux. En effet, cette migration (sur des profondeurs allant jusqu'à plusieurs micromètres) semble être spécifique au type de matériau utilisé pour la bande de roulement. Elle doit donc être une conséquence de la nature même du matériau couplée aux sollicitations tribologiques. Différents flux de matière doivent être considérés, ce qui fait appel à la notion de circuit tribologique. Enfin, il est essentiel de comprendre l'origine de cette migration, et pour cela, il est utile de rapprocher les résultats à des phénomènes bien connus (i.e. la diffusion). Réunir ces trois disciplines dans une même étude est une démarche délicate. Par exemple, l'existence même d'un processus diffusif au sein d'une interface solide et déformable reste à démontrer. Le but de cette étude est donc d'apporter une première description des phénomènes se déroulant dans une telle interface. Une représentation du mécanisme étudié est donnée fig. 2.

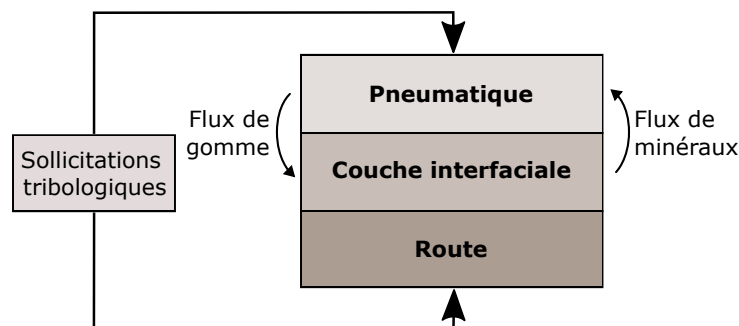


Figure 2: Illustration du mécanisme étudié

Pour comprendre les mécanismes en jeu, les observations expérimentales restent relativement insuffisantes. Par conséquent, l'utilisation d'un modèle numérique est à privilégier. Ce modèle doit cependant présenter certaines caractéristiques. Tout d'abord, la capacité des minéraux à se mélanger à la gomme. Pour ce faire, la gomme est modélisée comme un ensemble de corps discrets. Cela implique que les corps peuvent interagir les uns avec les autres par le biais de modèles de contact, grâce à un algorithme de détection de contact approprié. Les propriétés des matériaux doivent également être prises en compte, comme le module d'élasticité de la gomme, qui est relativement faible par rapport au niveau de contrainte. Par ailleurs, ce faible module ne peut pas être modélisé à l'aide de la méthode des éléments discrets (DEM), qui est limitée aux petites déformations. Il est de plus nécessaire de pouvoir modéliser les interactions entre des corps rigides (i.e. les minéraux) et des corps très déformables (i.e. la gomme), ce qui peut conduire à des distorsions géométriques significatives. Cela nécessite une méthode numérique robuste pour calculer les déformations et détecter les contacts. Enfin, tous ces corps doivent

être soumis à des sollicitations tribologiques avec des échelles d'espace et de temps appropriées. Pour toutes ces raisons, une approche multicorps sans maillage implémentée dans un code appelé MELODY est employée [Mollon, 2016].

L'étude se concentrera autour de quatre axes principaux. Premièrement, des essais expérimentaux seront réalisés pour démontrer cette migration dans des conditions contrôlées. Ils serviront de référence pour les analyses numériques. La deuxième étape consistera à caractériser un matériau modèle typique d'une utilisation pour une bande de roulement, composé de polyisoprène et d'autres constituants (e.g. noir de carbone). Ce matériau sera modélisé numériquement comme un ensemble de corps discrets. Par conséquent, une méthode spécifique sera élaborée, utilisant l'analyse inverse d'un essai d'indentation. Finalement, un modèle de cisaillement sera développé à partir de ces résultats (appelé modèle de diffusion par simplicité bien que le modèle intègre également d'autres mécanismes). L'analyse de ce dernier se fera en deux temps. Tout d'abord, les mécanismes de pénétration des minéraux dans la gomme seront étudiés. Ceux-ci diffèrent des mécanismes observés à plus long terme. Puis, une fois les minéraux suffisamment incorporés, les mécanismes de migration seront analysés, avec une étude plus approfondie de l'influence de certains paramètres.

## Essais expérimentaux

Pour étudier la migration des minéraux dans des conditions contrôlées, des essais d'usure ont été réalisés sur un tribomètre (UMT-2 CETR). La surface représentant le sol routier est composée d'agrégats (grès) liés par une résine. Le déplacement vertical de la surface supérieure est contrôlé afin de garantir une charge normale constante pendant l'essai. Une vitesse de rotation constante est appliquée par la surface inférieure. Une illustration du tribomètre et de l'éprouvette est présentée fig. 3.

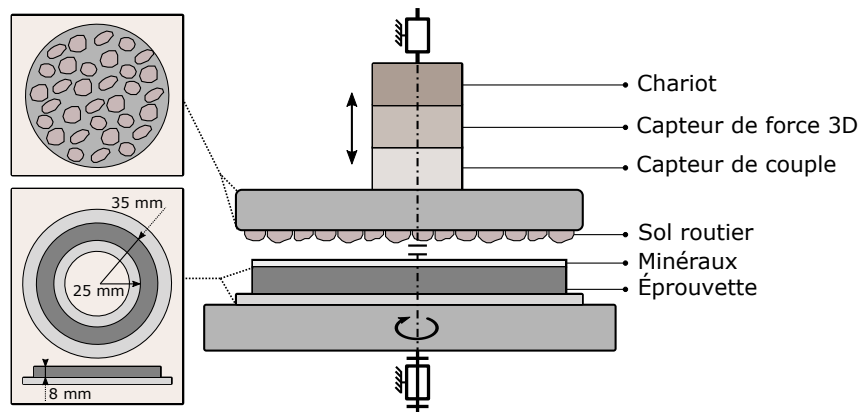


Figure 3: Illustration du tribomètre et des deux corps en contact

L'éprouvette d'usure est une couronne composée principalement de SBR (styrene butadiene rubber) avec un rayon intérieur de 25 mm, un rayon extérieur de 35 mm et une épaisseur de 8 mm. La composition est la suivante (en *pce*<sup>1</sup>) : 100 SBR, 50 N347, 3 6PPD, 1,5 acide stéarique, 3 ZnO, 1,3 CBS et 1,3 soufre. La température de transition vitreuse du SBR est égale à -48 °C. L'échantillon est cuit à 140 °C pendant 35 minutes. Pour reproduire l'effet des minéraux de la route, une fine couche (200 mg) de poudre de kaolin ( $Al_2Si_2O_5(OH)_4$ ) est déposée sur la surface de l'éprouvette à l'aide d'une spatule.

<sup>1</sup>partie pour cent d'élastomère

Pour étudier l'évolution de la surface au cours du glissement, 4 surfaces ont d'abord été observées pour plusieurs distances glissées (les essais sont réalisés sans interruption et les images correspondent donc à 4 éprouvettes différentes). Les essais d'usure ont été réalisés sous une charge normale de  $377\text{ N}$  ( $0,2\text{ MPa}$  rapporté à l'aire de contact apparente) et une vitesse de rotation de  $32\text{ RPM}$  ( $0,10\text{ m.s}^{-1}$  sur le rayon médian). Plusieurs vues caractéristiques de la surface pour des distances glissées différentes sont montrées fig. 4.

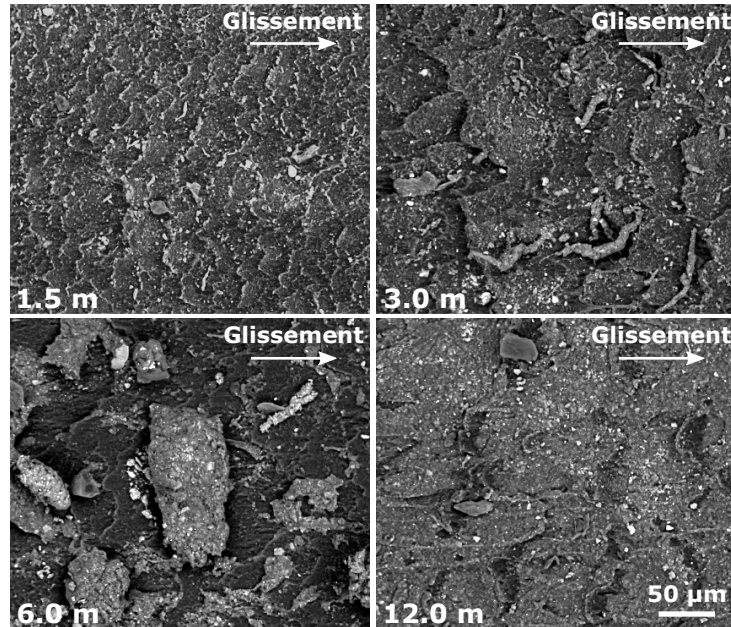


Figure 4: Images MEB avec un contraste correspondant au numéro atomique (Z-contrast) pour 4 distances glissées (1,5, 3,0, 6,0 et 12,0 m)

Pour une distance glissée de 1,5 m, de nombreuses particules (zones claires) composées d'un mélange de gomme et de minéraux sont visibles. Ces particules sont principalement situées près des rides de la surface. Pour une distance glissée de 3,0 m, ces particules sont plus grandes et moins nombreuses, ce qui suggère la formation d'agglomérats de particules. En outre, de petites particules restent visibles sur la surface, comme on peut le voir pour la distance glissée de 1,5 m. Une explication possible est que, parallèlement à l'agglomération des particules existantes, de nouvelles particules continuent à être générées car la quantité de minéraux reste suffisante pour le faire. Pour une distance glissée de 6,0 m, les particules sont à nouveau plus grandes et moins nombreuses. Certaines particules semblent avoir été cisailées et écrasées en surface. La plus grosse particule au centre de l'image a une forme allongée dans la direction orthogonale au glissement, avec plusieurs inclusions minérales. Elle correspond à l'aspect typique d'une particule d'usure de pneumatique [Kreider et al., 2010; Adachi and Tainosho, 2004; Morris and Kossyrev, 2018].

Pour une distance glissée de 12,0 m, seules quelques petites particules sont encore visibles. Deux mécanismes pourraient expliquer cette observation. Le premier est que, comme aucun minéral n'est ajouté pendant l'expérience, tous les minéraux seront à un moment donné éjectés ou incorporés. Cela entraîne un changement dans la génération de particules. Une autre explication est qu'au fur et à mesure que les particules à la surface deviennent de plus en plus grosses, la contrainte peut dépasser la résistance au cisaillement de ces particules. Cela conduit à la fragmentation de ces agglomérats, comme on peut le voir pour la distance glissée de 6,0 m. Des résultats similaires concernant la fragmentation des particules ont été obtenus numériquement [Milanese et al., 2020]. Une coupe longitudinale de l'éprouvette est réalisée après essai pour une



distance glissée de 3,0 m et est montrée fig. 5.

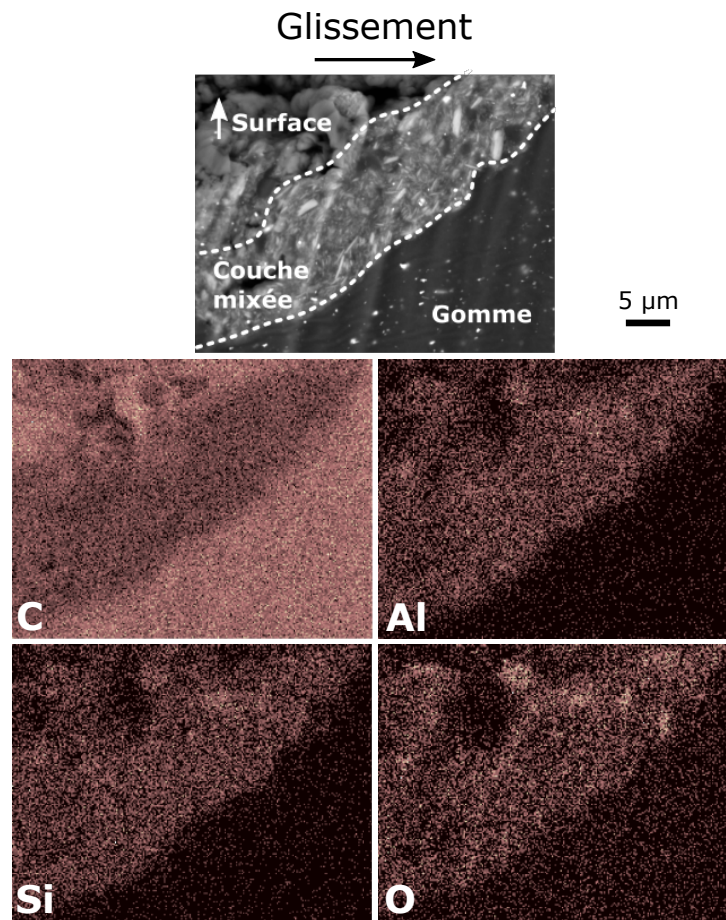


Figure 5: Image MEB avec un contraste correspondant au numéro atomique (Z-contrast) et cartes EDX correspondantes pour le carbone (C), l'aluminium (Al), le silicium (Si) et l'oxygène (O); la section longitudinale est obtenue par une coupe à la guillotine suivie d'un polissage ionique (Gatan, Ilion II); la charge normale est de 1508 N (0,8 MPa rapporté à l'aire de contact apparente), la vitesse de rotation de 32 RPM ( $0,10 \text{ m.s}^{-1}$  sur le rayon médian) et la longueur glissée de 3,0 m

Il apparaît ainsi que des minéraux ont été mélangés à la gomme jusqu'à une distance de 10-12  $\mu\text{m}$ . Un mélange de minéraux et de gomme est visible près de la surface. En effet, l'analyse EDX met en évidence une couche mixée avec une concentration plus élevée en C, Al, Si et O, ce qui est caractéristique de la composition de la kaolinite. De plus, il n'y a pas d'aluminium et de silicium dans la composition de la gomme. Cela ne peut donc être attribué qu'à la kaolinite. Les minéraux ont la forme de fines plaquettes. Il convient de noter que les taches blanches dans la zone sans minéraux correspondent à de l'oxyde de zinc (ZnO), qui est un agent de vulcanisation. Il existe une frontière nette entre la couche contenant des minéraux et celle sans minéraux.

Trois hypothèses peuvent être proposées pour expliquer cette frontière. Dans le cas d'un processus diffusif, la première est que la vue ne concerne que le premier stade de la diffusion et que celle-ci se poursuivra en raison du gradient proche de la frontière. Toutefois, cette hypothèse ne peut expliquer entièrement un tel gradient de concentration. La deuxième est que le matériau n'est pas suffisamment dégradé en dessous de cette frontière. En effet, une hypothèse est qu'il y a une dégradation des propriétés de la gomme lors du cisaillement, permettant aux minéraux de migrer. Cependant, cette dégradation est complexe et dépasse le cadre de cette étude. Enfin,



la troisième est une différence de taux de cisaillement de part et d'autre de la frontière. En effet, comme il sera vu par la suite, le taux de cisaillement pilote la diffusion. Cette dernière hypothèse sera étudiée en détail, en examinant les liens entre cinématique et diffusion.

## Indentation

Pour déterminer les propriétés mécaniques de la gomme et les incorporer dans le modèle numérique de diffusion, une analyse inverse d'un essai d'indentation est effectuée. Les essais d'indentation sont réalisés à des taux de déplacement constants et pour une profondeur maximale d'indentation ( $h_{max}$ ) de  $1 \mu m$ . Un modèle numérique d'indentation est aussi créé. Près de la pointe, le matériau est modélisé comme un ensemble de 1463 corps déformables circulaires. Les diamètres sont proches de la distribution utilisée pour le modèle de diffusion et suivent une distribution gaussienne avec une valeur moyenne ( $d_M^{rubber}$ ) de  $0,148 h_{max}$  et un écart type de  $0,026 h_{max}$ . Le domaine discret est délimité par un corps déformable et continu ayant les mêmes propriétés (modèles de contact et constitutif) que les corps du domaine discret. Le déplacement prescrit est nul sur sa frontière inférieure. La pointe a un demi-angle d'apex de  $70,3^\circ$ . Une illustration du modèle est donnée fig. 6.

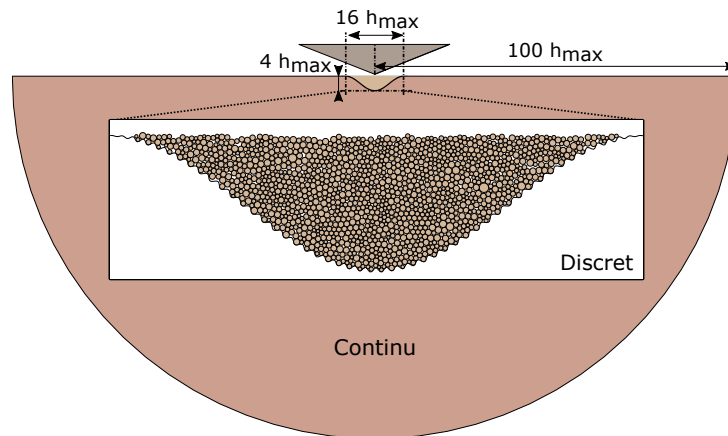


Figure 6: Illustration du modèle numérique d'indentation

Entre les corps discrets de la gomme, un modèle de contact purement cohésif est défini avec une composante normale ( $C_n$ ) et une composante tangentielle ( $C_t$ ). La composante normale est une contrainte limite de traction (le lien entre deux corps est supprimé si la force par unité de surface dépasse cette valeur). La composante tangentielle est une contrainte résistante (similaire à une force de frottement). Il est supposé que les deux sont égales et elles sont regroupées sous un seul paramètre appelé cohésion ( $C$ ). Tous les corps discrets représentant la gomme sont déformables. Un modèle hyperélastique Néo-Hookéen est utilisé avec notamment un module de Young ( $E$ ), appelé rigidité par la suite. Les essais sont effectués en supposant une cinématique de déformation plane et des conditions quasi-statiques. Le but de l'analyse inverse est de trouver la valeur de  $C$  et  $E$  de la gomme. Il n'y a pas de frottement entre l'indenteur et la gomme. Un exemple de la cinématique obtenue est présenté fig. 7 (la cohésion  $0.40 E$  n'est pas affichée car elle est très similaire à la cohésion  $0.20 E$ ).

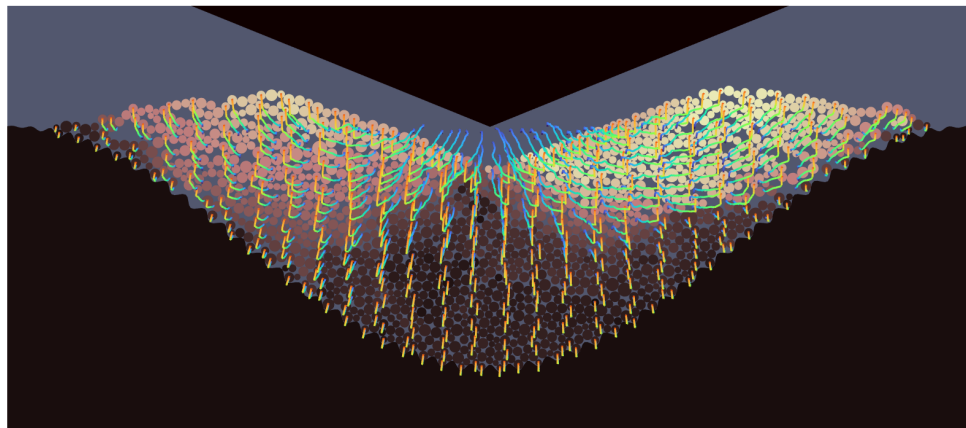
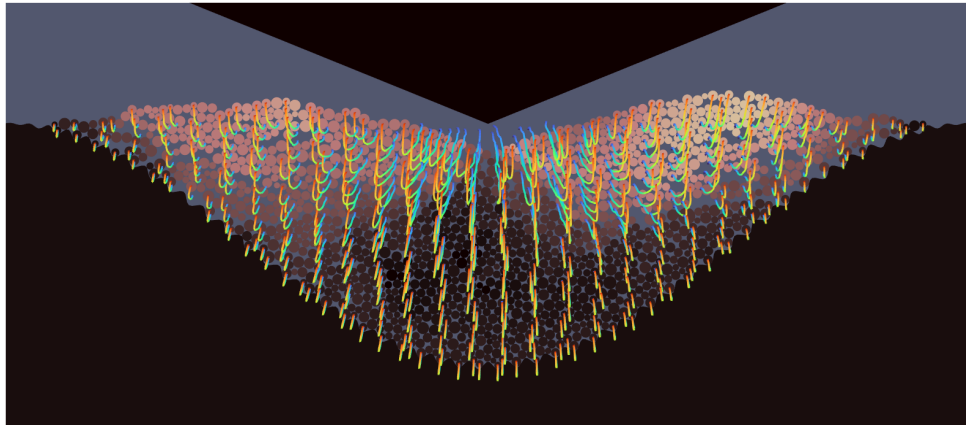
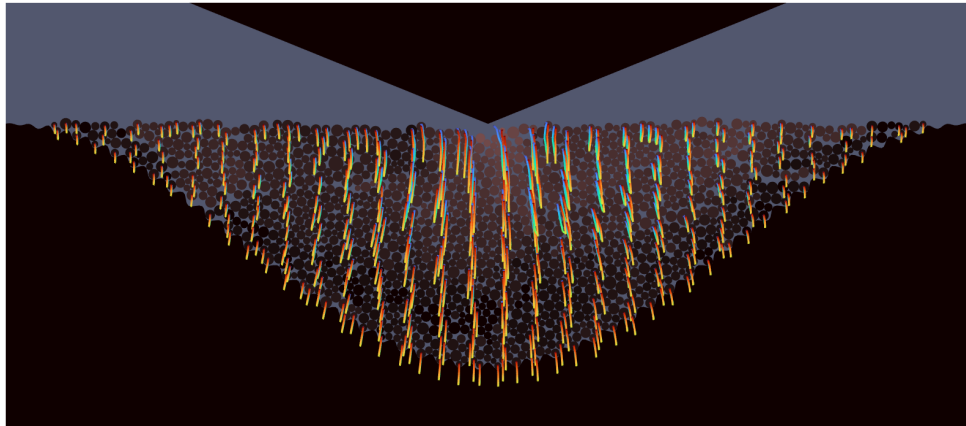
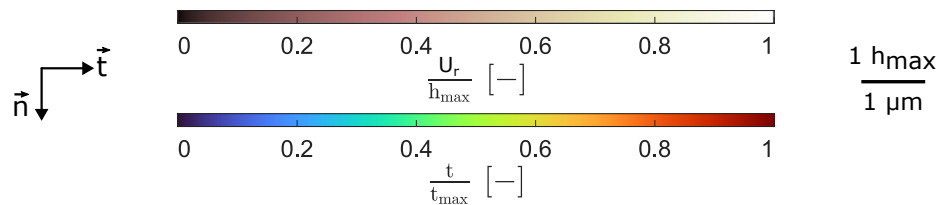
(a)  $C = 0.05 E$ (b)  $C = 0.10 E$ (c)  $C = 0.20 E$ 

Figure 7: Cinématique selon la cohésion normalisée ( $E = 5 \text{ MPa}$ ); le fond correspond au champ de déplacement résiduel ( $U_r$ ) normalisé par la profondeur maximale d'indentation ( $h_{max}$ );  $U_r$  est égal à la norme du déplacement de chaque centroïde entre l'état initial et l'état final; les lignes correspondent aux différentes positions des centroïdes au cours de l'indentation et la couleur au temps ( $t$ ) normalisé par le temps auquel l'indenteur est revenu à sa position initiale ( $t_{max}$ )

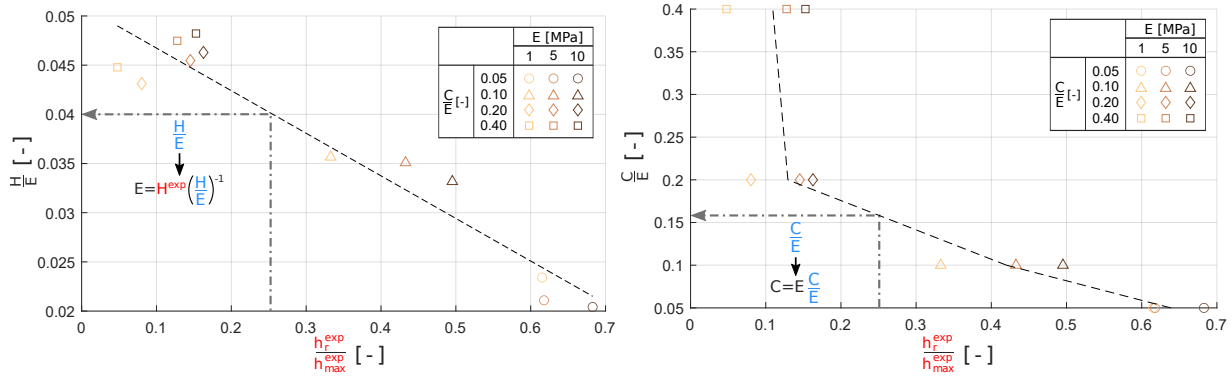
La plasticité peut être décrite comme un déplacement irréversible de la matière, qui correspond aux corps discrets dans ce modèle. Par conséquent,  $\frac{U_r}{h_{max}}$ ,  $U_r$  étant le déplacement résiduel, peut être considéré comme une quantité analogue à la plasticité. Les simulations vont d'indentations élasto-plastiques à des indentations élastiques. En effet, pour la cohésion la plus faible,  $U_r$  est localement supérieur à  $0.70 h_{max}$ , alors que pour la cohésion la plus élevée, il est plus proche de  $0.05 h_{max}$  dans l'ensemble du domaine. Pour une cohésion de  $0.05 E$ , les valeurs de  $U_r$  les plus élevées sont situées près de l'indenteur et les corps discrets forment une bosse à la surface. Cette bosse diminue avec l'augmentation de la cohésion. Pour des cohésions de  $0,05$ ,  $0,10$ ,  $0,20$  et  $0,40 E$ , le  $U_r$  maximum est respectivement égal à  $0,77$ ,  $0,57$ ,  $0,15$  et  $0,11 h_{max}$ . Cependant, pour des cohésions de  $0,20$  et  $0,40 E$ ,  $U_r$  n'est supérieur à  $0,05 h_{max}$  que pour un petit volume et il apparaît donc négligeable. Ces résultats sont cohérents avec d'autres études utilisant des modèles continus pour des indentations élasto-plastiques. Par exemple, il est montré numériquement dans [Taljat and Pharr, 2004] que la forme de bosse observée en surface est proportionnelle au rapport de la limite élastique divisée par la rigidité, qui est étroitement lié à  $\frac{C}{E}$ .

Pour obtenir une meilleure visualisation du flux de matière, plusieurs centroïdes sont suivis et représentés par des lignes fig. 7. Pour les corps discrets situés sous la pointe de l'indenteur, le déplacement normal augmente pendant le chargement ( $t < 0,5 t_{max}$ ) et diminue pendant le déchargement ( $t > 0,5 t_{max}$ ). Pour les corps plus éloignés de l'apex et proches de la surface, le déplacement normal augmente de manière continue pour la cohésion la plus faible. Quant au déplacement tangentiel, il augmente aussi de manière continue (ou est nul) pendant le chargement et est constant pendant le déchargement. Cela montre que l'écoulement tangentiel est essentiellement plastique (il n'y a pas de retour élastique tangentiel) alors que l'écoulement normal est élastique ou élasto-plastique. On peut également noter que le déplacement des corps plus en profondeur est plus faible lorsque la cohésion diminue. Ceci s'explique par une diminution de la charge avec l'augmentation du degré de plasticité.

L'analyse inverse est réalisée à partir de deux grandeurs mesurées expérimentalement. La première est la dureté ( $H$ ), qui correspond au rapport de la charge maximale au cours de l'indentation divisée par l'aire de contact correspondante. La seconde est le rapport de la profondeur résiduelle ( $h_r$ ) divisée par  $h_{max}$ . La profondeur résiduelle correspond à la profondeur à laquelle le contact est perdu entre l'indenteur et la surface. Pour une configuration donnée, cette profondeur est liée à la limite élastique du matériau. Comme cette profondeur n'est pas une déformation et qu'aucune limite élastique n'est formellement définie, la facilité du matériau à plastifier sera désignée ci-après par le terme "degré de plasticité". La valeur de ces paramètres, obtenus par une campagne de simulations, est présentée fig. 8.

Les paramètres avec un exposant "exp" font référence aux paramètres précédents qui peuvent être obtenus expérimentalement mais dont la valeur obtenue numériquement est affichée. La dureté est linéairement proportionnelle à la rigidité. Par conséquent, une variation de  $\frac{H}{E}$  en fonction de  $\frac{h_r^{exp}}{h_{max}^{exp}}$  indique l'influence du degré de plasticité sur la dureté. Il a été montré que plus le degré de plasticité est élevé, plus la dureté diminue (cf. fig. 8a). De plus,  $\frac{h_r^{exp}}{h_{max}^{exp}}$  est directement lié au rapport  $\frac{C}{E}$ . Plus ce rapport est faible, plus le degré de plasticité est important (cf. fig. 8b). Il est donc possible de déterminer  $E$  et  $C$  à partir de  $H$  et  $h_r$  mesurés expérimentalement.

L'un des principaux défis de l'analyse inverse est de garantir l'unicité de la solution. Cela signifie qu'un couple  $H$  et  $h_r$  doit donner un couple unique de  $E$  et  $C$ . Pour une gamme de cohésions normalisées inférieures à  $0,20$ - $0,40 E$ , les courbes de tendance sont strictement monotones sans atteindre une asymptote verticale, ce qui garantit l'unicité. En comparant ces données avec des mesures expérimentales, la valeur de  $E$  et  $C$  en fonction du taux de déformation



(a) Dureté normalisée en fonction de la profondeur résiduelle normalisée; la ligne pointillée correspond à une régression linéaire (b) Cohésion normalisée en fonction de la profondeur résiduelle normalisée; la ligne pointillée relie la valeur moyenne pour chaque cohésion normalisée

Figure 8: Méthode d'identification de  $E$  et  $C$  à partir d'une analyse inverse; les rapports obtenus numériquement sont mis en évidence en bleu et les valeurs qui peuvent être extraites des mesures en rouge

a été estimée. Par exemple, pour un taux de déformation de  $0,4 \text{ s}^{-1}$ , la rigidité est égale à  $18 \text{ MPa}$  et la cohésion à  $1,75 \text{ MPa}$ .

## Pénétration des minéraux

Une illustration du modèle numérique de diffusion est présentée fig. 9. L'objectif est de reproduire le dispositif expérimental (cf. fig. 3), qui consiste à cisailer une couche de minéraux par l'intermédiaire d'une surface semblable à un sol routier. Les minéraux et la surface de la gomme sont considérés comme une collection de corps discrets pour modéliser la diffusion. La surface assimilable au sol routier et le cœur de la gomme, pour lesquels la diffusion n'est pas attendue, sont modélisés comme des corps continus. Le sol routier et les minéraux sont considérés comme rigides, tandis que les particules de gomme sont considérées comme déformables. La taille des minéraux (en forme d'ellipse) suit une distribution log-normale, avec un diamètre équivalent moyen ( $D_M$ ) égal à  $0,1166 \mu\text{m}$ . Un modèle constitutif Néo-Hookéen est défini pour la gomme. Le type de modèle de contact entre les différents corps et la valeur des paramètres associés seront modifiés d'une simulation à une autre pour en étudier l'effet, tout comme la rigidité de la gomme. Il convient de noter que la configuration est inversée verticalement par rapport au contact pneu-chaussée, afin d'être cohérent avec le tribomètre utilisé expérimentalement. Cependant, la gravité est supposée nulle car elle est négligeable à cette échelle par rapport aux efforts de contact. Les résultats sont donc indépendants de l'orientation verticale. De plus, la pression de contact et la vitesse de glissement sont appliquées par le sol routier. Le déplacement transversal du sol routier est nul. Le cœur de la gomme a un déplacement longitudinal et transversal nul sur sa surface inférieure.

Les mécanismes au début du glissement diffèrent des mécanismes à plus long terme. En effet, ils correspondent davantage à une réorganisation progressive de la couche de minéraux, conduisant à un mélange initial de gomme et de minéraux. Ceci est différent de la vision d'un processus stochastique, tel que proposé dans le cadre de la diffusion. Cette étape doit donc être étudiée séparément et déterminera le taux d'apport en minéraux dans la gomme. Dans les simulations actuelles, une quantité relativement faible de minéraux est utilisée, et tous les minéraux sont la plupart du temps rapidement incorporés dans la gomme. Par conséquent, cette étape correspond principalement au début du glissement. Cependant, avec une quantité

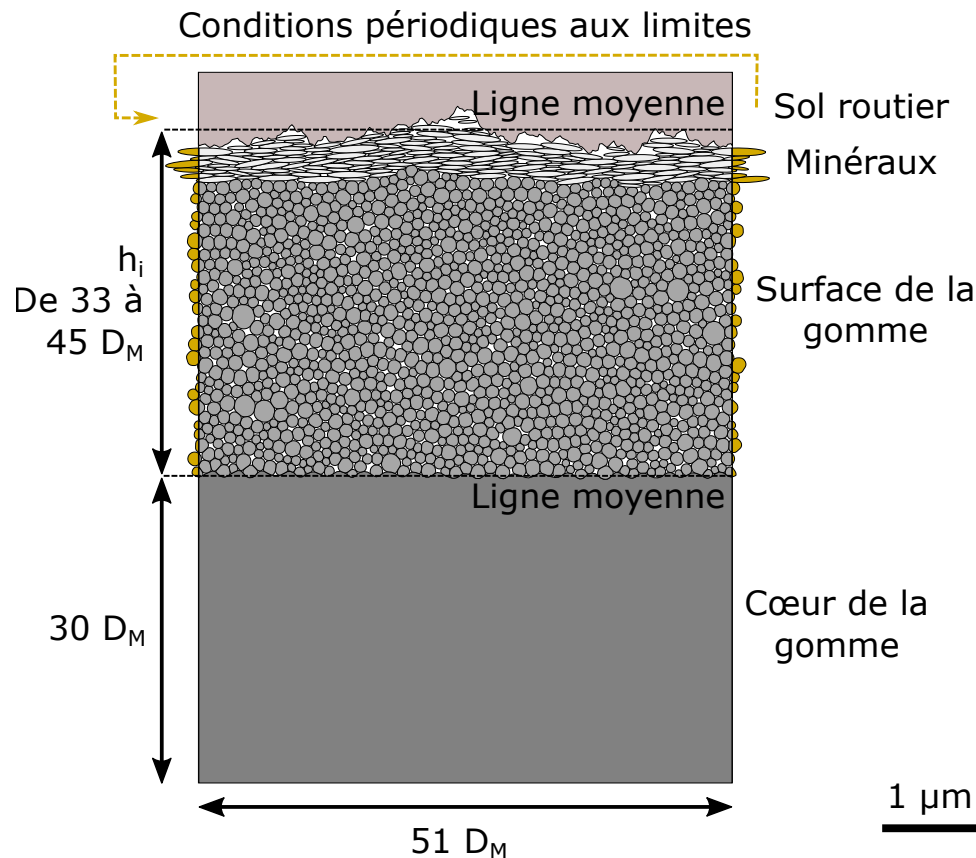


Figure 9: Illustration du modèle numérique de diffusion

plus importante, cette étape se produirait en parallèle de la diffusion des minéraux déjà incorporés, et est donc importante pour comprendre la diffusion globale. De plus, dans certaines configurations numériques, la pénétration des minéraux est si lente que certains minéraux ont déjà complètement diffusé, alors que d'autres commencent à peine à être incorporés. Enfin, certains phénomènes, comme la formation d'agglomérats, sont largement dictés par le mode de pénétration.

Le mode de pénétration le plus courant pour les configurations testées est un mécanisme pouvant être qualifié de labour. En raison de la distribution de tailles, de la forme et de la rigidité des minéraux, la couche de minéraux est relativement hermétique et présente une résistance au cisaillement importante par rapport à la couche de gomme. Pour ces raisons, la réorganisation locale de la couche de minéraux tend à former des aspérités à la surface de la gomme. Au fur et à mesure que les aspérités augmentent en taille, la contrainte de cisaillement augmente progressivement sur la couche de minéraux, qui se déforme de plus en plus. À un moment donné, la déformation devient si importante, qu'un agglomérat de minéraux est incorporé à la gomme. En fonction de la quantité de minéraux, ce processus est ensuite répété jusqu'à ce que tous les minéraux soient incorporés.

Le mécanisme de labour nécessite une réorganisation locale de la couche de minéraux, ce qui peut s'avérer impossible si la pression de contact est trop élevée. Il nécessite également une couche de minéraux suffisamment résistante pour résister au cisaillement, mais pas trop résistante pour pouvoir se déformer. Si les points ci-dessus ne sont pas respectés, il en résulte un mécanisme d'abrasion. En raison d'une légère réorganisation de la couche de minéraux, la contrainte de cisaillement est transmise par certains minéraux qui ont partiellement pénétré



dans la gomme, ainsi que par les efforts de cohésion entre la gomme et les minéraux. Dans le cas d'une pression de contact significative, les minéraux sont principalement orientés le long de l'axe de cisaillement, et ils exercent donc localement une force de cisaillement importante sur la gomme. Enfin, la force de frottement entre les minéraux est inférieure à la force de cisaillement transmise, et les agglomérats de minéraux sont incorporés dès que l'axe de cisaillement coïncide avec la frontière d'un minéral.

Le dernier mécanisme est spécifique à une gomme très cohésive et pour une épaisseur de couche interfaciale constante. Si la cohésion est importante, il est plus difficile pour la gomme de dissiper l'énergie introduite par le cisaillement, ce qui conduit à des phénomènes cycliques de stockage et de libération d'énergie. Ce phénomène est comparable à l'ouverture d'une fissure. Tout d'abord, une réorganisation de la couche de minéraux se produit également, mais sur des temps très courts du fait des efforts de cisaillement plus élevés. L'énergie peut être stockée jusqu'à ce que la contrainte dépasse la valeur de la cohésion. Dans ce cas, le lien cohésif est supprimé et une fissure s'ouvre. Cela entraîne une réaction en chaîne due à l'affaiblissement d'une bande de cisaillement. Il est à noter que ces mécanismes de fissuration sont principalement observés lors de la pénétration des minéraux, et dans une bien moindre mesure par la suite.

Il apparaît que la pénétration est retardée lorsque la rigidité de la gomme augmente. La raison principale est que pour un matériau plus mou, les minéraux peuvent plus facilement poinçonner la gomme, créant une localisation importante de la contrainte et initiant ainsi la pénétration plus rapidement. Pour une gomme plus rigide, le matériau est moins déformé et les minéraux ont tendance à glisser sur la surface. Cela conduit à un mécanisme proche de l'abrasion. Un résultat surprenant de prime abord est que plus la cohésion de la gomme est élevée, plus la pénétration est rapide. La raison est similaire à celle donnée pour la rigidité. La pénétration est facilitée par le poinçonnement d'un minéral sur la gomme, créant des localisations de la contrainte. Cependant, pour des valeurs de cohésion faibles, le lien cohésif entre les particules de gomme est rompu avant qu'une déformation significative ne soit atteinte. Par conséquent, un plan de glissement se produit à proximité de l'interface minéral-gomme, mais est cette fois-ci formé au sein de la gomme.

## Diffusion des minéraux

Lorsque les minéraux ont été suffisamment incorporés à la couche interfaciale, les mécanismes responsables de la migration sont différents de ceux observés précédemment. En prenant l'exemple d'une simulation, certains des résultats principaux concernant cet état plus avancé sont présentés fig. 10.

Tout d'abord, la position transversale ( $y$ ) d'un seul minéral (fig. 10a) peut être examinée en fonction de la distance glissée ( $s$ ), les deux étant normalisées par le diamètre équivalent moyen des minéraux ( $D_M$ ). Cette position correspond à la distance projetée dans la direction orthogonale au glissement entre le centroïde d'un minéral et la ligne moyenne du sol routier. Elle révèle une trajectoire erratique, avec une position qui se rapproche ou s'éloigne du sol routier. On peut également noter que pour une faible distance glissée ( $< 200 D_M$ ), il y a une évolution rapide et continue de la position. Cela suggère un changement dans les mécanismes de migration des minéraux. Maintenant, si l'on suit les trajectoires de tous les minéraux (fig. 10b), on constate qu'ils suivent une certaine tendance à migrer de plus en plus profondément. Ceci conduit à une homogénéisation de la concentration minérale ( $\varphi$ ) dans la couche interfaciale en fonction du temps (fig. 10c). On peut également noter qu'au début du glissement, il y a un certain effet de retenue des minéraux, avec une concentration plus élevée proche de la surface, qui diminue sur des temps plus longs que l'évolution du front. Ceci est dû au fait qu'il existe une densité maximale de minéraux, qui nécessite une progression suffisante du front pour que

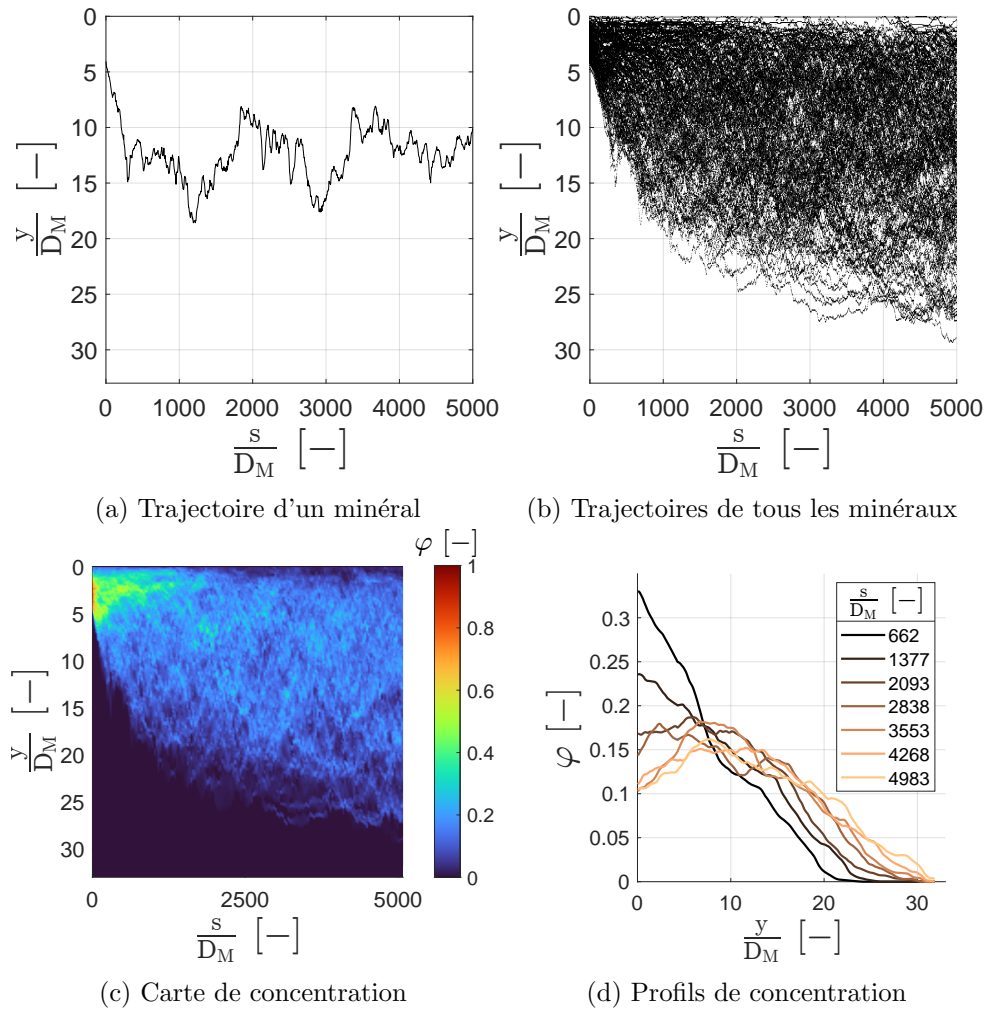


Figure 10: Principaux résultats concernant la diffusion

les minéraux restants commencent à migrer. L'évolution de la concentration en fonction de la profondeur suit une distribution gaussienne, qui tend à s'aplatir à mesure que la distance glissée augmente (fig. 10d).

Ces résultats sont très similaires à ceux pouvant être obtenus avec un algorithme de marche aléatoire ou en utilisant la 2e loi de Fick (loi décrivant un processus diffusif). En effet, dans un premier temps, le comportement semble stochastique à l'échelle d'un seul minéral, puis se révèle déterministe lorsque l'on considère l'ensemble des minéraux. De plus, on obtient une distribution gaussienne qui s'aplatit au cours du temps. Cela montre que ce processus est similaire à un processus diffusif, même s'il n'y a pas de notion de potentiel chimique. Cela permet notamment d'utiliser certains outils d'analyse spécifiques à la diffusion. Le fait de trouver des résultats similaires à ceux d'un processus diffusif est directement lié aux mécanismes de migration des minéraux, représentés fig. 11.

En raison du taux de cisaillement, les minéraux incorporés ont une vitesse relative entre eux, ce qui induit de nombreux contacts car les minéraux doivent se chevaucher. Deux modes de chevauchement sont observés. Le premier est dû à la forme non circulaire des minéraux. En effet, les minéraux sont en rotation continue et peuvent donc se croiser sans induire un déplacement transversal (cf. fig. 11a). Le second mode est un mécanisme plus classique, tel qu'il pourrait être obtenu dans un fluide ou milieu granulaire, avec un déplacement monotone des deux minéraux (cf. fig. 11b). En fonction de plusieurs facteurs (suivant les forces appliquées

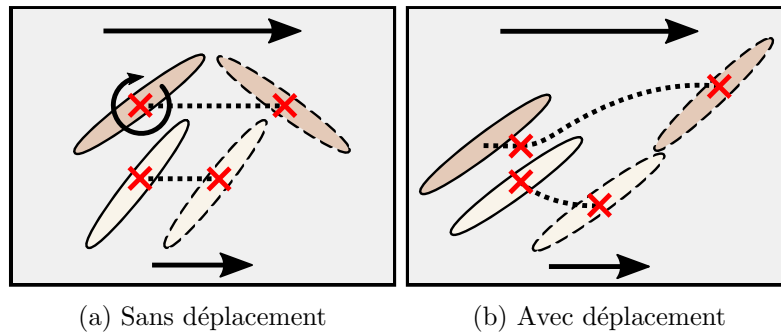


Figure 11: Illustration des mécanismes de chevauchement

sur les minéraux), le décalage peut être plus grand que le diamètre du minéral. De plus, ces deux modes peuvent être combinés, ce qui donne lieu à un décalage partiel. Dans cette étude, la migration des minéraux est induite par des contacts répétés. Chaque variation de position observée précédemment correspond à un contact entre minéraux. Dans le cas d'un processus diffusif "classique", ce sont également des contacts répétés, mais entre molécules sous l'effet de l'agitation thermique. Les deux processus, bien que de nature différente, conduisent à la diffusion.

La diffusion d'un minéral est directement liée à la variation de sa vitesse transversale (i.e. dans la direction orthogonale au glissement). Cette variation est à la fois locale en espace et brève en temps. Il est cependant possible de définir une vitesse caractéristique maintenue pendant un temps caractéristique, comme proposé dans [Macauley and Rognon, 2019]. Cette vitesse et ce temps permettent donc de remonter à un déplacement et donc à la diffusion. La vitesse caractéristique est appelée fluctuation de la vitesse et correspond à l'écart type de la vitesse transversale. Le temps de maintien, appelé persistance, correspond à l'intégrale de la fonction d'autocorrélation de la vitesse transversale.

En ce qui concerne les paramètres indépendants des propriétés de la gomme, plusieurs d'entre eux ont une influence sur la diffusion. Tout d'abord, lorsque la pression de contact augmente, la diffusion diminue. Ceci est attribué à une diminution de la fluctuation de la vitesse. Par ailleurs, il a été constaté que cette fluctuation est directement liée au taux de cisaillement et à la projection transversale moyenne de la surface des agglomérats de minéraux. Le taux de cisaillement dépend peu de la façon dont les minéraux sont distribués dans la couche, mais dépend fortement de la quantité totale de minéraux.

Concernant les propriétés de la gomme, il a été montré que la diffusion ne dépend pas de la rigidité, mais seulement de la cohésion. Cependant, il est important de rappeler que la rigidité est un paramètre majeur, mais uniquement en ce qui concerne la pénétration. Une plus grande cohésion augmente le stockage de l'énergie qui, lorsqu'elle est libérée, entraîne une variation importante de la vitesse transversale et donc une augmentation de la fluctuation de la vitesse. Il est également à noter que la persistance diminue avec la cohésion. Toutefois, cette diminution est inférieure à l'augmentation engendrée par la fluctuation de la vitesse, et la diffusion augmente donc fortement avec la cohésion.

## Conclusion et perspectives

Dans un premier temps, ce travail s'est concentré sur le développement d'une méthode de caractérisation adaptée aux particules déformables. Cette méthode implique une analyse inverse d'essais d'indentation, afin d'identifier les paramètres numériques que sont la rigidité et



la cohésion du matériau. Contrairement aux modèles discrets d'indentation plus conventionnels, cette approche permet un retour élastique significatif pendant la décharge. La cinématique obtenue est cohérente et l'unicité de la solution est vérifiée.

Concernant le cisaillement des minéraux sur une gomme de pneumatique, l'utilisation d'un matériau déformable comme la gomme permet d'observer plusieurs mécanismes de pénétration : le labour, l'abrasion et la fracturation. Le labour domine en raison de la plus grande résistance de la couche de minéraux. La pénétration rapide dépend de la capacité des minéraux à poinçonner la gomme, influencée par des paramètres tels que la rigidité et la cohésion de la gomme.

Le processus de migration des minéraux est assimilable à un processus diffusif, avec un comportement stochastique à l'échelle d'un minéral, puis déterministe si l'ensemble des minéraux est considéré. Le processus de diffusion est caractérisé par des variations locales et brèves de la vitesse transversale. Plusieurs paramètres modifient la diffusion. Par exemple, la cohésion a un effet significatif, montrant que la diffusion est un processus avant tout plastique.

Ce travail met en évidence plusieurs résultats intéressants et des pistes de réflexion à approfondir. Premièrement, il ressort que la diffusion pour les configurations testées est un processus irréversible influencé par la cohésion du matériau plutôt que par sa rigidité. Le rôle de la composante visqueuse de la gomme reste cependant assez flou et mériterait d'être approfondi. En effet, des changements de viscosité pourraient avoir un impact sur les forces exercées sur les minéraux et, par conséquent, sur la diffusion.

Cette étude soulève également des questions sur la relation complexe entre la diffusion des minéraux et le taux d'usure. Le taux de cisaillement, qui dépend de la quantité de minéraux présents dans la gomme, influence la diffusion. Cependant, cette quantité dépend directement du taux d'usure. De plus, lors des essais expérimentaux réalisés pour plusieurs distances glissées, une évolution significative de l'aspect de la surface a été observée. Ceci peut être interprété comme un changement dans les mécanismes d'usure, dû à l'éjection de minéraux. Cependant, le modèle actuel n'est pas en mesure de modéliser cette transition, qui peut avoir une origine différente de la modification du taux de cisaillement.

# Abstract

It can be seen from longitudinal sections of a tire tread that road minerals penetrate inside the tire. The aim of this work is to study experimentally and numerically the process leading to this penetration for an experimental configuration taken as a reference. This work is articulated around three main objectives.

The first was to propose a method for characterizing the rubber-like material, adapted to the numerical model used subsequently. To this end, a reverse analysis of an indentation test was carried out. The numerical model considers the material to be composed of a multitude of discrete and deformable bodies. The parameters to be identified are the stiffness and cohesion between each discrete body. The study showed that the kinematics obtained is close to that measured experimentally. A convergence criterion for the reverse analysis was defined, based on hardness and residual depth. It has been shown that the effect of stiffness can be isolated from that of cohesion. Since their dependence on the convergence criterion is monotonic, the solution is unique.

A numerical model was then developed to study mineral penetration and migration. It consists in shearing a layer of minerals on the surface of a rubber-like material, modeled as a collection of discrete and deformable bodies. First of all, it was shown that the initial penetration of minerals into the material differs from that observed over longer periods of time. In particular, three modes of penetration were defined: plowing, abrasion and fracture. These modes modify the rate at which minerals penetrate into the material.

When the minerals are sufficiently embedded within the material, they form what is referred to as the mixed layer. Minerals migrate deeper and deeper, due to repeated contacts between mineral agglomerates, caused by their relative velocities (characterized by the shear rate). In particular, it has been shown that these contacts lead to a stochastic evolution of the position of a mineral. If all the minerals are considered, the behavior becomes deterministic and follows an evolution close to what is expected for a diffusive process. This last point allows the use of diffusion tools, in particular the evaluation of a diffusion coefficient through transverse velocity fluctuation and persistence. It was shown that these two parameters are highly dependent on local plastic phenomena, which in the current model are driven by cohesion.



# General introduction

Tires are both an important and a complex product. Indeed, it is used extensively throughout the world, and although it has been in use for many years now, some of its properties are still misunderstood. In fact, a tire is composed mainly of rubber, a material with remarkable properties. Notably, one surprising observation is that if a longitudinal section of a tire tread is observed, then road minerals can be observed at significant depths inside the tire.

This penetration over significant depths is quite unexpected for a solid material. However, it is very important to understand its origin and effect. Indeed, the presence of minerals will potentially modify the mechanical properties of the tire. These properties are important from a safety point of view, as they govern the grip of the tire on the road. In addition, from an environmental point of view, the wear properties of the tire may also be affected. This phenomenon is at the crossroads of three major disciplines.

- The first is the field of rubber-like materials. Indeed, the properties of this type of material are highly complex. For example, they are time and temperature dependent, with potentially a non-linear behavior. In addition, this dependence is a function of the composition of the material, and there are probably as many compositions as there are applications, making analysis particularly challenging.
- The penetration of these minerals may be due to the shearing action between the tire and the road. This shear, coupled with the fact that there is a mixture of materials, involves the field of tribology. In particular, it refers to the concept of the tribological circuit, describing the flow of materials within the contact.
- The migration of one material into another can have many origins. It can fall into a general class of mechanical mixing, but also into what is known as diffusion. The latter has very distinct characteristics, notably that of a stochastic process that can be described using specific tools.

The aim here is to bring these three disciplines together. The migration of minerals inside a soft material such as rubber, into a sheared interface and with diffusion-like properties, is not yet understood. The objective of this work will therefore be to provide an initial understanding of why and how road minerals migrate into the tire tread. Once this has been achieved, a more in-depth understanding, in particular of the influence of different parameters, will be provided.



# Chapter 1

## State of the art and strategy

In this chapter, the objectives and context of this work are presented. To this end, rubber-like materials will first be introduced in section 1, focusing on their development and properties. Tire properties will then be presented in section 2, detailing the tire structure and its friction and wear properties. The tribological framework with the concept of third body and tribological circuit is described in section 3. A brief overview of the Hertz framework and related theories will be discussed in section 4. The existing friction and wear models will be presented in sections 5 and 6 respectively. Finally, the objectives and strategy employed will be developed in section 7.

### 1 Rubber-like materials

#### 1.1 From tree to automobile

##### 1.1.1 Genesis

It is difficult to discuss about tires without introducing rubber. Compared to the use of metals by modern man, the history of rubber is quite recent. The first archaeological evidence of the use of natural rubber comes from Mesoamerica, 3000 years ago [Serier, 1988]. Several excavations have uncovered figurines and balls made of rubber that were used in ball games, as shown fig. 1.1 [Keoke and Porterfield, 2002].



Figure 1.1: Monument 171 from Tonina showing a Maya ball game (from D. Stuart)

Before rubber can be obtained, latex must be collected by tapping a groove in the bark of a tree such as *Hevea brasiliensis*. Then, often in the form of a sticky white liquid, the latex flows slowly through the groove. When the latex is left in the open air, a coagulation process occurs

and latex solidifies to form the rubber we all know. This process has since been perfected, in particular to control the rate of coagulation.

### 1.1.2 Development

A few millennia were necessary to see an industrial exploitation. Everything accelerated with the European colonization of the Americas. This began with the importation of rubber samples by Charles Marie de La Condamine (1701-1774). He left the port of La Rochelle for South America to settle the controversy between Isaac Newton and Jacques Cassini about the shape of the earth. In 1745, he presented to the French Royal Academy of Sciences his observations and the mission report of the engineer of the King François Fresneau (1703-1770) [Petitet and Barquins, 2008]. The report describes the properties of the rubber and how it is collected.

An important milestone leading towards tires is the development of the vulcanization process. It is always difficult to distinguish myth from reality, but it was apparently discovered by Charles Goodyear (1800-1860). One evening in 1840, Charles Goodyear put a piece of sulfur-coated rubber (from a mailbag) on a stove. The piece caught fire, and when Charles Goodyear realized this, threw the piece outside. The next day, when he went to collect the sample, he was surprised to find that the piece was more elastic and less adhesive. He had thus unintentionally carried out the key stages of the vulcanization process [Petitet and Barquins, 2008]. However, the ownership of the process is highly controversial and was already partially mastered by the Mesoamericans [Hosler et al., 1999]. The work of Charles Goodyear seems to have been stolen by Thomas Hancock (1786-1865), who benefited from the economic spin-offs in Europe. The term vulcanization was proposed by William Brockedon (1787-1854) in reference to Vulcan, the god of fire including the fire of volcanoes, where sulfur is collected. This process is the cornerstone of tire manufacturing (an example is shown fig. 1.2) and explains the subsequent development of rubber materials.



Figure 1.2: Worker removing a tire from an industrial oven used for vulcanization and molding in 1943 (from Flickr, BiblioArchives/LibraryArchives)

### 1.1.3 A growth through the velocipedes

Initially, bicycles were devoid of pedals (as shown in fig. 1.3), which were added only in the 1860s to the front wheel, resulting in the bicycles known as velocipedes. The ancestor of the tire was a rubber band glued to the rims of velocipede wheels and developed by Thomas Sparow in

1868 [Serier, 1987]. Thanks to the many bicycle races won, this rubber coating quickly became popular compared to the usual metal rims. The invention of the tire (i.e. air-inflated) and more akin to a bicycle inner tube at the time, is attributed to John Boyd Dunlop (1840-1921) in 1888. At the time, tires were very fragile and glued to the rim, requiring several hours to change. The turning point for the tire we know today is a meeting between Edouard Michelin (1859-1940) and a cyclist in Clermont-Ferrand in France. Indeed, this event led to the invention in 1891 of the first dismountable bicycle tire by Edouard and André Michelin (1853-1931). Always under the influence of bicycle racing, this system became increasingly popular. In Europe, a double envelope with the inflated chamber covered by a tire soon appeared, which is the same technique used today. The progress of tires was then motivated by the automotive industry, which offered a greater technical challenge.



Figure 1.3: Pedestrian hobbyhorse, 1819 (from National Cycle Museum, Wales)

The final reason contributing to the expansion of the tire market is the development of synthetic rubbers. In 1879, Gustave Bouchardat (1842-1918) developed the first synthetic polyisoprene. Then, in 1909, Fritz Hoffmann (1866-1956) and his team also succeeded in polymerizing isoprene but on a more industrial scale. The first synthetic rubber to be commercialized was the neoprene in 1931, by the company Du Pont De Nemours. Synthetic rubber development was accelerated due to supply problems caused by geopolitical conflicts. For example, in 1940, the United States launched the “US Government Synthetic Rubber Research Program”, partly (but not only) because of the Second World War. The share of use between natural and synthetic rubber has fluctuated over the course of the 20th century. In 1980, the share of synthetic rubber had overtaken that of natural rubber (NR), mainly due to styrene-butadiene rubber (SBR), a trend that continues to this day [Serier, 1993]. Natural rubber is still widely used, notably in glove production and more generally in the medical field.

## 1.2 Manufacturing

### 1.2.1 Polymer

Rubber belongs to the class of polymeric materials. A polymer, as its name suggests, is made up of several monomers. A monomer is a molecule that can react with other monomers. For example, isoprene, which can be produced by plants and animals, is a monomer that is the main component of natural rubber. Its formula is represented in fig. 1.4.

Monomers (and therefore polymers) are essentially made of carbon. Due to interactions between other monomers, the same pattern of one or more monomers is repeated a multitude of times. An isomer is a special case in which all the monomers have the same chemical formula.





Figure 1.4: Isoprene

Because of this repetition, polymers are composed of long chains with the same pattern of atoms. These long chains are often used to explain the properties of the material on a larger scale. The reaction between the monomers is called polymerization. It can be achieved (e.g. in a reactor) by several methods, such as bulk, suspension, emulsion, two-step swelling and precipitation polymerization [Pérez-Moral and Mayes, 2004]. Isoprene polymerization can produce several isomers (as shown in fig. 1.5). However, rubber is mainly composed of cis-1,4-polyisoprene.

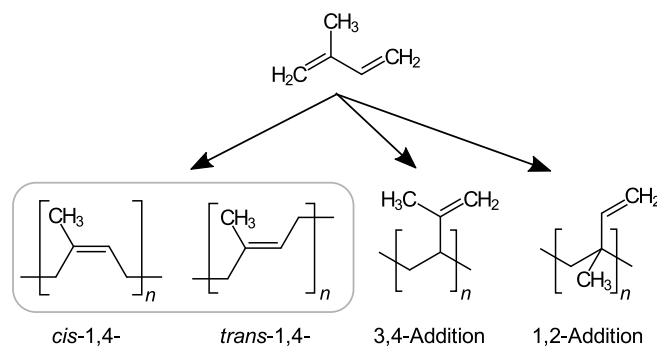


Figure 1.5: Polyisoprene (from Roland Chem)

The previous case remains relatively simple, because in practice, a chain can be composed of different monomers. This type of polymer is called a copolymer. A widely used copolymer is the styrene-butadiene rubber, also known as SBR. It is an essential component of tires and of many other applications.

### 1.2.2 Compounds

For high-performance applications, or simply to reduce costs, it is rare to use a polymer alone. Instead, several compounds are added. This makes it possible to adjust the properties of the material according to a specific application. Indeed, for this type of material, the benefit of one property often translates into the loss of another. Tailoring is therefore a crucial step for rubber manufacturers. The main compounds are summarized below:

- Fillers: mostly carbon black and silica; changes are manifold (mechanical, electrical, chemical, etc.), such as an increase in tensile stiffness [Edwards, 1990]
- Diluent: talc, chalk, sawdust, etc.; contributes to reducing costs
- Plasticizer: facilitates the mixing process (discussed thereafter); decreases viscosity, glass transition temperature, hardness, etc. [Altenhofen da Silva et al., 2011]
- Vulcanizing agent: mostly sulfur; required for the vulcanization process (discussed thereafter)

- Protective agents: amino derivatives such as 6PPD; to preserve the properties of the material during storage and subsequent use, as its structure can be altered by the effects of the environment (temperature, light, etc.)

### 1.2.3 Mixing

The compounds presented in the previous sections are usually in a granulated or powder form. This requires an additional step to obtain a homogeneous mixture of all the compounds. An example of several compounds before mixing is shown in fig. 1.6.



Figure 1.6: Granules and powders used in the mixing process

There are several types of mixing processes, but two main ones can be mentioned [Petitet and Barquins, 2008]:

- Mixer consisting of two co-axial cylinders with a relative velocity; the spacing between the two cylinders and the relative velocity depend on the mixture; the process must be performed several times
- Mixer with an endless screw; the process can be carried out in a single operation but may lead to excessive temperature rise; can be coupled with the process described above to obtain a particular shape

After these operations, the mixture usually takes the form of a roll or sheet plate (fig. 1.7), whose thickness depends on the manufacturer and the application. A rolling process can also be carried out afterwards.



Figure 1.7: Rubber mixture after the mixing process (from indiamart)

### 1.2.4 Vulcanization

The cross-linking of polymer chains is a crucial process for tires, otherwise the properties of the material would not be at all as expected. The vulcanization process refers to cross-linking using sulfur. Sulfur is first added to the rubber mixture as previously described. The material is then cured. In the case of a tire, a mold can be used to shape the grooves (see fig. 1.2). The temperature and duration of vulcanization are part of the expertise of rubber manufacturers. A simplistic view of polyisoprene vulcanization can be found fig. 1.8.

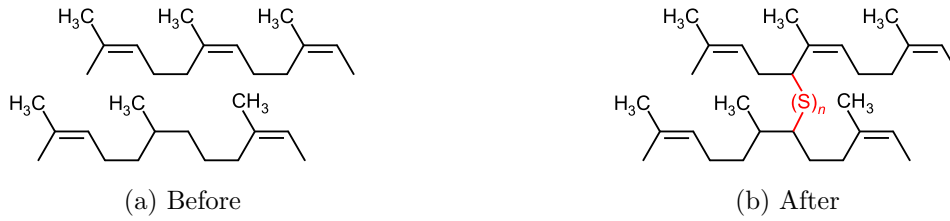


Figure 1.8: Vulcanization of polyisoprene

The polymer chains are linked by  $n$  sulfur atoms in series. One of the main purposes of vulcanization is to increase the elastic recovery of the material. Sulfur bonds can be considered as springs that facilitate the return of polymer chains to their initial state. It can be evaluated by the so-called loss tangent or loss angle in whose relationship is given by eq. (1.1).

$$\tan(\delta) = \frac{E''}{E'} \quad (1.1)$$

with  $\delta$  the loss angle describing the dissipation of the material under cyclic loading,  $E''$  the loss modulus describing viscosity and  $E'$  the storage modulus describing elasticity. If a cylinder is subjected to a radially oscillating load, the deformation may be shifted by an angle  $\delta$  with respect to the loading axis. An illustration for an oscillating displacement can be found in fig. 1.9.

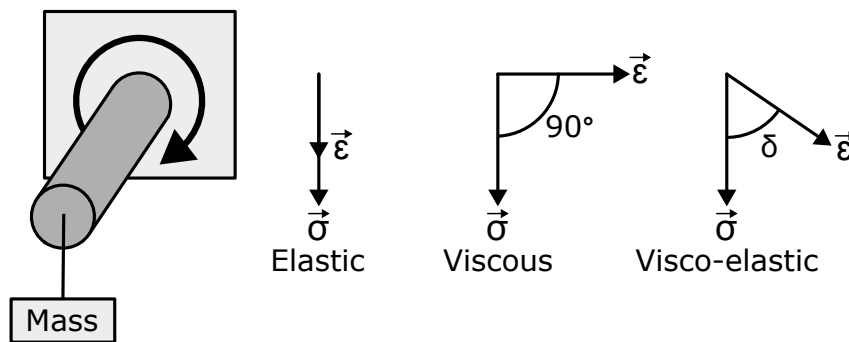


Figure 1.9: Illustration of the loss angle

If the stress ( $\sigma$ ) is plotted as a function of time, as well as the strain ( $\epsilon$ ), then the two signals will be out of phase according to the value of  $\delta$ . This offset is linked to dissipation under cyclic loading, the so-called hysteresis. The higher is the dissipation, the higher is the  $\delta$ . It is therefore zero for a purely elastic material. As discussed later, a significant contribution to the kinetic friction coefficient ( $\mu$ ) is due to dissipation under cyclic loading. The loss angle is therefore an important material property.

It was shown in [Boochathum and Prajudtake, 2001] that for a polyisoprene,  $\tan(\delta)$  can be divided up to 2.3 after vulcanization (depending on temperature). This is mainly due to a decrease in the loss modulus, as the storage modulus remains approximately constant [Fan et al., 2020]. Due to the increase in elastic recovery, the material after vulcanization is often referred to as an elastomer, in contrast to the initial polymer. The advantages of vulcanization are numerous, as illustrated in fig. 1.10.

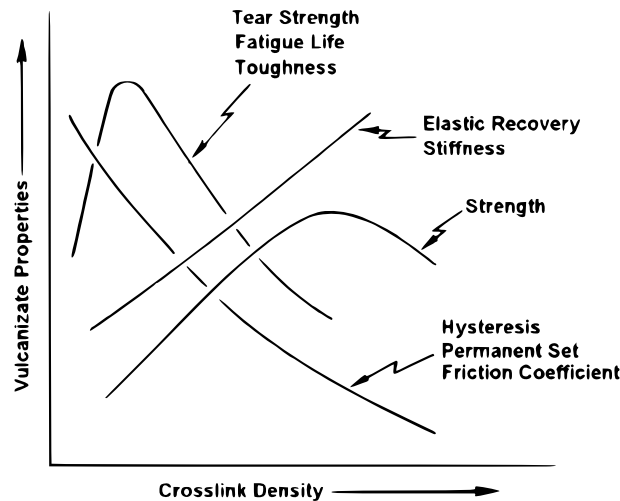


Figure 1.10: Properties as a function of crosslink density (from [Coran, 2003])

## 1.3 Properties

### 1.3.1 Temperature dependency

The behavior of polymeric materials is highly dependent on temperature. Hereafter, for the sake of simplicity, the storage modulus ( $E'$ ) will be referred to as modulus. In addition, emphasis will be put on the mechanical response of the material, although the effects are manifold. An illustration of the temperature dependency can be found in fig. 1.11.

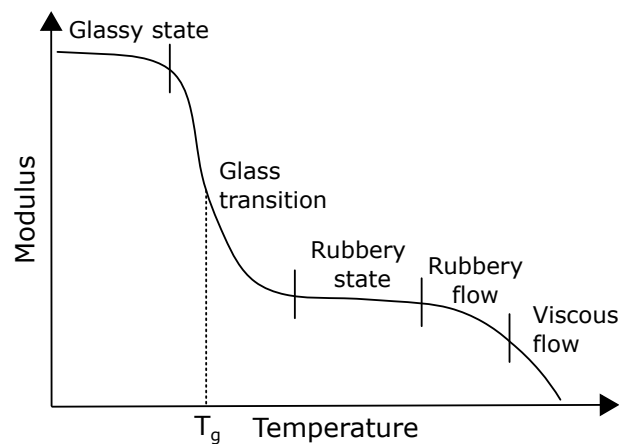


Figure 1.11: Modulus as a function of temperature

Several temperature-dependent regions can be observed:

- Glassy state: molecular movements are reduced to vibrations and low amplitude rotations, resulting in a high modulus
- Glass transition: fast transition with a significant change in modulus; linked to coordinated molecular movements of large amplitude; the corresponding temperature is called the glass transition temperature ( $T_g$ )
- Rubbery state: chains are more mobile and can stretch, resulting in a lower modulus, less sensitive to temperature

- Rubbery flow: depends on the time scale; for a short one, the material cannot relax; for a long one, the temperature allows the chains to move in a coordinated manner and then to flow
- Viscous flow: behavior similar to a Newtonian fluid

Behavior beyond  $T_g$  depends on several parameters. For a highly crosslinked elastomer, the decrease in modulus beyond  $T_g$  is smaller, and thermal decomposition (pyrolysis) occurs before the rubbery flow state is reached. Moreover, it also depends on whether the polymer is amorphous or semi-crystalline. For amorphous polymers, the rubbery state tends to disappear, and the modulus decreases continuously after  $T_g$ . Even if the material is used beyond  $T_g$ , the gap between the temperature of use and  $T_g$  is an important design parameter. The glass transition temperature strongly depends on the material, with a value of  $-70\text{ }^\circ\text{C}$  for natural rubber [Loadman, 2005] and  $170\text{ }^\circ\text{C}$  for polycarbonate [Shamim et al., 2014]. Moreover,  $\tan(\delta)$  also depends on temperature, with a parabolic dependency peaking at  $T_g$ . An important step for the rubber manufacturer, is to adapt the formulation to obtain the most appropriate  $T_g$  according to the application.

### 1.3.2 Time dependency

The modulus also depends on the loading time (referred to as time thereafter). This time may correspond to a frequency (e.g. road roughness) or a velocity (e.g. tensile velocity). There is a close link between time and temperature. At low frequencies, time is sufficiently high to allow local rearrangement of polymer chains, resulting in a lower modulus. At higher frequencies, local rearrangement is restricted and artificial blockage occurs, resulting in a higher modulus. The effect of temperature is similar, facilitating or preventing this rearrangement. A correspondence between time and temperature has been established for linear viscoelasticity, the so-called time-temperature superposition [Urzhumtsev, 1975]. It can be described by the WLF (Williams-Landel-Ferry) model [Williams et al., 1955], whose main principle is described in eq. (1.2).

$$E(t, T) = E(a_{T \rightarrow T_0} t, T_0) \quad (1.2)$$

with  $E$  the modulus,  $t$  the time,  $T$  the temperature,  $a$  the horizontal translation factor and  $T_0$  a reference temperature. The model is valid only for linear viscoelasticity and for temperatures ranging from  $T_g$  to approximately  $T_g + 100\text{ }^\circ\text{C}$ . The equation of the horizontal translation factor can be found in eq. (1.3).

$$\log(a_{T \rightarrow T_0}) = -\frac{C_1(T - T_0)}{C_2 + (T - T_0)} \quad (1.3)$$

with  $C_1$  and  $C_2$  positive constants depending on the material and the reference temperature  $T_0$ . If  $E(t, T_0)$  is plotted on a logarithmic space for a given temperature  $T_0$ , and then for another temperature  $T_1$ , the modulus will be shifted horizontally by a factor  $a_{T \rightarrow T_0}$ . For this reason,  $a$  is called the translation factor. It is therefore possible to overlap the curves using  $a_{T \rightarrow T_0}$ , and the resulting curve is called the master curve. Many results, such as the friction coefficient, also obey this correspondence [Grosch and Bowden, 1997]. In particular, from eqs. (1.2) and (1.3), this model can be used to predict modulus at temperatures or times that cannot be reached experimentally. For example, lower and higher  $t$  can be predicted by  $T$  values in a given  $t$  interval [Álvarez Vázquez et al., 2020], as illustrated in fig. 1.12.

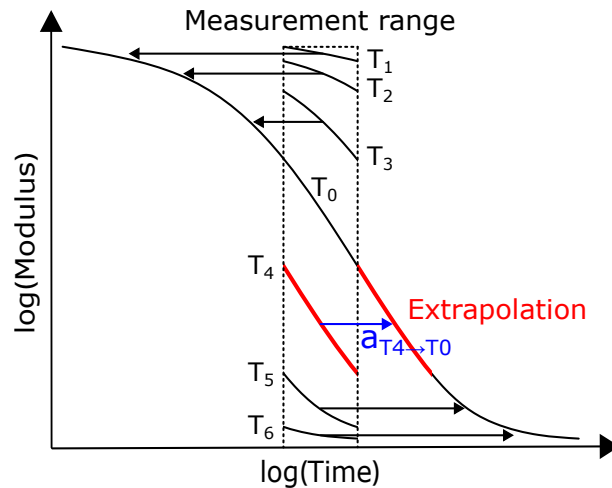


Figure 1.12: Extrapolation using the WLF method

### 1.3.3 Strain dependency

In addition to time and temperature dependencies, the modulus is not constant at small strains ( $< 10\%$ ). This is known as the Payne effect, described for the first time in [Payne, 1962]. It can be defined as a non-linear softening effect of rubber materials for increasing strain, which is important for materials subjected to cyclic loading. Indeed, this type of loading generally operates at small strains, making the non-linearity of the modulus important to take into account. This effect is attributed to the breakage and recovery of weak bonds between filler structures [Wang, 1999].

Several studies have investigated the influence of the fillers on the Payne effect. For example, [Shi et al., 2021] performed oscillating shear. The tests were carried out for different amounts of carbon black fillers, for different shear strain amplitudes and for a given loading frequency. The significance of the Payne effect is expressed by the variation in modulus as a function of strain amplitude. It was shown that for a low fraction of carbon black, the Payne effect was almost zero, while for the highest fraction, the modulus can be divided by 5 in the linear viscoelastic region. It is therefore highly dependent on filler content, which is consistent with the proposed mechanism. This was already demonstrated by A. R. Payne, as illustrated in fig. 1.13. Above approximately 10% strain, the modulus becomes independent of strain (e.g. fig. 1.13). This is because all weak bonds are broken and polymer chains become increasingly parallel. Modulus is thus the result of the elongation of these untangled chains. This mechanism is the basis of several constitutive models, describing the orientation of polymer chains according to a probability function [Edwards, 1965]. However, the modulus becomes non-constant again at strains exceeding several hundred percent, making the behavior difficult to model [Kawahara et al., 2022].

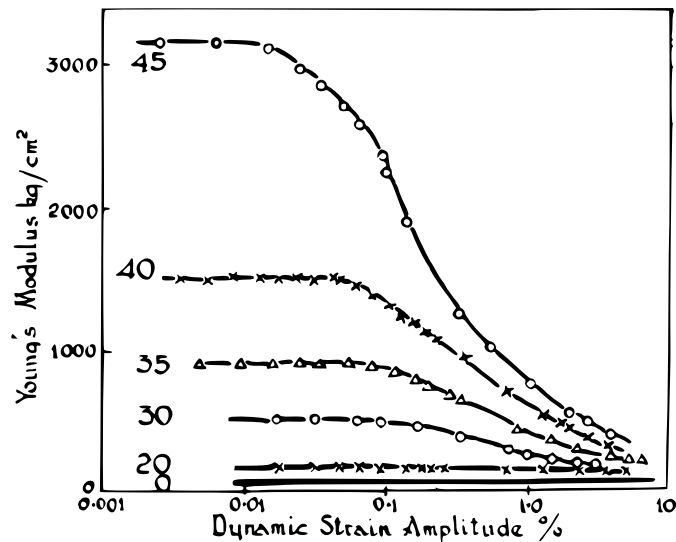


Figure 1.13: Modulus of a natural rubber as a function of the dynamic tensile strain amplitude and for different amounts of carbon black fillers given as a percentage of total volume (from [Payne, 1962])

### 1.3.4 Mullins effect

The Mullins effect corresponds to a softening effect of rubber-like materials during the first loading cycles. It was first described in [Mullins, 1969] and has since been extensively studied. For example, in [Diani et al., 2009], an oscillating tension test with a 50 phr carbon black filled SBR is performed and the results are displayed in fig. 1.14. Mullins effect occurs whenever the maximum strain exceeds the maximum strain previously encountered. To highlight this, every 5 cycles, the maximum strain is increased. This corresponds to 3 changes in fig. 1.14 (i.e. Mullins effect should at least appear 3 times). It can be seen that for a given range of 5 cycles, the first cycle is very different from the others. Thereafter, the curves tend to overlap. According to this study, 10 cycles are generally necessary to consider this effect negligible, as long as the maximum strain is not exceeded. This effect appears in both filled and non-filled rubbers, such as natural rubber [Harwood et al., 1965]. The mechanisms are not fully understood, and could correspond to breakage of the filler structure [Kraus et al., 1966] or disentanglement [Hanson et al., 2005].

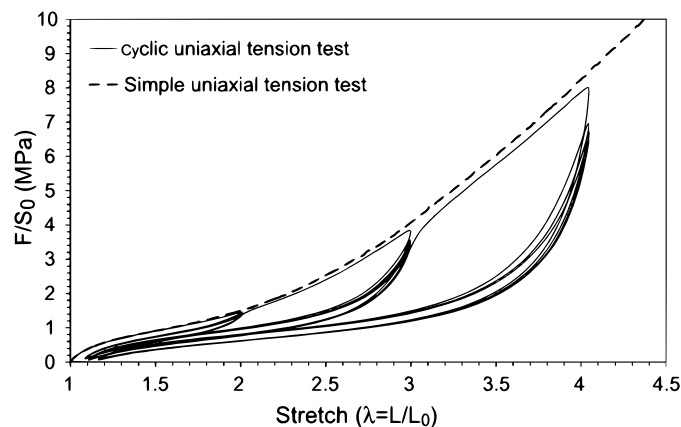


Figure 1.14: Stress-strain curves for a 50 phr carbon-black filled SBR under a simple and a cyclic uniaxial tension test (from [Diani et al., 2009])

### 1.3.5 Rheological models

The behavior of rubber-like materials is often described by rheological models. Assuming elastic springs ( $\sigma = E\varepsilon$ ) and viscous dampers ( $\sigma = \eta\dot{\varepsilon}$ ), a constitutive model  $\sigma(\varepsilon)$  can easily be derived. Note that the terms stiffness and modulus will be used without distinction, as their mechanical meanings are closely related. For these models,  $\sigma$  corresponds to stress,  $\varepsilon$  to strain,  $E$  to stiffness and  $\eta$  to viscosity. These models can be derived for tensile or shear loading. Springs and dampers can be connected in series, in parallel, or both, to form models of varying complexity. The three main ones are presented in fig. 1.15.

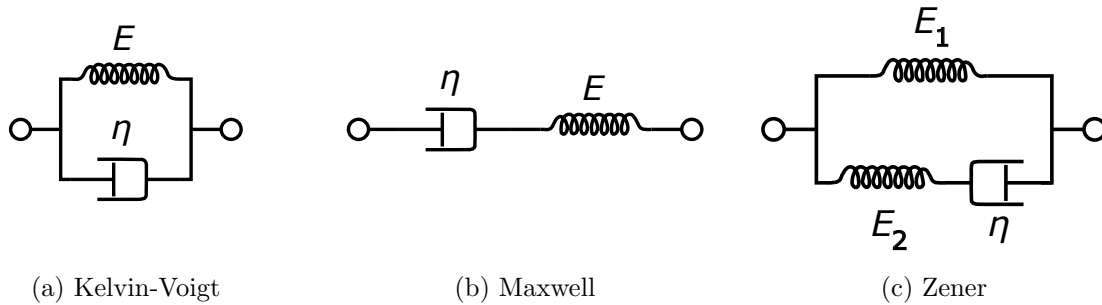


Figure 1.15: Rheological models describing rubber-like materials

These models can be summarized as follows [Bui and Chaillat, 2009]:

- Kelvin-Voigt: more appropriate for modeling solids; for a relaxation experiment, leads to an elastic behavior which is not consistent
- Maxwell: more appropriate for modeling fluids; for a creep experiment, leads to a liquid behavior which is not consistent
- Zener: simplest model to accurately describe the behavior of rubber-like materials with a non-zero modulus for a time tending towards infinity (unlike the model of Maxwell)

These models are useful for obtaining simple analytical solutions. More sophisticated models can be developed, but the greater the number of parameters, the more complicated identification becomes. In practice, for the numerical models, a strain energy density function is often preferred, such as the Ogden–Roxburgh model to take in account the Mullins effect [Ogden and Roxburgh, 1999].

## 2 Tire properties

### 2.1 Structure

A tire is a complex composite material made of several elements. An illustration of the main components can be found in fig. 1.16.



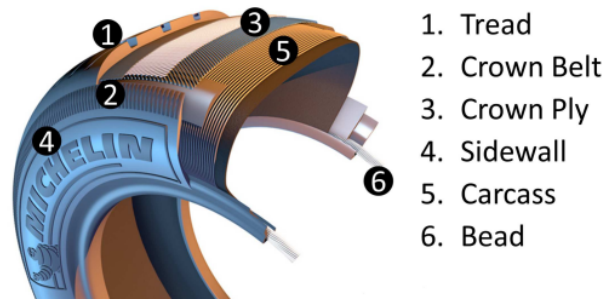


Figure 1.16: Structure of a radial tire

Each element has the following role:

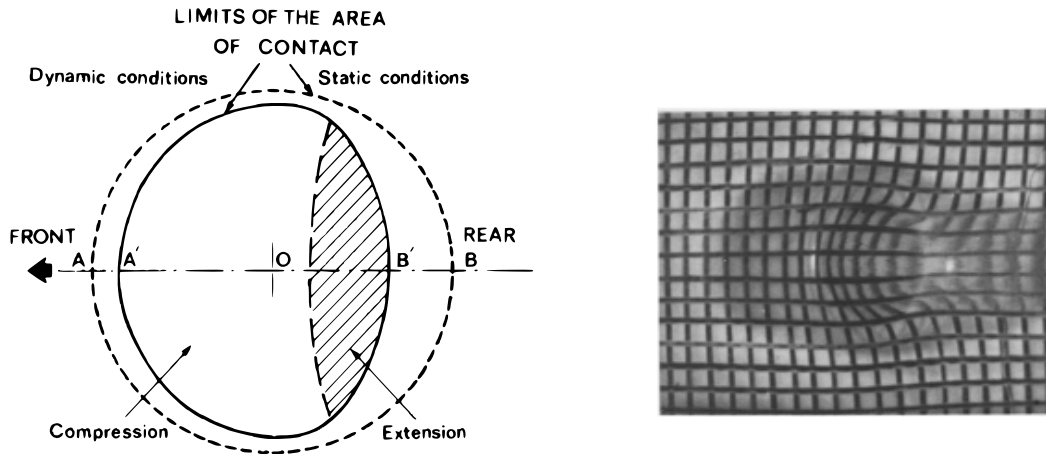
1. Tread: layer of rubber in direct contact with the road; grooves (if any) are molded directly into the tread; this will be the main component studied in this work
2. Crown belt: layer of textile cables to increase stiffness
3. Crown ply: layer of steel cables to connect the tread to the carcass and increase tread strength
4. Sidewall: made of rubber, connects the tread to the bead and protects the carcass
5. Carcass: made of one or several casing plies, it gives the tire its strength to withstand air pressure, the weight of the car or the shocks
6. Bead: reinforced steel cables to connect the tire to the wheel

Each rubber component has a specific formulation depending on the desired properties. For example, butyl rubber can be used for the inner liner to ensure a good sealing. As described previously, rubber sheet plates can be obtained during the manufacturing process (cf. fig. 1.7). At this stage, vulcanization has not yet been performed and the rubber is therefore very sticky. There are some specific aspects, but the manufacturing process is mainly based on positioning these layers on a building drum which can be inflated. This positioning is facilitated by the sticky property of rubber. Once the layers have been assembled, they are vulcanized. The result is a crosslinked tire whose grooves are shaped by the vulcanizing mold.

## 2.2 Friction

### 2.2.1 Stationary state

To have a better understanding of how tires slide, it is useful first to look at a simplified situation. Several studies have been carried out on transparent materials. A common approach is to use a hemispherical glass slider and a transparent rubber plate. The camera records through the slider and the contact is illuminated through the rubber plate. The pioneering work of [Schallamach, 1971] shows that the friction force in the contact can be divided into a compressive and tensile zone, as shown in fig. 1.17.



(a) Illustration of friction force with a compressive and tensile zone (from [Barquins, 1985]) (b) Rubber deformation represented by a mesh on its surface (from [Schallamach, 1971])

Figure 1.17: Sliding of a hemispherical glass slider on a transparent rubber plate in a stationary state

Note that the zones in fig. 1.17a are valid for a stationary state. These results are consistent with what is measured or numerically obtained for a tire. For example, in [Guan et al., 2023], a sensor array is developed to measure the tri-axial stress distribution of a real tire. The test was carried out on a 1502 kg vehicle, using a Michelin PRIMACY 4215/50R17 radial tire (four grooves) at a pressure of 2.4 bar. The vehicle drove over the sensor array at a constant speed of 16 km.h<sup>-1</sup>. The results are displayed fig. 1.18.

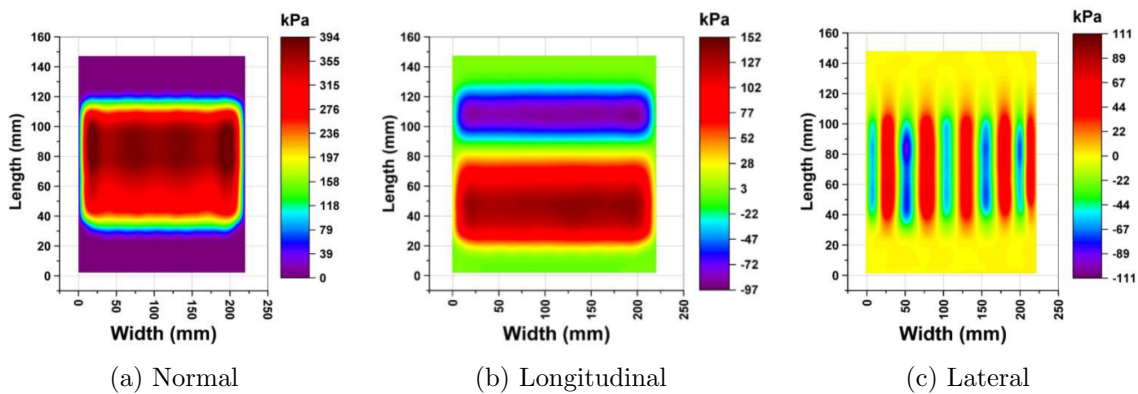


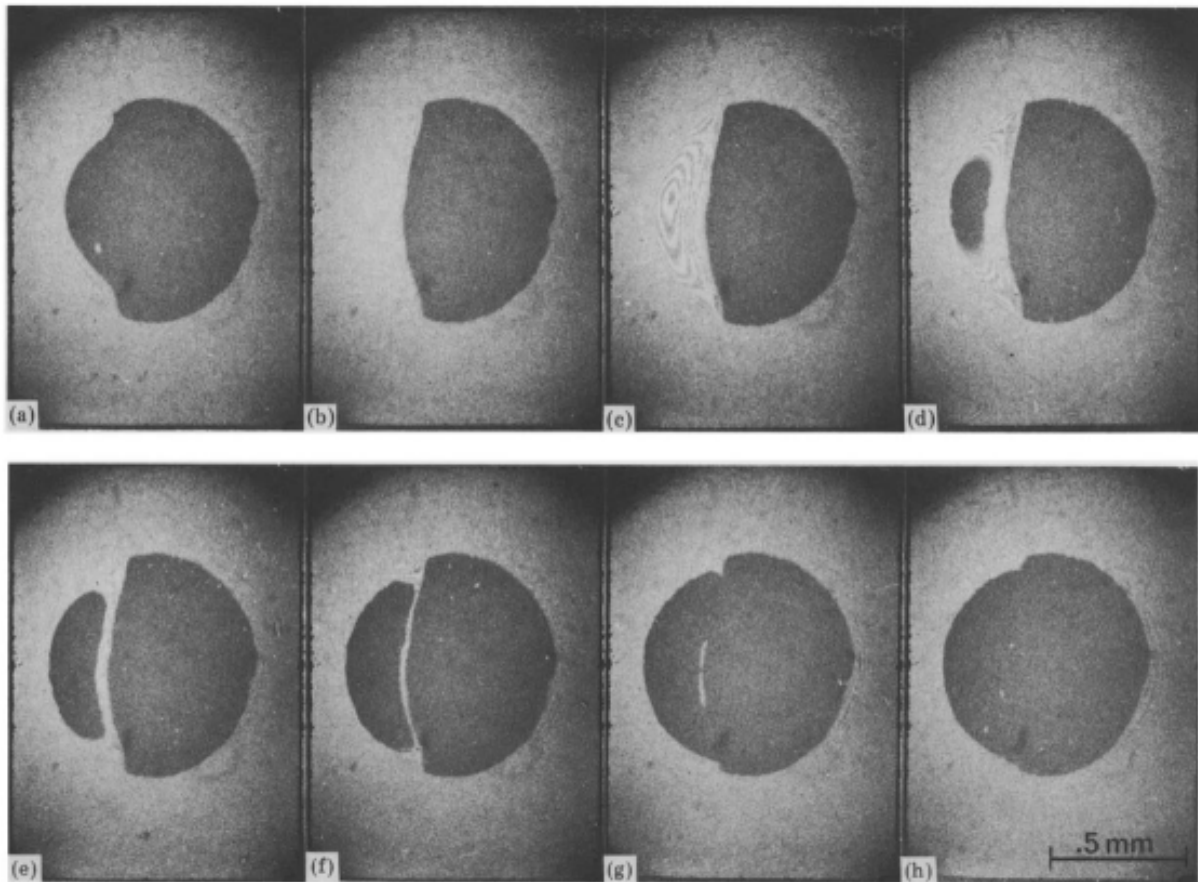
Figure 1.18: Load per unit area (from [Guan et al., 2023])

In fig. 1.18a, it can be seen that the contact pressure is close to 400 kPa with an apparent contact area of 90 x 215 mm<sup>2</sup>. In fig. 1.18b, a compressive and tensile zone can be observed, which is consistent with previous experiments (cf. fig. 1.17a). Finally, in fig. 1.18c, the effect of the four grooves is highlighted (there is also a slight effect on the contact pressure). However, each sensor measures a width of 15 mm, giving only 14 sensors across the width of the tire. Spatial resolution therefore prevents small-scale interpretations.

### 2.2.2 Peeling phenomenon

In [Barquins, 1985], experiments were carried out in the same configuration as described above, with a hemispherical glass slider and a transparent rubber plate. If the radius of curvature of the slider is large enough, the previous stationary regime is replaced by a new one (for an

8 mm radius instead of the 2 mm used previously). Successive snapshots and corresponding illustrations are shown in fig. 1.19.



(a) Successive snapshots

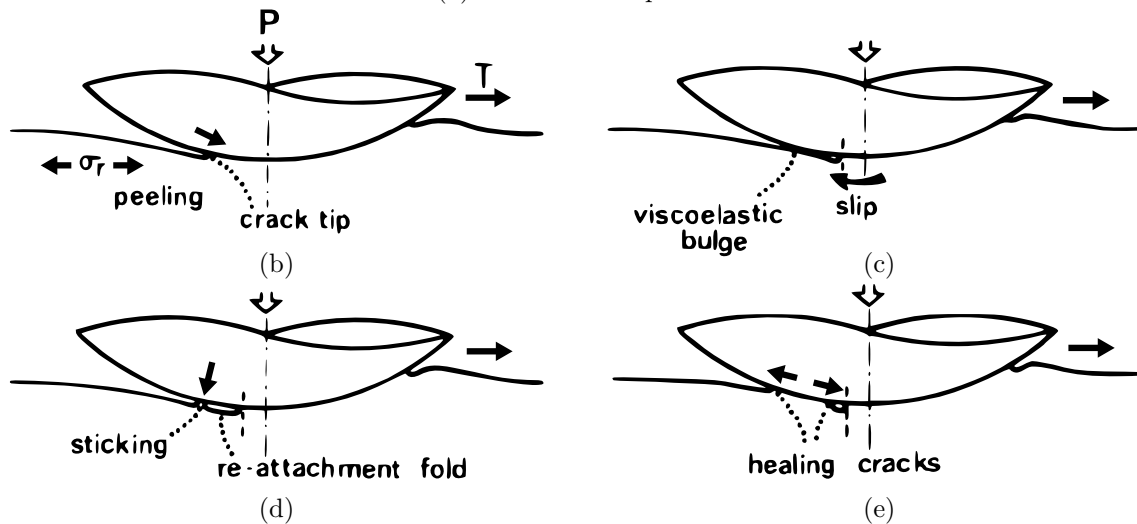


Figure 1.19: Sliding (from left to right) of a hemispherical glass slider on a transparent rubber plate in a non-stationary state (from [Barquins, 1985])

The following steps can be observed:

- Behind the slider, a crack tip appears at the rear of the contact (snapshots a to c and fig. 1.19b)

- The contact is renewed at the rear end, leaving a contact-free zone on the inside (snapshot d and figs. 1.19c and 1.19d)
- The contact-free zone becomes smaller and smaller (snapshots e to g and fig. 1.19e)
- There is no longer contact-free zone (snapshot h)
- This process is repeated again and again

### 2.2.3 Schallamach waves

Schallamach waves were first observed in [Schallamach, 1971]. In the same configuration as previously described (with a 2 mm radius of curvature), they were then studied in [Barquins, 1985] and the results are presented in fig. 1.20.

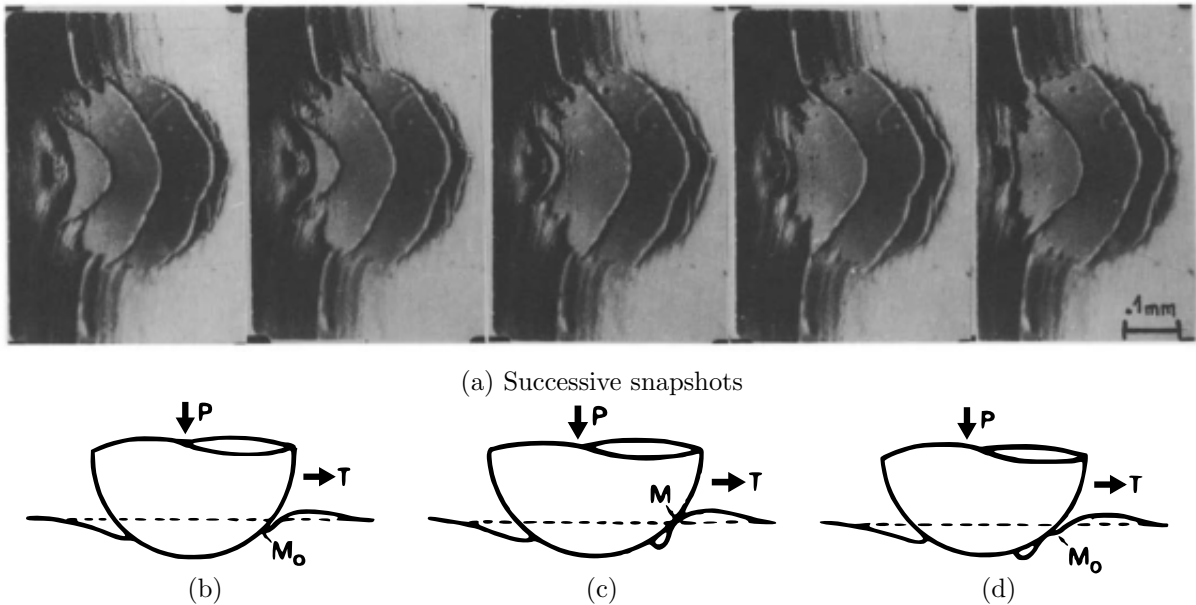


Figure 1.20: Schallamach waves observed for the sliding (from left to right) of a hemispherical glass slider on a transparent rubber plate in a non-stationary state (from [Barquins, 1985])

In fig. 1.20a, several Schallamach waves can be observed. In front of the slider, a bump on the rubber surface is observed because of the slider (fig. 1.20b). However, due to surface instabilities, contact between the slider and the rubber surface may be initiated, leaving a contact-free zone on the inside (see fig. 1.20c). This contact-free zone moves towards the rear (cf. fig. 1.20d) at a velocity significantly greater than the slider velocity. The displacement of Schallamach waves is therefore opposite to that of the peeling phenomenon. If the slider velocity is low enough, the contact-free zone may disappear before reaching the rear.

### 2.2.4 Friction coefficient

The various mechanisms underlying energy dissipation (i.e. friction coefficient) in tires are still being intensively studied. Some of them are more clearly defined than others. The friction coefficient can be divided into four main sources, as shown in eq. (1.4).

$$\mu = \mu_h + \mu_a + \mu_c + \mu_i \quad (1.4)$$

with  $\mu$  the overall friction coefficient,  $\mu_h$  the loss due to hysteresis,  $\mu_a$  the loss due to adhesion,  $\mu_c$  the loss due to crack opening and  $\mu_i$  the loss due to dissipation in a viscous interfacial layer. Among them, two sources are well documented:

- $\mu_h$ : rubber is a viscoelastic material and therefore dissipates energy when it is deformed. This deformation occurs every time there is a contact with an asperity of the road. This occurs at a frequency of  $\frac{V_S}{\lambda}$  with  $V_S$  the sliding velocity and  $\lambda$  a characteristic wavelength of the road roughness, which is a distribution in practice [Persson, 1998]. Several works have been carried out to take into account all the length scales of roughness using the self-affine properties of the road surface [Emami et al., 2021]. As already mentioned, the dissipative behavior of the material due to hysteresis can be described by the  $\tan(\delta)$  (cf. eq. (1.1)).
- $\mu_a$ : there is creation and destruction of free surfaces between the tread and the road due to adhesive forces. Their origins are less well defined and may be the result of several forces such as capillary, van der Waals and electrostatic [Savkoor, 1965; Kummer, 1966]. Adhesion is highly dependent on the real contact area. The forces will generate a deformation and therefore a dissipation linked to the loss modulus  $E''$ .

To compare these two mechanisms, a smooth and rough surface can be used. If the surface is smooth, hysteresis will be low and the real contact area maximum (and the contrary for a rough surface). This was performed in [Grosch, 2007] and the results are shown in fig. 1.21.

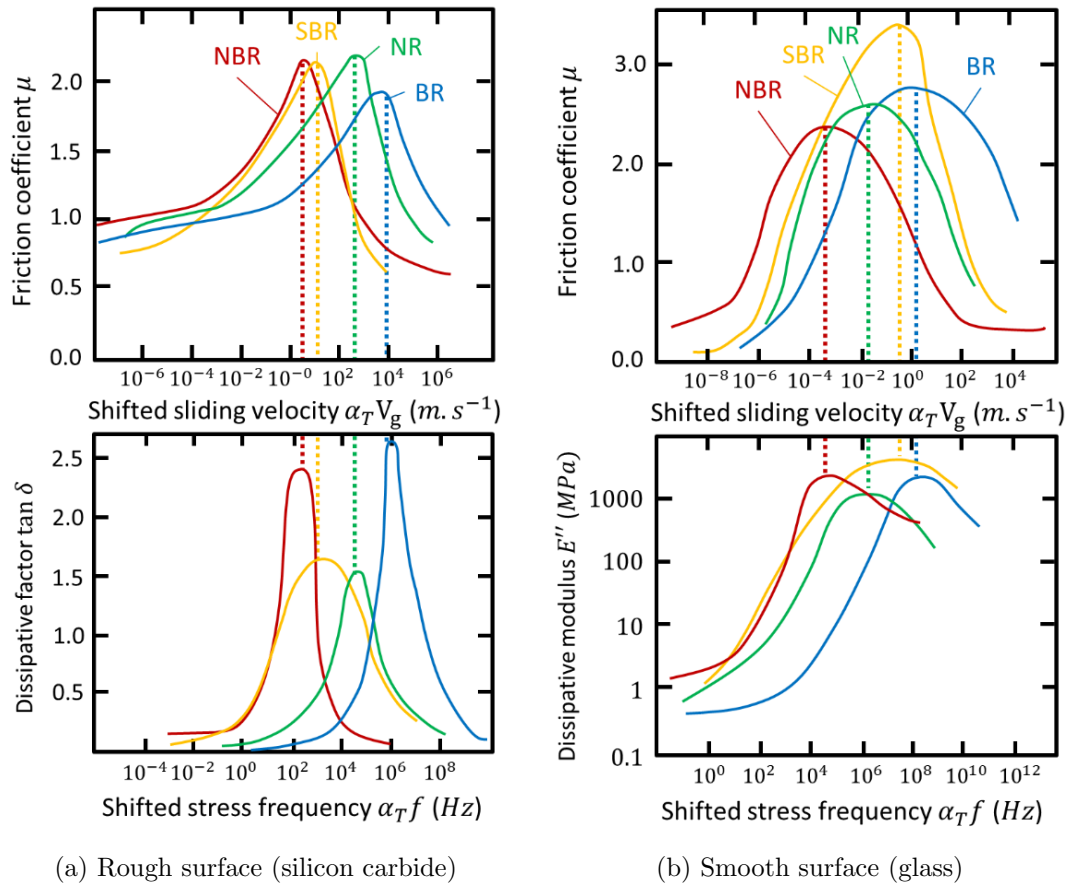


Figure 1.21: Friction test for nitrile butadiene rubber (NBR), styrene butadiene rubber (SBR), natural rubber (NR) and butadiene rubber (BR), with two counter surfaces and for several sliding velocity ( $V_g$ ); frequencies ( $f$ ) are obtained using an equivalent wavelength and are multiplied by the translation factor ( $\alpha_T$ ) (from [Grosch, 2007; Hemente, 2019])



First, it can be seen that the friction coefficient is highly dependent on sliding velocity. It can be multiplied by more than 2 depending on velocity. For a rough surface (fig. 1.21a), the peak of friction coefficient is clearly linked to the  $\tan(\delta)$ . This shows that the loss is mainly due to hysteresis  $\mu_h$ . For the smooth surface (fig. 1.21b), the friction coefficient peak is linked to the loss modulus and  $\mu_a$  dominates. Two other sources can be found in the literature, but are less documented:

- $\mu_c$ : loss due to crack opening; crack propagation energy also depends on sliding velocity [Lorenz et al., 2011]
- $\mu_i$ : loss due to dissipation in the interfacial layer; this layer is essentially considered as a fluid, particularly for studying friction in rainy weather [Persson et al., 2004]; it can also be considered as a solid flow, but is usually studied empirically without a deep understanding of the underlying mechanisms [Morris and Kossyrev, 2018]

In practice, dissipation modes are often coupled. For example, any asperity will indent the material and increase the real contact area (so there is a link between  $\mu_h$  and  $\mu_a$ ). Wear can also create an interfacial layer that reduces direct contact between the tread and the asperities of the road. This makes the notion of roughness, and hence hysteresis, more difficult to appreciate.

## 2.3 Wear

### 2.3.1 Emissions

The emissions of microplastics are a real scourge for the environment. From the 1950s to 2015, an estimated 8.3 billion metric tons of virgin plastics were produced, from which 9% had been recycled, 12% incinerated and 79% landfilled or released into the environment [Geyer et al., 2017]. However, plastics are used in practically every sector of activity, from medical equipment to the paint in our homes. It is therefore essential to identify the sources of microplastics collected in the environment so that targeted actions can be taken.

However, this identification is not easy. Indeed, microplastics have undergone several transformations (notably chemical) as a result of their interactions with the environment. Combined with the fact that there are many possible applications for a given material, the question becomes even more difficult. One way to proceed is to find chemical markers. Some of these may be clearly associated with one application, such as 2-(Methylthio)benzothiazole for tires [Zeng et al., 2004], or with several applications, such as triphenylene for tires and brakes [Rogge et al., 1993]. Tire and road wear particles (TRWP) represent a significant share of emissions into the environment. On average, these emissions are equal to 0.8 *kg/year/inhabitant*, which is highly country-dependent [Kole et al., 2017].

Even if the sources are identified, it is then necessary to determine how the particles were transported. In the case of tire wear particles (TWP), less than 5% were found to be airborne and 1% in gaseous form [Cadle and Williams, 1978]. More generally, the airborne fraction of TRWP is very small [Panko et al., 2013; Charbouillot et al., 2023]. TRWP are released at 60% into the soil, at 20% into the surface water (the proportion reaching the estuary depends on the distance from the emission point to the sea) and at 18% into the stormwater management system [Unice et al., 2019]. An extensive review was carried out in [Baensch-Baltruschat et al., 2020] and the main results are presented in fig. 1.22.

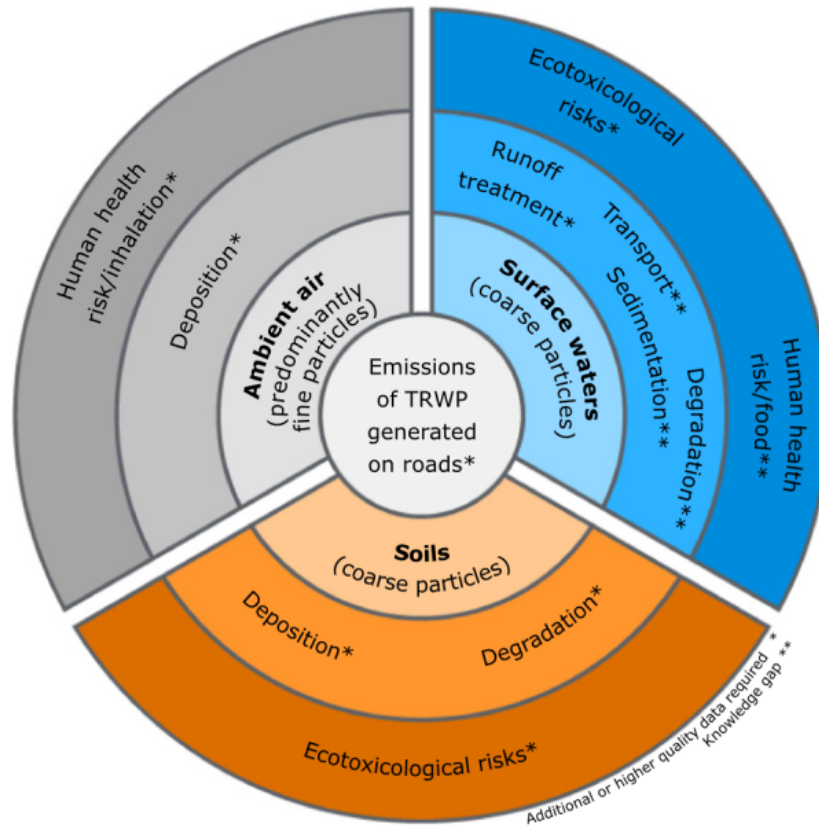


Figure 1.22: Main TRWP transport modes and the associated risks (from [Baensch-Baltruschat et al., 2020])

### 2.3.2 Observations

TRWP are composed of several elements from a wide range of sources. Road dust samples were analyzed in [Adachi and Tainosho, 2004] using a field emission scanning electron microscope (FESEM) equipped with an energy dispersive X-ray spectrometer (EDX). The particles were classified into four groups: brake dust, heavy minerals, yellow paint and tire tread. The tread particles were found to have a higher concentration of Al, Si and Ca, corresponding to road minerals. Several studies have focused on TWP. The same results as described above (i.e. the presence of minerals) were found. For example, it can be highlighted by using single particle mass spectrometry [Dall’Osto et al., 2014]. Some studies have complemented their analysis with scanning electron microscope (SEM) observations. For example, in [Kreider et al., 2010], TWP are observed and the corresponding images are displayed in fig. 1.23.

This particle has the typical aspect of a TWP. The particle is elongated in shape and several mineral incrustations can be observed. Morphological parameters were determined using transmission optical microscopy. Size was found to follow a bimodal distribution (in % of particles) with peaks at 5 and 25  $\mu\text{m}$ . Aspect ratio (ratio of width to length) follows a Gaussian distribution (in % of particles) with an average value of 0.64.

However, the reasons why rubber forms such a complex mixture with minerals are still not clearly defined. The mechanisms that occur prior to wear are even less understood. This will be discussed later, but if minerals are embedded in the interfacial layer, they can modify the frictional behavior of the tire, which, in addition to wear, is a key parameter.

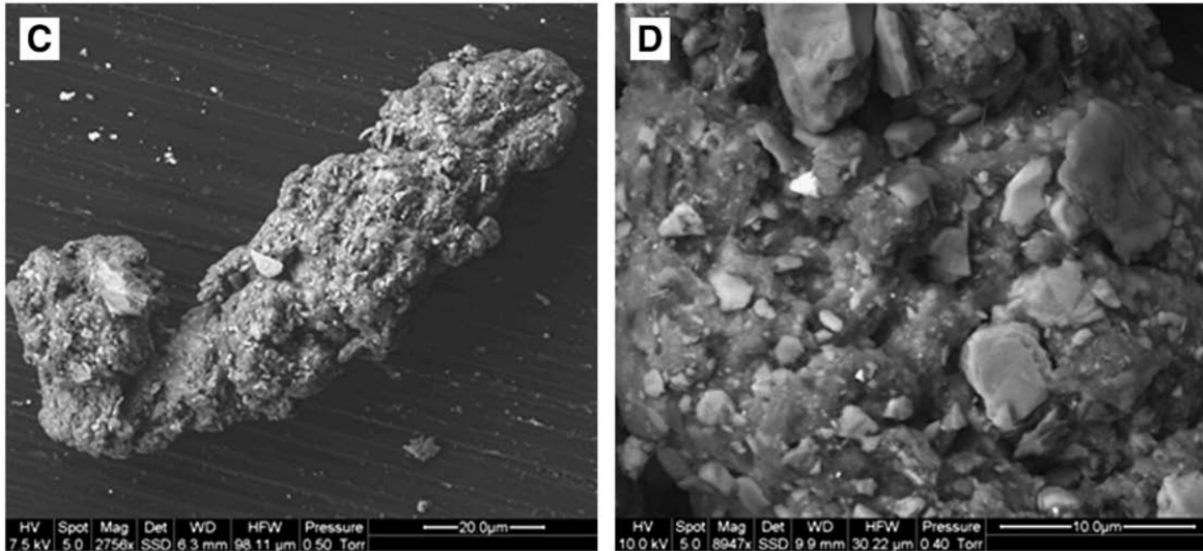


Figure 1.23: SEM images of a TWP for different magnifications (from [Kreider et al., 2010])

### 3 Tribological framework

#### 3.1 Context

##### 3.1.1 A brief history

Tribology, in its most elementary definition, is the science of friction. A more complete definition would be the science of bodies in relative motion. Friction is everywhere and at all times, from the control of fire by early humans to the most sophisticated aerospace applications. However, it took some time before a real commitment was made to controlling friction. One of the first examples of this is the lubricant used to help carry heavy loads in ancient Egypt, as shown in fig. 1.24.

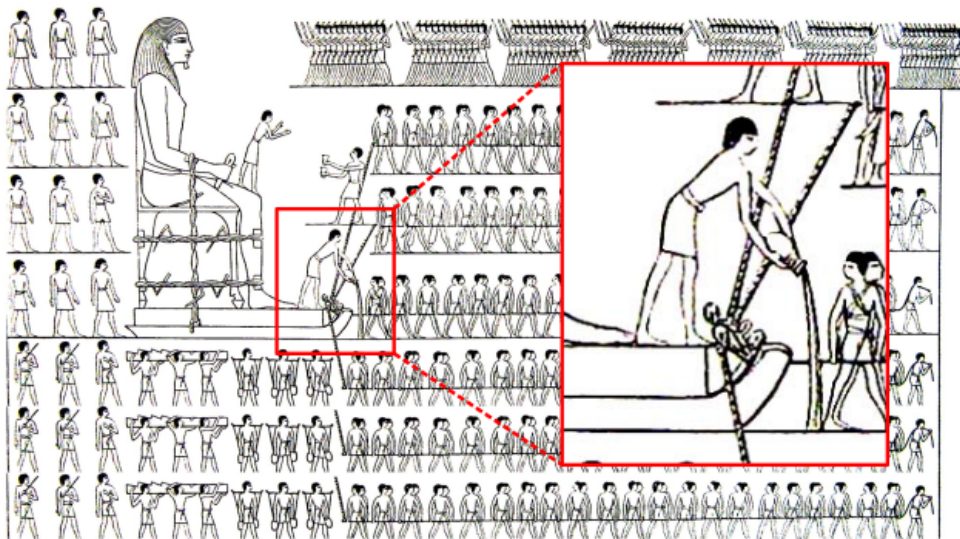


Figure 1.24: Tomb of Tehuti-Hetep, El-Bersheh, 1880 BC (adapted from [Dowson, 1998])



Several millennia passed before the first works on friction emerged. The famous works of Leonardo da Vinci (1452-1519) studied the relationship between normal and tangential force. A few centuries later, Guillaume Amontons (1663-1705) and Charles-Augustin Coulomb (1736-1806) formalized the notion of dry friction [Coulomb, 1821]. They found that the frictional force is proportional to the normal one, and is independent of the apparent contact area and sliding velocity.

A more mathematical description of the contact is developed a few years later. In 1881, Heinrich Hertz (1857-1894) formalized the solution for two elastic spheres in contact with several assumptions such as frictionless contact [Hertz, 1882]. In 1885, Osborne Reynolds (1842-1912) derived the pressure distribution of a thin film for a viscous fluid [Reynolds, 1886]. This equation, known as the Reynolds equation, is still widely used today due to its validity for many applications and its simplicity to solve. It should be noted, however, that research is still highly active in this field, whether by modifying the Reynolds model or concerning its numerical resolution [Decote et al., 2024]. The work of Reynolds marks a relatively important point in the separation of lubrication and dry friction studies. Unfortunately, it is more complicated to establish a well-defined mathematical expression for dry friction. In the case of lubrication, the continuous nature of the fluid facilitates its development. The work of Richard Stribeck is also worth mentioning, in particular his 1902 work on lubrication regimes [Stribeck, 1903] and the well-known curve of Stribeck [Andablo-Reyes et al., 2011].

### 3.1.2 Limitation of the friction coefficient

A contact is generally reduced to two bodies with a given friction coefficient. However, the reproducibility and meaning of this coefficient is not very accurate. If the configuration changes even slightly, it can vary significantly. For example, the Versailles Project on Advanced Materials and Standards (VAMAS) studies the reproducibility of a friction experiment [Czichos et al., 1987]. The corresponding friction coefficients are displayed fig. 1.25.

Friction coefficient

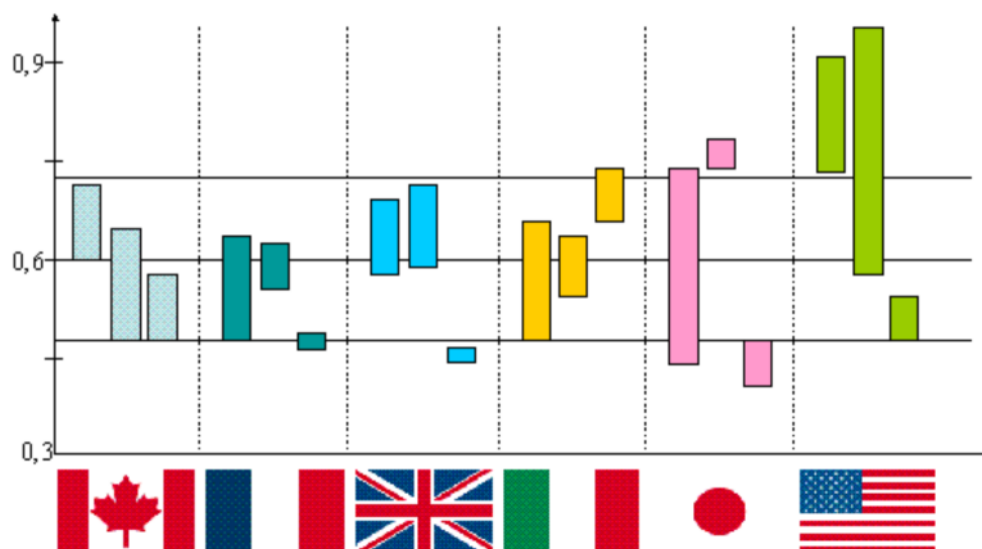


Figure 1.25: Results of the VAMAS experiment; each bar represents the amplitude of the friction coefficient for a given laboratory; horizontal lines correspond to the mean value  $\pm$  the standard deviation over all laboratories (results from [Czichos et al., 1987] and graphic adapted from CETIM magazine)

The behavior of two materials (ceramic  $\alpha - Al_2O_3$  and steel AISI 52100) is studied under controlled operating conditions (load, sliding velocity, temperature and sliding distance). A protocol for sample preparation and testing was defined and repeated in 26 different laboratories. For steel-steel contact,  $\mu$  was equal to 0.60 on average, with a standard deviation of 0.11. Consequently, even under laboratory conditions, there is significant variability in  $\mu$ . In the case of a tire, for which humidity, load, temperature and many other factors are not constant, it seems difficult to postulate a friction coefficient, even if there are often no other alternatives. Much effort has been devoted to understanding the physics governing contact. One important contribution has been brought by the notion of third body.

### 3.2 Third body

The concept of third body was developed in [Godet, 1984]. The two contacting bodies are called the first bodies. They interact via an interfacial layer, called the third body. The third body is a medium with very specific characteristics compared to the first bodies. Firstly, as discussed later, the third body is a mixture of several elements (i.e. materials). Secondly, due to a multitude of coupled effects (mechanical, thermal, chemical, etc.), its properties can also be altered. Finally, loading conditions are significantly different, with shear rates easily exceeding  $10^7 \text{ s}^{-1}$ . While for lubrication, the presence of this third body appears obvious, this is less true for dry contact, and the third body is therefore often overlooked. However, there is several experimental evidence supporting the existence of this third body and its effect on the contact.

With specific materials, it is possible to film the third body during sliding. In [Dvorak et al., 2007] (also previously performed in [Descartes and Berthier, 2002]), a  $Pb - Mo - S$  coating on an M50 hardened steel substrate is studied. Two counter-surfaces were used (borosilicate glass and sapphire) with a hemispherical shape. Their transparency enables real-time visualization using a CCD (charge-coupled device) at  $30 \text{ frames.s}^{-1}$ . A link has been established between the way velocity is transmitted between the two bodies and the friction coefficient. This change in velocity could be controlled by changing the air humidity. This example demonstrates the strength of the third-body concept. Indeed, in the previous VAMAS experiment, air humidity could not be controlled. However, the single use of a friction coefficient failed to explain why a change in humidity could lead to a change in friction. The third body brings an additional tool to explain such differences.

### 3.3 Tribological circuit

An important point raised by the third body concept is the consideration of all the material flows inside the contact. Indeed, if wear particles are ejected from the contact or trapped inside, this can modify the behavior of the contact. For example, it is shown in [Morris and Kossyrev, 2018] that during sliding, wear rate and  $\mu$  are increased if particles are removed from the wear track (also highlighted in [Tiwari et al., 2021; Huang et al., 2018]). This question can be formalized by the so-called tribological circuit [Taylor et al., 1996]. This consists in balancing all the material flows inside the contact. It is represented in fig. 1.26.

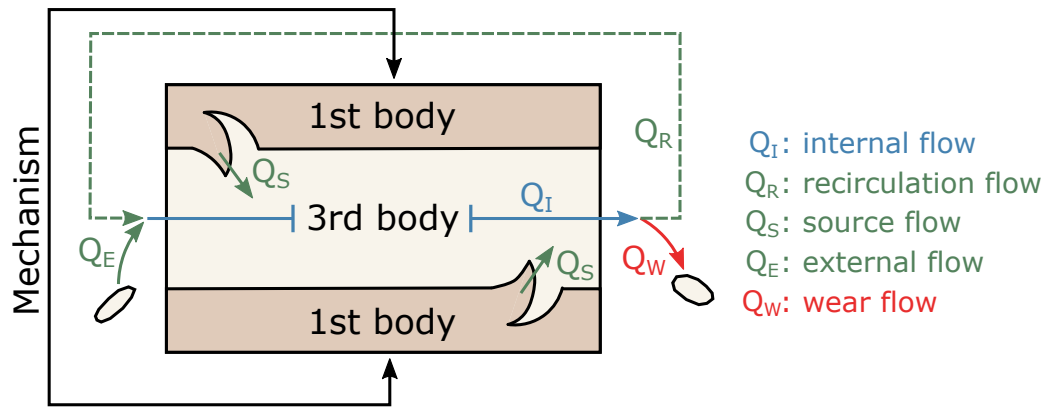


Figure 1.26: Illustration of the tribological circuit with  $Q_I$  the internal flow,  $Q_R$  the recirculation flow,  $Q_S$  the source flow,  $Q_E$  the external flow and  $Q_W$  the wear flow

The following flows can be found:

- $Q_I$ : internal flow (i.e. third body flow); this is the sum of all incoming flows minus the wear flow
- $Q_S$ : source flow; this corresponds to what is usually considered to be wear, but which in this concept is first incorporated in the third body
- $Q_W$ : wear flow: this corresponds to the particles ejected from the contact
- $Q_R$ : recirculation flow; in the case of a closed contact, the third body remains within it and recirculates; in an opened contact, a fraction may recirculate according to the wear rate
- $Q_E$ : external flow; the third body can be supplied by external elements such as road aggregates for tire-road contact

Firstly, it shows that wear depends on the balance of flows. Relatively to other flows, the mass of the third body can be close to zero if wear flow is high, can increase continuously if source flow is high compared to wear flow or reach a steady state [Fillot et al., 2007]. Secondly, wear is considered only for the particles that no longer play a role in the contact. This framework can be used to explain certain phenomena, such as the one described above, where wear particles left on the track modify the wear rate.

## 4 Hertzian framework

A significant amount of work has been carried out to find the stress distribution within a contact. It all began with Hertzian theory which, because of its relatively restrictive assumptions, has been progressively improved.

### 4.1 Static contact

Before addressing complex mechanisms involving an interface, an underlying question concerns the stress and strain fields in the non-sliding first bodies. This can be used to determine whether the stress exceeds the yield strength, or to estimate the number of admissible loading cycles [Tallian, 1992].

#### 4.1.1 Without adhesion

One of the fundamental works, which remains a key element in most of recent models, is the theory developed by Heinrich Hertz, known as Hertzian theory [Hertz, 1882]. Hertzian contact is based on several assumptions. In particular, it is assumed that the contact is purely elastic, frictionless and without relative displacement (i.e. there is no sliding between the two bodies). The theory is developed for several contact geometries (a reduced geometry can be assumed using a parabolic approximation), as shown in fig. 1.27.

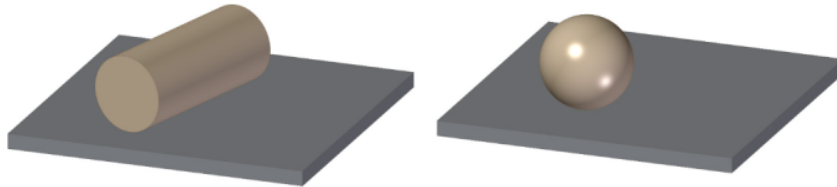


Figure 1.27: Different contact geometries covered by Hertzian theory (cylinder/plane, sphere/plane) (from [Bouillanne et al., 2021])

Generally speaking, Hertzian theory is often used to obtain, for a given load or displacement, the resulting contact area and corresponding normal pressure. For a sphere-sphere contact, the contact area is a circle of radius  $a$ , whereas for a cylinder-cylinder contact, it is a rectangle of half-width  $b$  (the length being that of the cylinders). The contact area can also be elliptical, such as for certain gears. It is shown that for a sphere-sphere contact, the depth of maximum shear stress below the surface is close to  $0.5 a$  and for a cylinder-cylinder, it is closer to  $0.78 b$ . This gives some powerful rules to explain many observations such as crack initiation. The stress field can be derived analytically as a function of several parameters such as the maximum contact pressure [Johnson, 1987]. The theory also provides scaling relationships between different quantities. For a sphere-sphere contact, for example, it states that  $a \propto F_n^{\frac{1}{3}}$  with  $F_n$  the normal load. All these solutions provide relatively simple tools for sizing and studying systems with elementary geometries such as gears [Vouaillat et al., 2019].

#### 4.1.2 With adhesion

An important assumption of Hertzian theory is that adhesion is neglected. However, adhesion forces may be significant for specific applications such as unvulcanized soft rubber. To take this into account, a theory known as JKR (Johnson, Kendall and Roberts) has been developed in [Johnson et al., 1971]. For adhesive materials, the Hertzian theory tends to underestimate the actual contact area. This is because, close to the contact boundaries, adhesion forces tend to bring the surfaces into contact. An alternative theory that takes adhesion into account is the DMT (Derjaguin, Muller and Toporov) model developed in [Derjaguin et al., 1975]. Unlike the JKR model, the contact area remains unchanged from the Hertzian theory, but the tensile force arising at the boundary due to adhesion is taken into account. An illustration of these three theories can be found in fig. 1.28.

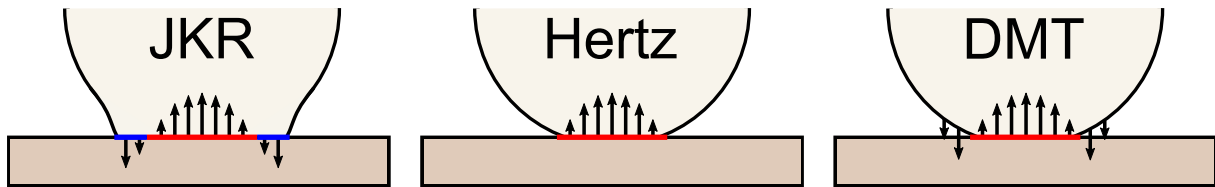


Figure 1.28: Illustration of the differences between the JKR, Hertzian and DMT theories; the red line represents the Hertzian contact area; the blue line represents the contact area due to adhesion forces

The significance of the adhesion forces depends on the contact load. As demonstrated in the original work of the JKR model, Hertzian and JKR theories tend relatively towards the same contact area when the contact load increases. This is because the adhesion forces become negligible compared to the contact load.

## 4.2 Rolling contact

### 4.2.1 Description

Rolling contact models were first developed for wheel-rail applications and then adapted to tire-road contact. Two types of rolling contact can be found and are illustrated in fig. 1.29.

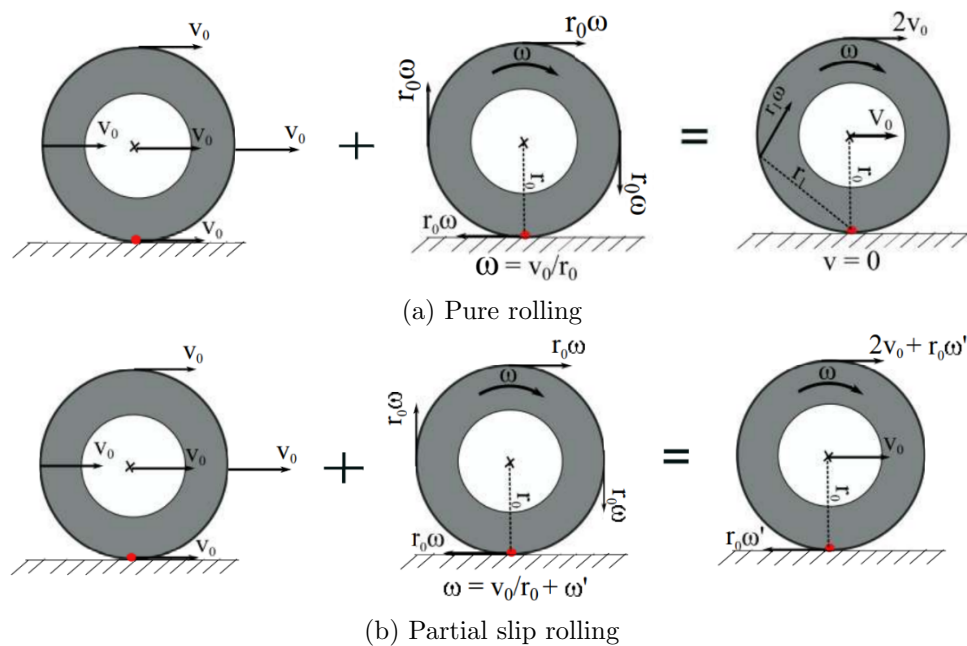


Figure 1.29: Illustration of a rolling contact (from [Manyo, 2019])

In fig. 1.29a, the angular velocity ( $\omega$ ) of the wheel at the interface (red dot) is equal to the forward velocity ( $V_0$ ) divided by the wheel radius ( $r_0$ ). This corresponds to pure rolling. There is no relative velocity between the first bodies and therefore theoretically no friction. However, this case is an idealization and does not exist in practice. Indeed, a more realistic case is presented in fig. 1.29b. Due to several external disturbances (inertia, rolling resistance, etc.), a perturbation in angular velocity occurs ( $\omega'$ ). This leads to a relative velocity between the first bodies and therefore friction.

### 4.2.2 Analytical model

A work extending Hertzian theory to rolling contact was published in [Carter, 1926], the so-called theory of Carter. It was found that if friction is taken into account, there are two distinct zones in the contact, a sliding and adhesive zone, which is consistent with what is observed experimentally. An illustration of the theory can be found in fig. 1.30.

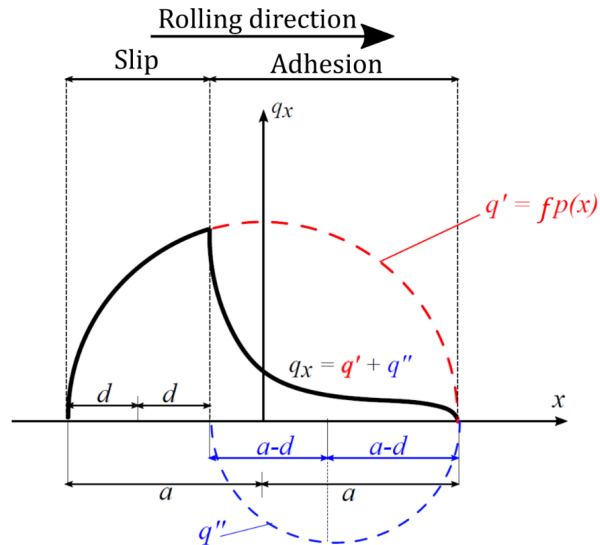


Figure 1.30: Illustration of the theory of Carter with  $x$  the spatial dimension and  $q_x$  the friction force per unit area (from [Wallace, 2022])

This model gives the profile of the friction force per unit area ( $q_x$ ). A Hertzian profile for the cylinder-plane contact is assumed and multiplied by  $\mu$  to obtain the tangential component, giving  $q'$ . With the same idea, to model adhesive forces, a negative force  $q''$  is derived but shifted by  $2d$ , which is the slip distance. The value of the half-slip distance  $d$  is determined from the total tangential tensile force and the normal force. The corresponding profile is then the sum of  $q'$  and  $q''$ , giving  $q_x$ . This theory has since been improved, notably with the widely-used theory of Kalker [Kalker, 1990].

## 5 Friction modeling

Energy dissipation is an essential feature in many industrial sectors. This dissipation can be minimized (e.g. bearings), maximized (e.g. brakes) or both (low rolling resistance tires). One indicator of this dissipation is the well-known kinetic friction coefficient, which describes the degree of power transmission between bodies in relative motion. However, while friction often refers to interface phenomena, it may be the result of more multiscale and coupled mechanisms, such as the viscoelasticity of the first bodies. Because of this complexity, these mechanisms are often isolated and studied on specific time and space scales. For all these reasons, friction cannot be reduced to energy dissipation. Rather, it can be generalized to the study of relevant mechanisms when two bodies are in relative motion.

### 5.1 Analytical

#### 5.1.1 Empirical models

Analytical models essentially describe the dependency of the tangential force or friction coefficient on several parameters. The first type of model is the empirical model. Their aim is

to give the most accurate value of the frictional force, without necessarily having a mechanical meaning. The most frequently used model is undoubtedly the friction model of Coulomb in eq. (1.5).

$$F_t = \mu F_n \quad (1.5)$$

with  $F_t$  the friction force,  $\mu$  the friction coefficient and  $F_n$  the normal force. From this equation, it is possible to predict heat generation in a sliding interface as a function of normal load. However, this model reaches its limits for rubber-like materials. Firstly, an important assumption of the work of Coulomb is that the real contact area and friction coefficient do not depend on the contact pressure. This assumption is not always valid for soft and adhesive rubber-like materials. The friction coefficient can be rewritten as shown in eq. (1.6) [Denny, 1953].

$$\mu = \frac{1}{A\sigma_N + B} \quad (1.6)$$

with  $\mu$  the friction coefficient,  $A$  representing the pressure dependence,  $\sigma_N$  the contact pressure and  $B$  the inverse of  $\mu$  at zero pressure. This relationship takes into account the evolution of the real contact area as a function of pressure, as well as adhesion forces. At higher  $p$ , the friction coefficient becomes independent of contact pressure.

Finally, the friction coefficient, which results from the viscoelastic behavior for rubber-like materials (see eq. (1.4)), depends also on sliding velocity and temperature. The pioneering work of A. Schallamach shows a logarithmic relationship between friction force and sliding velocity, as shown in eq. (1.7) [Schallamach, 1953].

$$F_t = \gamma^{-1} \left( E + \ln \left( \frac{V_S}{A} \right) kT \right) \quad (1.7)$$

with  $F_t$  the friction force,  $V_S$  the sliding velocity,  $T$  the temperature and  $\gamma$ ,  $E$ ,  $A$  and  $k$  are constants. This relationship shows that, depending on the material, the evaluation of a coefficient of friction could be difficult. Indeed, the friction coefficient may depend on pressure, velocity and temperature, with potential interaction effects between them and in a non-linear manner.

### 5.1.2 Physics-based models

The second type of model includes a description of the contact, notably by considering some roughness descriptors. One model that seems very intuitive is the Bristle model in eq. (1.8) [Haessig and Friedland, 1991].

$$F_t = \sum_{i=1}^N \sigma_0 (x_i - b_i) \quad (1.8)$$

with  $F_t$  the friction force,  $i$  the bristle index,  $N$  the number of bristles,  $\sigma_0$  the bristle stiffness,  $x_i$  the position of the upper bristle and  $b_i$  the position of the lower bristle. An illustration can be found in fig. 1.31.



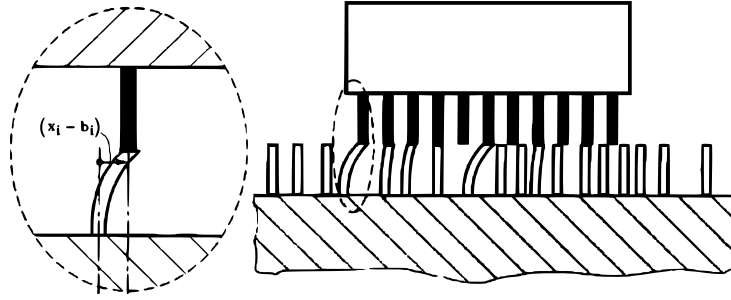


Figure 1.31: Illustration of the bristle model (from [Iurian et al., 2005])

The bristles correspond to an idealization of the contact asperities. Although this model seems consistent, it is not used in practice, as it involves many unknown parameters and is numerically inefficient. An effective model must therefore be based on an average bristle behavior to be computed efficiently. A very popular model, and probably among the first to be published, is the Dahl model in eq. (1.9) [Dahl, 1968].

$$\frac{dF_t}{dx} = \sigma_0 \operatorname{sgn} \left( 1 - \operatorname{sgn}(V_S) \frac{F_t}{F_C} \right) \left| 1 - \operatorname{sgn}(V_S) \frac{F_t}{F_C} \right|^{\delta_D} \quad (1.9)$$

with  $F_t$  the friction force,  $x$  the body displacement,  $\sigma_0$  the asperity stiffness,  $V_S$  the sliding velocity,  $F_C$  the Coulomb friction force (i.e. eq. (1.5)) and  $\delta_D$  a coefficient corresponding to hysteresis. The model was developed to study symmetrical hysteresis loops in bearings subjected to sinusoidal excitation. This model was improved in [de Wit et al., 1995] resulting in the LuGre model. An illustration of both models can be found in fig. 1.32.

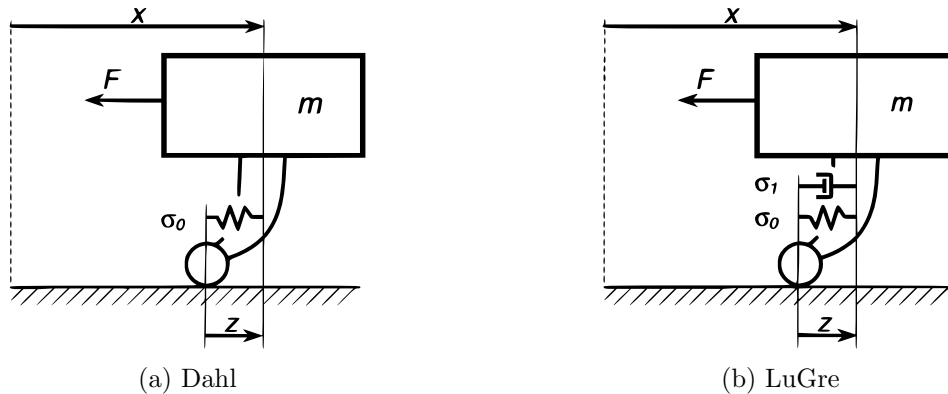


Figure 1.32: Illustration of two physics-based models (adapted from [Piatkowski, 2014])

$z$  corresponds to a state variable linked to the elastic deformation of asperities and which can be introduced into eq. (1.9) if the equation is rewritten [Piatkowski, 2014]. The LuGre model is similar to the bristle model but is based on an average bristle behavior, which makes it much more efficient.

However, all the above relationships give no information on the behavior and effect of the third body. As previously mentioned, if two bodies are sliding, an interfacial layer is formed, called the third body, which should be taken into account. The non-continuity of the third body makes it difficult to model analytically. Consequently, taking it into account often requires the use of numerical models.



## 5.2 Numerical

### 5.2.1 Scales entanglement

The choice of numerical method depends mainly on the medium to be modeled. A solid flow, where many decohesions are expected, will not be modeled in the same way as the bending of a wind turbine. This is because certain numerical approaches facilitate the addition of constitutive models adapted to a given problem. There are therefore a large number of numerical methods, each with its own advantages and disadvantages. An illustration of the methods closely related to dry friction modeling can be found in fig. 1.33.

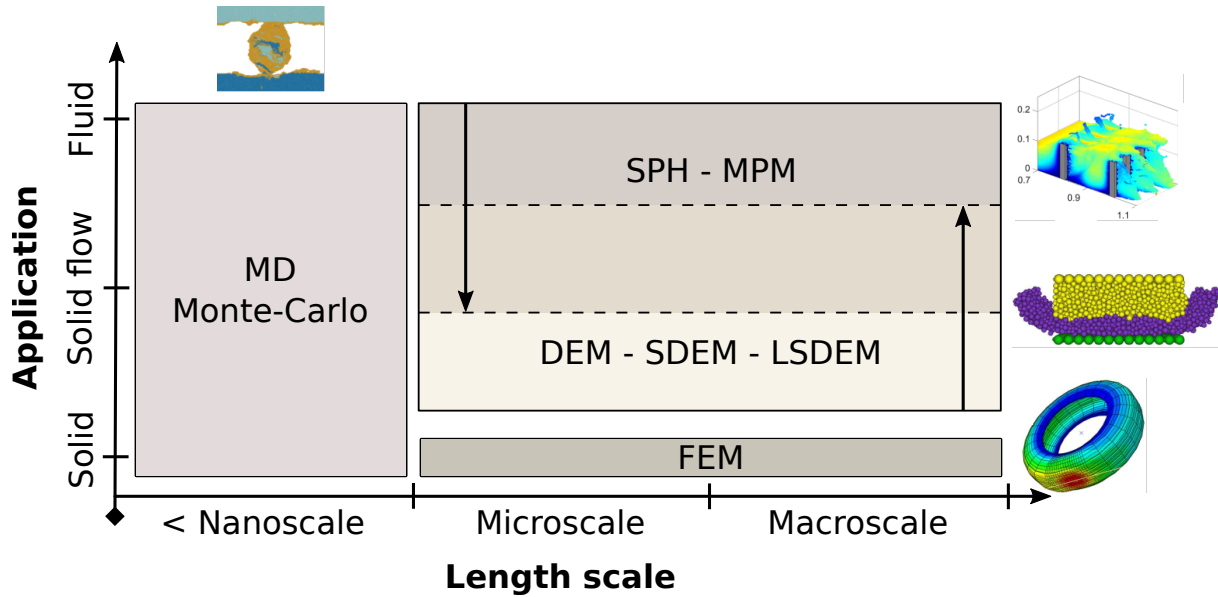


Figure 1.33: Illustration of different methods related to dry friction (simulation images from [Milanese et al., 2020; Fillot, 2004; Yang et al., 2021; Mashadi et al., 2019])

This figure classifies the methods according to their most frequent use in dry friction studies, although there are occasional counter-examples. The use of a method depends on the scale and application considered, as well as the availability of other methods. For example, solid flows often exhibit complex boundary dynamics. Therefore, although the finite element method (FEM) can model a continuous solid flow, a meshfree method such as smoothed particle hydrodynamics (SPH) will be preferred for modeling a rock avalanche. The characteristics of these methods will be discussed later.

Friction models can be highly dynamic and non-linear if phenomena such as contact are taken into account. This often requires the use of an explicit scheme. An important point is that, numerically, spatial and temporal scales are strongly linked. Indeed, the equation governing the physics of the system must be discretized in time and space (for mechanics at least). Consequently, each time step must be small enough to take into account the minimum characteristic spatial variation. These small variations generally correspond to the local oscillation of the material and lead to a critical time step ( $\Delta t_c$ ). In its simplest version, assuming that the material is locally a mass-spring system, a general rule can be found in eq. (1.10) [Bouillanne et al., 2021].

$$\Delta t_c \propto l \sqrt{\frac{m}{k}} \quad (1.10)$$

with  $l$  describing a characteristic length (e.g. mesh size),  $m$  describing local mass and  $k$  describing local stiffness. For a continuous and homogeneous material, the immediate conclusion is that  $\Delta t_c$  will be determined by the smallest  $l$  directly related to the spatial scale. For a discrete model composed of particles, the smaller is the particle, the smaller is the particle mass and therefore  $\Delta t_c$ . Even by coupling different methods depending on the medium being modeled (solid, solid flow or fluid), a small spatial scale generally implies a small time scale.

The size of a tire is close to  $10^{-1} m$ , whereas the third body will be closer to  $10^{-6} m$ . As space and time scales are linked, it is not possible (at the time of writing) to model the space scale of the third body on the time scale of the first bodies. A modeling choice must therefore be made. Each scale has its advantages and disadvantages. At the macroscale, models can provide quantitative results, useful for sizing systems such as tire grooves. At the third-body scale, the way in which power is transmitted between the tire and the road can be studied. It is even possible to go to a lower scale, by modeling the interactions between polymer chains and studying the effect of chemical composition. The characteristics of the main numerical methods are presented below.

### 5.2.2 Continuous models

Most of the continuous dry friction models do not explicitly consider the third body. They take it into account through a contact model. As described above, Hertzian theory assumes that there is no relative displacement between the first bodies and that contact is frictionless. Therefore, even if the third body is not explicitly considered, numerical models can provide interesting results. Moreover, if the geometry becomes more complex, or if the stress exceeds the yield strength, the use of a numerical model is mandatory. Friction models require two important contact features. The first is a contact detection algorithm. Indeed, the boundary of each body must be detected by the other. This point will be discussed later. The second concerns surface interactions (i.e. forces at the interface as a function of several parameters). This last point, when it comes to a contact problem, is particularly important. Indeed, whereas elasticity is described by the constitutive models of deformable bodies, the mechanical description of a contact is described by the contact model. However, as presented in the analytical section, finding a model that describes the complexity of an interface is challenging. Consequently, friction and wear models are often constrained to extrapolate macroscopic models to the interface scale. An illustration is given in fig. 1.34.

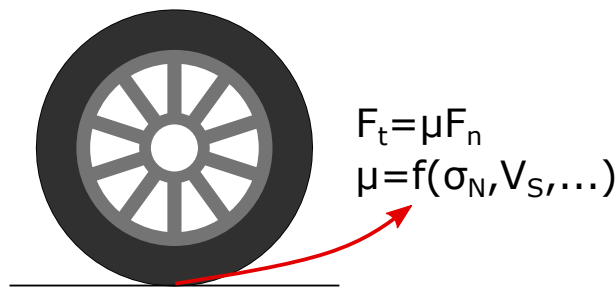


Figure 1.34: Illustration of a model at the scale of the first bodies

A common way of considering interface phenomena is to assume a Coulomb friction. Depending on the material, friction coefficient may be considered constant or as a function of pressure, sliding velocity, etc. At the first body scale, the vast majority of models are using FEM. For example, in [Yoon and Kang, 2023], is studied the influence of the friction coefficient for a compression molding process. A Coulomb friction law is assumed (eq. (1.5)) and a distinc-

tion is made between static and kinetic friction coefficient. This makes it possible to find out how the shear angle is influenced by  $\mu$ , which could not be solved analytically.

As mentioned above, the friction coefficient of rubber materials depends on pressure, velocity and temperature. Although these parameters can be considered constant on a macroscopic scale, this is no longer the case if the law is applied locally. For example, in [Hofstetter et al., 2006], the effect of tire grooves when a rubber material is sliding on a counter-surface is studied. In this study, a Coulomb friction law is used, but with a  $\mu$  that depends on pressure and velocity. Thermal interactions are also modeled. The influence of temperature on  $\mu$  is taken into account by calculating an equivalent velocity using time-temperature superposition. Although the third body is not explicitly considered, complexity can quickly emerge as a function of the contact model. At this scale, it is possible to study the coupling of various parameters and establish a direct link with the quantities to be optimized ( $\mu$ , wear rate, etc.).

### 5.2.3 Discrete models

The third body is a combination of several material flows (fig. 1.26). In addition, stresses, strains and corresponding rates may be significant. This combination of several flows, with the formation and destruction of potential agglomerates, is hardly compatible with a continuous model. For these reasons, discrete modeling is often used. This consists in assuming that the third body (and potentially the first bodies) is composed of a collection of several interacting particles. The most widely used method is the discrete element method (DEM), which assumes, in its simplest version, a collection of rigid spheres.

DEM was originally developed for granular media [Cundall and Strack, 1979]. Indeed, the behavior of these media is determined primarily by the interactions between the different grains and not within each grain. The equation governing DEM is given eq. (1.11).

$$m_i \frac{dv_i}{dt} = \sum F_i \quad (1.11)$$

with  $m_i$  the mass of a grain,  $v_i$  its velocity,  $t$  the time and  $F_i$  the forces acting on the grain. The popularity of DEM, even for non-granular media, can be explained for several reasons:

- The resolution method is simply based on eq. (1.11), which can be easily implemented
- The use of rigid spheres simplifies contact detection (contact occurs if the distance between centroids is less than the sum of the radii)
- Contact models can be easily implemented ( $F_i$  in eq. (1.11))
- The method is relatively affordable in terms of computation time
- This last point makes it possible to use a large number of grains (several million for some simulations)
- For a long time, there was no alternative solution for modeling solid flows

In DEM, the mechanical description is based on the contact models between the grains. An illustration of these contacts is presented in fig. 1.35.

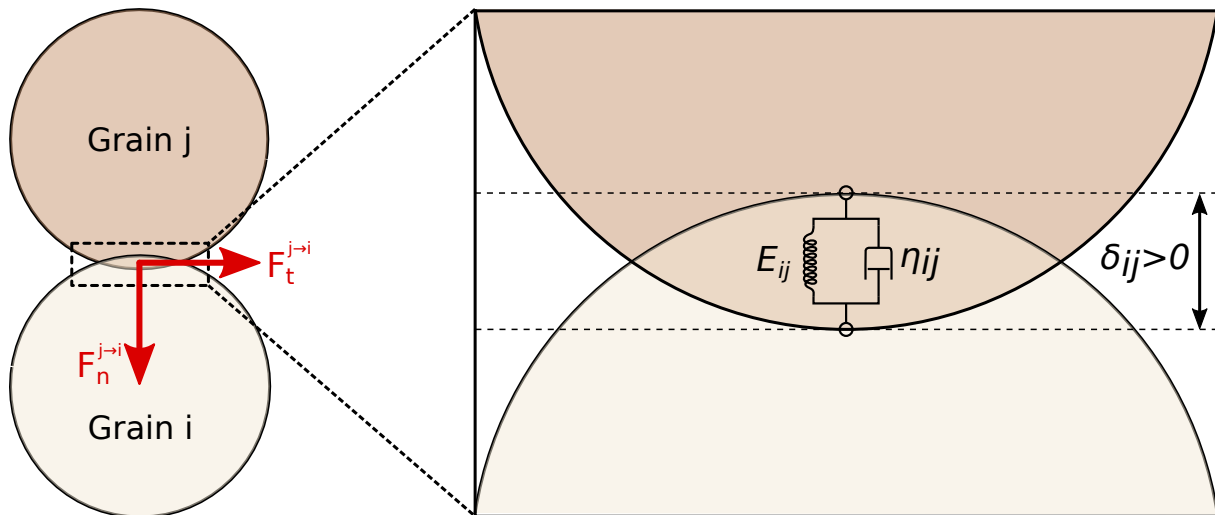


Figure 1.35: Illustration of two rigid grains in contact

Several comments can be made:

- Contact model defines the forces at the interface as a function of several parameters. It can often be reduced to a rheological model with a purely elastic spring ( $E$ ) and a viscous damper ( $\eta$ ), as already seen in section 1.3.5
- The rheological model depends on the interpenetration distance ( $\delta$ ) and the corresponding velocity ( $\dot{\delta}$ )
- For the sake of clarity, only normal interpenetration is shown, but tangential interpenetration can also be defined
- More complex rheological models can be defined as a function of the material, but a Kelvin-Voigt model is often preferred as the parameters are easier to identify, through overall strain (giving  $E$ ) and dissipation (giving  $\eta$ ); tangentially, the contact model depends on the medium being modeled and a Coulomb friction law may be preferred for ductile materials while Mohr-Coulomb may be a better candidate for brittle materials
- The modeling of different material flows is made possible by the definition of different contact models (for example, a lower  $E$  is defined for rubber-rubber contact than for steel-steel contact in the same simulation)

The first DEM models close to tribological applications were related to granular sliding interfaces [Campbell and Brennen, 1983] or to specific lubrication solutions such as powders [Sawyer and Tichy, 2000]. It was only in the early 2000s that studies with a primary tribological interest appeared [Jordanoff and Berthier, 1999; Fillot, 2004]. One advantage of DEM is the ability to study how the velocity is transmitted, which provides a wealth of information on the transmission of power between first bodies. In [Kim and Kamrin, 2020], DEM simulations are carried out under several conditions. The results show that, in the absence of gravity, the particles follow a classical Couette flow. Then, depending on the direction of gravity (not necessarily vertical for chute flows), particles approach a Couette-Poiseuille flow. However, a friction coefficient is calculated and revealed to be highly dependent on granular quantities such as compacity or inertial number [Chialvo et al., 2012]. The parallel with real contact, where particles do not have a definite size, with plastic and elastic deformation, is therefore not obvious. DEM can also be used for rubber-like materials. For example, in [Vignali et al., 2016] a rotary shear rheometer is modeled to study a mixture of bitumen, limestone filler and crumb rubber

particles. The complex shear modulus could be derived and the simulations show accurate results compared to experiments.

It is possible to add a number of interesting features to DEM and bring it closer to a contact configuration. Firstly, it is possible to establish a coupling between FEM and DEM. In this case, the first bodies are generally modeled by the FEM and the third body by the DEM. This makes it possible to simulate stick-slip events or dissipation in the first bodies, and therefore, to calculate a more realistic friction coefficient [Wang et al., 2014]. The shape of the particles can also be improved compared with the spherical assumption. The first solution is to use overlapping spheres to keep the contact detection algorithm [Ferrellec and McDowell, 2010] (a contact is detected according to the sum of the radii). A second solution is to modify the contact algorithm. One method that has become increasingly popular in recent years is the use of level set functions (LSDEM). This involves defining a background grid corresponding to each particle. For each node of this grid, the distance to the contour is computed (once only) and the grid follows the displacement of the particle. If a second body is approaching, thanks to a master-slave algorithm and the grid, the interpenetration distance can be calculated [Duriez and Bonelli, 2021]. It allows any type of contour to be used and more realistic grains to be implemented [Mollon and Zhao, 2013].

However, all the previous points do not change the main drawback of DEM in the case of a sliding interface, which is the assumption of rigid grains. Indeed, DEM is limited to small strains and the mechanisms occur mainly at the interface of each grain. As already discussed, some results depend directly on grain size (e.g. friction coefficient), which is debatable given that the third body is not always composed of grains with a definite size.

Few models take grain deformation into account. For example, in [Cantor et al., 2020], a non-smooth contact dynamics (NSCD) [Jean, 1999] is used to deal with contacts of soft grains and deformation is computed using FEM. However, this method has two potential drawbacks. The first is that FEM requires a minimum number of discretization nodes to give satisfactory results. This can lead to significant computation times, depending on the number of grains considered. The second is that FEM is not well suited to large mesh distortions.

Another method for modeling soft grains is proposed in [Mollon, 2016]. The main difference lies in the method used to compute the deformation. Indeed, a meshless method, analogous to the classical element free Galerkin (EFG) method is used. First and foremost, meshless methods offer higher accuracy for a given computation time. They are particularly well suited to the case of contact, where the aim is to understand the phenomena and not to provide a sizing tool. In the latter case, a FEM approach as described above may be recommended. Computation time can even be further reduced by modeling only a few deformation modes to minimize the number of degrees of freedom [Mollon, 2021]. Secondly, the meshless method allows significant mesh distortion, making it possible for sharp rigid bodies to interact with very soft grains. This method will be used for the numerical models in this work and will be described in the next chapter. An illustration of a method using soft grains is shown in fig. 1.36.



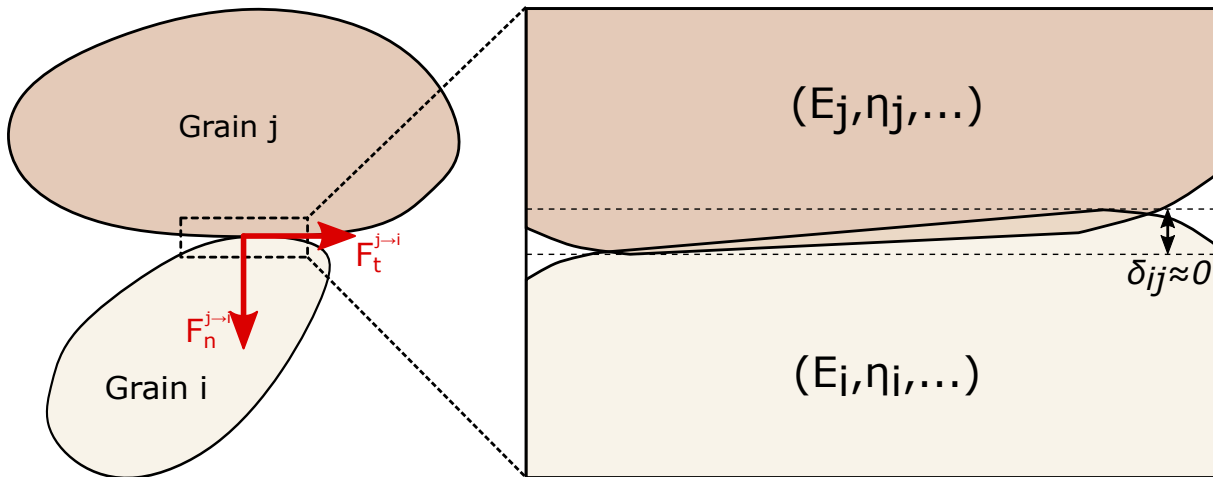
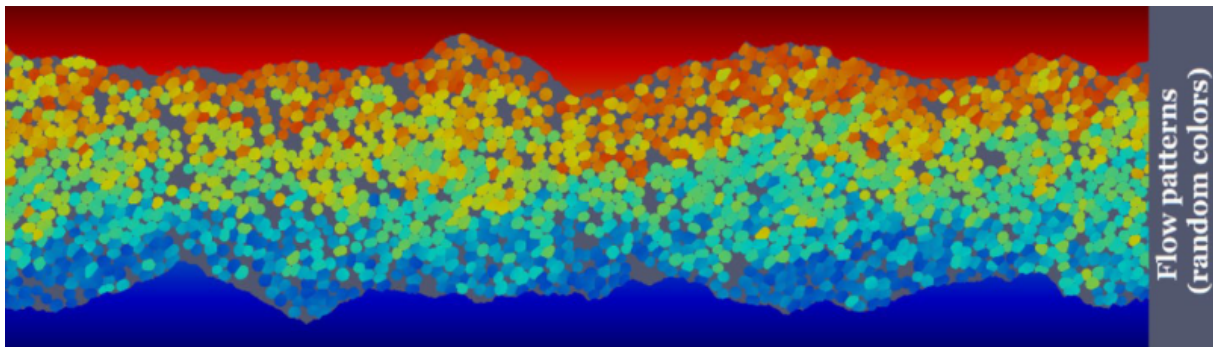
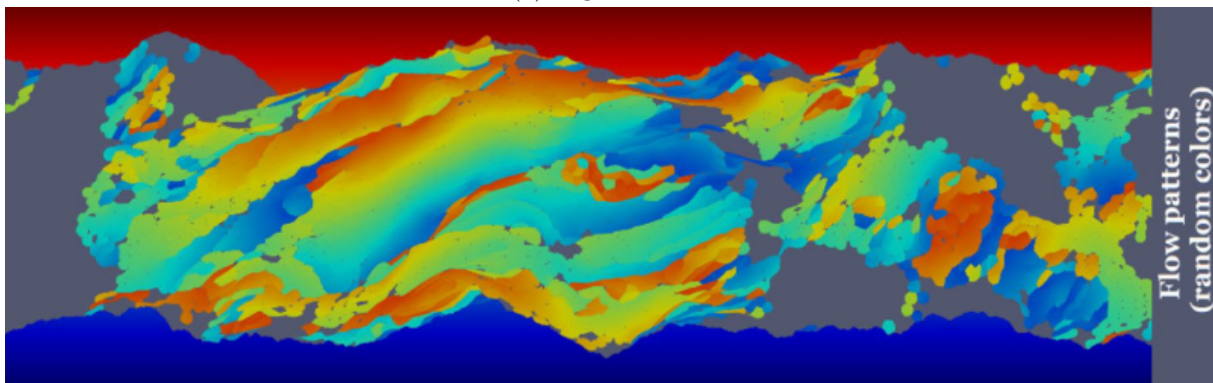


Figure 1.36: Illustration of two soft grains in contact

The main difference is that mechanical behavior is described by deformation and interaction. Stiffness is now modeled by a constitutive model in each grain, which is accurate even at large strain. The damper is now a dissipation throughout the whole volume of each grain. This approach also makes it possible to define contact models between each grain and to calculate the resulting forces. Consequently, the use of soft grains is not incompatible with the DEM framework, but is an extension of it, as illustrated in fig. 1.37.



(a) High stiffness



(b) Low stiffness

Figure 1.37: Simulations using the same grain contact model with high and low grain stiffness (from [Mollon, 2019])

If stiffness is high enough, results similar to DEM are obtained, with low grain deformation and with a classical Couette flow. If the grains become softer, they can form agglomerates

that are not possible to obtain with DEM. The main reason for this is that, as the grains are deformable, a significant contact surface can be obtained and therefore numerous adhesion forces from neighboring grains. Moreover, this method allows to obtain continuous velocity and stress fields in a highly discontinuous domain.

#### 5.2.4 Continuum-based particle models

Some models use continuous methods to study solid flows. The two main ones are the smoothed particle hydrodynamics (SPH) and the material point method (MPM), allowing, for example, to study the contact of a single asperity [Mekicha et al., 2021]. These models are similar to the previous meshless method using soft grains (cf. fig. 1.37). However, for this method, the resolution domain corresponds to each individual grain. In SPH and MPM, the resolution domain corresponds to the entire flow.

The SPH method was originally developed for astrophysical problems [Gingold and Monaghan, 1977] before being adapted to fluid and solid mechanics. This method is mathematically continuous, as the use of an appropriate Kernel function (similar to a shape function for FEM) allows a continuous field to be obtained. However, this function uses quantities (in particular mass and velocity) in discrete moving nodes. Unlike conventional continuous methods, the SPH method is compatible with complex domain boundaries, which is particularly well suited to solid flows. For example, it is possible to model rock avalanches and evaluate the effect of baffles and check dams [Yang et al., 2021]. Concerning tire applications, this method is often used to study tire behavior on wet surfaces [Hermange, 2017; Khodja, 2022]. The method is also relatively versatile, and can be used to simulate solid materials in cutting processes [Limido et al., 2007].

#### 5.2.5 Molecular models

Below a certain scale, materials cannot be considered continuous, and atoms must be explicitly modeled. There are two main methods: molecular dynamics (MD) [Hansson et al., 2002] and Monte-Carlo [Furlong et al., 2009]. The example of MD will be taken as it is similar to DEM in many aspects. Indeed, the material is modeled as a collection of particles interacting according to given models. However, there are two main differences. The first is that each particle corresponds to an atom or a molecule. The second is that distant interaction models are defined, such as an interatomic potential [Tsuneyuki et al., 1988]. This results in a reaction force that can be either attractive or repulsive, and avoids contact between particles, unlike DEM. Even at this scale, it is possible to study the formation of agglomerates within a contact. For example, in [Aghababaei et al., 2016], the contact between two asperities is studied. It was found that the formation of an agglomerate depends in particular on the size of the junction between these two asperities.

## 6 Wear modeling

Wear models are similar in many ways to the friction models, as they both relate to third-body modeling. The main difference concerns the subject under study, which is mainly energy loss for friction, whereas it is material loss for wear. Concerning wear, analytically, the notion of tribological circuit is often neglected due to its complexity. Numerically, wear models can be classified into three categories. The first considers that wear particles are instantaneously removed from contact. This means that the effect of source flow (cf. fig. 1.26) is neglected. The second explicitly models source flow within the contact. However, this requires modeling the third body, which is much more complex. The third case is an intermediate one between the previous two.

## 6.1 Analytical

The most frequently used relationship to model wear is the one developed by Archard in [Archard, 1953] and given in eq. (1.12).

$$\frac{dW}{ds} = KF_n \quad (1.12)$$

with  $W$  the total wear,  $s$  the sliding distance,  $K$  a coefficient describing wear strength and  $F_n$  the normal load. In the original work, the linearity between  $\frac{dW}{ds}$  and  $F_n$  is explained by the contact area. Indeed, a circular contact area of radius  $a$  is assumed and also that  $W \propto a^3$ . From this, the effective sliding distance is presumed to be  $\propto a$  and  $F_n \propto a^2$ . It implies that the wear rate is linearly proportional to  $F_n$ , with a slope determined by  $K$ . Based on these assumptions, the linear relationship is not valid in several configurations, in particular if  $F_n$  is no longer  $\propto a^2$ .

Like the friction law of Coulomb, the model of Archard is not suitable for making predictions about experimentally untested configurations. For example, depending on humidity,  $K$  can be increased by a factor of 100 for brass [Finkin, 1979]. This means that  $K$  is in fact a function of a multitude of parameters. Several studies have adapted the model of Archard to a given problem, to model the influence of other parameters. One widely used modification is to include the influence of hardness as shown in eq. (1.13), which is an important wear parameter [Wang et al., 2005].

$$\frac{dW}{ds} = K' \frac{F_n}{H} \quad (1.13)$$

with  $W$  the total wear,  $s$  the sliding distance,  $K'$  a coefficient describing wear strength,  $F_n$  the normal load and  $H$  the hardness. This allows to add a design parameter and to provide a mechanical explanation for a change in wear. In particular, if applied locally by a numerical model, it can be used to study the potential coupling between hardnesses for the two contacting bodies. However, even this relationship needs to be adapted to the tested configuration, depending on whether hardness tends to increase or decrease the wear rate. The coefficients  $K$  and  $K'$  can be determined using reverse analysis, by measuring the wear rate for a specific configuration (i.e. a given  $F_n$  and  $H$ ).

## 6.2 Numerical

### 6.2.1 Particles instantaneously removed

First, some models assume that particles are instantaneously removed from the contact. The main advantage of this assumption is that the third body is not explicitly modeled. It allows the use of continuous methods such as FEM, whose computation times are more reasonable. Another advantage, again for reasons of computation time, is the possibility of using two-dimensional models. Indeed, particle ejection, which can occur in the third dimension, can therefore be neglected. The vast majority of models use the model of Archard (or closely related) to update the first body geometry. The eq. (1.12) is rewritten as in eq. (1.14) to take into account only the variation in one dimension [Teoh et al., 2002].

$$\frac{dh}{ds} = k\sigma_N \quad (1.14)$$



with  $h$  the surface height,  $s$  the sliding distance,  $k$  a coefficient describing wear strength and  $\sigma_N$  the contact pressure. This law is applied locally to each element. The corresponding nodes are then shifted according to the value of eq. (1.14) and the mesh is updated [Molinari et al., 2001]. An illustration of the mesh update and particle removal is displayed fig. 1.38.

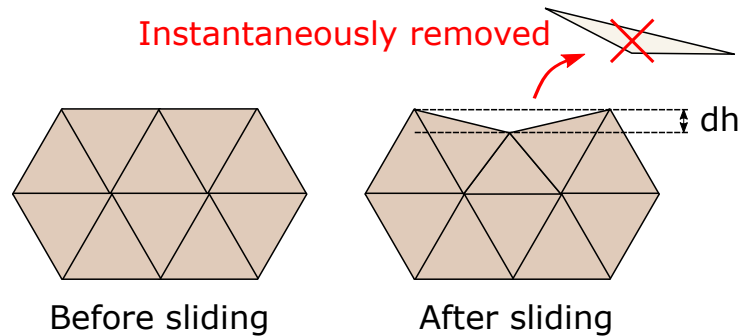


Figure 1.38: Illustration of the mesh before and after particle removal

Even if wear particles are not explicitly considered, this type of model can access several mechanisms. First, the evolution of the contact surface is taken into account. This will modify contact pressure and therefore wear (cf. eq. (1.14)). It also makes it possible to follow the evolution of the friction coefficient and to perform thermal analysis [Pödra and Andersson, 1999]. Secondly, the difference in wear between the two contacting bodies can be studied [Hegadekatte et al., 2004], which is useful for sizing systems. Moreover, although at the scale of mechanisms, sliding can be considered continuous, this is less true locally. Consequently, some wear localization may occur with zones that are not in contact for a given period of time. This allows the access to strain and stress fields that differ from the Hertzian theory for long sliding distance [Garcin et al., 2015]. Finally, as mentioned previously, there are many adaptations of the model of Archard, depending on the application. For example, polymers may exhibit a non-linear dependency between wear and contact load. Consequently, as the original model of Archard is linear and the pressure is no longer constant if the law is applied locally, it needs to be adjusted. For example, [Martínez et al., 2012] studied polymer-steel contact and used the law in eq. (1.15).

$$\frac{dh}{ds} = \alpha \left( \frac{\sigma_N}{E} \right)^\beta \quad (1.15)$$

with  $h$  the surface height,  $s$  the sliding distance,  $\sigma_N$  the contact pressure,  $E$  the initial Young's modulus of the material,  $\alpha$  and  $\beta$  are constants. In particular,  $\beta$  indicates the non-linear dependency on load. In this study, through several wear tests,  $\beta$  was found to be equal to 1.88, showing a significantly non-linear behavior.

## 6.2.2 Particles partially modeled

Fretting is an ideal case for studying the influence of wear debris. It can be defined as two bodies in contact subjected to an oscillatory relative displacement of low amplitude. This type of loading can be found, for example, in the blades of an aircraft engine. This is an interesting case because wear particles are often trapped in the contact, forming a third body layer that can hardly be ignored. Some studies take into account the influence of wear particles without explicitly modeling them. For example, in [Done et al., 2017], a contact between a cylinder and a flat surface is considered. The influence of wear particles is modeled by assuming that the particles adhere completely to the cylinder. This means that the flat surface is progressively worn and the size of the cylinder increases. The results of this model were compared with those

of a model in which the wear particles are removed instantaneously. It was shown that the model taking into account wear particles adhering to the surface was closer to the experiments. Without wear particles, the worn profile tended to be wider and shallower.

### 6.2.3 Particles explicitly modeled

Several works explicitly consider wear particles. In most cases, the wear flow is modeled by DEM. To avoid generating discrete wear particles during simulation, a common practice is to consider a pre-cut material. Wear behavior will therefore be modeled by the contact models between each discrete particle. As described in the section on friction modeling, the description of a consistent contact model is therefore mandatory. One way to proceed is to use a CZM (cohesive zone model) [Alfano and Crisfield, 2001]. This consists in assuming that the link between two particles is progressively damaged. An illustration can be found in fig. 1.39.

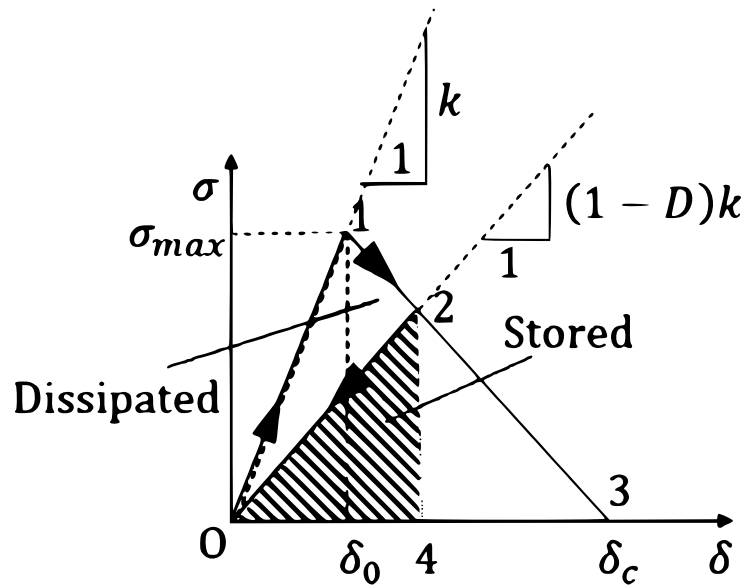


Figure 1.39: Illustration of the CZM (from [Škec et al., 2018])

In fig. 1.39,  $\sigma$  corresponds to the normal stress between two particles and  $\delta$  to the distance between their contours. If the stress exceeds  $\sigma_{max}$  (stress corresponding to index 1), the bond is weakened. This weakening is taken into account in the  $D$  factor. Subsequently, the stress to be overcome to weaken the bond will be lower (stress corresponding to index 2). This corresponding stress will decrease each time the stress exceeds the maximum stress, until it becomes zero and the bond is broken.

As in the case of fretting, it is possible to model a wear flow that remains inside the contact. Wear is therefore defined as a loss of material from the first bodies. For example, [Quacquarelli et al., 2023] studies the wear of diamond tools. Voronoi tessellation was used to obtain a pre-cut first body with a high compacity. A third body composed of rigid discrete particles is modeled. The results show two characteristic phases. Firstly, for low sliding distances, the wear rate increases. Then, a steady state is reached with a constant wear rate. During this phase, the thickness of the third body increases. Interestingly, this thickness does not seem to affect the wear rate. For certain applications, such as tire-road contact, wear particles can easily be ejected from the contact. This ejection may require a third dimension, as shown in [Fillot, 2004] for which results are presented fig. 1.40. In particular, this study shows that if particle ejection is significant compared to particle detachment from the first bodies, the results tend towards

a model of Archard. This confirms that the model of Archard is a special case in which wear particles are instantaneously ejected from the contact.

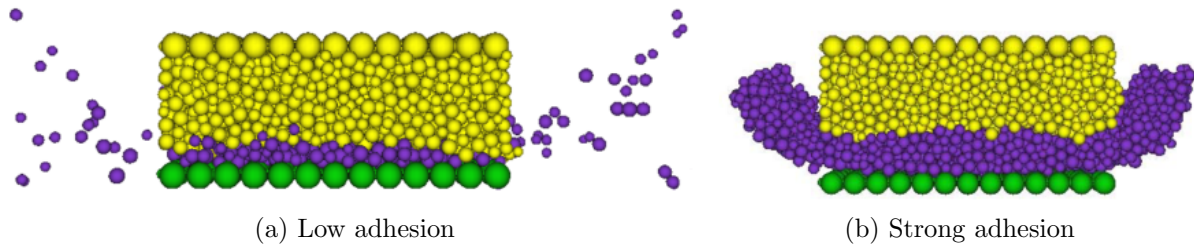


Figure 1.40: Wear model using DEM for which particles can be ejected from the contact; yellow and green particles represent first bodies and purple particles represent particles detached from first bodies (from [Fillot, 2004])

## 7 Objectives

### 7.1 Observations

Rubber-like materials are complex, with time and temperature dependent properties [Urzhumtsev, 1975], strain amplitude dependent properties [Payne, 1962], and with a significant viscous component [Boochathum and Prajudtake, 2001]. Added to this, there is a modification of these properties near the surface, as observed (but not quantified) in [Smith and Veith, 1982]. In addition, this work is dedicated to a pneumatic application, involving a strong interaction with the external environment, which is essential to understand. It is not possible to deal with all these topics at once, and it is therefore important to delimit the subject, and clearly define the underlying question. This work will focus on the interaction of the tire with the external environment. More specifically, it has been observed that tire wear particles are composed of mineral inclusions [Kreider et al., 2010]. However, this observation concerns a very advanced state, ignoring all the mechanisms that occur prior to wear. The aim is therefore first to retrace the steps leading to this mixture of minerals from the road and rubber from the tire, and identify what is known and what is not.

As discussed above, it has been shown in the literature that tire wear particles are composed of mineral inclusions (cf. fig. 1.23). Therefore, according to the tribological circuit framework, this means that at some point in time, these minerals were part of the third body, brought in by an external flow and ejected by means of a wear flow (cf. fig. 1.26). In addition, it is also known that the third body could affect the friction and wear rate [Morris and Kossyrev, 2018]. A preliminary question is whether these minerals modify the wear properties.

To study the effect of minerals, several wear tests were carried out on a tribometer under continuous shearing. The specimen is a carbon-black filled SBR sliding against a road-like surface. In one case, a layer of minerals is added on the specimen surface at the beginning of the test. Details of the protocol are given in the next chapter. The worn specimens are shown in fig. 1.41.

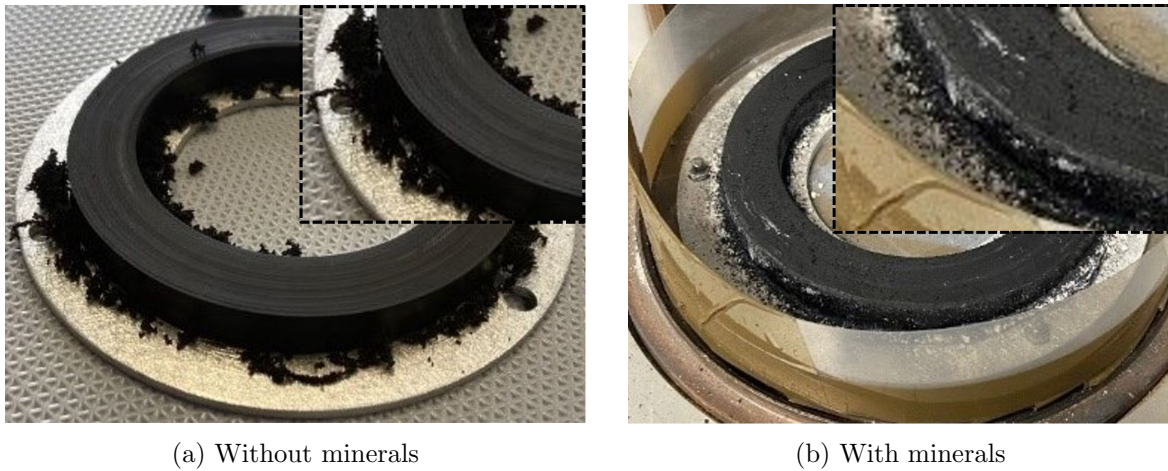


Figure 1.41: Photos of the worn specimens

By looking at the photos, it can already be seen that the wear particles have a different aspect. Without minerals, the particles form relatively large aggregates. With minerals, the particles are closer to a powder of fine particles. It would therefore suggest that minerals modify the wear process. For a better understanding, the surface of a specimen that has been worn with minerals can be observed using SEM fig. 1.42.

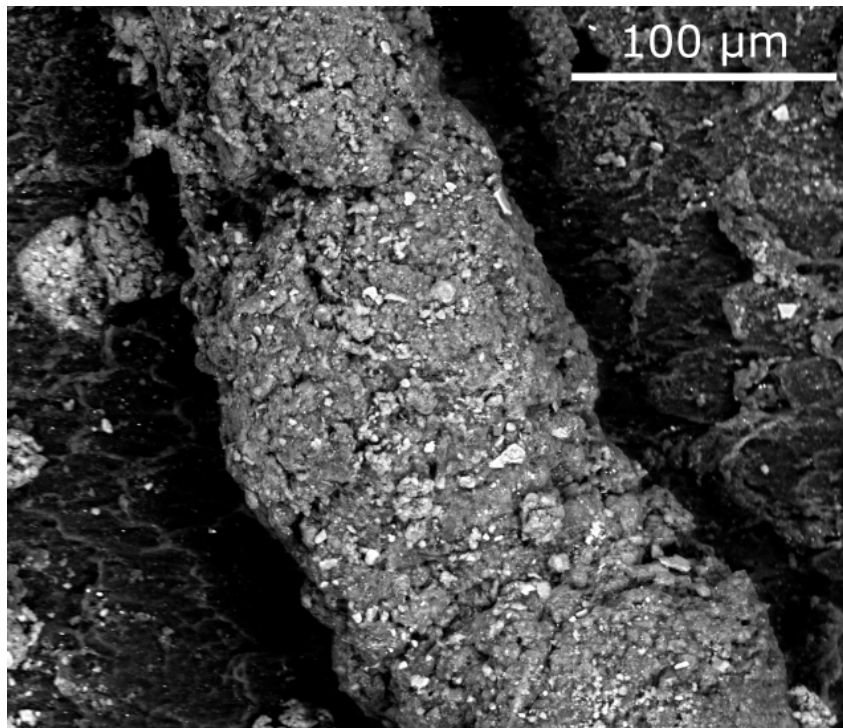


Figure 1.42: SEM image of a particle on the surface of a worn specimen (color representing Z-contrast)

By zooming in on one of the particles on the surface, mineral incrustations can be seen. The particles thus appear to be composed of a mixture of rubber and minerals, as could be seen for tire wear particles (cf. fig. 1.23). To get an initial understanding of mechanisms that occur prior to wear, a longitudinal section can be performed of the wear specimen (i.e. not the wear particle) in the direction of friction. An example is shown in fig. 1.43.



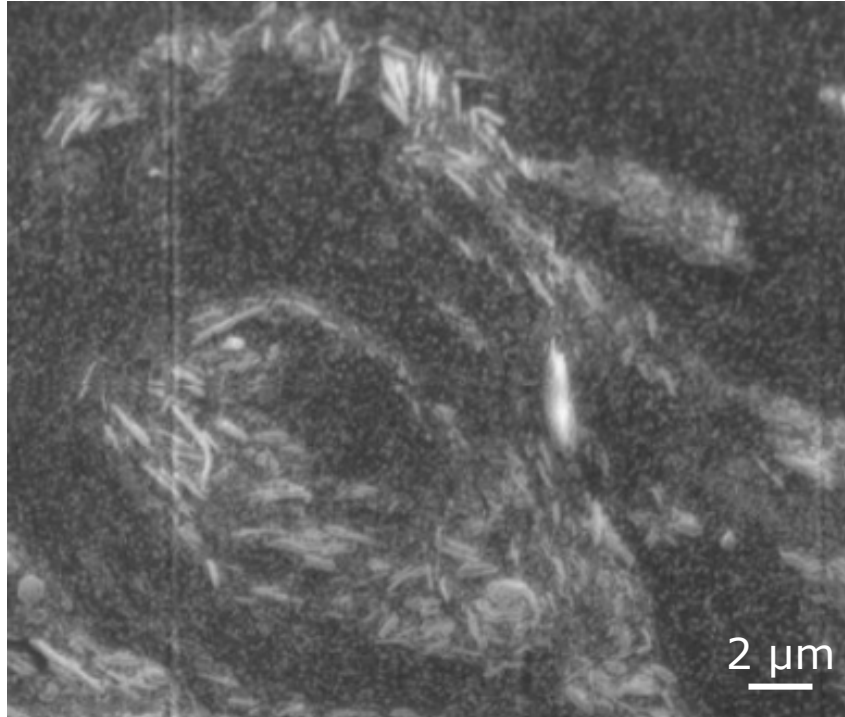


Figure 1.43: SEM image of a longitudinal section of a wear specimen (color representing the Z-contrast); sliding direction is horizontal

The minerals appear to diffuse into the surface of the rubber specimen. This could explain why the rubber and minerals form such a mixture. The pattern of minerals also seems to reflect a solid flow near the surface.

The tribological circuit is therefore slightly more complex than the one previously proposed. Indeed, the source flow was seen only as a flow of material from the first bodies towards the third body. However, in the previous image, although the distinction between the third body and the surface of the first body might be difficult, there is clearly a flow of minerals through the rubber specimen. This process can be seen as shear-induced diffusion and the corresponding framework will be detailed in the next chapter.

In the light of the literature and the preliminary tests carried out, it appears that minerals modify the wear properties. The approach proposed in this study is to get to the root of the phenomenon, which is the penetration of minerals into the first and third bodies. There are two main gaps in knowledge. The first concerns how a solid material can diffuse into another solid material, highly deformable, highly viscous and under tribological stresses. The second concerns how these minerals might alter the third body flow. The above comments raise several further questions: what are the mechanisms governing mineral diffusion? If minerals alter the properties of the third body, what effect does this have on wear? Is there a link between the diffusion rate and the wear rate? To summarize, this work will attempt to answer the following question:

Why and how road minerals are diffusing within the tire tread?

## 7.2 Strategy

All the previous questions are complex, and the scope of the study must be carefully defined. First, since mineral diffusion involves a kinematic process that takes place during sliding, *post-mortem* observations are not appropriate. Moreover, it seems reasonable to assume that mineral diffusion can hardly be studied without modeling the third body. If the third body and the minerals are taken into account, this will make it possible to understand the potential changes in third body kinematics. In an attempt to simplify the model, wear flow will be neglected. The aim is to develop a model like the one shown in fig. 1.44.

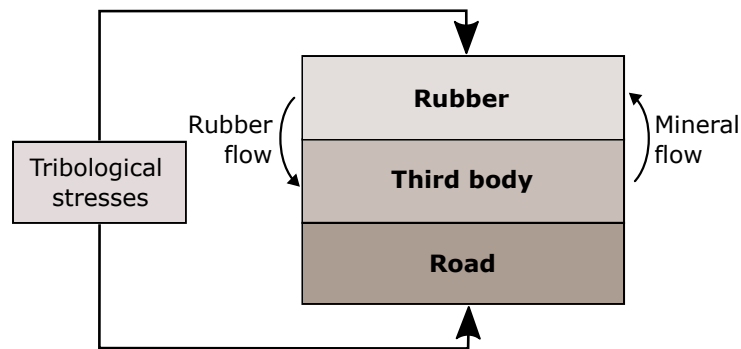


Figure 1.44: Illustration of the main features required by the model

As already mentioned, the behavior of the third body is far too complex to study it using analytical solutions. This will require the use of numerical models. It will be discussed later, but the size of a mineral is close to  $0.1 \mu\text{m}$ , which suggests a model close to the microscopic scale. In addition, the model must be able to deal with solid flows, and more precisely, with the mixture of rubber and minerals. As suggested by fig. 1.33, both discrete and continuum-based particle methods could meet these criteria. However, due to the specific size and geometry of the minerals, a discrete method will be preferred.

The main characteristics of a diffusive process will be introduced in chapter 2. This will give an understanding of the mechanisms leading to diffusion, and what type of discrete numerical method could best capture such mechanisms. From there, the numerical model and corresponding method will be presented. The numerical results will be supported by several experimental tests and the set-up will also be detailed.

The model will require several input parameters, and a characterization process using reverse analysis will be carried out. For this purpose, a new method using discrete elasto-plastic indentation is developed and will be presented in chapter 3.

An overview of the results about initial mineral penetration will first be given in chapter 4. Then, the main steps of a given simulation will be described, showing why mineral migration on a longer time scale can be considered as a diffusive process. This will set the groundwork for subsequent analysis. In particular, the results will be compared with several experimental tests.

Emphasis will then be placed on what will hereafter be referred to as steady-state diffusion in chapter 5. This will provide statistically significant evidence of the effect of certain parameters on diffusion. In particular, the effect of contact pressure and rubber properties will be investigated.



# Chapter 2

## Framework

This chapter introduces the concept of diffusion and the method used in this work to study it. First, the experimental set-up is described in section 1. Then, a brief description and state of the art of diffusion is given in section 2. The numerical method is first presented in section 3, followed by a description of the model in section 4.

### 1 Experimental set-up

#### 1.1 Tribometer

To study mineral diffusion under controlled conditions, wear tests were carried out on a tribometer (UMT-2 CETR). The road-like surface is composed of resin-bonded aggregates (sandstone). The vertical displacement of the top surface is controlled to ensure a constant normal load during the test. A constant rotational speed is applied by the lower surface. An illustration of the tribometer and the specimen is shown in fig. 2.1.

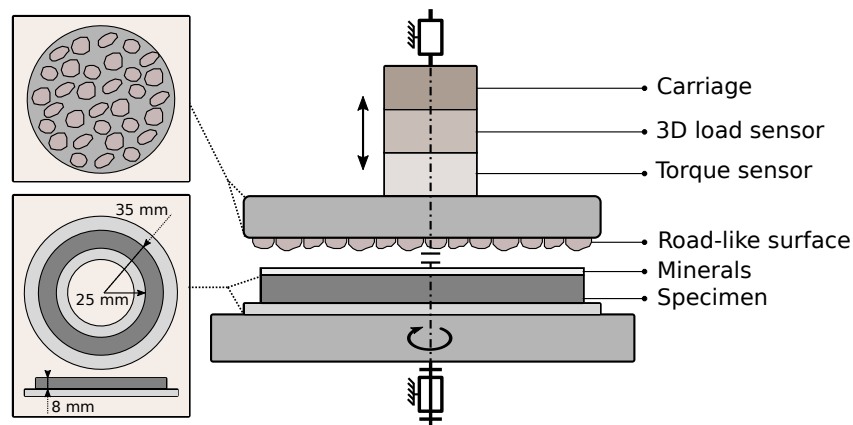


Figure 2.1: Illustration of the tribometer and the two bodies in contact

#### 1.2 Specimen

The wear specimen is a ring made of SBR (and several other compounds) with an inner radius of 25 mm, an outer radius of 35 mm and a thickness of 8 mm. The composition is as follows (in  $phr^1$ ): 100 SBR, 50 N347, 3 6PPD, 1.5 stearic acid, 3 ZnO, 1.3 CBS and 1.3 sulfur.

<sup>1</sup>parts per hundred of rubber



The glass transition temperature of the SBR is equal to  $-48\text{ }^{\circ}\text{C}$ . The specimen is cured at  $140\text{ }^{\circ}\text{C}$  for 35 minutes.

### 1.3 Observations

Several observations were made on a Thermofisher QUANTA 600 environmental scanning electron microscope (ESEM), using a water vapor pressure of  $350\text{ Pa}$  to avoid charging problems. A gaseous analytical detector (GAD) is equipped. The GAD is a backscattered electrons (BSE) detector with a conical shape to prevent dispersion of the electron beam in the SEM chamber gaseous environment. Some of these observations will be supported by energy dispersive X-ray (EDX) analysis. In addition, some longitudinal sections are obtained using a crosspolisher (Gatan, Ilion II). An illustration of the cutting plan is shown in fig. 2.2.

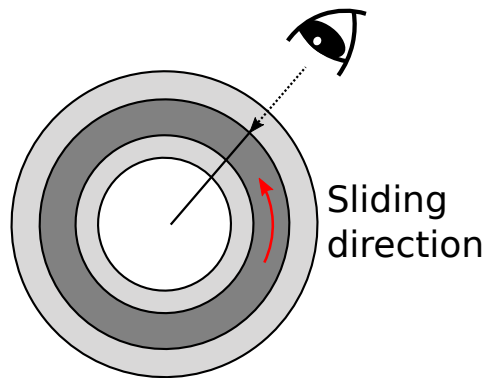


Figure 2.2: Cutting plan of the longitudinal sections

### 1.4 Minerals

To reproduce the effect of road minerals, a thin layer ( $200\text{ mg}$ ) of kaolinite powder ( $\text{Al}_2\text{Si}_2\text{O}_5(\text{OH})_4$ ) is spread over the surface of the rubber specimen using a spatula. Preliminary tests were carried out with different quantities of minerals ( $50$ ,  $100$ ,  $200$  and  $400\text{ mg}$ ), which did not significantly affect the mass loss and tangential force. In fact, most of the kaolinite is ejected at the beginning of sliding and only a small quantity remains at the interface.

To obtain the mineral size distribution, several images from internal tests within Michelin were segmented. This consists from a matrix of pixels (i.e. an image), in creating a corresponding binary matrix with a 1 if the pixel belongs to a mineral and a 0 otherwise. The boundaries of each body are then reconstructed. This operation was carried out using a custom code based on standard methods (connectivity, gradient, standard deviation, etc.) but adapted to noisy SEM images containing many bodies.

The segmented images correspond to longitudinal sections of worn samples in the same plane as the numerical model (relative to the sliding direction as shown in fig. 2.2). As minerals can potentially be fractured, this choice was made to be as close as possible to the *in situ* configuration compared to usual granulometry methods such as laser diffraction. It is assumed that size distribution does not depend on the configuration (e.g. contact pressure). In addition, two segmentations were performed for two sliding distances to determine whether it evolves during sliding. The results are shown in fig. 2.3.

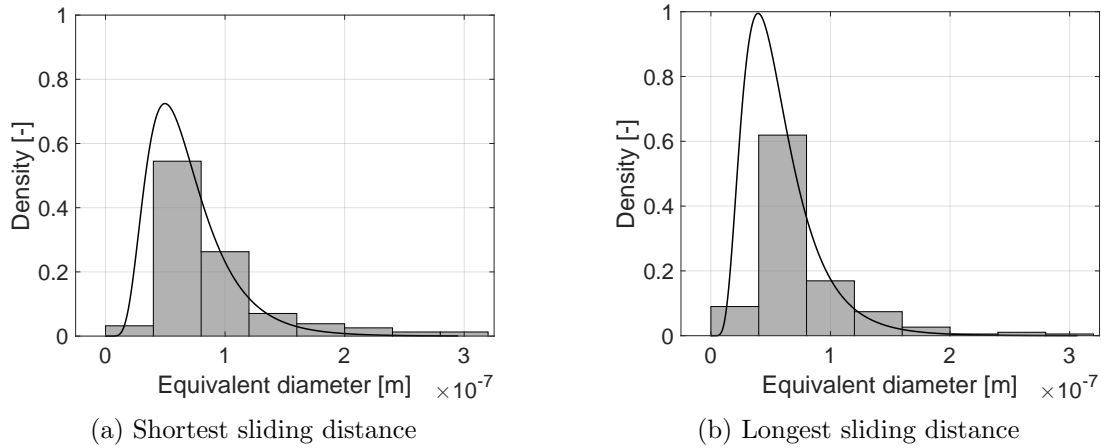


Figure 2.3: Mineral size distribution obtained from segmentation analysis; the equivalent diameter corresponds to the diameter of the circle to obtain the same area

The mineral size follows a log-normal distribution. For the shortest and longest sliding distance, the mode is respectively equal to 0.049 and 0.040  $\mu\text{m}$ , the mean to 0.098 and 0.085  $\mu\text{m}$  and the standard deviation to 0.108 and 0.098  $\mu\text{m}$ . Due to the dispersion between two tests, these results are not different enough to identify an effect of sliding distance. The minerals are in the form of thin platelets. For each segmented mineral, an elliptical shape is considered and is fitted using a least-squares criterion, as shown in fig. 2.4.

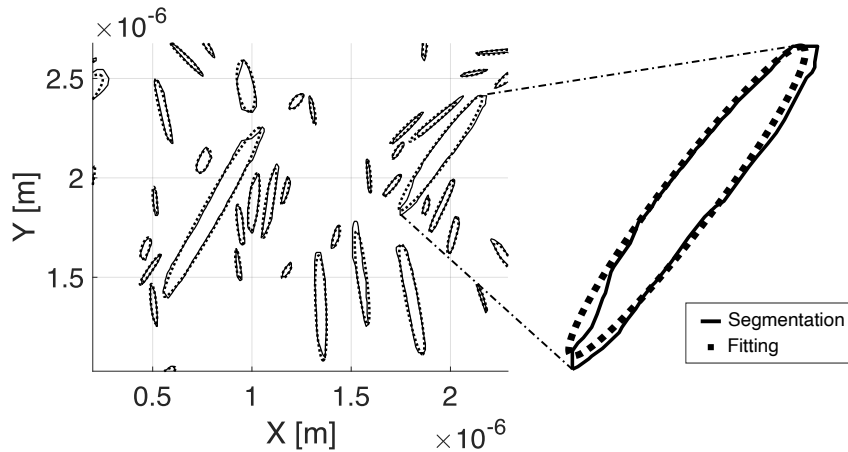


Figure 2.4: Fitting from mineral segmentation

From these ellipses, the ratio of major to minor axis can be determined. For the shortest and longest sliding distance, it is equal on average to 6.98 and 6.57 respectively.

## 1.5 Surface topography

The road is reproduced experimentally with a surface composed of resin-bonded aggregates (sandstone). The topography of one of these aggregates is characterized by interferometry using a 3D non-contact optical surface profiler (Zygo, ZeGage TM Pro). An illustration of the apparent contact area in red, compared with the real surface acquisition in blue (not to scale), is displayed in fig. 2.5a. The captured surface measures 340 by 283  $\mu\text{m}$  and is displayed fig. 2.5b.

This surface can be characterized using well-known indicators such as the arithmetic average of surface height deviations from the mean plane ( $S_a$ ). However, the values given by this kind of indicator are difficult to interpret, as they depend on the spatial scale under consideration.

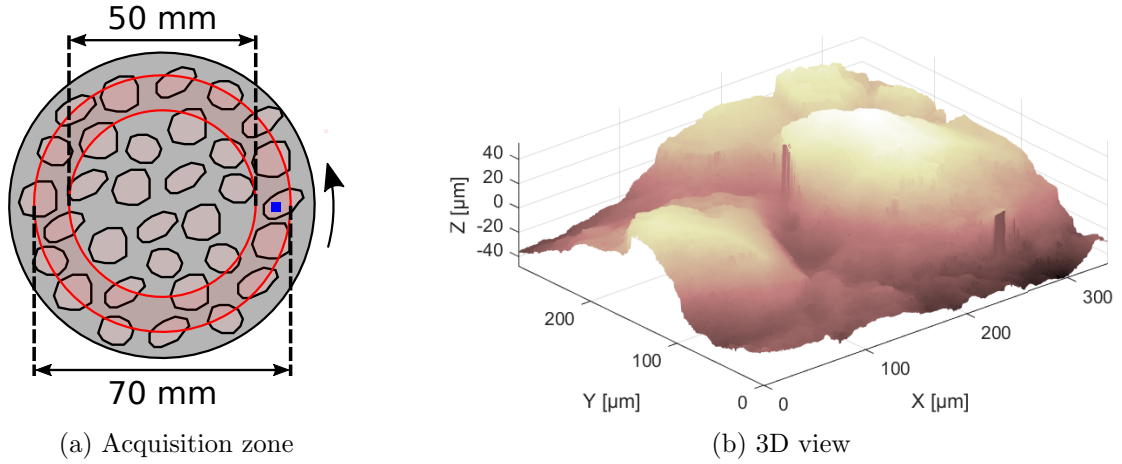


Figure 2.5: Surface topography measured by interferometry

As described in [Candela et al., 2012], a natural surface may exhibit a self-affine topography. This is a typical property of fractals, and corresponds to the repetition of a shape or part of it according to a given scaling factor. It can be described by two coefficients (the Hurst exponent and a prefactor). In particular, this makes it possible to extrapolate topography to smaller (or larger) length scales, which will be useful for the numerical model.

Along one direction, a set of 2D profiles (successive cuts of the 3D surface) is obtained and a discrete Fourier transform (DFT) is performed. This gives the spatial frequencies in the form of a 2D matrix with a size of [ $\langle \text{Number of nodes per profile} \rangle \times \langle \text{Number of profiles} \rangle$ ]. Next, the average value along the second dimension is computed to obtain a 1D matrix with a size of [ $\langle \text{Number of nodes per profile} \rangle$ ]. Then, the power spectral density (PSD) is computed. This process is carried out for the directions orthogonal and parallel to sliding. Finally, a power law is fitted as written in eq. (2.1).

$$S_{xx} = S_P f^{-1-2S_H} \quad (2.1)$$

with  $S_{xx}$  the power spectral density,  $S_P$  the prefactor,  $f$  the spatial frequency and  $S_H$  the Hurst exponent. It should be noted that for higher frequencies, the PSD as a function of frequency tends to flatten out due to the inherent noise compared to the magnitude of the topography. The fitting was therefore performed before the inflection point, which in this case was arbitrarily defined as  $5 \times 10^5 \text{ m}^{-1}$ . The results are displayed in fig. 2.6.

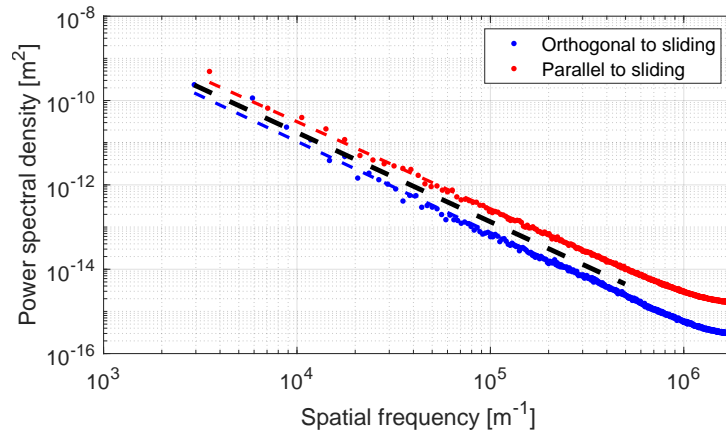


Figure 2.6: Power spectral density as a function of spatial frequency; the markers correspond to the 1D PSD matrix and the dotted lines to the fittings

The global Hurst exponent and the prefactor (i.e. the fitting that includes the PSD of orthogonal and parallel directions) are respectively equal to 0.5588 and  $5.160 \times 10^{-3} m^2$ .

## 2 Diffusion framework

### 2.1 Stochastic view

When particles are suspended in a liquid or gas, they exhibit an apparent random motion known as Brownian motion. This motion is due to collisions between particles, so the term “random” refers more to unpredictability than to a true random process. The origins of these collisions are manifold. Primarily, they are associated with the chemical potential, which is most often reduced to the temperature, linked to the vibration of atoms and creating a series of collisions. This potential also depends on other quantities such as pressure. However, as discussed below, it is possible to observe this motion at a larger scale, where quantities like thermal agitation no longer have any effect. Depending on the system, other more macroscopic quantities can lead to a series of collisions, such as shear.

This motion was originally studied by Robert Brown in 1827 to describe the movement of pollen particles in water. As a result of collisions, particles immersed in a chemical species tend to homogenize in space and time, as illustrated by fig. 2.7.

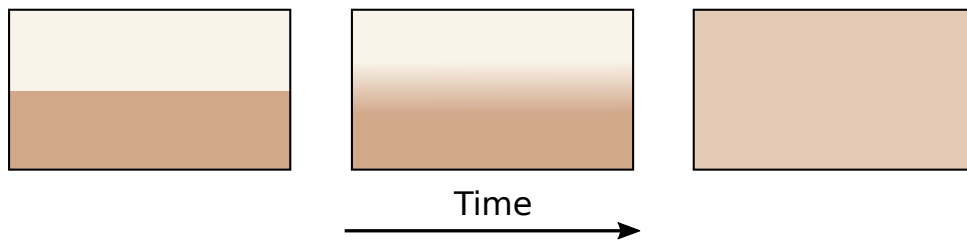


Figure 2.7: Illustration of a diffusive process between two chemical species

This process is called diffusion. By taking the example of a liter of water, which is composed of more than  $10^{23}$  molecules, it is clear that it is not possible to model each molecule explicitly. Even for a single water molecule, it is estimated that it undergoes  $10^{14}$  collisions per second [Feynman, 1962]. For these reasons, diffusion will be considered as a stochastic process. This means that each interaction has a given probability of occurrence. One way to proceed is to model diffusion as a random walk process [Gorenflo et al., 2002]. This consists of applying a variation according to a probability distribution and repeating the operation for several iterations. In the case of diffusion, the position ( $y$ ) of a particle is shifted ( $\Delta y$ ) according to a certain time period ( $\Delta t$ ) and the trajectory is tracked as a function of time ( $t$ ). This procedure is then repeated for a large number of particles. An example of a result from the algorithm in its simplest version is shown fig. 2.8.

In the example fig. 2.8a, a displacement (-1, 0 or 1) is randomly applied to a particle at each iteration ( $t = 2, t = 3$ , etc.). At the scale of a particle, this displacement is highly erratic. This can be used, for example, to model fluctuations in stock market prices, as proposed in [Bachelier, 1900]. If the procedure is repeated for a large number of particles (fig. 2.8b), the overall behavior becomes more predictable and follows a Gaussian distribution (figs. 2.8c and 2.8d). This result is particularly interesting given that no distribution has been specified, and that the behavior tends to be deterministic even for a relatively small number of particles and iterations. This is moreover consistent with macroscopic observations of diffusion, which in most cases show a deterministic evolution.

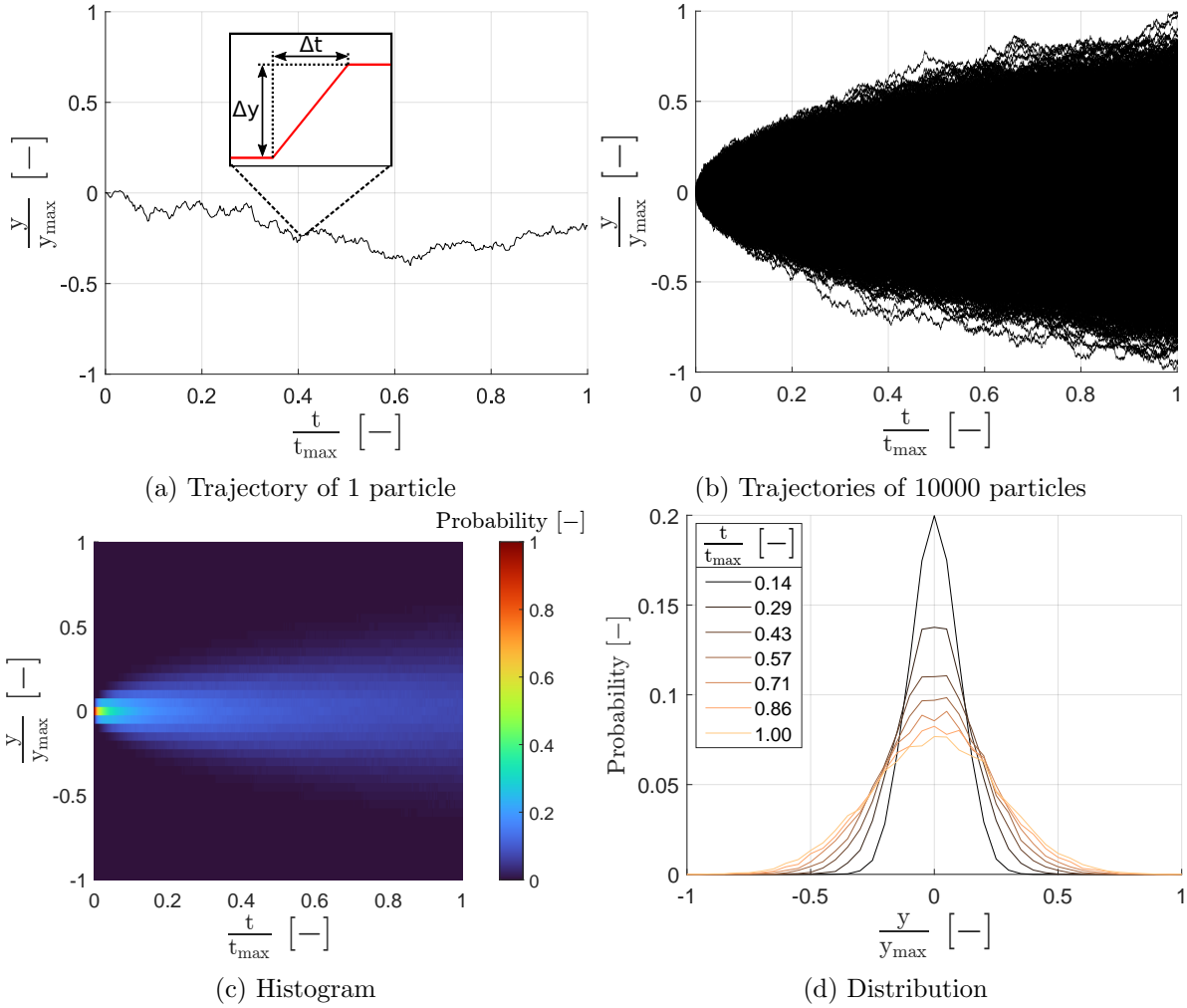


Figure 2.8: Random walk algorithm for 10000 particles and 10000 iterations (i.e. time steps); at each time step, a particle is randomly (without defining a probability distribution) shifted by -1, 0 or 1;  $y_{max} = 392$ ,  $t_{max} = 10000$  and the bin width is equal to  $0.05 y_{max}$  for the histogram

## 2.2 Deterministic view

As already mentioned, at a scale larger than the particle, the behavior becomes deterministic. The main objective of diffusion is to study the concentration of a given species as a function of space and time. This can be expressed by using a continuous mathematical equation. The most commonly used model is probably the second law of Fick, written in eq. (2.2) for a one-dimensional case.

$$\frac{\partial \varphi}{\partial t} = \frac{\partial}{\partial y} \left( D \frac{\partial \varphi}{\partial y} \right) \quad (2.2)$$

with  $\varphi$  the concentration (which depends on space and time),  $t$  the time,  $y$  the spatial dimension and  $D$  the diffusion coefficient. This coefficient describes the diffusion ability of the species and is often assumed to be constant. In this case, the time derivative of  $\varphi$  is proportional to the Laplacian of  $\varphi$ . Note that  $D$  is not an intrinsic property of the species and depends on external parameters such as temperature. Several analytical solutions exist for relatively simple cases. An example of a result for arbitrary parameters is presented in fig. 2.9.

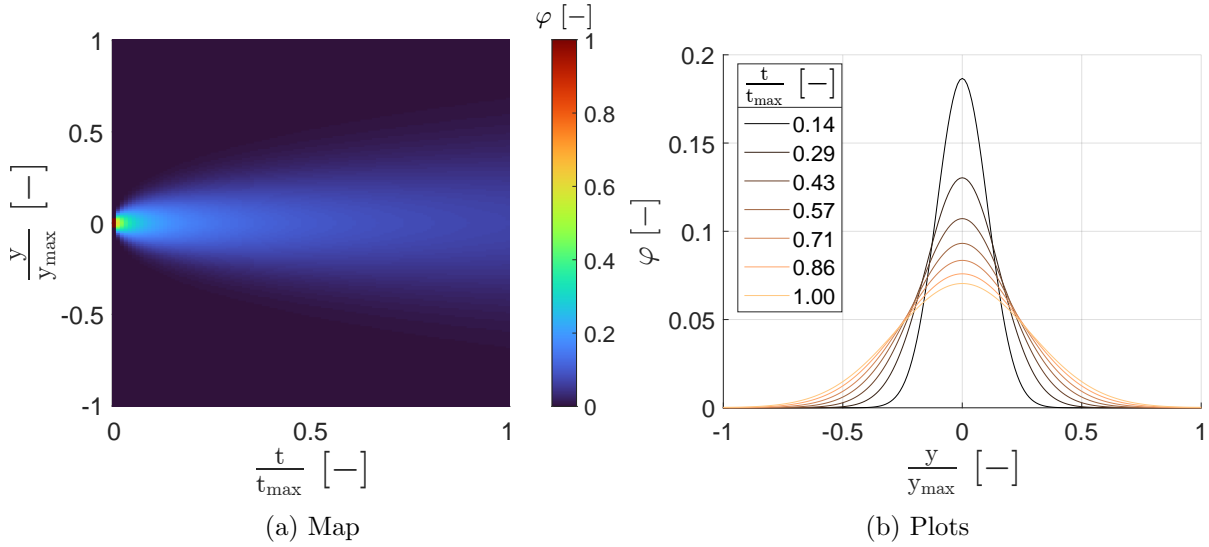


Figure 2.9: Concentration according to the second law of Fick for arbitrary parameters ( $y_{max} = 1$  m,  $t_{max} = 1$  s,  $D = 4.10^{-2}$  m<sup>2</sup>.s<sup>-1</sup>,  $\varphi = 1$  for  $y \in [-0.025, 0.025] \times y_{max}$  and  $t = 0$  s)

The resulting concentration follows a Gaussian distribution according to space with an increasing standard deviation for increasing time. The plots correspond to the distributions that can be obtained from the random walk algorithm. The results between these two are very similar (depending on the probability distribution used for the random walk). Some processes do not follow a Fickian diffusion and are referred to as non-Fickian or anomalous diffusion. This will be discussed later.

### 2.3 From stochastic to deterministic

Studying the displacement of each particle is often irrelevant, as it is not representative of the overall behavior. Moreover, this would lead to a considerable amount of data to process. To overcome this difficulty, it is possible to reduce all the individual displacements to a mean square displacement (MSD), as described in eq. (2.3) [Fry et al., 2019].

$$MSD(t) = \frac{1}{N} \sum_{i=1}^N (y_i(t) - y_i(t_0))^2 \quad (2.3)$$

with  $MSD$  the mean square displacement,  $t$  the time,  $N$  the number of particles,  $i$  the particle index,  $y_i$  the particle position and  $t_0$  the reference time. The  $MSD$  should follow a power law with time as written in eq. (2.4).

$$MSD(t) = \alpha t^\beta \quad (2.4)$$

with  $MSD$  the mean square displacement,  $t$  the time,  $\alpha$  and  $\beta$  are constants. For a normal diffusive behavior,  $\beta$  is equal to 1 and thus diffusion  $\propto \sqrt{t}$  (as the  $MSD$  corresponds to a quadratic displacement). This is consistent with some of the analytical solutions of the second law of Fick and provides a first link between the stochastic and deterministic points of view.

A more rigorous link can be established. Indeed, a probability density function of a variation in space can be defined (but it could be any quantity such as temperature). Then, by using Taylor series and assuming a normal distribution, the relation of Einstein in eq. (2.5) can be derived [Einstein, 1906]

$$MSD(t) = 2Dt \quad (2.5)$$

with  $MSD$  the mean square displacement,  $t$  the time and  $D$  the diffusion coefficient. This relationship makes it possible to introduce stochastic results into a deterministic model through the use of a diffusion coefficient. It should be noted that neither the second law of Fick nor the relation of Einstein aims to explicitly model the physics behind diffusion (i.e. particle collisions). Indeed, the first uses a concentration Laplacian that is meaningless at the particle scale. The second is based on a random walk. Consequently, these relationships should be considered as models of any stochastic process more than the diffusion of a chemical species. It is also worth remembering that the term random does not mean that the result is not affected by any parameter. Rather, it depends on a probability density function, which in turn depends on physical quantities.

The previous comment explains why relationships similar to diffusion can be found in other fields. For example, the first law of Fick states that diffusion flux is proportional to concentration gradient. The fact that a quantity evolves according to a certain gradient can be found in several physics. For example, a comparison can be made between the first law of Fick describing diffusion ( $\propto$  concentration gradient), the law of Fourier describing heat conduction ( $\propto$  temperature gradient) and the law of Newton describing shear stress in a viscous flow ( $\propto$  velocity gradient) [Won and Ramkrishna, 2019].

Diffusion of a chemical species is due to the Brownian motion induced in particular by thermal agitation, which leads to a multitude of action/reaction forces [Tsimpanogiannis et al., 2019]. A similar process occurs for shear-induced diffusion. However, thermal agitation becomes negligible compared to the agitation induced by shear forces [Buradi et al., 2019]. For granular media, the analogy is even stronger, as contacts can be quantified.

## 2.4 Shear-induced diffusion

As mentioned earlier, in terms of overall behavior, the results of the random walk algorithm (i.e. the stochastic view) and the second law of Fick (i.e. the deterministic view) are close. In most cases, random walk already represents a homogenization, with one particle in the algorithm actually representing a group of particles in reality. Shear-induced diffusion in discrete media (e.g. granular) is very similar from both points of view. An illustration is given in fig. 2.10.

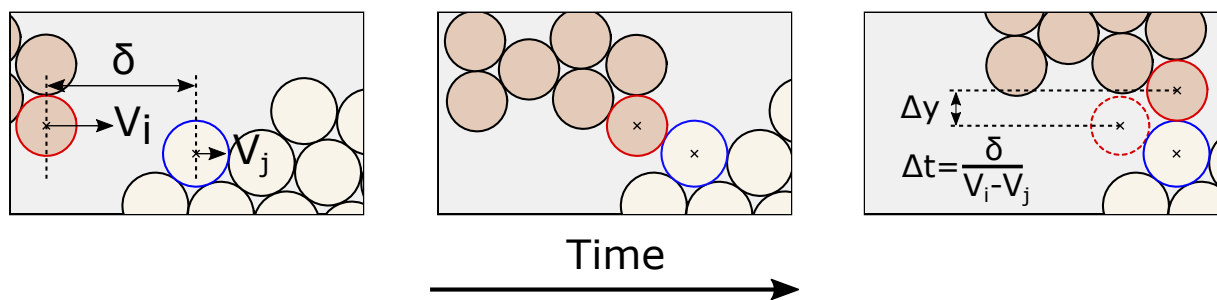


Figure 2.10: Illustration of a particle jump due to a collision with another particle

The previous illustration is a simplification as, in practice, a particle is in quasi-permanent contact with other particles and, after a collision, both particles are shifted. Two agglomerates of particles with relative velocities ( $V_i$  and  $V_j$ ) will collide, resulting in a displacement. This process is very similar to a random walk, with a variation of  $\Delta y$  each  $\Delta t$ . The main objective of shear-induced diffusion studies is to understand how these two parameters are influenced by others, such as sliding velocity, contact pressure, etc.



Several works exist to model diffusion in a medium composed of discrete particles. Such modeling is essentially carried out for granular media using discrete element method (DEM) [Fan et al., 2015]. Firstly, particle size plays a role in the diffusion process, as shown by [Cai et al., 2019]. While for rigid particles, the link between this size and  $\Delta y$  is clear, for soft particles, the notion of a well-defined size vanishes. Concerning  $\Delta t$ , it depends on the relative velocity between particles, as shown in the previous illustration. This relative velocity is linked to the shear rate and explains why shear rate drives diffusion [Artoni et al., 2022]. The aim is often to find a functional form as given in eq. (2.6).

$$D \propto f(\Delta y, \Delta t) \propto f(\phi, d, \dot{\gamma}) \quad (2.6)$$

with  $D$  the diffusion coefficient,  $\Delta y$  a characteristic spatial variation,  $\Delta t$  a characteristic time period,  $\phi$  the compacity,  $d$  a characteristic particle size and  $\dot{\gamma}$  the shear rate. It should be noted that the proposed illustration represents a quasi-collisional flow and in practice, diffusion is highly dependent on the flow regime (dense or collisional) [Rognon and Macaulay, 2021].

The main objective of this work is to study experimentally and numerically the diffusion of minerals within the tire tread. First, experimentally, a rubber-like specimen similar to the tire tread material must be subjected to friction against a road-like surface, with the possibility of adding minerals. This will be achieved thanks to the tribometer as already discussed. Then, on the numerical side, the model will require several features. Firstly, the ability of minerals to diffuse into the rubber. To this end, rubber can be modeled as a collection of separable bodies. This requires the bodies to interact with each other through contact models, thanks to an appropriate contact algorithm. Material properties must also be taken into account, such as the elastic modulus of the rubber. Indeed, it is relatively low compared to the stress level and rubber cannot be considered as rigid or with low strain. It is therefore not compatible with DEM. In addition, interactions between rigid and highly deformable bodies must be modeled. This can lead to significant geometric distortions, and will require a robust numerical method for computing strains and detecting contacts. Finally, all these bodies must be subjected to tribological stresses with appropriate space and time scales. For all these reasons, a multibody meshfree approach implemented in a code called MELODY is employed [Mollon, 2016].

## 3 Numerical method

### 3.1 Overview

#### 3.1.1 Main features

MELODY2D (Multibody ELeMent-free Open code for DYnamic simulation in 2D) is an open source software. It is currently only developed for plane-strain kinematics. The method is particularly suitable for modeling a collection of bodies subjected to tribological stresses, but is relatively versatile and can be used for other loading configurations. Firstly, it allows to simulate a large number of deformable bodies, which extends the DEM framework to materials subjected to large strains. Secondly, the method can handle both rigid and deformable bodies in a single simulation. Finally, the use of an appropriate contact detection algorithm makes it possible to model bodies with complex geometries. This is particularly useful for geological applications [Casas, 2022] or to study fracture of brittle materials as shown in fig. 2.11.

In this work, the possibility of using soft bodies will be particularly important. Indeed, as already discussed, rubber has a low elastic modulus compared to the typical stress level. Moreover, for rigid bodies, diffusion depends on particle size, which does not seem accurate for a third body which is not granular. Instead, results should rely on parameters such as material

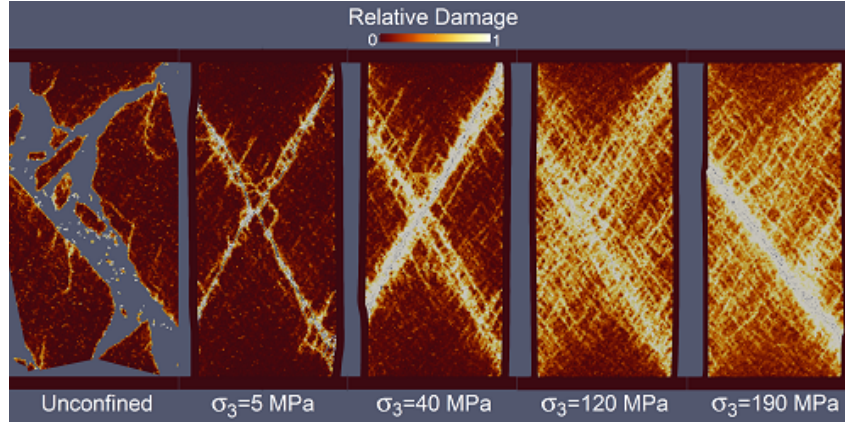


Figure 2.11: Compression of a brittle material under several confining stresses (from [Mollon et al., 2023])

properties (e.g. elastic modulus). The use of soft bodies gives a wider range of flows that could be obtained with rigid bodies.

A parametric study has been carried out in [Mollon, 2019] for a sliding interface and sets the groundwork for results that can be obtained from discrete modeling with deformable bodies. In this study, the third body is modeled as a collection of soft bodies interacting with each other (cf. fig. 1.37). Each body has a given stiffness ( $\tilde{E}$ ) and viscosity ( $\tilde{\alpha}$ ). Between the particles, a purely cohesive model ( $\tilde{c}$ ) is defined with a normal and a tangential component. The normal component is a tensile cut-off stress (the link between two bodies is removed if the load per unit area exceeds this value). The tangential component is a resisting stress. Both are assumed to be equal. All these parameters are normalized in a logarithmic space and more details can be found in the original study.

A global friction coefficient is computed and decomposed into friction from bulk phenomena  $\mu_b$  (i.e. viscosity) and from surface phenomena  $\mu_s$  (i.e. the creation of a cohesive link is energy-free compared to removal and from sliding between particles). Results are shown in fig. 2.12.

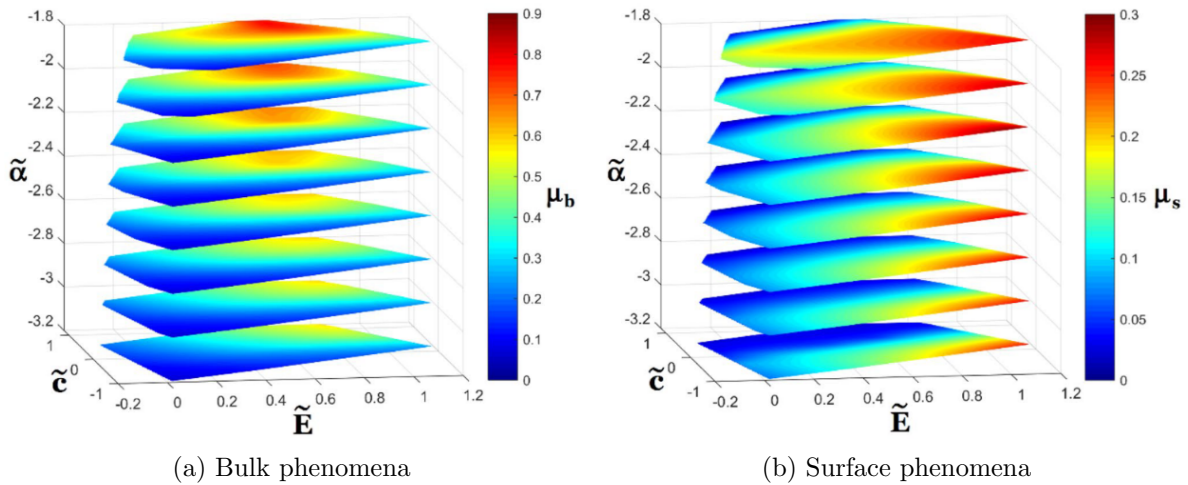


Figure 2.12: Friction coefficients of a sliding interface model using soft bodies (from [Mollon, 2019])

These results show that, depending on the parameters, a significant proportion of the energy

dissipation can be due to bulk phenomena. Even at lower viscosities,  $\mu_b$  remains significant compared to  $\mu_s$ . This does not mean that more classical DEM models would underestimate the friction coefficient by assuming  $\mu_b$  to be zero. Rather, it implies that contact model parameters would be modified by modeling bulk dissipation as contact dissipation (e.g. by increasing contact damping). However, this approach is limited and a lack of physical meaning quickly arises.

An important point highlighted by these results is the highly nonlinear behavior of such an interface. Indeed, if only the friction coefficient is considered, very different combinations of  $\tilde{E}$ ,  $\tilde{\alpha}$  and  $\tilde{c}$  can give the same friction coefficient. The main reason for this is the variety of velocity transmission regimes. It can follow a classical plastic laminar flow with the creation and destruction of cohesive links between bodies. However, if cohesion is high relative to stiffness and contact pressure, an agglomerated regime is formed. As the particles can be deformed more easily, the contact surface between them increases, and therefore also the cohesive forces. This results in agglomerates that are resistant enough not to be milled by shear. Energy is therefore dissipated mainly by viscous dissipation within the agglomerate(s) (depending on the value of  $\tilde{\alpha}$ ).

It should be noted that multibody models are widely used for granular media, which can be characterized as highly dissipative (friction coefficient can easily exceed 0.5) with highly rigid bodies. The word “grains” is sometimes used even for soft bodies. Indeed, the term particle is often associated with wear and body to a continuous body at the macroscopic scale. Hereafter, discrete bodies may be referred to as grains, particles or bodies.

The aspect of the third body is also highly parameter-dependent. Several snapshots are displayed in fig. 2.13 for a given viscosity. For cases E, C and F, the local solid fraction becomes close to 1 for increasing  $\tilde{c}$ . While a characteristic particle size exists for rigid particles, in this study, it is less obvious for several cases such as F. The fact that the jump ( $\Delta y$ ) depends on particle geometry could still be true, but if so, geometry now depends on  $\tilde{c}$  and  $\tilde{E}$ . Moreover, in the case of dense granular flow, for a particle to jump, a local reorganization of the other particles is required to obtain a free room. In the case of soft bodies, this could be achieved by deformation and not necessarily by displacement of the particles. Finally, velocity transmission (which determines  $\dot{\gamma}$  and therefore  $\Delta t$ ) is essentially close to a Couette flow, except in some cases where the values of  $\tilde{c}$  are high enough as discussed above.

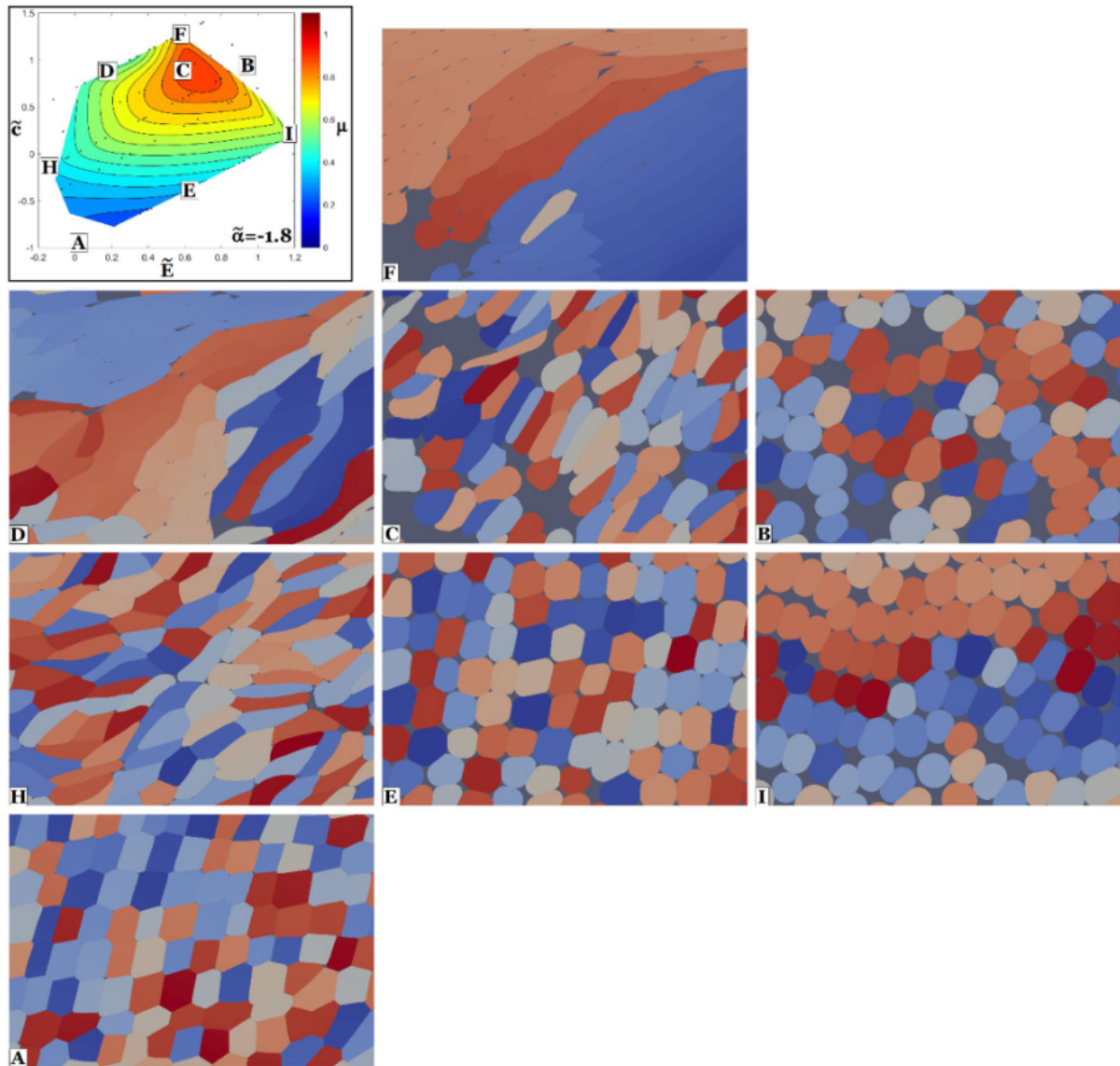


Figure 2.13: Snapshots (particle color is arbitrary) for a given viscosity and for several stiffnesses and cohesions (from [Mollon, 2019])

### 3.1.2 Pre-cut material

A common misinterpretation of discrete models when they are applied to tribology is to consider that each particle represents a wear particle that has meaning if taken individually. Instead, the whole discrete domain should rather be considered as a pre-cut material, especially for deformable particles. By taking the example of a tensile test (fig. 2.14a), if there is no decohesion between particles, except for potential empty spaces between them, there is no difference with a continuous material. In the case of a sliding interface (fig. 2.14b), the same comment can be made. The difference is that shear strain increases continuously and decohesions are much more significant. For example, when examining the F case in fig. 2.13, a single particle is meaningless, and only particle agglomerates should be considered.

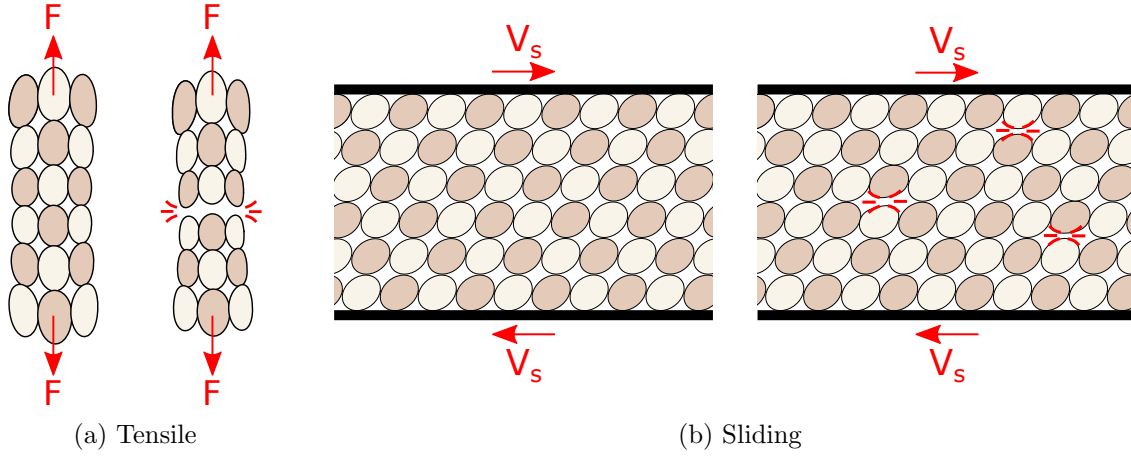


Figure 2.14: Illustration of pre-cut materials with  $F$  a tensile force and  $V_s$  a sliding velocity

### 3.1.3 Dynamic equilibrium

This method allows the use of soft bodies. Whereas for rigid bodies, a single force is applied through the center of mass (cf. eq. (1.11)), for soft bodies, a more sophisticated relationship including strain must be used. This will be discussed later, but it will be necessary to introduce a spatial field discretization of each body as described in fig. 2.15.

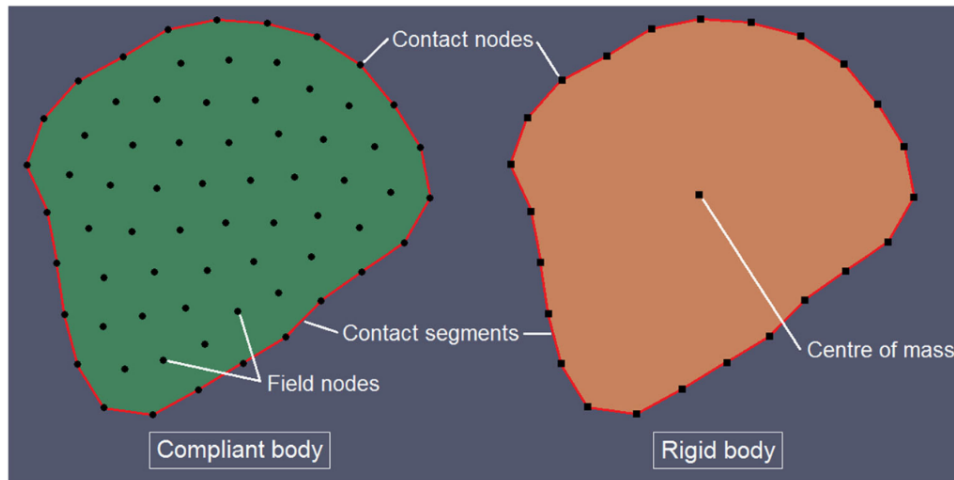


Figure 2.15: Comparison of soft and rigid bodies (from [Mollon, 2018b])

Firstly, the implementation of soft bodies requires the use of a constitutive model (equivalent to a contact model in DEM). Secondly, forces (such as inertia) are no longer homogeneous within each body. Moreover, the body boundary is time-dependent. Dynamic equilibrium is then written in a weak form for the reference configuration, as described in eq. (2.7).

$$\begin{aligned} & \int_{\Omega_U} \bar{\bar{S}}(u) : \bar{\bar{E}}(v) dS - \int_{\Omega_U} \rho \bar{f} \cdot v dS - \int_{\partial\Omega_N} \bar{T}_N \cdot v dX - \int_{\partial\Omega_C} \bar{T}_c \cdot v dX \\ & = - \int_{\Omega_U} \rho \frac{\partial^2 u}{\partial t^2} \cdot v dS - \int_{\Omega_U} c \frac{\partial u}{\partial t} \cdot v dS \quad \forall v \in V_0 \end{aligned} \quad (2.7)$$

with  $\Omega_U$  the domain covered by the union of the bodies,  $\bar{\bar{S}}$  the second Piola-Kirchhoff stress tensor,  $u$  the displacement (without representing the tensor bar for clarity),  $\bar{\bar{E}}$  the Green-Lagrange strain tensor,  $v$  the virtual displacement (without representing the tensor bar for



clarity),  $\rho$  the density,  $\bar{f}$  the body forces,  $\partial\Omega_N$  the boundary covered by Neumann boundary conditions with  $\bar{T}_N$  the external forces,  $\partial\Omega_C$  the boundary covered by possible contact surface with  $\bar{T}_C$  the contact forces,  $t$  the time,  $c$  the damping and  $V_0$  the Sobolev space with homogeneous Dirichlet boundary conditions. The stress tensor can be derived from a hyperelastic model according to eqs. (2.8) and (2.9).

$$\bar{\bar{S}} = \frac{\partial W}{\partial \bar{\bar{E}}} \quad (2.8)$$

$$\bar{\bar{E}} = \frac{1}{2} \left( \underline{\nabla}_X u + (\underline{\nabla}_X u)^T + (\underline{\nabla}_X u)^T \cdot \underline{\nabla}_X u \right) \quad (2.9)$$

with  $\bar{\bar{S}}$  the second Piola-Kirchhoff stress tensor,  $W$  the strain energy density function (i.e. the hyperelastic model),  $E$  the Green-Lagrange strain tensor and  $u$  the displacement. Dynamic equilibrium is by far too complex to solve analytically. Consequently, a numerical approximation with spatial and temporal discretization is used.

## 3.2 Spatial discretization

### 3.2.1 Discretization

The aim of a numerical method is generally to solve a system of differential equations that cannot be solved analytically (eq. (2.7) in the present study). This may involve a spatial discretization with a physical quantity associated with each node. Hereafter, the term node will refer to the nodal Lagrangian coordinates (i.e.  $X$ ) and the nodal value to the corresponding physical quantity (i.e.  $u$ ). A moving least squares (MLS) method, similar to the element free Galerkin (EFG) method [Belytschko et al., 1994] is employed. The objective is to present the main principle of this method, and the more rigorous set of equations can be found in [Mollon, 2016] for a slightly different approach (radial point interpolation method). A comparison with FEM is made, as this is probably the most widely used method.

Each body is discretized into several nodes. In practice, a gradient of node density (i.e. mesh size for FEM) is defined with more nodes near the boundary. For simplicity, a homogeneous discretization is presented in fig. 2.16.

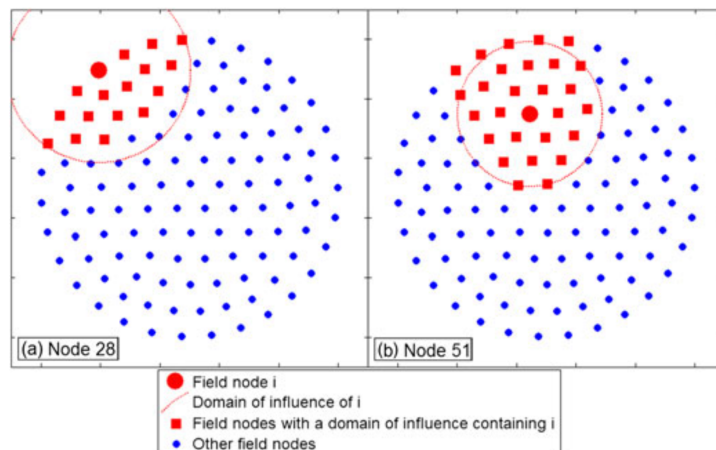


Figure 2.16: Discretization nodes of a soft body (from [Mollon, 2016])

### 3.2.2 Approximation

Thereafter, 3 different types of displacement will be used. The first is  $u(X)$ , the exact displacement field. The second is  $\tilde{u}(X)$ , the approximate displacement field. The third is  $\hat{u}$ , the displacement associated with each node, which is a finite vector. In FEM, displacement is approximated as in eq. (2.10).

$$\tilde{u}(X_\Omega) = \sum_{i \in \Omega}^N \phi_i(X_\Omega) \hat{u}_i \quad (2.10)$$

with  $\tilde{u}$  the approximate displacement field,  $X_\Omega$  any spatial coordinates (from which the domain  $\Omega$  is defined),  $\phi_i$  and  $\hat{u}_i$  respectively the shape function and nodal displacement of a given node  $i$  among  $N$  nodes included in  $\Omega$ . This domain corresponds to the domain containing all the nodes influencing the value at  $X_\Omega$ . The main feature of most FEM discretizations is that  $N$  does not correspond to the total number of nodes. This is because the shape functions are chosen so that only a few nodes influence the solution at a given  $X_\Omega$ . In a 1D case, for linear shape functions  $N$  is equal to 3, for quadratics it is equal to 6 and  $\frac{(k+1)(k+2)}{2}$  for a degree  $k$ . In practice, the shape functions are chosen so that if  $X_\Omega = X_i$ , with  $X_i$  the coordinates of a given node, only  $\phi_i$  is non-zero and  $\phi_i(X_i) = 1$ . This gives  $\tilde{u}(X_i) = \hat{u}_i$  since FEM is based on interpolations. However, as discussed below, MLS is based on regression and so  $\tilde{u}(X_i) \neq \hat{u}_i$ .

In MLS, the domain  $\Omega$  includes more nodes than FEM (nearly 20 in the current method), as shown by the red circle and nodes in fig. 2.16. Displacement is approximated as in eq. (2.11).

$$\tilde{u}(X_\Omega) = \sum_{j=1}^M p_j(X_\Omega) a_j(X_\Omega) \quad (2.11)$$

with  $\tilde{u}$  the approximate displacement field,  $X_\Omega$  any spatial coordinates (from which the domain  $\Omega$  is defined),  $p$  a series of  $M$  monomials and  $a$  the corresponding scalar coefficients. A major difference is that FEM gives a functional relationship of the whole field. In MLS, even if the displacement can be evaluated at any point (i.e. not necessarily a discretization node), it is only known at a finite number of points (at  $X_\Omega$  for the current example). Furthermore, although shape functions can be derived for a given case and a given point, there is no explicit mathematical relationship of them. Several degrees of monomials can be defined and are implemented as written in eq. (2.12) for the current method.

$$p = [p_1, p_2, \dots, p_M]^T = [1, x, y, x^2, y^2, xy]^T \quad (2.12)$$

In eq. (2.11), the coefficients ( $a$ ) are unknown and the nodal values ( $\hat{u}$ ) do not appear, which seems strange at first sight. The MLS method is based on finding  $a$  to obtain the closest approximation of  $\tilde{u}(X_\Omega)$  in the least squares sense. First, another approximation written in eq. (2.13) is defined to express  $a(\hat{u})$ .

$$\tilde{v}(X_i, X_\Omega) = \sum_{j=1}^M p_j(X_i) a_j(X_\Omega) \quad (2.13)$$

with  $\tilde{v}$  the approximate displacement field,  $X_i$  any nodal coordinates in  $\Omega$ ,  $X_\Omega$  any spatial coordinates (from which the domain  $\Omega$  is defined),  $p$  a series of  $M$  monomials and  $a$  the corresponding scalar coefficients. The idea is that the  $\tilde{u}$  field near  $X_\Omega$  is approximated by eq. (2.11). If this approximation is accurate, by taking it (i.e. expressing  $a$  at  $X_\Omega$ ) and calculating the displacement at other coordinates (i.e. expressing  $p$  at  $X_i$ ), this should give  $\tilde{v}(X_i, X_\Omega) \approx \hat{u}_i$ . By adopting this strategy in the reverse order, the aim is to find the coefficients  $a$  that allow the approximation found in  $X_\Omega$  to be as accurate as possible in  $X_i$ .



### 3.2.3 Squared deviation

To evaluate the accuracy of the approximation from  $X_\Omega$  to  $X_i$ , it is possible to compute the squared deviation between  $\tilde{v}(X_i, X_\Omega)$  and  $\hat{u}_i$  as written in eq. (2.14).

$$\Delta u_i^2 = w(X_i, X_\Omega) [\tilde{v}(X_i, X_\Omega) - \hat{u}_i]^2 = w(X_i, X_\Omega) \left[ \sum_{j=1}^M p_j(X_i) a_j(X_\Omega) - \hat{u}_i \right]^2 \quad (2.14)$$

with  $\Delta u_i^2$  the squared deviation for the node  $i$ ,  $w$  a weight derived from a radial basis function,  $X_i$  any nodal coordinates in  $\Omega$ ,  $X_\Omega$  any spatial coordinates (from which the domain  $\Omega$  is defined),  $\tilde{v}$  the approximate displacement field,  $\hat{u}_i$  the nodal value,  $p$  a series of  $M$  monomials and  $a$  the corresponding scalar coefficients. The radial basis function allows to reduce the influence of the most distant nodes. It applies a weight  $w$  that decreases as the distance between  $X_i$  and  $X_\Omega$  increases. In the current method, a Gaussian function is used, as written in eq. (2.15).

$$w(X_i, X_\Omega) = \exp\left(-\left(\frac{3d_i}{D_i}\right)^2\right) \quad (2.15)$$

with  $w$  a weight derived from a radial basis function,  $X_i$  any nodal coordinates in  $\Omega$ ,  $X_\Omega$  any spatial coordinates (from which the domain  $\Omega$  is defined),  $d_i$  the Euclidean distance between  $X_i$  and  $X_\Omega$  and  $D_i$  the radius of the circular domain as represented in fig. 2.16. The previous squared deviation applies only to a given node  $i$ . To evaluate the accuracy of the approximation over the whole domain, the squared deviation is computed for each node  $\in \Omega$  and summed as shown in eq. (2.16).

$$\Delta u^2 = \sum_{i \in \Omega} \Delta u_i^2 = \sum_{i \in \Omega} w(X_i, X_\Omega) \left[ \sum_{j=1}^M p_j(X_i) a_j(X_\Omega) - \hat{u}_i \right]^2 \quad (2.16)$$

with  $\Delta u^2$  the total squared deviation,  $\Delta u_i^2$  the squared deviation for the node  $i$  among  $N$  nodes in  $\Omega$ ,  $w$  a weight derived from a radial basis function,  $X_i$  any nodal coordinates in  $\Omega$ ,  $X_\Omega$  any spatial coordinates (from which the domain  $\Omega$  is defined),  $\hat{u}_i$  the nodal value,  $p$  a series of  $M$  monomials and  $a$  the corresponding scalar coefficients.

### 3.2.4 Minimization

From the previous equations, two unknowns remain: the coefficients  $a$  and the nodal values  $\hat{u}_i$ . However, the squared deviation must be minimized which will give an additional equation to reduce the problem to one unknown. As  $\Delta u^2$  is a real functional equal to or greater than zero, it can be achieved by calculating its derivative according to  $a$  as written in eq. (2.17).

$$\frac{\partial \Delta u^2}{\partial a_j} = 0 \quad (2.17)$$

with  $\Delta u^2$  the total squared deviation and  $a$  the coefficients. The demonstration will not be written here, but from this equation, the values of  $a$  can be easily derived as a function of  $\hat{u}_i$  (eqs. (2.18) to (2.22)). This minimization is the reason why  $\tilde{u}(X_i) \neq \hat{u}_i$ . This is not necessarily a negative point of the method, and explains why, thanks to its smoothing properties, the differential equation can be approximated faithfully with few nodes.

$$a(X_\Omega) = A^{-1}(X_\Omega) B(X_\Omega) \hat{u} \quad (2.18)$$

$$A(X_\Omega) = P^T W(X_\Omega) P \quad (2.19)$$

$$B(X_\Omega) = P^T W(X_\Omega) \quad (2.20)$$

$$P = \begin{bmatrix} p_1 & \dots & p_M \\ \vdots & \ddots & \vdots \\ p_1 & \dots & p_M \end{bmatrix} \quad (2.21)$$

$$W(X_\Omega) = \begin{bmatrix} w(X_1, X_\Omega) & 0 & \dots & 0 \\ 0 & w(X_2, X_\Omega) & \dots & \vdots \\ \vdots & \vdots & \ddots & \vdots \\ 0 & \dots & \dots & w(X_N, X_\Omega) \end{bmatrix} \quad (2.22)$$

### 3.2.5 Comparison with a mesh-based method

A mesh is created using Gauss quadrature to perform the numerical integration of eq. (2.7). It should be noted that the term mesh can refer to two main aspects. The first relates to the connectivity matrix used for the shape functions (i.e. influencing nodes in the domain  $\Omega$ ). The second concerns the surface integration. However, the main drawbacks of mesh-based methods have more to do with connectivity than integration. Since a mesh is used, the term meshless is a little counter-intuitive, even if the advantages are clear. The term “connectivity-free methods” might therefore be more appropriate.

## 3.3 Temporal discretization

### 3.3.1 Integration scheme

As already mentioned, due to significant non-linearities (contacts, geometry, etc.), an implicit scheme is not fully suitable despite all its advantages. Consequently, a semi-implicit Euler scheme is used as shown in eqs. (2.23) and (2.24).

$$\dot{U}_{t+\Delta t} = \dot{U}_t + \Delta t \ddot{U}_t \quad (2.23)$$

$$U_{t+\Delta t} = U_t + \Delta t \dot{U}_{t+\Delta t} \quad (2.24)$$

with  $U$  all the degrees of freedom of the system (two translational and one rotational per node),  $\Delta t$  the time step, the lower index  $t$  corresponds to the current time step and  $t + \Delta t$  to the next one. The results are then applied to  $\hat{u}$ .

### 3.3.2 Adaptive time step

The critical time step is not constant during a simulation. The value of  $\Delta t$  must be as close as possible to it to ensure convergence while minimizing computation time. To achieve this, an adaptive time step is used. To evaluate the error at the next time step, the displacement is first computed for a particular  $\Delta t$ , giving  $\hat{u}_{t+\Delta t}$ . The computation is then repeated, but for half the previous time step (which requires two iterations), giving  $\hat{u}_{t+2 \times 0.5 \Delta t}$ . By comparing these two values, an error associated with the temporal discretization can be computed, as written in eq. (2.25).

$$e_{t+\Delta t} = \max \left( \frac{|\hat{u}_{t+\Delta t} - \hat{u}_{t+2 \times 0.5 \Delta t}|}{d} \right) \quad (2.25)$$

with  $e_{t+\Delta t}$  the maximum error for the next time step,  $\hat{u}_{t+\Delta t}$  the displacement computed with  $\Delta t$ ,  $\hat{u}_{t+2 \times 0.5\Delta t}$  the displacement computed with two iterations of  $0.5\Delta t$  and  $d$  a typical distance in the neighborhood of each node. For each iteration, the time step is updated according to eq. (2.26).

$$\Delta t_{updated} = \Delta t \left( \frac{e_c}{e_{t+\Delta t}} \right)^\beta \quad (2.26)$$

with  $\Delta t_{updated}$  the updated time step,  $\Delta t$  the previous time step,  $e_c$  a critical error that must not be exceeded,  $e_{t+\Delta t}$  the actual error and  $\beta$  a numerical parameter. Note that if  $e_{t+\Delta t} > \alpha e_c$  with  $\alpha$  a numerical parameter, the  $t + \Delta t$  step is recomputed with the updated time step. For the current model,  $e_c$ ,  $\alpha$  and  $\beta$  are respectively equal to  $10^{-4}$ , 2 and 0.2.

### 3.4 Contacts

#### 3.4.1 Proximity detection

As bodies can have complex geometries depending on their initial or deformed shape, a suitable contact detection algorithm needs to be implemented. This is described in detail in [Mollon, 2018b]. Each body (deformable or not) is discretized into several segments on its contour (cf. fig. 2.15). The aim is to determine whether two contours overlap and, if so, to compute the interpenetration distance. A contact detection algorithm could require a lot of computation time, so two preliminary procedures are performed to reduce the number of computations. They are displayed in fig. 2.17.

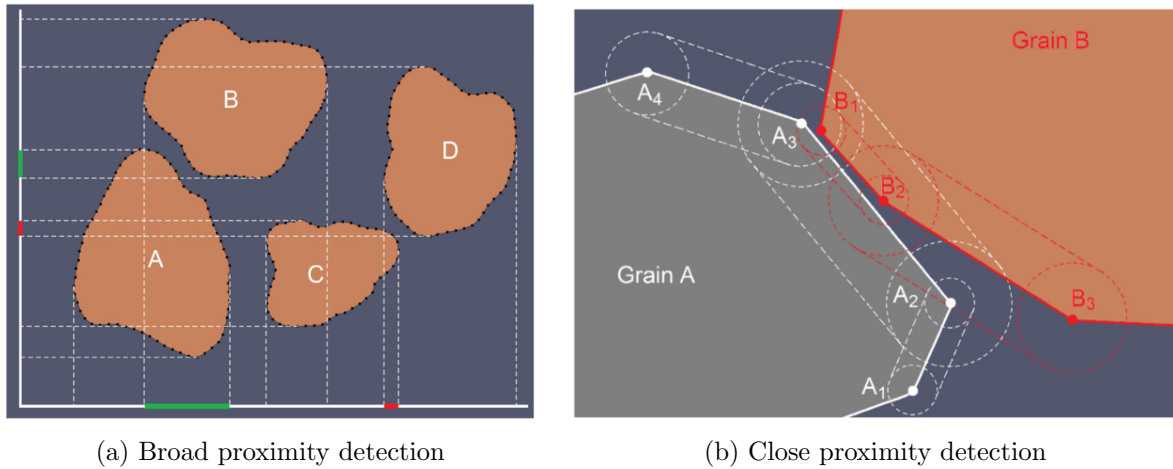


Figure 2.17: Proximity detection stages (from [Mollon, 2018b])

These preliminary procedures are carried out according to a user-defined period ( $6 \cdot 10^{-12}$  s in this work). This value is highly dependent on the velocity and size of each particle. Moreover, it is greater than or equal to  $\Delta t$ . The preliminary procedures can be summarized as follows:

1. Broad proximity detection (fig. 2.17a): two bodies can only be in contact if their projections on the horizontal and vertical axes overlap. For example, bodies A and B overlap on the green projection, and bodies C and D overlap on the red projection.
2. Close proximity detection (fig. 2.17b): performed for potential contacting bodies detected by the broad proximity stage. Each segment is bounded by an oblong border (i.e. two circles centered on the nodes and connected by two segments tangent to the circles). The diameter of the circle is equal to half the length of the segment. If a node of another body

enters within this boundary, a potential contact is detected. For example, this is detected for the node  $B_1$  with the segments  $A_4A_3$  and  $A_3A_2$ .

### 3.4.2 Contact detection

The previous methods determine whether two bodies are potentially in contact, but do not evaluate any distance. In the algorithm, there is no master and slave status. This means that the computation will be performed for nodes of  $B$  in body  $A$  and then for nodes of  $A$  in body  $B$ . An example is shown in fig. 2.18.

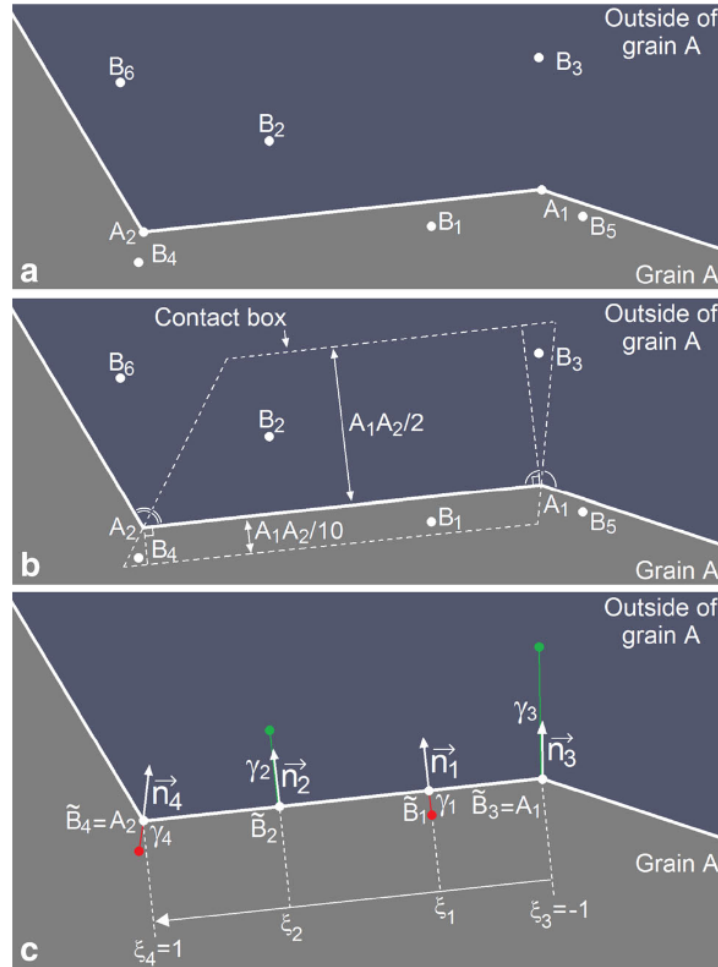


Figure 2.18: Computation of the interpenetration distance of nodes from body  $B$  in body  $A$  (from [Mollon, 2018b])

For each node, the nearest distance ( $\gamma$ ) between the node and the contour is computed. To avoid problems of loss or double detections, a contact box is defined. This box is defined by two bisecting lines (with the two neighboring segments) and two lines parallel to the current segment. These parallel lines are offset from the segment by half the segment length outside the body and by 0.1 of the segment length inside the body.

The nearest distance will also define the normal and tangential direction used for the contact model. The normal direction corresponds to the segment normal, except for nodes close to bisectors (e.g.  $\tilde{B}_4$ ). Moreover, some of the contact models are expressed in terms of force per unit area. For the penetrating node, this area corresponds to the sum of half the length of the

two neighboring segments. For the penetrated segment, the inverse force is shared between the two nodes composing the segment according to the value of  $\xi$  (i.e. if the penetrating node is closer to one of the two nodes, the load will be higher).

## 4 Diffusion model

### 4.1 Overview

#### 4.1.1 Description

An illustration of the numerical model can be found in fig. 2.19. For the sake of brevity, this model will be referred to as the diffusion model, although it allows the study of other phenomena, such as mineral penetration. The aim is to reproduce the experimental set-up (cf. fig. 2.1), which consists of shearing a layer of minerals over a rubber-like material via a road-like surface. The minerals and the surface of the rubber material are considered as a collection of discrete bodies to model diffusion. The road-like surface and the bulk of the rubber material, for which diffusion is not expected, are modeled as individual bodies. The bulk is used to model larger-scale phenomena such as global material deformation or stick-slip events. It should be noted that the configuration is reversed vertically in comparison to tire-road contact, in order to be consistent with the tribometer used experimentally. However, gravity is assumed to be zero as it is negligible at this scale compared to the contact forces. The results are therefore independent of the vertical orientation. In addition, contact pressure and sliding velocity are applied through the road-like surface also to be consistent with the tribometer. The lower surface of the bulk has a zero horizontal and vertical displacement. Finally, periodic boundary conditions are applied. This means that every particle that leaves the contact through the right boundary re-enters into the contact through the left boundary (and vice-versa). This is represented by the yellow particles.

The minerals are modeled as ellipses, which is supported by segmentation analysis of longitudinal sections from the worn rubber sample (cf. fig. 1.43). The mean equivalent diameter of the minerals ( $D_M$ ) is equal to  $0.1166 \mu m$  and more details on mineral generation will be given later. Rubber particle size follows a Gaussian distribution. The mean diameter ( $d_M^{rubber}$ ) is equal to  $1.10 D_M$  and the standard deviation to  $0.21 D_M$ . As for minerals, the effect of the size of the rubber particles will be investigated. The distance between the average height of the road-like surface and the bulk is called the thickness ( $h_i$ ). This domain, which contains both rubber particles and minerals, corresponds to the interfacial layer (i.e. third body).

The energy introduced by the sliding of the road-like surface is dissipated by two mechanisms. The first is through the deformation of each body thanks to a Rayleigh damping (weighted sum of mass and stiffness matrices). This corresponds to  $\mu_b$  in fig. 2.12. The weight is equal to zero for the mass matrix and to  $1 \cdot 10^{-9} s$  for the stiffness matrix. The second occurs through the creation/destruction of free surfaces (removal of the link) between two bodies. This corresponds to  $\mu_s$  in fig. 2.12. Indeed, energy is required to remove a link, whereas creation is energy-free.

As previously discussed, tire tread is composed of rubber and several other compounds to modify the properties of the material. During manufacturing, vulcanization notably increases elastic recovery by creating sulfur bonds between polymer chains [Coran, 2003]. However, close to the surface, these bonds can be damaged through highly multi-physical phenomena [Smith and Veith, 1982]. In the case of carbon black-filled rubber, there is also an increase in the concentration of carbon black and oxygen close to the surface [Rodríguez et al., 2013]. All these phenomena contribute to the formation of a layer with specific properties near the surface and the material is referred to as degraded rubber.

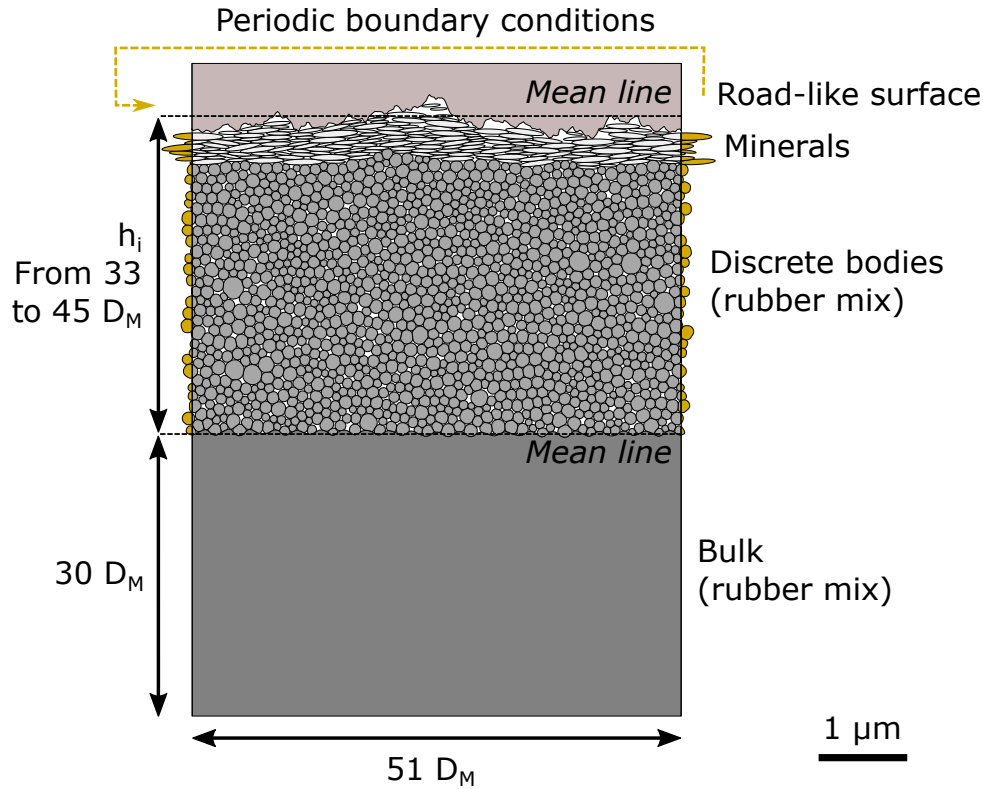


Figure 2.19: Illustration of the diffusion model

The above comments suggest two main scenarios. The first is that the material close to the surface is damaged. The second concerns recovery. As the cross-linking network is damaged, the material is highly viscous near the surface. However, the time scale of the simulations is much lower than the relaxation time of the material. When combined with the fact that the tribological stresses are significant, this suggests a highly plastic flow. In the current model, this plasticity is modeled by non-reversible relative displacements between the discrete bodies. Consequently, modeling the surface as a collection of discrete bodies is motivated not only by the necessity of modeling diffusion, but also due to the higher degree of plasticity close to the surface.

#### 4.1.2 Road-like surface

The spatial resolution of the road-like surface topography acquisition is low relative to the scale of the model (around 22 nodes for the width) and a 2D profile cannot be directly extracted. To generate a profile, the same procedure as for determining the Hurst exponent and the prefactor will be employed, but in the reverse order. A range of frequencies from the inverse of the model width to the inverse of the spatial discretization step is defined. The PSD is then calculated from eq. (2.1) using the previous  $S_P$  and  $S_H$  and the corresponding amplitude can be derived. However, the phase information of the initial surface has been lost during the preliminary procedure and a random phase matrix must be generated. This tends to create a smoother profile. Finally, from the amplitude and phase, an inverse DFT is performed, resulting in the 2D profile. The generated profile is displayed in fig. 2.20 and will be used for the road-like surface in the numerical model. For some simulations, a high-pass filter ( $\lambda_c^{max}$ ) or a low-pass filter ( $\lambda_c^{min}$ ) will be applied, corresponding to a cut-off period to remove the smallest or largest asperities.

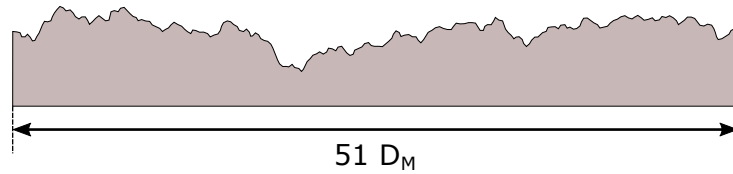


Figure 2.20: Generated 2D profile for the road-like surface

### 4.1.3 Minerals

A given quantity of minerals is generated as a function of a mass based on an equivalence of contact area with the specimen used experimentally. This means that the mass specified for the numerical models corresponds to the mass that should be used experimentally to obtain the same thickness of the mineral layer in the initial state. For a mineral density of  $2860 \text{ kg.m}^{-3}$ , 3 distributions are generated for 1, 2 and 4  $\text{mg}$  of minerals. In comparison, 200  $\text{mg}$  are used experimentally. However, numerically, this quantity corresponds to the effective amount incorporated into the rubber, whereas experimentally a fraction is ejected outside the contact. Hereafter, these masses will be expressed as the solid fraction of the mineral phase ( $\phi^{mineral}$ ) divided by the solid fraction of the rubber one ( $\phi^{rubber}$ ).

Based on the two previous mineral segmentations, the mean values of the mean diameter, the diameter standard deviation and ellipse axis ratio have been taken. Therefore, it will be assumed that all the minerals have the same axis ratio. Starting with a single mineral, a log-normal area distribution is generated. Then, the process is repeated by adding one mineral and by generating a totally new distribution. This operation is performed until the total mass (i.e. area) exceeds the expected one. The area of the largest mineral is then reduced by the mass surplus to obtain exactly the expected mass. By knowing the axis ratio, a collection of ellipses can be generated from this area distribution. The mean equivalent diameter of the minerals ( $D_M$ ) is equal to  $0.1166 \mu\text{m}$ . The results are displayed in fig. 2.21. In addition, some simulations will study different mineral sizes, which will be specified by the effective mean equivalent diameter of the minerals ( $d_M^{rubber}$ ).



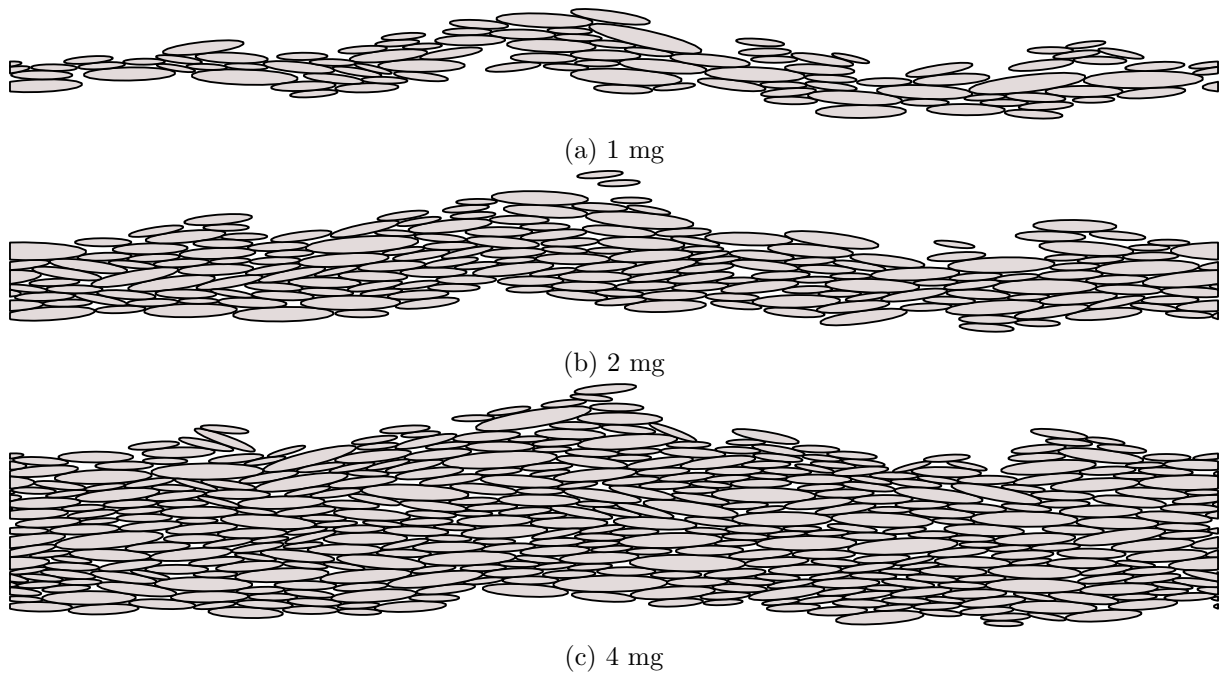


Figure 2.21: Minerals after a compaction stage for several quantities; masses are expressed in terms of contact area equivalence between the experimental set-up and the numerical model

#### 4.1.4 Boundary conditions

The road-like surface has a zero vertical displacement and a constant sliding velocity ( $V_S$ ) of  $16 \text{ m.s}^{-1}$  is applied horizontally. In addition, some simulations will study different sliding velocities, which will be specified by the effective sliding velocity ( $v_S$ ). The whole interface thickness (controlled by the fixed vertical position of the road-like surface) is defined to guarantee a given compacity (area covered by all the particles divided by the area bounded by the first bodies). This allows to tend, from different initial mineral positions, towards the same contact pressure for high sliding distances. If this is not specified, the compacity ( $\phi$ ) is equal to 0.87 and corresponds to a stabilized mean contact pressure of  $0.1 \text{ MPa}$ . However, some numerical parameters (e.g. stiffness) modify the contact pressure for a given compacity. These simulations will therefore be carried out at different contact pressures, which will be specified in the corresponding sections. Imposing a contact pressure instead of a displacement could lead to significant vertical oscillations, which can modify kinematics and thus diffusion. This is particularly true at the beginning of the sliding, as there is a local reconfiguration of the mineral layer, as shown by fig. 2.22.

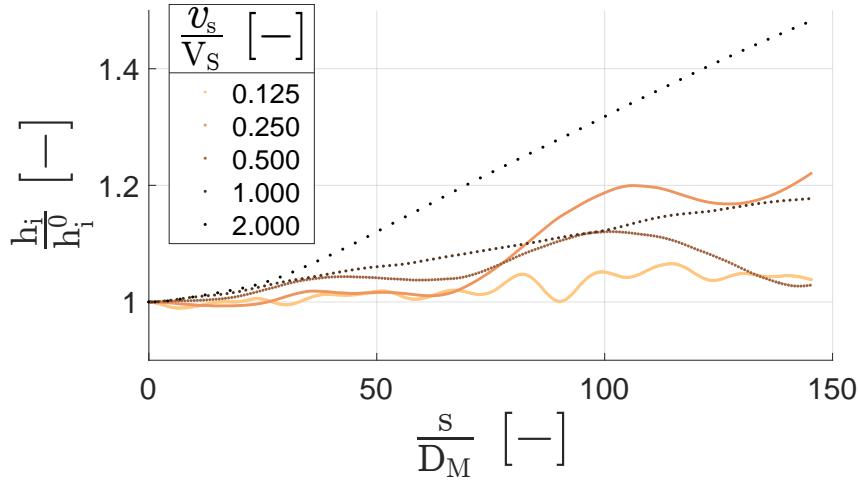


Figure 2.22: Typical thickness variation for an imposed contact pressure, for several sliding velocities  $v_S$  and as a function of the sliding distance;  $h_i^0$  corresponds to the thickness at the initial state

These oscillations can be reduced by decreasing the sliding velocity (at least by applying a suitable ramp at the beginning). However, they are still occurring, reinforced by the presence of rigid bodies (i.e. minerals) compared to a simulation where only soft bodies are used. Neither imposed pressure nor imposed displacement is a perfect solution. In the case of imposed pressure, the inertia of the sliding surface is unknown, so it has to be defined arbitrarily. In the case of imposed displacement, this removes a degree of freedom (limiting the formation of agglomerated regimes, which are facilitated by a progressive increase in  $h_i$ ).

#### 4.1.5 Constitutive model

The stiffness of the road-like surface and the minerals is greater than 1 *GPa* [Riabokon et al., 2021; Húlan and Štubňa, 2020], whereas for the current rubber-like material, it is closer to 1 *MPa*. These bodies are therefore considered as perfectly rigid in the current model. A neo-Hookean hyperelastic model is used for rubber particles, which provides a good description of the behavior of materials such as carbon-black-filled SBR, even under large strain [Aloui and El Yaagoubi, 2021; Fujikawa et al., 2014]. In this model, a Young's modulus ( $E$ ) is specified (referred to hereafter as stiffness or elastic modulus). Several DMA (dynamic mechanical analysis) shear tests were carried out on the material. For frequencies from  $10^{-1}$  to  $10^2$  *Hz*, the elastic modulus varies from 0.1 to 10 *MPa*. However, as already mentioned, the modulus depends on several parameters, such as temperature, strain, cross-link density, etc. For the sake of simplicity, it will be assumed constant and equal to 1 *MPa*. This will be discussed in more detail in the characterization section. Rubber particles are also considered to be quasi-incompressible, with a density of 940 *kg.m*<sup>-3</sup>. The bulk has the same properties as discrete rubber particles.

#### 4.1.6 Contact models

As already mentioned, a contact model is defined for each possible interaction between two bodies with a given material. In this model, two categories of materials will be used. The first is rubber-like materials with discrete rubber particles and the bulk. The second is rock-like materials with the road-like surface and minerals.

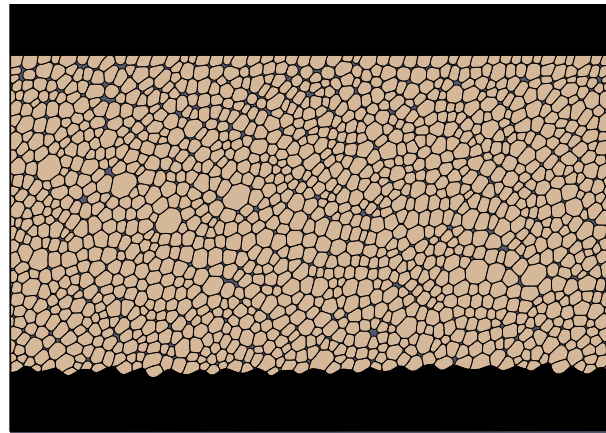
Between rubber-like materials, a purely cohesive model is defined with a normal component ( $C_n$ ) and a tangential component ( $C_t$ ). The normal component is a tensile cut-off stress (the link between the bodies is removed if the load per unit area exceeds this value). The tangential

component is a resisting stress. Both are assumed to be equal and are merged under a single parameter called cohesion ( $C$ ). If this is not specified,  $C$  is equal to  $0.10 \text{ MPa}$ . This will be discussed in more detail in the characterization section. Between rock-like materials, a Coulomb friction model is defined with a friction coefficient ( $\mu_{rock}^{rock}$ ) equal to 0.6 [Roshan et al., 2017; Zhang et al., 2019; Shimamoto and Logan, 1981].

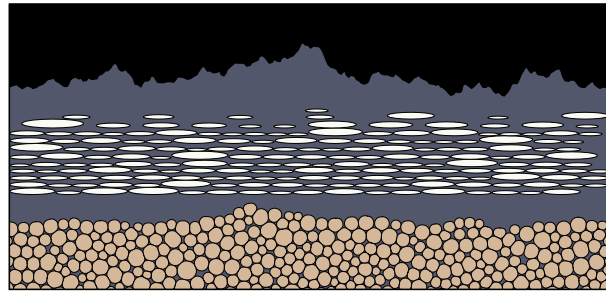
Defining a contact model between rubber-like and rock-like materials is challenging. Indeed, if a Coulomb friction model is defined, the coefficient (i.e. internal friction coefficient) may be different from the one that can be obtained macroscopically. Moreover, a cohesive model seems more consistent since contact involves rubber on a microscopic scale. Consequently, the same model as for rubber-like materials is defined, which is a purely cohesive model with a normal and a tangential component. Both are assumed to be equal and are merged under a single parameter called  $C_{rock}^{rubber}$ . If this is not specified,  $C_{rock}^{rubber}$  is equal to  $0.05 \text{ MPa}$  to keep the value below the one used for rubber. As this value is not based on any data, its effect will be studied later. In particular, the cohesive model will be replaced by a Coulomb friction model for several friction coefficients ( $\mu_{rock}^{rubber}$ ).

#### 4.1.7 Preliminary procedure

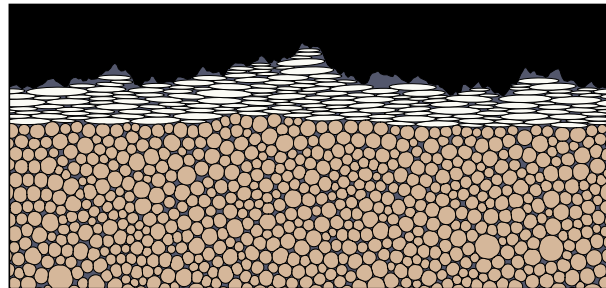
Before each simulation, a preliminary procedure is performed and is displayed fig. 2.23. First, a collection of soft rubber particles (without contact forces) is compacted by a top plate. Contact forces are then activated to obtain the desired mechanical properties. These bodies are sheared by this top plate (fig. 2.23a), which is finally removed. A layer of minerals is then imported (fig. 2.23b) and compacted by the upper rigid rough surface (fig. 2.23c). Note that a tangential velocity can be added during compaction. This gives to the minerals a preferential orientation. Several simulations have been carried out for different orientations and show that, except in particular cases (low quantity of minerals with low or high mean orientation), there is no significant effect. Thereafter, no tangential velocity is added during compaction and the mean orientation is close to 0. Once the velocity field is almost 0, the interfacial layer is sheared to study diffusion (fig. 2.23d).



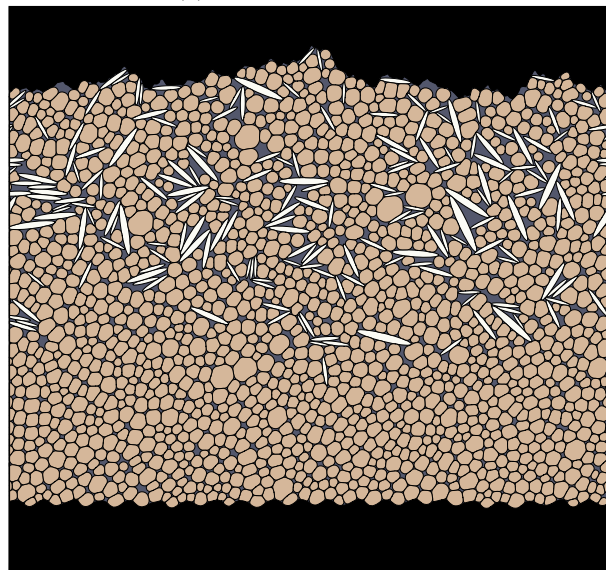
(a) Initial shear



(b) Mineral importation



(c) Mineral compaction



(d) Shear-induced diffusion

Figure 2.23: Main stages of a given simulation

## 4.2 Descriptors

### 4.2.1 Mean square displacement

Depending on the quantity under consideration, an absolute time ( $t$ ) or a relative one ( $\Delta t$ ) will be used. Absolute time takes as reference the beginning of the sliding ( $t_0$ ). It is useful for studying quantities that may evolve with time (e.g. kinematics), but gives noisier results. Relative time takes as reference all possible time steps over a given time range. It is useful for obtaining statistically significant quantities, but requires these quantities to be relatively independent of  $t_0$  for the range considered (referred to hereafter as steady state). For example, the absolute mean square displacement ( $MSD^0$ ) is computed as shown in eq. (2.27) and the relative one ( $MSD$ ) as shown in eq. (2.28).

$$MSD^0(t) = \frac{1}{M} \sum_{m=1}^M (y^m(t) - y^m(t_0))^2 \quad (2.27)$$

$$MSD(\Delta t) = \frac{1}{MN} \sum_{m=1}^M \sum_{i=1}^N (y^m(t_0^i + \Delta t) - y^m(t_0^i))^2 \quad (2.28)$$

with  $MSD^0$  the absolute mean square displacement,  $t$  or  $t^i$  the time,  $M$  the number of minerals,  $y^m$  the centroid position of a mineral,  $t_0$  or  $t_0^i$  the reference time,  $MSD$  the relative mean square displacement,  $N$  the number of time steps and  $\Delta t$  a time relative to  $t_0^i$ . The centroid position corresponds to the transverse distance between the centroid of a mineral and the mean line of the road-like surface. It should be noted that the result of  $MSD^0$  (and more generally quantities derived from a moving temporal average), depends on the time range being considered and the maximum value of  $\Delta t$ . This choice depends on the evolution of the quantity. Indeed, the variation of the quantity must be sufficiently significant, but too high values of  $\Delta t$  reduce the number of reference times ( $N$ ). An example of what can be obtained is shown in fig. 2.24.

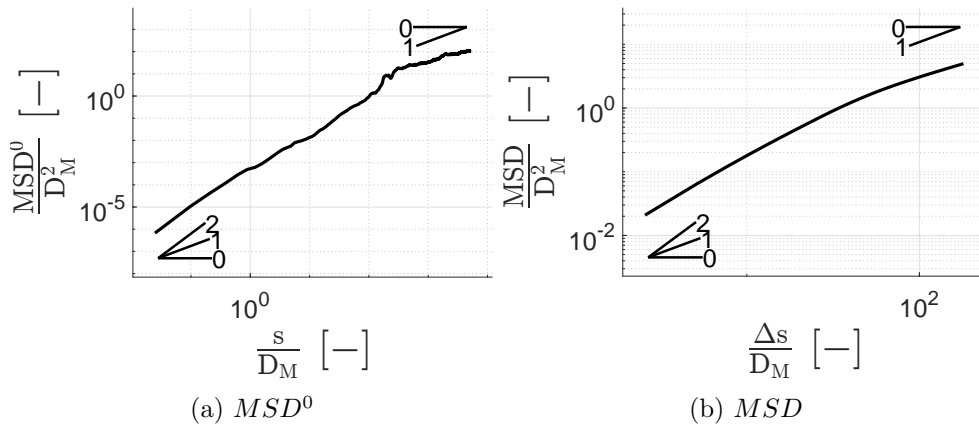


Figure 2.24: Example of MSD for a given simulation

Most of the time,  $t$  will be replaced by  $s$  which corresponds to the sliding distance ( $s = tV_S$ ) and  $\Delta t$  by  $\Delta s$  ( $\Delta s = \Delta tV_S$ ). The same moving temporal average method will be used for other quantities introduced later. The  $MSD$  displayed above corresponds to an average over 800 time steps for which a steady state has been identified. The  $MSD$  allows the study of the overall diffusion process, in particular by looking at the slope in logarithmic space ( $\beta$  in eq. (2.4)), which shows the evolution of diffusion kinematics. This allows the diffusion to be classified into three categories: super-diffusive ( $\beta > 1$ ), diffusive or normal-diffusive ( $\beta \approx 1$ ) and sub-diffusive

( $\beta < 1$ ). From  $MSD$ , a diffusion coefficient can be derived using the framework of Einstein, as rewritten in eq. (2.29) for the sake of clarity.

$$D(\Delta t) = \frac{MSD(\Delta t)}{2\Delta t} \quad (2.29)$$

with  $D$  the diffusion coefficient,  $\Delta t$  the relative time and  $MSD$  the relative mean square displacement. This relationship is valid only for  $\Delta t \rightarrow \infty$  and in the normal-diffusive regime (since  $\Delta t$  is linearly proportional to  $MSD$ ). However, it is possible to find the instantaneous diffusion coefficient for  $\beta \neq 1$  by looking at the slope of  $MSD^0$  at a given  $t$ . To obtain  $D$  for a finite time and corresponding to an average, a linear regression is performed for the section of  $MSD$  with a slope of 1 (i.e. high  $\Delta t$  values). Arbitrarily, the  $\Delta t$  corresponds to 70 time steps, and the slope has been derived from the last 28 steps. The framework of Einstein refers to the fact that  $D$  is derived from  $MSD$ .

Another method to find  $D$ , called thereafter the framework of Green-Kubo, will be preferred if a steady state is found, as it provides far more information on the internal phenomena that lead to diffusion. However, it will be introduced in a subsequent chapter. Indeed, the only fact that mineral migration in a solid-soft interface corresponds to a diffusive process and not to a more general class of mechanical mixing must be established. Secondly, while the framework of Einstein provides a direct coefficient between displacement and time (and can therefore hardly give inaccurate results if used properly), this is less true for the framework of Green-Kubo. Its validity in the case of a solid-soft interface also needs to be demonstrated, and is an integral part of the work carried out here.

#### 4.2.2 Mineral fraction

The  $MSD$  is a good indicator for reducing diffusion to a scalar. However, it does not reflect local mechanisms, such as a depth where mineral fraction is higher. To this end, a map of mineral fraction along depth is computed, which corresponds to  $\varphi$  in the second law of Fick (cf. eq. (2.2)). This will also be used to determine the layer containing a certain percentage of minerals. To extract the spatial distribution of minerals, the depth is discretized into several layers whose thicknesses are very small in relation to the size of the minerals. The geometric intersections between each layer and the mineral phase are computed. The mineral fraction is determined by computing the ratio between the sum of mineral areas and the area of the layer. An illustration of the method can be found in fig. 2.25.

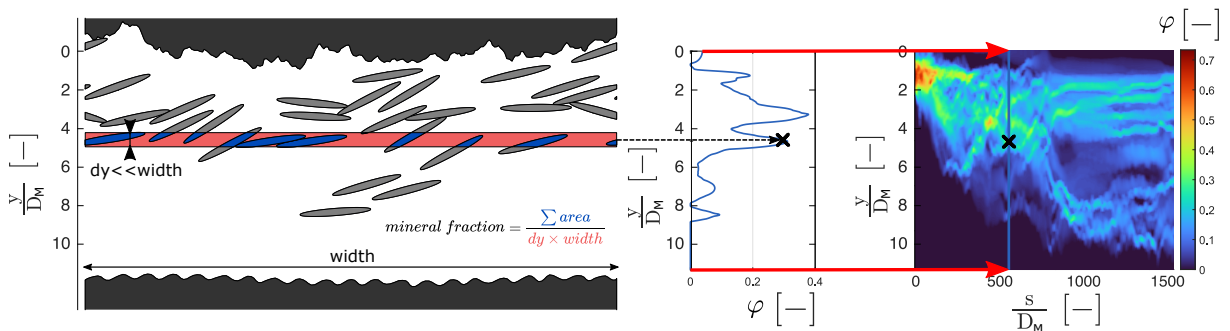


Figure 2.25: Illustration of the mineral fraction computation for a rough description of mineral size distribution

#### 4.2.3 Velocity profile



Velocity will most often be decomposed into two components. A longitudinal velocity ( $V_L$ ), which corresponds to the velocity projection in the sliding direction, and a transverse velocity ( $V_T$ ), which corresponds to the velocity projection in the orthogonal direction to the sliding. The mean longitudinal velocity of each body (including rubber particles and minerals) is first computed from the velocity field. To obtain the velocity profile, a moving average as a function of depth is performed using a Gaussian filter acting on a thickness of  $1 D_M$ . For the steady state, the filter is applied to a data set containing all the bodies and all the time steps. An illustration of the velocity profile for one step can be found in fig. 2.26.

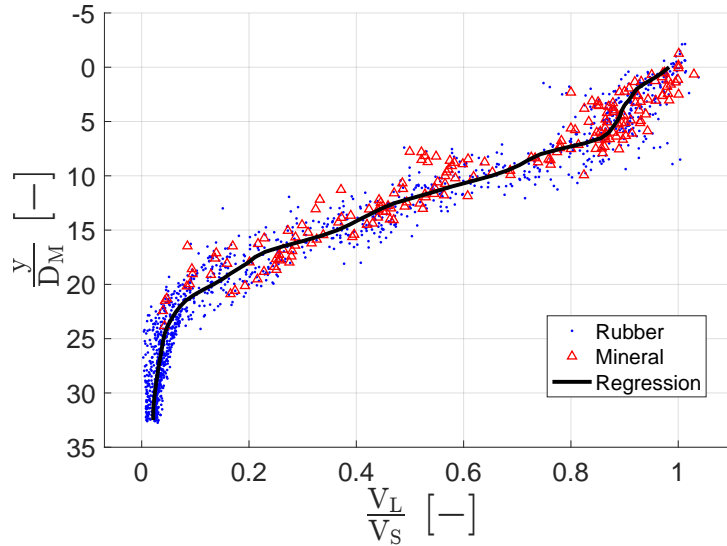


Figure 2.26: Illustration of the velocity profile computation

#### 4.2.4 Shear rate

Estimating the shear rate ( $\dot{\gamma}$ ) is particularly important (cf. eq. (2.6)), as it is one of the main diffusion parameters. However, the shear rate is not constant throughout the whole interfacial layer. As discussed later, it is only the shear rate in the layer containing the minerals that drives diffusion. For this reason, a layer called the mixed layer is defined. It is delimited by the depths at which respectively 90% and 10% of the minerals are located below (and the layer therefore contains 80% of the minerals). This makes it possible to exclude the effect of minerals close to the boundaries, which can be very noisy. These depths are found using the same method as for the velocity profile but for  $\varphi$ . Indeed, a moving average for  $\varphi$  as a function of depth is first performed using a Gaussian filter acting on a thickness of  $1 D_M$ . Then, the corresponding boundaries of the mixed layer (depths for 90% and 10% of the minerals) can easily be derived from this mean concentration profile. To determine  $\dot{\gamma}$ , the smooth velocity and mineral fraction profiles are used (including potentially several time steps). An example of the shear rate computation is presented in fig. 2.27.



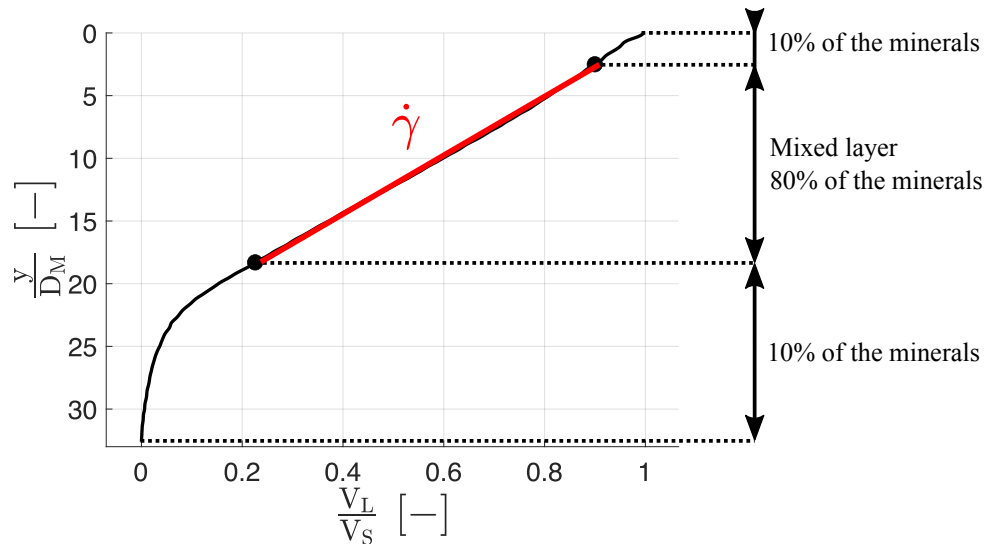




















Figure 2.27: Illustration of the shear rate computation










For all simulations for which a steady state is found, the shear rate is nearly constant in the mixed layer. The shear rate is derived from the slope of a linear regression of the velocity profile, performed only for the mixed layer. It is therefore important to note that each shear rate given hereafter corresponds to the shear rate in the mixed layer. In some simulations, where a steady state is not observed, the shear rate might not be constant in the mixed layer. In this case, it will be specified, but the shear rate is derived using the same method.










### 4.3 List of performed simulations

The main numerical parameters used for simulations in this work (and the corresponding animations through the QR code) are given in table 2.1 (see the nomenclature for the description of each parameter).

Ref	$\frac{E}{C}$	$\frac{C_{rubber}}{C_{rock}}$	$\mu_{rock}^{rubber}$	$\mu_{rock}^{rock}$	$\frac{h_i}{D_M}$	$\phi$	$\frac{\phi_{mineral}}{\phi_{rubber}}$	$\frac{d_M^{mineral}}{D_M}$	$\frac{d_M^{rubber}}{D_M}$	$\frac{v_s}{V_S}$	$\frac{\lambda_c^{max}}{D_M}$	$\frac{\lambda_c^{min}}{D_M}$
#1 	10		0.4	0.3	33	0.87	0.123	1	1.10	1	51.46	0.44
#2 	10		0.4	0.3	36	0.87	0.113	1	1.10	1	51.46	0.44
#3 	10		0.4	0.3	41	0.87	0.099	1	1.10	1	51.46	0.44
#4 	10		0.4	0.3	45	0.87	0.090	1	1.10	1	51.46	0.44
#5 	10		0.4	0.1	33	0.87	0.123	1	1.10	1	51.46	0.44
#6 	10		0.4	0.2	33	0.87	0.123	1	1.10	1	51.46	0.44
#7 	10		0.4	0.4	33	0.87	0.123	1	1.10	1	51.46	0.44
#8 	10		0.3	0.3	33	0.87	0.123	1	1.10	1	51.46	0.44
#9 	10		0.5	0.3	33	0.87	0.123	1	1.10	1	51.46	0.44

Ref	$\frac{E}{C}$	$\frac{C^{rubber}}{C^{rock}}$	$\mu_{rock}^{rubber}$	$\mu_{rock}^{rock}$	$\frac{h_i}{D_M}$	$\phi$	$\frac{\phi^{mineral}}{\phi^{rubber}}$	$\frac{d_M^{mineral}}{D_M}$	$\frac{d_M^{rubber}}{D_M}$	$\frac{v_s}{V_S}$	$\frac{\lambda_c^{max}}{D_M}$	$\frac{\lambda_c^{min}}{D_M}$
#10 	10		0.6	0.3	33	0.87	0.123	1	1.10	1	51.46	0.44
#11 	10	0.500		0.6	33	0.87	0.123	1	1.10	1	51.46	0.44
#12 	10	1.000		0.6	33	0.87	0.123	1	1.10	1	51.46	0.44
#13 	10	2.000		0.6	33	0.87	0.123	1	1.10	1	51.46	0.44
#14 	10	4.000		0.6	33	0.87	0.123	1	1.10	1	51.46	0.44
#15 	10	0.500		0.6	33	0.87	0.123	1	1.10	0.5	51.46	0.44
#16 	10	0.500		0.6	33	0.87	0.123	1	1.10	2	51.46	0.44
#17 	10	0.500		0.6	33	0.87	0.123	1	1.10	4	51.46	0.44
#18 	10	0.500		0.6	36	0.87	0.113	1	1.10	1	51.46	0.44

Ref	$\frac{E}{C}$	$\frac{C_{rubber}}{C_{rock}}$	$\mu_{rock}^{rubber}$	$\mu_{rock}^{rock}$	$\frac{h_i}{D_M}$	$\phi$	$\frac{\phi_{mineral}}{\phi_{rubber}}$	$\frac{d_M^{mineral}}{D_M}$	$\frac{d_M^{rubber}}{D_M}$	$\frac{v_s}{V_S}$	$\frac{\lambda_c^{max}}{D_M}$	$\frac{\lambda_c^{min}}{D_M}$
#19 	10	0.500		0.6	41	0.87	0.099	1	1.10	1	51.46	0.44
#20 	10	0.500		0.6	45	0.87	0.090	1	1.10	1	51.46	0.44
#21 	10	0.500		0.6	33	0.87	0.123	1	1.40	1	51.46	0.44
#22 	10	0.500		0.6	33	0.87	0.123	1	1.77	1	51.46	0.44
#23 	10	0.500		0.6	33	0.87	0.123	1	2.09	1	51.46	0.44
#24 	10	0.500		0.6	34	0.84	0.123	1	1.10	1	51.46	0.44
#25 	10	0.500		0.6	32	0.90	0.123	1	1.10	1	51.46	0.44
#26 	10	0.500		0.6	30	0.93	0.123	1	1.10	1	51.46	0.44
#27 	10	0.500		0.6	33	0.87	0.123	1	1.10	1	3.23	0.44

Ref	$\frac{E}{C}$	$\frac{C^{rubber}}{C^{rock}}$	$\mu_{rock}^{rubber}$	$\mu_{rock}^{rock}$	$\frac{h_i}{D_M}$	$\phi$	$\frac{\phi^{mineral}}{\phi^{rubber}}$	$\frac{d_M^{mineral}}{D_M}$	$\frac{d_M^{rubber}}{D_M}$	$\frac{v_s}{V_S}$	$\frac{\lambda_c^{max}}{D_M}$	$\frac{\lambda_c^{min}}{D_M}$
#28 	10	0.500		0.6	33	0.87	0.123	1	1.10	1	10.33	0.44
#29 	10	0.500		0.6	33	0.87	0.123	1	1.10	1	51.46	1.32
#30 	10	0.500		0.6	33	0.87	0.123	1	1.10	1	51.46	4.30
#31 	10	0.500		0.6	31	0.87	0.062	1	1.10	1	51.46	0.44
#32 	10	0.500		0.6	36	0.87	0.247	1	1.10	1	51.46	0.44
#33 	10	0.500		0.6	33	0.87	0.123	1 (homogeneous)	1.10	1	51.46	0.44
#34 	10	0.500		0.6	33	0.87	0.123	2 (homogeneous)	1.10	1	51.46	0.44
#35 	10	0.500		0.6	33	0.87	0.123	4 (homogeneous)	1.10	1	51.46	0.44
#36 	10	0.500		0.6	33	0.87	0.123	8 (homogeneous)	1.10	1	51.46	0.44







Ref	$\frac{E}{C}$	$\frac{C^{rubber}}{C}$	$\mu_{rock}^{rubber}$	$\mu_{rock}^{rock}$	$\frac{h_i}{D_M}$	$\phi$	$\frac{\phi^{mineral}}{\phi^{rubber}}$	$\frac{d_M^{mineral}}{D_M}$	$\frac{d_M^{rubber}}{D_M}$	$\frac{v_s}{V_S}$	$\frac{\lambda_c^{max}}{D_M}$	$\frac{\lambda_c^{min}}{D_M}$
#37 	5	0.500		0.6	33	0.87	0.123	1	1.10	1	51.46	0.44
#38 	20	0.500		0.6	33	0.87	0.123	1	1.10	1	51.46	0.44
#39 	40	0.500		0.6	33	0.87	0.123	1	1.10	1	51.46	0.44
#40 	20.0	1.000		0.6	33	0.87	0.123	1	1.10	1	51.46	0.44
#41 	5.0	0.250		0.6	33	0.87	0.123	1	1.10	1	51.46	0.44
#42 	2.5	0.125		0.6	33	0.87	0.123	1	1.10	1	51.46	0.44

Table 2.1: List of the simulations and their associated numerical parameters





## Chapter 3

# Rubber characterization

As discussed in the previous chapter, the numerical model includes several parameters based on material properties, which must therefore be characterized. Due to the complexity of characterizing rubber-like materials in the very large strain regime, the method proposed below will be developed in parallel to the diffusion model. Consequently, the material parameters of the diffusion model are not precisely defined and will therefore be included in the parametric study. The first aim of this chapter is to propose a reverse analysis method compatible with models that consider the material as a collection of soft bodies. The second is to understand how the numerical parameters are influenced by the strain rate for viscoelastic materials. The third is to give a range of admissible values to determine how the parameters of the diffusion model approach them. First, a major characterization requirement is introduced and a brief state of the art on indentation is given in section 1. Next, the employed experimental and numerical methods are presented in section 2. Then, several numerical results are discussed in section 3, especially to ensure that the model is physically consistent. Finally, a reverse analysis procedure is proposed in section 4.

## 1 State of the art

### 1.1 Unicity of the solution

For a numerical model, the identification of input parameters related to material properties always constitutes a challenge. Indeed, a result obtained from a model is the outcome of a multitude of parameters. Some of them only make sense through their interactions with each other in a specific framework (e.g. shear, compression, etc.), and they cannot be identified individually. This is why there are as many characterizations to be made as there are numerical configurations.

A popular approach to identifying these parameters is to numerically reproduce an experimental set-up. The objective is to obtain the same result (e.g. normal stress) in the experimental and numerical version of the test. This is achieved by modifying the input parameters of the numerical model until the desired result is reached. A common difficulty with this method concerns the unicity of the solution. Indeed, by taking the example of a friction model, as shown in [Mollon, 2019], the same friction coefficient can be obtained from several input parameters, as illustrated in fig. 3.1.

Non-unicity can therefore lead to a false detection of parameters. A mandatory step for any reverse analysis procedure is therefore to ensure the unicity of the solution. It should be noted that it is the selected output that may not be unique, not the configuration itself (i.e. all the outputs). In the previous example (fig. 3.1), the parameters  $\sigma$  and  $\mu$  could refer to any

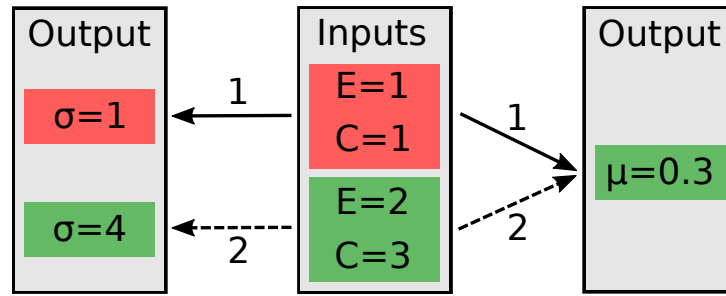


Figure 3.1: Illustration of non-unicity for arbitrary parameters; the specified parameters could refer to any parameters, such as  $\sigma$  a stress,  $\mu$  a friction coefficient,  $E$  the Young's modulus and  $C$  the cohesion.; if the reverse analysis is performed based on  $\mu$ , it might give the wrong set of input parameters and a wrong value of  $\sigma$

parameters, such as a stress and a friction coefficient respectively. If the reverse analysis is performed according to  $\mu$  only, the model may give an incorrect set of inputs ( $E$  and  $C$  in this example) and thus an incorrect  $\sigma$ . But if the analysis is performed on  $\mu$  and  $\sigma$ , the correct set of inputs could be identified. It may therefore be possible to define a set of outputs as a convergence criterion, and thus verify the unicity. However, the number of measurable (and therefore identifiable) quantities for a friction test is relatively limited (e.g. tangential force, normal force, displacement of first bodies, temperature).

The objective is to determine, for a material modeled as a collection of soft particles, the stiffness ( $E$ ) and the cohesion ( $C$ ) between each particle. In practice, identifying  $E$  is fairly straightforward, as all it requires is a method involving the evaluation of a stress, for a given strain, and in an elastic regime (e.g. tensile test, DMA, etc.). However, the evaluation of  $C$  is more complex as it implies a material flow (i.e. decohesions). Another way of approaching the problem of non-unicity is through the kinematics. In the previous example, the non-unicity of the friction coefficient is mainly due to the fact that several velocity transmission regimes occur when inputs are modified. This suggests the need of a characterization method involving a material flow with a limited number of kinematics. For these reasons, indentation seems a good candidate.

## 1.2 Indentation method

Indentation is a common technique for assessing mechanical properties [Oliver and Pharr, 2004] thanks to its great flexibility. It is adapted to many materials, such as brittle materials [Moradkhani et al., 2023] or even soft materials, thanks to a resolution below  $10^{-6}$  N [McKee et al., 2011]. One of its main advantages is that it can be used on several length scales, notably to investigate small-scale properties [Woodcock and Bahr, 2000] or for particular applications such as thin films [Suresh et al., 1999]. This is also particularly useful for reverse analyses, since numerical models may study only a fraction of the mechanism (e.g. a tire-road contact model without modeling the whole tire), and must therefore take into account the local material properties.

Indentations on rubber-like materials have been carried out in several studies. Particular attention has been paid to the sensitivity of the material to displacement and loading rates [Chen et al., 2013; Klapperich et al., 2000; Oyen and Cook, 2003]. However, in the case of a damaged cross-linking network and soft material such as the one in the present study, several difficulties may arise. Firstly, surface detection can be challenging. Indeed, for most indenters, if external disturbances are considered, the load resolution is slightly lower than  $10^{-9}$  N [VanLandingham

et al., 2001]. Consequently, the position of the surface may be incorrect, or the surface may not even be detected. This can be solved by applying a preload and taking this into account in the post-processing [Ebenstein and Wahl, 2006]. Secondly, adhesion forces can be significant compared to penetration force. For example, in [Grunlan et al., 2001], indentations were carried out on polystyrene and polyethylene. It was found that adhesion is higher with a diamond tip than with a tungsten tip, leading to a substantial error if not taken into account (a hardness 2 to 3 times higher for the diamond tip). These specific characteristics need to be addressed and will be examined later.

It is possible to extract the mechanical properties of an indentation test from analytical solutions. There are several approaches, but most are based on the Oliver-Pharr method [Oliver and Pharr, 1992]. This method allows to extract information with only the data provided by the indenter. It relies on a purely elastic contact [Sneddon, 1965] to estimate the contact area. This allows to establish a link between the initial slope at unloading, which can be extracted from the measurements, and the reduced stiffness. For a soft material (compared to tip stiffness), this corresponds to eq. (3.1).

$$S = \left. \frac{dP}{dh} \right|_{h=h_{max}} = \frac{2E}{1-\nu^2} \sqrt{\frac{A}{\pi}} \quad (3.1)$$

with  $S$  the contact stiffness,  $P$  the normal load,  $h$  the indentation depth,  $h_{max}$  the maximum indentation depth,  $E$  the sample Young's modulus,  $\nu$  the sample ratio of Poisson and  $A$  the contact area. However, indentations are often performed in an elasto-plastic regime. Nevertheless, the results with this method remain accurate if the surface sinks-in (cf. fig. 3.2a), but become less relevant if it piles-up (cf. fig. 3.2b) [Yan et al., 2012; Bolshakov and Pharr, 1998].

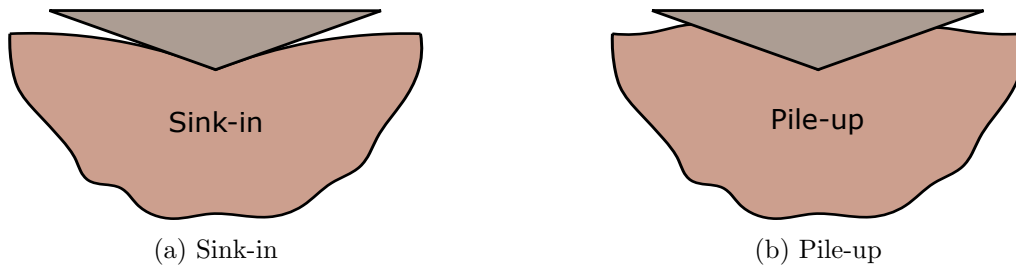


Figure 3.2: Illustration of pile-up and sink-in phenomena

As already discussed, if the material is adhesive, other models exist (cf. fig. 1.28). Firstly, there is the Johnson-Kendall-Roberts (JKR) model [Johnson et al., 1971]. In particular, it takes into account changes in the contact area. Another commonly used model is the Derjaguin-Muller-Toporov (DMT) model [Derjaguin et al., 1975]. Unlike the JKR model, the contact area remains unchanged, but adhesion forces are taken into account in the stress field. Both can be applied to indentation, and the choice of one over the other will depend on parameters such as material properties and tip radius. This can be quantified using the parameter of Tabor [Tabor, 1977; Ebenstein and Wahl, 2006]. However, these models remain valid in relatively simple cases, and numerical simulations can also be used.

### 1.3 Numerical approach

The question of unicity also arises for the simulations of an indentation test. Usually, three quantities are extracted from the load-displacement curve as shown in fig. 3.3: the curvature of the loading curve ( $C_u$ ), the initial unloading slope ( $S$ ) and the ratio between the residual depth

and the maximum indentation depth ( $\frac{h_r}{h_{max}}$ ) [Lee et al., 2009]. To extract the curvature, the load is often described by the law of Kick, which assumes that  $P = C_u h^2$  during loading [Dao et al., 2001]. For a reverse analysis, the aim is to converge towards these three quantities using a standard minimization method. The material parameters to be identified may vary. For example, they could correspond to stiffness, yield strength and a strain hardening exponent. However, in practice, it has been demonstrated that the quantities are not completely independent, and that the solution therefore becomes non-unique if the model has more than two parameters [Tho et al., 2004]. There are several solutions, most of which involve additional measurements. For example, two tips with different geometries can be used to determine the strain hardening exponent.

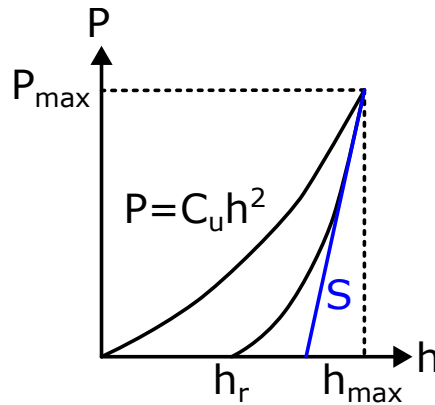


Figure 3.3: Illustration of a load-displacement curve of an indentation test

Numerical simulations of indentation are mainly performed on continuous materials using FEM. The focus is mostly put on the identification of parameters from constitutive models, such as for viscoelastic materials [Liu et al., 2009; Ngan et al., 2005]. Some models study indentation on discrete domains. This may be to study the failure of brittle materials, for example, by examining cracking paths through the failure of contact forces between bodies. It can also be used to study granular materials such as powders. Since the final objective of this work is to characterize parameters such as cohesion, which only makes sense for a material composed of discrete bodies, a discrete approach will also be employed.

Discrete models beyond the molecular scale are almost exclusively performed using DEM. However, this type of method is restricted to small strains at the grain scale. The direct consequence is that only a small amount of elastic energy can be stored during loading. This means that indentation with DEM is more suitable for studying irreversible processes. However, for ductile materials such as steel or for rubber, this method is not appropriate. In the current study, soft bodies will be used to identify the elastic component of the rubber-like material. The indentation model will then combine the advantages of a continuous elastic medium with those of a discrete one.

It is worth remembering that the diffusion model considers a degraded rubber. Indeed, close to the surface, the sulfur bonds created during vulcanization (i.e. cross-linking network) are damaged by highly multi-physical phenomena [Smith and Veith, 1982]. This process, however, is not yet fully understood and is beyond the scope of this study. The fact that the material is modeled as a collection of particles is not only because this allows the modeling of diffusion, but also to model a material whose properties differ from those of an undamaged rubber-like material. Consequently, since the aim of characterization is to find the numerical parameters of the diffusion model, this implies that indentation will also be carried out on a damaged rubber-like material.

## 2 Method

### 2.1 Experimental set-up

Indentations are performed on a KLA-Tencor G200 nanoindenter with a Berkovich diamond tip (three-sided pyramid with two reference angles:  $65.3^\circ$  and  $76.9^\circ$ ). One of the main hypotheses of the experimental section will be to consider that the cross-linking network is completely damaged. To this end, indentations will be performed on a rubber mixture for which no vulcanization has been carried out (but without changing the compounds). The composition is as follows (in *phr*<sup>1</sup>): 100 isoprene rubber (IR), 50 N347, 3 6PPD, 1.5 stearic acid, 3 ZnO, 1.3 CBS and 1.3 sulfur. The composition is therefore slightly different from that used for testing on the tribometer, where SBR is used instead of IR. This choice was made because after the friction tests, SBR seemed to be more representative of a real application. IR was kept for the indentation part, as the materials are roughly equivalent and the aim was above all to propose a procedure. The sample is 2.8 mm thick and is bonded to a metallic support using a heat-softening glue (CRYSTALBOND 555).

As already mentioned, performing indentations on a soft and adhesive material can present a number of difficulties. First, the adhesion force is close to the maximum force that can be exerted by the indenter to withdraw from the surface. Moreover, the surface is detected by a change in the measured force (i.e. equivalent to a contact stiffness). However, the low stiffness of the material combined with stress relaxation due to its viscoelasticity, may lead to the surface being detected too late. This results in a significant error in the depth corresponding to the measured force. To overcome these difficulties, the surface is coated with a 15 nm thick layer of gold, using a Safematic CCU-010 compact coating unit. This thickness reduces the effect of adhesion sufficiently to allow the tests to be performed, with a low effect on the measured force, and also to neglect adhesion in the post-processing. This last point is important, because if an adhesive force has to be added to the numerical model, the solution may no longer be unique. It should also be noted that the final reverse analysis will be carried out on the loading section, which is less affected by adhesion.

Several acquisitions of surface topography were made by interferometry using a 3D non-contact optical surface profiler (Zygo, ZeGage TM Pro). On some samples, the coating did not appear to adhere correctly (a wavy pattern was observed) and these samples were removed from the study. The surfaces acquired measure 174 by 174  $\mu m$  and, after coating, have on average an arithmetic mean height equal to 0.63  $\mu m$ . The maximum indentation depth is equal to 1  $\mu m$ , which corresponds to a contact area of 4.95 by 4.95  $\mu m$ . Therefore, roughness is negligible at the scale of the indentation. An example of one of these surfaces is shown in fig. 3.4.

The displacement rate of the tip is constant during loading and unloading (without holding time). This choice is made to facilitate the comparison with the numerical model, whose results are not time-dependent. The maximum indentation depth ( $h_{max}$ ) is equal to 1  $\mu m$ , because for the numerical model, it allows to keep the same body size distribution used for the diffusion model (while indenting a significant number of bodies). Indentations are performed for 9 displacement rates (10, 20, 30, 40, 50, 60, 100, 200 and 500  $nm.s^{-1}$ ). The aim is to evaluate the influence of this rate on material parameters ( $E$  and  $C$ ). In post-processing, only the stiffness of the tip holder is corrected. Indeed, the stiffness of the metallic support and the frame are much higher than the stiffness of the sample. Furthermore, there is no correction for thermal drift due to viscosity effects.

---

<sup>1</sup>parts per hundred of rubber

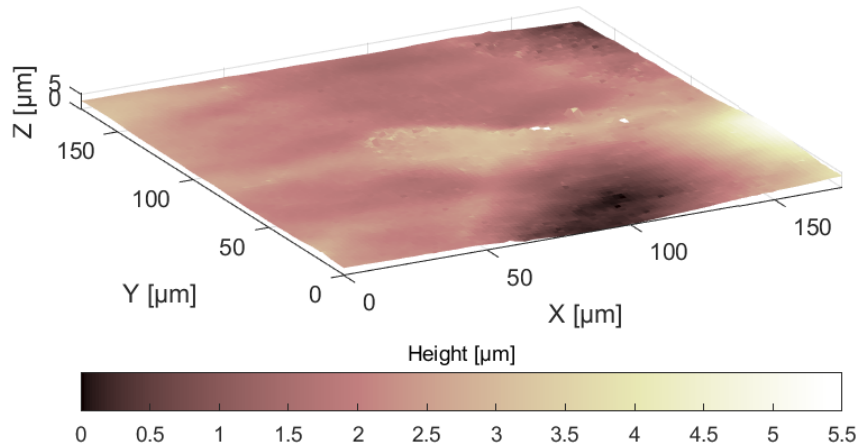


Figure 3.4: Surface topography measured by interferometry

These results of conventional indentation tests are supported by continuous stiffness measurement (CSM) tests. These tests make it possible to carry out a large number of indentations without complete unloading, and to extract the sensitivity of material properties according to the loading frequency, which can be expressed as a strain rate. This consists in adding small oscillations to a main indentation and analytically deriving stiffness as a function of depth (using eq. (3.1)). This is equivalent to performing successive indentations for an increasing depth. The load is controlled to ensure a constant strain rate during indentation (displacement has an exponential form). The maximum indentation depth for the CSM tests is set to  $2 \mu\text{m}$ , the strain rate to  $0.05 \text{ s}^{-1}$  and oscillations with an amplitude of  $2 \text{ nm}$  at a frequency of  $75 \text{ Hz}$  are added.

## 2.2 Indentation model

An indentation model is created to identify  $E$  and  $C$  by reverse analysis. As the final objective is the diffusion study, the indentation model will aim to be as close as possible to the diffusion model framework, particularly in terms of how viscosity is considered. The damage of the cross-linking network suggests a highly viscous material. However, the time scale of the simulations is much lower than the relaxation time of the material, and combined with the high tribological stresses, this would suggest a highly elasto-plastic flow. However, such scales of time, space and stress level are not accessible by indentation, and viscosity will inevitably be an experimental parameter. To obtain results close to those of a material unable to exhibit relaxation, viscosity will be modeled by relative and irreversible displacements between bodies, which can be compared to plasticity. In summary, this approach consists in modeling the visco-elasto-plastic material with an elasto-plastic model. The indentation model is not designed to capture this viscosity dependence. The aim is to reproduce a given experimental configuration, with assumptions that appear consistent at the scale of the diffusion model. The model also assumes a plane-strain kinematics, which will be discussed later.

The model is divided into two distinct domains. The first one is a domain near the tip, where elasto-plastic strain is expected. It will be modeled using discrete soft bodies. The second one is a domain where purely elastic strain is assumed. It will be modeled using a continuous soft body (for computation time reasons). Indentations are performed numerically under quasi-static conditions. A comparison between the experimental and numerical configurations is presented in fig. 3.5.



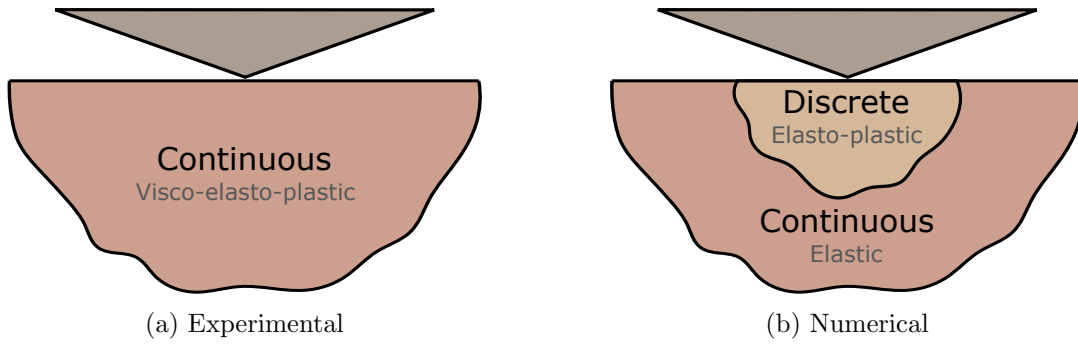
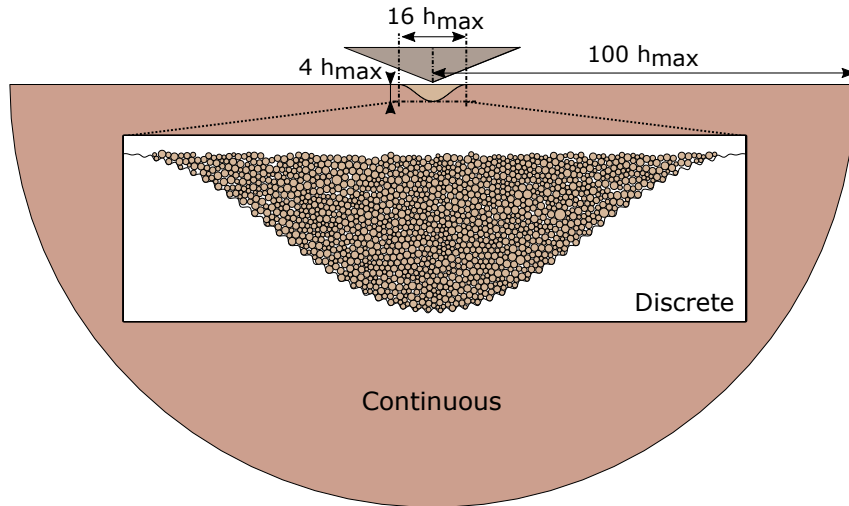


Figure 3.5: Configurations used for the indentations

The velocity of the tip (hereinafter referred to as the displacement rate) during loading and unloading is identical and constant (with a smooth transition between the two). The maximum indentation depth ( $h_{max}$ ) is equal to  $1 \mu m$ . An illustration of the model is shown in fig. 3.6.

Figure 3.6: Illustration of the indentation model;  $h_{max}$  corresponds to the maximum indentation depth ( $1 \mu m$ )

Close to the tip, the material is modeled as a collection of 1463 circular soft bodies. The diameters are close to the distribution used for the diffusion model and follow a Gaussian distribution with a mean value ( $d_M^{rubber}$ ) of  $0.148 h_{max}$  and a standard deviation of  $0.026 h_{max}$ . Moreover, as already mentioned, the value  $h_{max}$  was chosen to perform indentations on a significant number of bodies while keeping computation times reasonable. The discrete domain is bounded by a continuous soft body with the same properties (contact and constitutive models) as discrete-domain bodies. The prescribed displacement is zero on its lower boundary.

The continuous domain has a semicircular shape and is discretized by 6539 nodes, with a higher node density close to the tip. Between nodes, a typical nodal distance of  $0.03 h_{max}$  is defined near the tip and of  $3.00 h_{max}$  near the lower boundary (cf. fig. 3.7a). To determine the size of the domain, preliminary continuous simulations were carried out to evaluate the maximum load during indentation ( $P_{max}^i$ ) as a function of the semicircular radius ( $R$ ). These results were compared with a radius of  $200 h_{max}$ , which is considered as infinitely large and giving  $P_{max}^\infty$ . The radius was finally chosen equal to  $100 h_{max}$ , the error being a few percent for an elastic case (cf. fig. 3.7b).



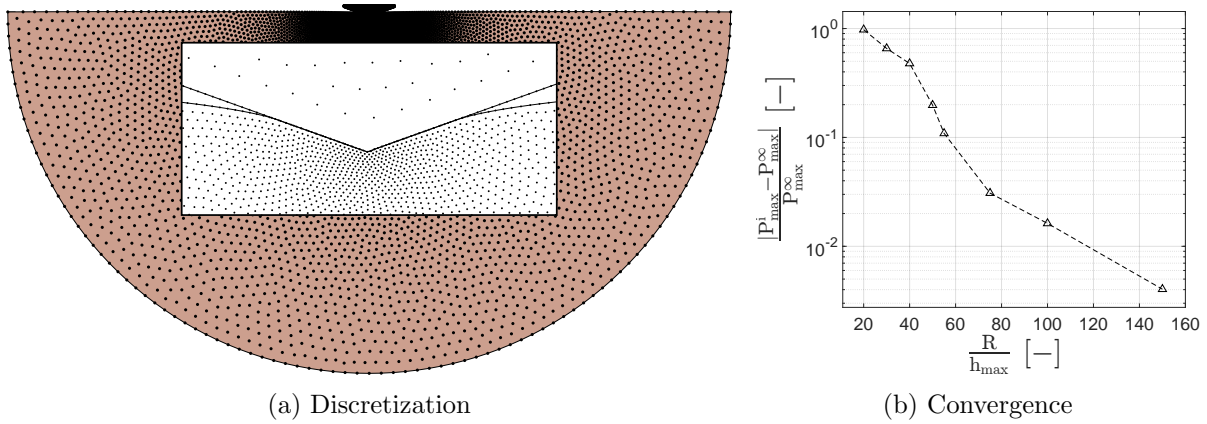
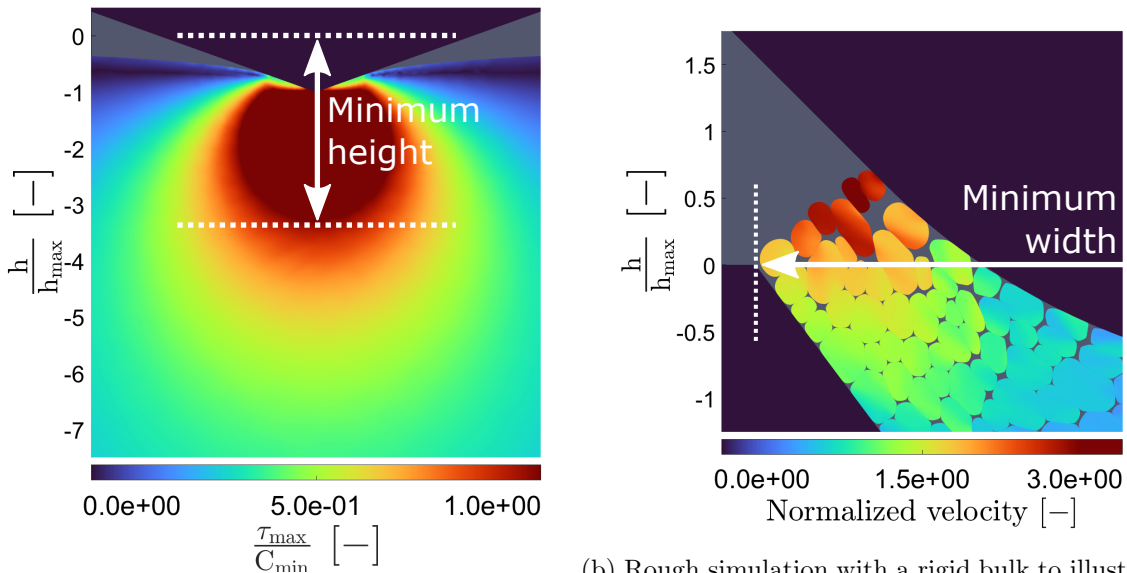


Figure 3.7: Preliminary study to determine the semicircular radius

The size of the discrete domain must be chosen carefully. The main difference is that for this domain, relative internal displacements are allowed. These displacements are expected if the stress locally exceeds the interparticle cohesion value. To obtain the height of the discrete domain, an indentation on a continuous (without discrete bodies) and purely elastic domain was performed. By assuming the lowest cohesion value to be studied, it was shown that stress will be strictly lower than cohesion beyond  $4 h_{max}$  (fig. 3.8a). The domain can therefore be assumed to be continuous (i.e. purely elastic) beyond this depth. Note that, as discussed later, if plasticity is taken into account, the stress decreases and the value of the previous height therefore corresponds to the maximum height to be considered. Furthermore, during indentation, the width of the discrete domain must be sufficiently large to allow relative lateral displacements without excessive compressive stress (fig. 3.8b). A width of  $16 h_{max}$  gives satisfactory results (a reorganization of the discrete medium occurs near the surface without ejection of particles) for the current sharp tip. In addition, a sinusoidal shape for the domain is defined to be close to the shape of the non-zero stress field.



(a) Maximum shear stress normalized by the minimal cohesion value

(b) Rough simulation with a rigid bulk to illustrate an insufficiently large width; velocity is normalized by the displacement rate

Figure 3.8: Preliminary study to determine the size of the discrete domain

In addition, a smooth transition between the discrete and continuous domains must be guaranteed. To this end, a sinusoidal surface roughness at the interface of these domains is defined, with an amplitude of  $1 d_M^{rubber}$  and a period of  $2 d_M^{rubber}$ . This ensures a good force transmission between the two domains while using the same contact model as the one used between the discrete bodies (and therefore preserving the unicity of the solution).

Before each indentation, a preliminary procedure is carried out, as shown in fig. 3.9. The bodies are initially free of contact and cohesionless (fig. 3.9a). The discrete bodies are compacted by a top plate inside the discrete domain area, bounded by the continuous domain (fig. 3.9b). The cohesion is then activated and the top plate is removed (fig. 3.9c) and indentation is performed once the velocity field is negligible compared to the displacement rate. Note that this procedure must be carried out with care. Indeed, as indicated by the black arrows in fig. 3.9b, during compaction, the continuous domain will also be compressed. Consequently, when the top plate is removed, it will exert a tensile force on the discrete domain, as illustrated by the black arrows in fig. 3.9c. Therefore, if the compaction pressure is too high, it will result in considerable residual stresses. One way of reducing this effect (i.e. bulk deformation) is to increase the density of the continuous domain during compaction. Indeed, the continuous domain will be less deformed due to inertial effect. An increase in stiffness would cause a significant increase in computation time (cf. eq. (1.10)). On the other hand, if the compaction pressure is too low, the discrete bodies will be dispersed inhomogeneously (with significant porosity in the discrete domain).

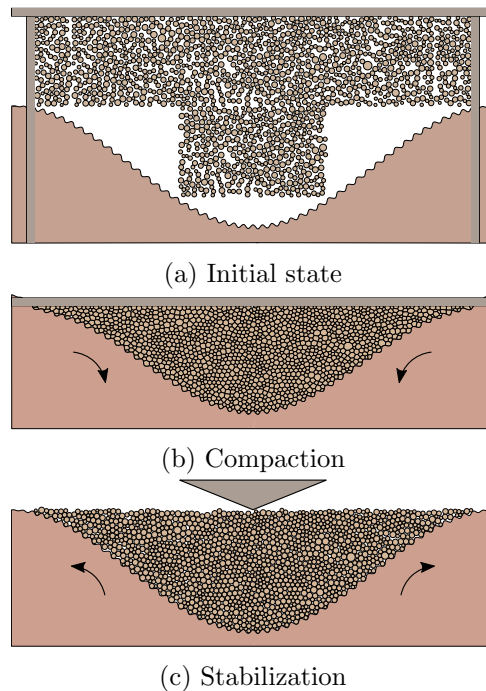


Figure 3.9: Main preliminary stages

Experimental indentations will be performed using a Berkovich tip. To simulate this type of indentation, the majority of 2D models use axisymmetric simulations (whereas the current method can only model plane-strain kinematics). This consists in assuming a conical tip with a half apex angle of  $70.3^\circ$ . This gives the same contact area ( $A$ ) as a 3D model for a given indentation depth ( $h$ ). Several studies have shown that a 2D model faithfully reproduces some of the results (e.g. load-depth curves) obtained by a 3D model [Lichinchi et al., 1998; Shim et al., 2007]. Note that the contact area is the area projected onto the plane orthogonal to the

indentation axis. However, the previous technique cannot be used with plane-strain kinematics. Indeed, in this case, the contact area varies linearly ( $A \propto h$ ), whereas for a Berkovich tip (3D or 2D with axisymmetric kinematics), it varies quadratically ( $A \propto h^2$ ). Nevertheless, these studies show that for a given configuration, the results depend mainly on the contact area. For this reason, the reverse analysis will be carried out on quantities that do not depend on this area. The first one, is the hardness ( $H$ ), which corresponds to the ratio of the maximum load ( $P_{max}$ ) divided by the contact area. The second one, for elasto-plastic materials only, is the ratio of the residual depth ( $h_r$ ) divided by  $h_{max}$ . The residual depth corresponds to the depth at which contact is lost between the tip and the surface. For the sake of comparison, the half apex angle will be equal to  $70.3^\circ$ .

The discrete bodies and the continuous one have the same mechanical properties. These properties, which are described in the constitutive and contact models, are identical to those used in the diffusion model for the rubber material. The tip is considered rigid. Contact between the tip and the discrete bodies is assumed to be frictionless. Indeed, friction for a high tip angle, such as the one used in the model, remains low [Warren and Guo, 2006; Tabor, 2000]. Adhesion is also neglected to ensure the unicity of the solution.

Before performing a reverse analysis, the objective is to demonstrate the unicity of the solution by defining a parametric space  $\{E, C\}$ . As discussed later, cohesion can be reduced to a normalized cohesion  $\frac{C}{E}$ . The parametric space is composed of 12 simulations, with 3 stiffnesses (1, 5 and 10 MPa) and 4 cohesions (0.05, 0.10, 0.20 and 0.40  $E$ ). Based on these simulations, a procedure for the reverse analysis is proposed. An alternative procedure, using the same method, is also proposed for finding  $E$  and  $C$  without a pre-existing study and in a few iterations.

#### Highlights

- The aim is to identify the stiffness ( $E$ ) and the cohesion ( $C$ ) used in the numerical model by reverse analysis.
- Experimentally, indentations will be performed using a Berkovich tip on a carbon black filled IR.
- Numerically, indentations will be performed on an elasto-plastic medium composed of discrete bodies, bounded by a continuous elastic medium.
- To compare 3D measurements with a 2D model, reverse analysis will be performed according to hardness ( $H$ ) and residual depth ( $h_r$ ).

## 3 Numerical results

### 3.1 Kinematics

Ensuring a consistent kinematics is mandatory for a reverse analysis, otherwise an arbitrary set of inputs might erroneously lead to the expected target output. For irrelevant kinematics, there is no guarantee that if the configuration changes, the set of inputs (i.e.  $E$  and  $C$ ) will be in agreement with the material properties. Kinematics can be studied by examining, after indentation, the residual displacement field  $U_r$  (which corresponds to the norm between the initial and the final state) and by tracking centroid positions. The results are presented in fig. 3.10 (the 0.40  $E$  cohesion is not displayed as it is very similar to the 0.20  $E$  cohesion).

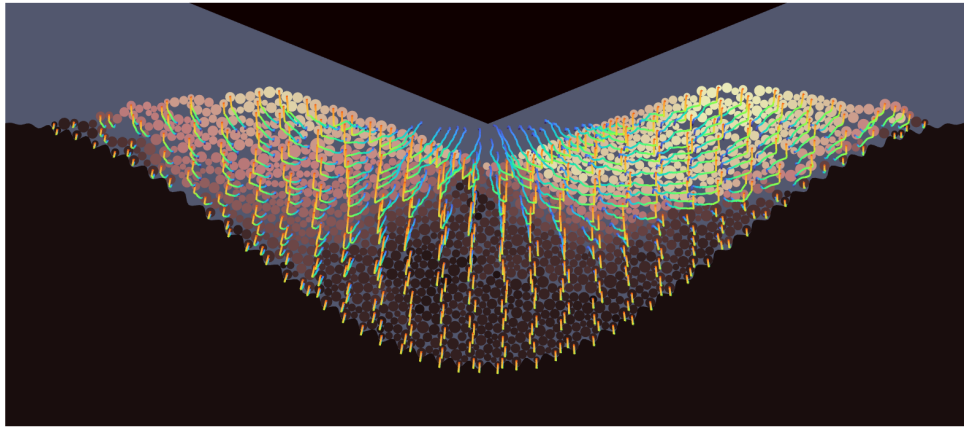
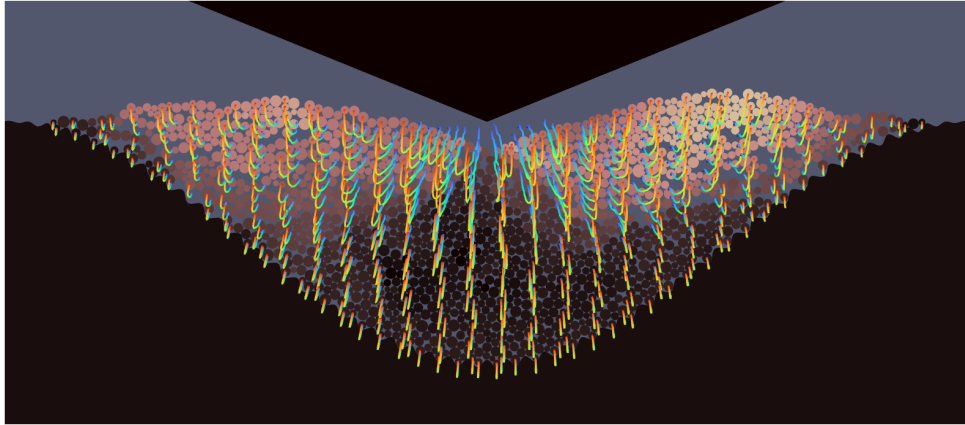
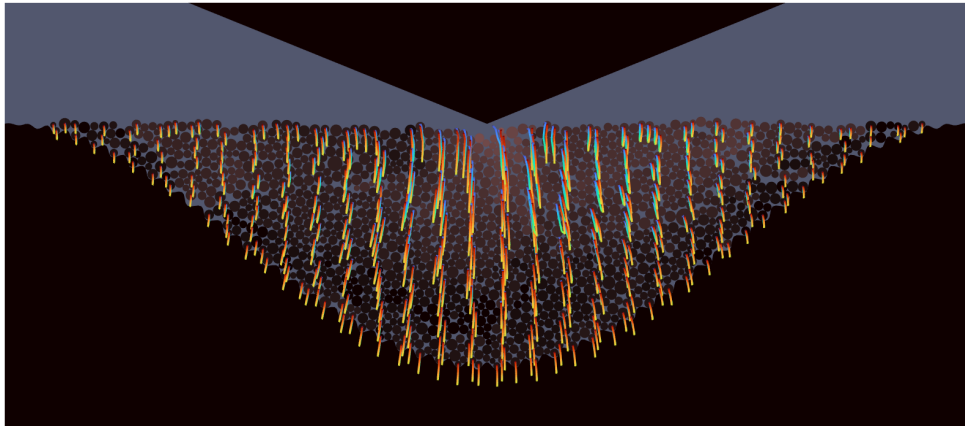
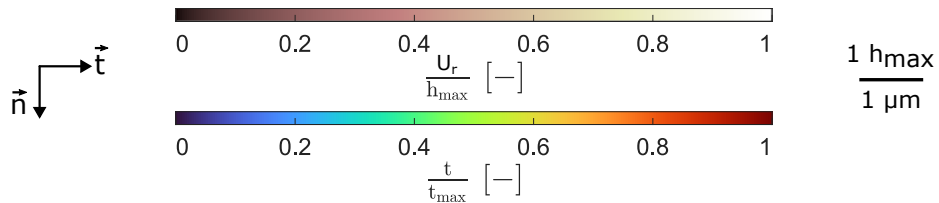
(a)  $C = 0.05 E$ (b)  $C = 0.10 E$ (c)  $C = 0.20 E$ 

Figure 3.10: Kinematics according to normalized cohesion ( $E = 5 \text{ MPa}$ ); the background corresponds to the residual displacement field ( $U_r$ ) normalized by the maximum indentation depth ( $h_{max}$ );  $U_r$  is equal to the centroid displacement norm between the initial and final states; the lines correspond to various centroid positions during indentation and the color to time ( $t$ ) normalized by the time at which the tip has returned to its initial position ( $t_{max}$ ) (►)

Plasticity can be described as irreversible displacements of matter, which corresponds to the bodies in this model. Consequently,  $\frac{U_r}{h_{max}}$  can be considered as an analogous quantity to plasticity. Simulations range from elasto-plastic to elastic indentations. Indeed, for the lowest cohesion,  $U_r$  is locally higher than  $0.70 h_{max}$ , whereas for the highest cohesion it is closer to  $0.05 h_{max}$  in the whole domain. For a cohesion of  $0.05 E$ , the highest  $U_r$  values are located close to the tip and the bodies form a bump on the surface. This bump is decreasing with increasing cohesion. A small asymmetry can be observed with  $U_r$  higher on the right side. This is attributed to the size and position of the bodies, which are not evenly distributed. For cohesions of  $0.05$ ,  $0.10$ ,  $0.20$  and  $0.40 E$ , the maximum  $U_r$  is respectively equal to  $0.77$ ,  $0.57$ ,  $0.15$  and  $0.11 h_{max}$ . However, for cohesions of  $0.20$  and  $0.40 E$ ,  $U_r$  is only above  $0.05 h_{max}$  for a small volume. It therefore appears negligible. These results are consistent with other studies using continuous models for elasto-plastic indentations. For example, [Taljat and Pharr, 2004] used FEM with elasto-plastic solids. This study shows that the bump, often referred to as the pile-up phenomenon, is linked to the ratio of yield stress divided by the stiffness, which is closely related to  $\frac{C}{E}$ .

To get a better view of material flow, several centroid positions during indentation are represented by lines in fig. 3.10. For a cohesion of  $0.05 E$ , a displacement in the normal ( $\vec{n}$ ) and tangential ( $\vec{t}$ ) directions can be observed. For bodies below the tip apex, normal displacement increases during loading ( $t < 0.5 t_{max}$ ) and decreases during unloading ( $t > 0.5 t_{max}$ ). For bodies more distant from the apex and close to the surface, the normal displacement increases continuously for the lowest cohesion. Regarding tangential displacement, it increases continuously (or is null) during loading and is constant during unloading. This shows that tangential flow is mainly plastic (there is no tangential elastic recovery) whereas normal flow is elastic or elasto-plastic. To support this analysis, is it possible to look at the cohesion of  $0.20 E$ . This indentation is mainly elastic. Indeed, centroid positions during unloading overlap those during loading. In this simulation, tangential flow is negligible compared to normal flow. Finally, the cohesion of  $0.10 E$  is an intermediate case in which tangential flow is non-zero, but lower than the cohesion of  $0.05 E$ . It can also be noted that the displacement of deeper bodies is lower for lower cohesion. This is explained by a decrease in load for an increasing degree of plasticity and will be discussed later.

Several studies have investigated the dependence of the velocity field on several parameters (material, tip geometry, etc.). For example, in [Udupa et al., 2019] is measured how the velocity field is modified as a function of the apex angle for a wedge tip. Indentations are made on copper and the velocity field is acquired by image correlation using a high-speed camera. The results show that below the tip apex, material flow is mainly normal. On the sides of the tip, the tangential component increases compared to the normal one. These results are consistent with the kinematics found in the current model.

Bodies located close to the tip apex have been subjected to significant stresses which do not result in relative displacements. Consequently, during unloading, these bodies will recover their initial strains and positions. If plasticity were modeled within the bulk of each body,  $U_r$  under the tip apex would be higher [Dean and Clyne, 2016; Sakharova et al., 2009]. However, the effect of this plastic deformation only concerns a small volume and will be considered negligible.

### 3.2 Load-depth curves

For several cohesion and stiffness values, the corresponding load-depth curves are displayed in fig. 3.11. Normal load ( $P$ ) is normalized by  $E$  and the maximum contact area ( $A_{max} = 5.58h_{max}L$ ) with  $L$  the length in the transverse direction (i.e. one unit of length). The indentation depth ( $h$ ) is normalized by  $h_{max}$ . If the ratio  $\frac{C}{E}$  is kept constant, the load-depth curves



overlap. Firstly, this shows that as  $A_{max}$  is constant for all simulations,  $P$  is linearly proportional to  $E$ . Secondly, if  $\frac{C}{E}$  varies, then  $P$  is modified. These properties will be discussed in detail in the reverse analysis section. Furthermore, there is no significant change in curvature at the very beginning of each indentation. This shows that even if the contact is applied to a few bodies, the results remain consistent with higher  $h$ . For cohesions of 0.05 (fig. 3.11a) and 0.10 (fig. 3.11b)  $E$ , results are noisier during the second half of loading. This is attributed to local reorganization reinforced by low cohesion values.

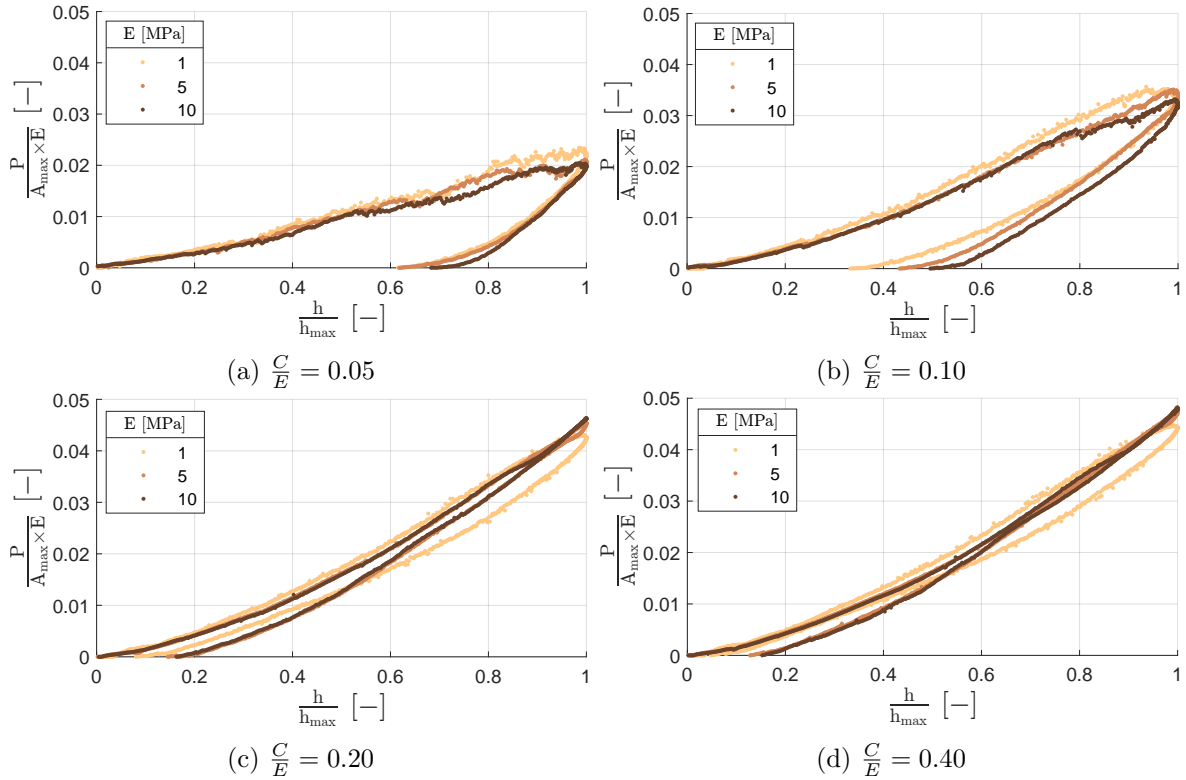


Figure 3.11: Load-depth curves according to the stiffness (1, 5 and 10 MPa) and for several normalized cohesions (0.05, 0.10, 0.20 and 0.40)

During the loading, the slope of the load-depth curves changes as a function of several parameters. Firstly, plastic flow leads to a decrease in the slope. As shown in fig. 3.10, material tends to flow tangentially for elasto-plastic indentations. As a result, the volume of material under the tip also decreases, and therefore the load. This can be assessed by looking at the maximum load. For cohesions of 0.05, 0.10, 0.20 and 0.40  $E$ , the normalized maximum load is on average equal to 0.022, 0.035, 0.045 and 0.047 respectively. The second parameter affecting the slope is the contact area. For a wedge tip, the contact area increases linearly during loading ( $A \propto h$ ). Therefore, in the absence of plasticity, the slope should increase with  $h$ . For example, the increase in slope can be observed for a cohesion of 0.40  $E$  (fig. 3.11d), which is mainly elastic.

Unloading, like loading, depends on plasticity and contact area. However, as discussed in the kinematics section, tangential flow only occurs during loading. A key quantity during the unloading is the residual depth. This depth provides an independent evaluation of the degree of plasticity (i.e. only influenced by normalized cohesion). Indeed, as previously discussed,  $P$  depends on both stiffness and normalized cohesion, which cannot therefore be identified. The residual depth increases as normalized cohesion decreases.

From a cohesion of 0.20  $E$ , the results start to become less sensitive to normalized cohe-

sion. This gives an upper limit to the normalized cohesion that can be identified by the model. Furthermore, for these cohesions, the unloading and loading stages are not perfectly overlapping. Further simulations show that this gap can be reduced by decreasing the displacement rate. Inertial forces must also be negligible compared to cohesive forces, otherwise non-physical decohesions close to the surface will occur. This gives a lower limit to the normalized cohesion, which is mainly limited by computation time. However, lower values are beyond the scope of this study. From the point of view of a friction model, lower cohesions would be well below the typical stress level and would therefore be negligible.

#### Highlights

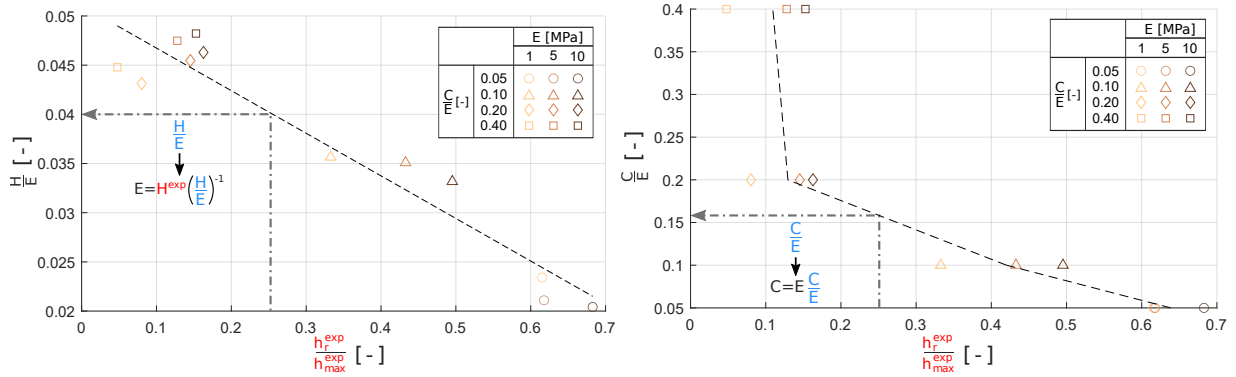
- The numerical model is suitable for studying elasto-plastic indentations, unlike the more conventional discrete models with rigid particles, which are more adapted to irreversible processes (e.g. fracture of a brittle material).
- The kinematics during indentation corresponds to a normal elasto-plastic flow and a tangential plastic flow.
- Load-displacement curves are extracted, showing a slope evolving with depth and a significant elastic recovery during unloading.

## 4 Reverse analysis

### 4.1 General method

The results depend on two main parameters:  $E$  and  $C$ . As it could be seen on the indentation curves (fig. 3.11), these two parameters have an effect on the load and the residual depth. However, as previously mentioned, it is not possible to directly compare numerical and experimental load due to plane-strain kinematics. For this reason, it was decided to only use  $H$  (hardness) and  $h_r$  (residual depth). As the experimental real contact area is unknown, for the sake of comparison,  $H$  is assumed to be equal to  $\frac{P_{max}}{A_{max}}$ . Note that using results at  $h_{max}$  reduces the inertial effects, as the velocity gradually decreases at this moment. In addition, it maximizes the number of involved bodies which reduces the dispersion (less dependent on one body position). The values of  $H$  and  $h_r$  as a function of  $E$  and  $C$  are displayed in fig. 3.12. Ratios highlighted in red with the superscript “exp” for experimental, refer to data obtained numerically but which can also be extracted from measurements. Ratios highlighted in blue refer to numerical data only.





(a) Normalized hardness as a function of normalized residual depth; the dotted line corresponds to a linear regression  
 (b) Normalized cohesion as a function of normalized residual depth; the dotted line connects the mean value for each normalized cohesion

Figure 3.12: Method for identifying  $C$  and  $E$  from reverse analysis; ratios obtained numerically are highlighted in blue and values that can be extracted from measurements in red

In fig. 3.12a, dependency of normalized hardness on residual depth is displayed. Hardness is normalized by the stiffness. As  $H$  is linearly proportional to  $E$ , a change in  $\frac{H}{E}$  describes how hardness is influenced by plasticity, characterized by  $\frac{h_r}{h_{max}}$ . The ratio  $\frac{H}{E}$  decreases with increasing  $\frac{h_r}{h_{max}}$ . The slope of the regression is equal to  $-0.043$ . For the lowest normalized cohesion compared to the highest one, hardness is reduced by half. The ratio  $\frac{h_r^{exp}}{h_{max}^{exp}}$  can be obtained from the experimental data to find the corresponding  $\frac{H}{E}$ . Then, using the experimental hardness  $H^{exp}$ ,  $E$  can be derived.

In fig. 3.12b, dependency of normalized cohesion on residual depth is displayed. As shown in fig. 3.11, normalized cohesion decreases as residual depth increases. For cohesions of 0.05, 0.10, 0.20 and 0.40  $E$ ,  $h_r$  is on average respectively equal to 0.64, 0.42, 0.13 and 0.11  $h_{max}$ . For the same normalized cohesion, lower stiffnesses tend to give lower  $h_r$ . One way of minimizing this effect would be to take a depth before loss of contact (e.g. 90% of unloading). Indeed,  $h_r$  is very sensitive to local reorganization near the surface. In addition, the displacement rate could also be reduced. As mentioned above, the ratio  $\frac{h_r^{exp}}{h_{max}^{exp}}$  can be obtained from the experimental data, which allows to find the corresponding  $\frac{C}{E}$ . Since  $E$  is already known,  $C$  can be derived.

One of the main challenges for reverse analysis is to ensure the unicity of the solution. This means that a set of  $H$  and  $h_r$  must give a unique set of  $E$  and  $C$ . In fig. 3.12a, it can be seen that for a given  $\frac{h_r}{h_{max}}$ , there is only one corresponding  $\frac{H}{E}$ . However, as shown in fig. 3.12b, for  $C$  greater than 0.20  $E$ , the results start to become less sensitive to normalized cohesion (i.e. different  $\frac{C}{E}$  give close  $h_r$ ). For this graph and the tested range of normalized cohesions, the trend curve is strictly monotonic without reaching a vertical asymptote. As a result, it guarantees unicity for cohesions below 0.20-0.40  $E$ .

Note that the method is presented for a pre-existing numerical campaign exploring the parametric space. Without these results, a way to proceed is described in algorithm 1.

**Algorithm 1** Reverse analysis procedure**Require:**  $\{H^{exp}, \left(\frac{h_r}{h_{max}}\right)^{exp}\}$ 

- 1: Assume an initial stiffness  $E^0$
- 2: Take the initial parameters as follows:  
 $k - 1 : \{E^{k-1} = E^0, C^{k-1} = 0.05 E^0\}$   
 $k : \{E^k = E^0, C^k = 0.40 E^0\}$   
with  $k$  the iteration number
- 3: Complete steps 4, 5 and 6 for  $k-1$
- 4: Perform a simulation for  $\{E^k, C^k\}$
- 5: Extract the following numerical ratios:  
 $\left\{\left(\frac{h_r}{h_{max}}\right)^k, \left(\frac{H}{E}\right)^k, \left(\frac{C}{E}\right)^k\right\}$
- 6: Calculate  $dh$ :  
 $dh^k = \left(\frac{h_r}{h_{max}}\right)^k - \left(\frac{h_r}{h_{max}}\right)^{exp}$
- 7: Calculate  $f'$ :  $(f')^k = \frac{dh^k - dh^{k-1}}{\left(\frac{H}{E}\right)^k - \left(\frac{H}{E}\right)^{k-1}}$
- 8: Calculate the expected normalized hardness:  
 $\left(\frac{H}{E}\right)^* = \left(\frac{H}{E}\right)^k - \frac{dh^k}{(f')^k}$
- 9: Update the stiffness:  
 $E^{k+1} = H^{exp} \left(\left(\frac{H}{E}\right)^*\right)^{-1}$
- 10: Calculate  $g'$ :  
 $(g')^k = \frac{dh^k - dh^{k-1}}{\left(\frac{C}{E}\right)^k - \left(\frac{C}{E}\right)^{k-1}}$
- 11: Calculate the expected normalized cohesion:  
 $\left(\frac{C}{E}\right)^* = \left(\frac{C}{E}\right)^k - \frac{dh^k}{(g')^k}$
- 12: Update the cohesion:  
 $C^{k+1} = E^{k+1} \left(\frac{C}{E}\right)^*$
- 13: Repeat steps 4 to 12 until the criterion (to be defined) is reached

With this method, a close result for  $E$  is expected after 2-3 iterations, as  $\frac{H}{E}$  as a function of  $\frac{h_r}{h_{max}}$  should be linear. A few more iterations will be needed to obtain  $C$ . The use of ratios is not mandatory and a more classical minimization method can be used on  $\{|H - H^{exp}|, \left|\frac{h_r}{h_{max}} - \left(\frac{h_r}{h_{max}}\right)^{exp}\right|\}$ . However, particular attention must be paid to the relevance of cohesion values (which must be positive and below 0.2-0.4  $E$ ).

## 4.2 Experimental results

Rubber-like materials have visco-elastic properties. Consequently, the mechanical response during indentation depends on the displacement rate. To evaluate this effect, several indentations were performed at different displacement rates (10, 20, 30, 40, 50, 60, 100, 200 and 500  $nm.s^{-1}$ ). The strain rate ( $\dot{\epsilon}$ ) is approximated by  $\frac{V}{h_{max}}$  with  $V$  the displacement rate. Results are presented in fig. 3.13.

Indentation curves are displayed in fig. 3.13a. For the sake of clarity, only the mean load-depth curve has been plotted for each displacement rate. During loading, the more the strain rate increases, the more the load increases. For a depth below 50  $nm$  (0.05  $h_{max}$ ), a change in curvature can be observed. This may correspond to gold coating (15  $nm$ ), rubber compounds (carbon black, zinc oxide, etc.) or tip defects. However, it remains at a small scale compared to  $h_{max}$ . The slope is almost constant during loading, except for a strain rate of 0.50  $s^{-1}$ , with

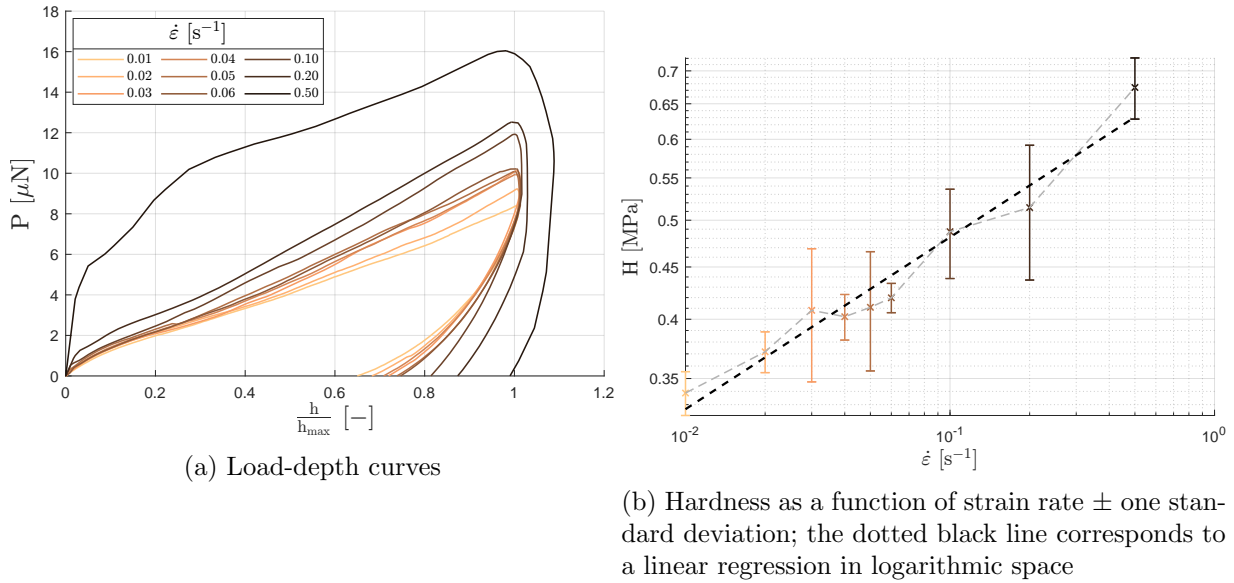


Figure 3.13: Experimental results for several strain rates (0.01, 0.02, 0.03, 0.04, 0.05, 0.06, 0.10, 0.20 and 0.50  $s^{-1}$ )

an inflection point at  $0.27 h_{max}$ . Depth should decrease when the tip reaches  $1 h_{max}$ . However, the indenter was less and less able to fully satisfy this condition for increasing displacement rates. During unloading, the load evolves until there is no longer a contact between the tip and the surface. The residual depth depends on several parameters. Even with a gold coating, a small adhesion effect is still present. More importantly, residual depth is a contribution from plasticity and viscosity. The relevance of using  $h_r$  to measure the visco-plastic effect will be discussed thereafter.

The dependency of hardness on strain rate can be observed in fig. 3.13b. As the real contact area is unknown,  $H$  is assumed to be equal to  $\frac{P_{max}}{A(P_{max})}$  with  $A(P_{max}) = 24.56h(P_{max})^2$ . Note that the area is calculated for the  $h$  corresponding to  $P_{max}$  (which may slightly differ from  $h_{max}$ ). The more  $\dot{\epsilon}$  increases, the more  $H$  increases. The standard deviation of hardness remains low, with a mean value of 0.04 MPa. A power law can be derived, giving an exponent ( $m$ ) of 0.17. This exponent reflects the sensitivity of the material to strain rate. In contrast, for PC and PMMA, the  $m$  exponent is respectively equal to 0.05 and 0.10 [Kermouche et al., 2006]. The current material is therefore highly dependent on the strain rate.

It should be noted that the strain rates obtained here ( $\leq 0.50 s^{-1}$ ) are much lower than those obtained in the diffusion model. Indeed, as discussed later, the shear rates obtained in the diffusion model are close to  $1 \cdot 10^7 s^{-1}$ . The possibility of extrapolating the values obtained here over several orders of magnitude remains unknown, and would deserve further investigations. There are a few characterization techniques that can attain significant strain rates. For example, the Hopkinson technique allows to reach strain rates of the order of  $10^4 s^{-1}$  [Sobczyk et al., 2022].

When a visco-elastic material undergoes a given strain, it exhibits an instantaneous response driven by the instantaneous modulus ( $E_0$ ), followed by a temporal evolution. The Oliver-Pharr method mentioned above can be used to find  $E_0$ . However, applying this method to indentation without holding time at  $h_{max}$  and with a relatively slow unloading rate, leads to inaccurate results [Cheng et al., 2005]. For this reason, it cannot be used to identify  $E_0$  with the previous measurements and additional CSM tests have been carried out. One of the main advantages is that the derived stiffness depends on the strain rate driven by the oscillations. This makes it

possible to obtain much higher strain rates and reach a stiffness plateau [Cifuentes et al., 2014]. This stiffness, which corresponds to a significant shear rate, should therefore be the one used in the diffusion model.

As a reminder, the maximum indentation depth is set to  $2 \mu\text{m}$ , the strain rate to  $0.05 \text{ s}^{-1}$  and oscillations with an amplitude of  $2 \text{ nm}$  at a frequency of  $75 \text{ Hz}$  are added. The results are presented in fig. 3.14.

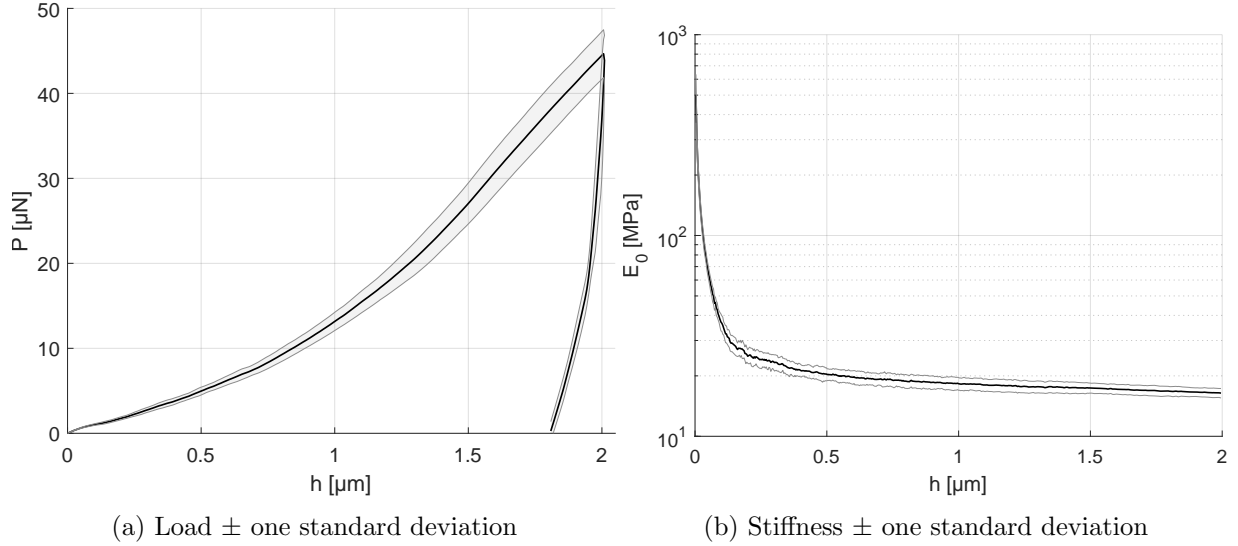


Figure 3.14: Results according to indentation depth from CSM tests

First, as the displacement rate is a bit different from the previous measurements (with constant displacement rates), the load in fig. 3.14a differs slightly from that in fig. 3.13a for a strain rate of  $0.05 \text{ s}^{-1}$  (+29% at  $1 \mu\text{m}$  but unchanged at  $0.5 \mu\text{m}$ ). Regarding  $E_0$  in fig. 3.14a, it can be seen that after  $0.5 \mu\text{m}$ , the variation in modulus is relatively low. This shows that for the previous hardness and current modulus, the effect of gold coating is negligible. For a depth of  $1 \mu\text{m}$ ,  $E_0$  is equal to  $18 \text{ MPa}$ .

### 4.3 Reverse analysis results

To fully identify  $E$  and  $C$ , it is necessary to extract  $H$  and  $h_r$  from the measurements. However, for visco-elastic materials,  $h_r$  corresponds more to a contact loss depth, than a real measure of visco-plastic properties. Indeed, for a strain rate of  $0.50 \text{ s}^{-1}$ ,  $h_r$  is close to  $1 h_{max}$  (cf. fig. 3.13a). Therefore, if a reverse analysis were performed, it could lead to  $H$  being zero,  $C$  being zero and  $E$  being undefined (cf. fig. 3.12), which does not seem accurate. However, it should be noted that the previous method remains perfectly suitable for elasto-plastic indentations. First, only the dependency of hardness on the visco-elasto-plastic effect will be used. This provides a range of values for  $E$  and  $C$ . The results are shown in fig. 3.15.

In fig. 3.15a, the dependency of hardness on normalized cohesion is presented. These results are similar to those of fig. 3.12a, as  $h_r$  is directly related to normalized cohesion. They confirm that the more cohesion decreases, the more hardness decreases due to tangential flow. Furthermore, it shows that beyond a cohesion of  $0.20\text{-}0.40 E$ , there is no further increase in hardness. Indeed, for this cohesion, the plastic contribution to hardness becomes negligible. For a given  $E$ , the ratio  $\frac{H}{E}$  can be derived from  $H^{exp}$ , which corresponds to a certain  $\dot{\epsilon}$ . This allows to find the corresponding  $\frac{C}{E}$ . Since  $E$  is already known,  $C$  can be derived.

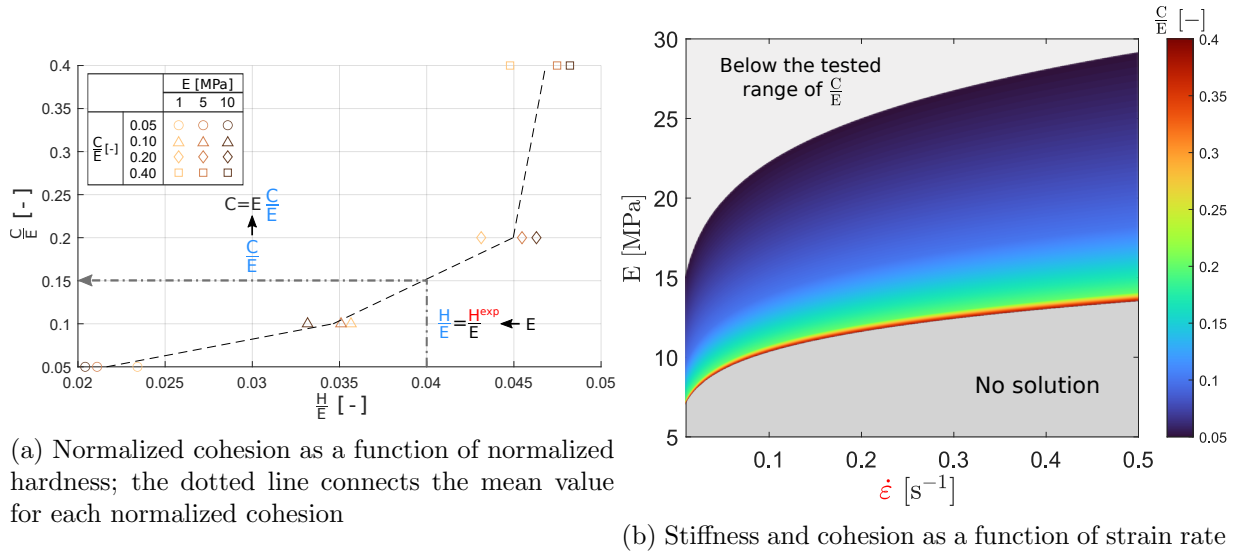


Figure 3.15: Reverse analysis procedure; ratios obtained numerically are highlighted in blue and values that can be extracted from measurements in red

Reverse analysis is performed using the results presented in fig. 3.13b and fig. 3.15a. In fig. 3.13b, the power law is used to obtain  $H_{exp}$  between each tested  $\dot{\epsilon}$ . In fig. 3.15a, for a given  $\frac{C}{E}$ , the mean  $\frac{H}{E}$  is calculated. Then, between each  $\frac{C}{E}$ , a linear interpolation is performed on the mean values. These interpolations are used to obtain the corresponding  $\frac{H}{E}$  between each simulated  $\frac{C}{E}$ . It should be noted that the results are extrapolated to higher stiffnesses, as the data points in fig. 3.15a overlap closely.

The results of the reverse analysis can be found in fig. 3.15b. The upper boundary of the surface delimits cohesions below 0.05  $E$ , which are outside the scope of this study. The lower boundary delimits the hardness that cannot be obtained for a given stiffness ( $C$  having no effect beyond 0.20-0.40  $E$ ). The non-unicity of the solution lies on this boundary. For a given  $\dot{\epsilon}$ , the more the stiffness increases, the more the normalized cohesion decreases. Indeed, to keep  $\dot{\epsilon}$  (i.e.  $H$ ) constant, the plastic contribution must reduce  $H$  as it is increased by the elastic contribution. For a given  $E$ , the more the  $\dot{\epsilon}$  increases, the more the normalized cohesion increases. This is due to a decrease in plasticity to increase  $H$  without a change in  $E$ .

One solution to fully identifying  $E$  and  $C$  is to determine  $E$  using a different method that does not involve plasticity (e.g. dynamic mechanical analysis). In this study, it is proposed to assume that stiffness is equal to the instantaneous stiffness measured by CSM. Indeed, for a sliding interface, the shear rate easily exceeds  $10^7 \text{ s}^{-1}$ , suggesting that stiffness is close to the instantaneous one. The distinction between plasticity and time-dependent stiffness is not easy. It is highly dependent on the chosen time scale. For this reason, both plasticity and time-dependent  $E$ , for a given strain rate, will be included in  $C$ . By taking  $E_0$  equal to 18 MPa, the constitutive relationship displayed in fig. 3.16 is obtained. For the tested strain rates, cohesion should therefore range between 0.050 and 0.105  $E$ .

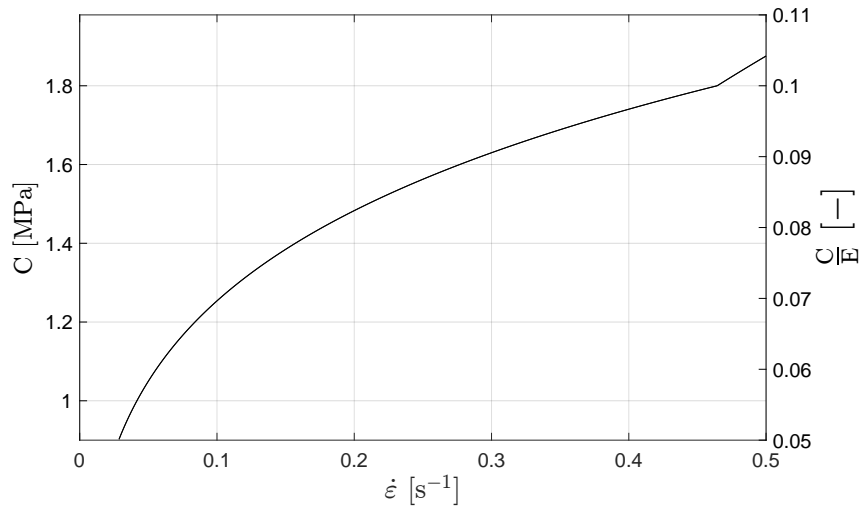


Figure 3.16: Results from the reverse analysis for  $E = E_0 = 18 \text{ MPa}$

### Highlights

- Numerically, stiffness is linearly proportional to hardness and has little effect on residual depth for a given normalized cohesion. Moreover, as cohesion decreases, hardness decreases and residual depth increases.
- Experimentally, for a carbon black filled IR, hardness depends on strain rate according to a power law with an exponent of 0.17, which is particularly high.
- Stiffness and cohesion values as a function of strain rate are obtained, giving, for a strain rate of  $0.4 \text{ s}^{-1}$ , a stiffness of  $18 \text{ MPa}$  and a cohesion of  $1.75 \text{ MPa}$ .

## Conclusion

A reverse analysis must satisfy several conditions. Firstly, the kinematics obtained numerically must be consistent with what is expected experimentally. This allows to reinforce the validity of the numerical parameters if the configuration changes. For the current model, the obtained normal and tangential flows are consistent with velocity field measurements from the literature. The second condition concerns the unicity of the solution. The objective was to evaluate the numerical  $E$  and  $C$  by using the experimental  $H$  and  $\frac{h_r}{h_{max}}$ . The use of these experimental parameters allows to compare simulations using plane-strain kinematics with three-dimensional experiments. It has been shown that the numerical parameters depend on the experimental ones in a non-asymptotic and strictly monotonic way (for  $C$  less than  $0.20\text{-}0.40 E$ ). Consequently, the unicity of the solution is satisfied for the range of tested cohesions.

The numerical model is able to simulate a wide range of behaviors, from elastic to elastoplastic indentations. The corresponding load-depth curves could be established. The results show that hardness depends on cohesion and stiffness. Indeed, if cohesion is decreasing, tangential flow is increasing. As a result, the volume of material under the tip is reduced and therefore the hardness. In addition, there is a close link between this tangential flow and residual depth. Finally, it has been shown that hardness is linearly proportional to the stiffness. The dependence between  $C$ ,  $E$ ,  $H$  and  $h_r$  was established. This made it possible to extend the validity of the study to lower and higher stiffnesses. For cohesion, the results are valid for  $C$  between  $0.05$  and  $0.20\text{-}0.40 E$ .

Several indentations were experimentally performed on the material. Measurements show that hardness depends on strain rate according to a power law. Based on the hardness measurements and the numerical study, a map of  $E$  and  $C$  as a function of  $\dot{\epsilon}$  was established. This shows that for a cohesion between 0.05 and 0.20-0.40  $E$ , stiffness should range from 7 to 29  $MPa$ . These measurements were supplemented by CSM tests which show that the influence of the gold coating is negligible and that the instantaneous stiffness is equal to 18  $MPa$ . By assuming that stiffness is equal to the instantaneous one, it was shown that  $C$  should range between 0.050 and 0.105  $E$ .





# Chapter 4

## Mixing mechanisms

The aim of this chapter is to present a more qualitative and comprehensive view of how minerals are mixed with the rubber material. Firstly, several types of mineral intake into the rubber material are identified and described in section 1. Then, the main features leading to mineral diffusion, different from those of the intake, are presented in section 2. Next, emphasis is placed on the long time scales of mineral diffusion in section 3. In particular, the different stages of diffusion will be shown, and depending on the model parameters, a steady state (i.e. constant shear rate) may or may not be observed. A special transient case will be introduced in section 4. Finally, several observations after wear tests on the tribometer are presented in section 5. For all the simulations, the corresponding numerical parameters can be found in table 2.1 by referring to the superscript # and available animations are indicated by a ►.

### 1 Intake

The mechanisms at the very beginning of sliding differ from long-term mechanisms (i.e. diffusion ones). Indeed, they correspond more to a progressive reorganization of the mineral layer, leading to an initial mixture of rubber and minerals. This is different from the vision of a stochastic process, as proposed in the diffusion framework. This stage must therefore be studied separately and will determine the rate of mineral intake into the rubber material. In the current simulations, a relatively small thickness for the initial mineral layer is used (100 times less than in the experimental configuration), and all minerals are rapidly incorporated into the rubber. Consequently, this stage corresponds mainly to the onset of sliding. However, with a more realistic thickness (compared with the experimental configuration), this stage would occur in parallel to the diffusion of deeper minerals, and is therefore important for understanding the overall diffusion. Moreover, in some simulations, the mineral intake is so slow that some minerals have already completely diffused, while others are just beginning to do so. Finally, certain phenomena, such as the formation of agglomerates, are largely dictated by the mode of intake.

#### 1.1 Plowing

One of the most prevalent intake modes for the tested configurations is a plowing-type mechanism, as shown in fig. 4.1. The snapshots show a higher quantity of minerals than used in other simulations (twice more), but the comments that follow remain valid for a lower quantity. Due to the size distribution of the minerals, shape and stiffness, the mineral layer is relatively sealed and has a significant shear strength compared to the rubber layer. The term sealed refers here to the ability of rubber particles to penetrate inside the mineral phase. For these reasons,

local reorganization of the mineral layer tends to form a roughness on the surface of the rubber layer (fig. 4.1a). As the asperities increase in size, the shear stress progressively increases on the mineral layer, which becomes increasingly deformed (fig. 4.1b). At some point, the deformation becomes so severe that an agglomerate of minerals is embedded (fig. 4.1c). Depending on the quantity of minerals, this process is then repeated until all the minerals are incorporated into the rubber material.

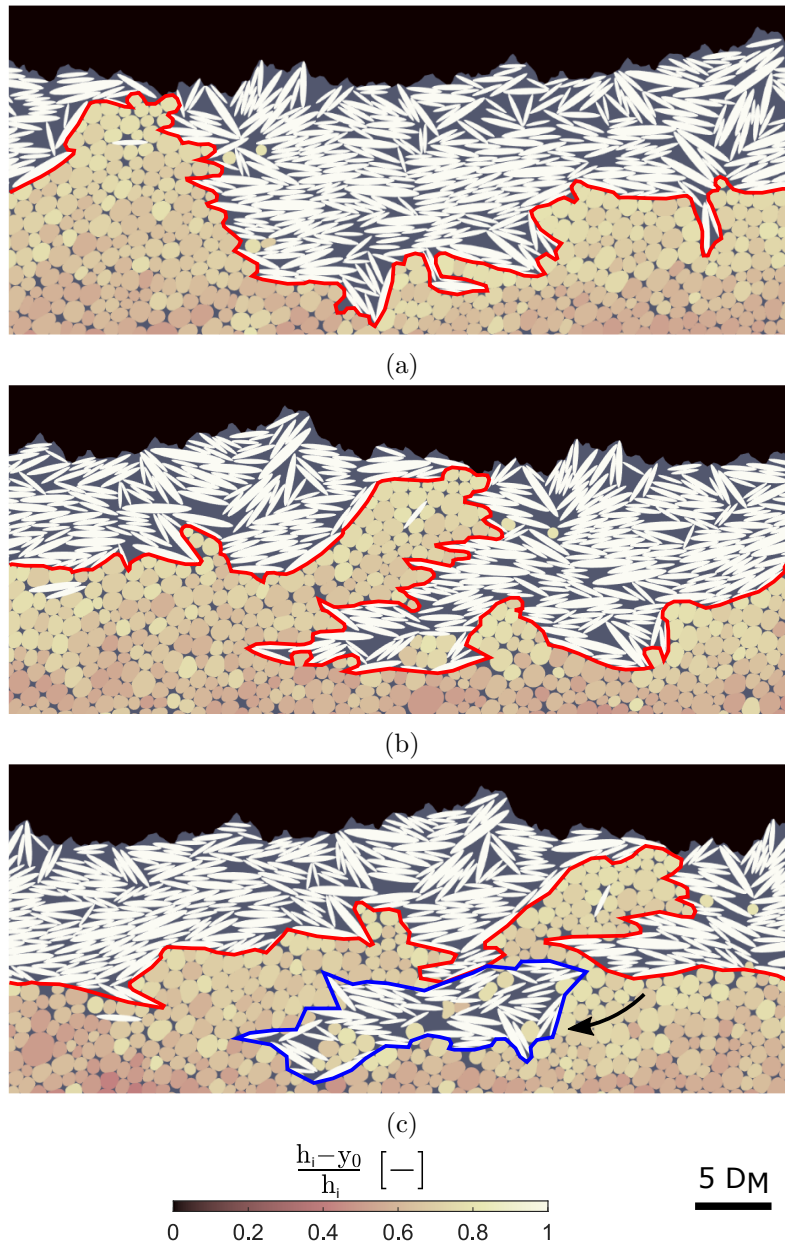


Figure 4.1: Different stages of the steady plowing mechanism<sup>#32</sup>; the color field corresponds only to the rubber particles, and the color of the minerals and the road-like surface is arbitrary;  $D_M$  corresponds to the mean equivalent diameter of the minerals,  $y_0$  to the initial depth of each centroid and  $h_i$  to the thickness of the interfacial layer (►)

The above mechanism requires a relatively sealed mineral layer. This depends on several parameters such as contact pressure, but also on the chaotic nature of such a simulation (one rubber particle position at a given time). A slightly different example is presented in fig. 4.2. In this example, only the quantity of minerals has changed compared to the previous example (half the previous quantity of minerals). It should be noted, however, that the difference does

not come from this quantity but rather from the statistical variation from one simulation to another. At the beginning, as before, a roughness is formed on the rubber surface (fig. 4.2a). Depending on how local reorganization occurs in the mineral layer, the solid fraction of this layer can be particularly low (fig. 4.2b). Firstly, this leads to a lower geometric interlocking and therefore a lower shear strength. Secondly, it leads to the incorporation of rubber particles, which further weakens the strength of the mineral layer. As a result, the mineral layer is too weak to form a highly deformed agglomerate and is rapidly dislocated (fig. 4.2c). This process tends to generate fewer mineral agglomerates. This mechanism is qualified as unsteady in the sense that a mineral agglomerate is also formed in the present case, but persists over shorter times than in the previous case.

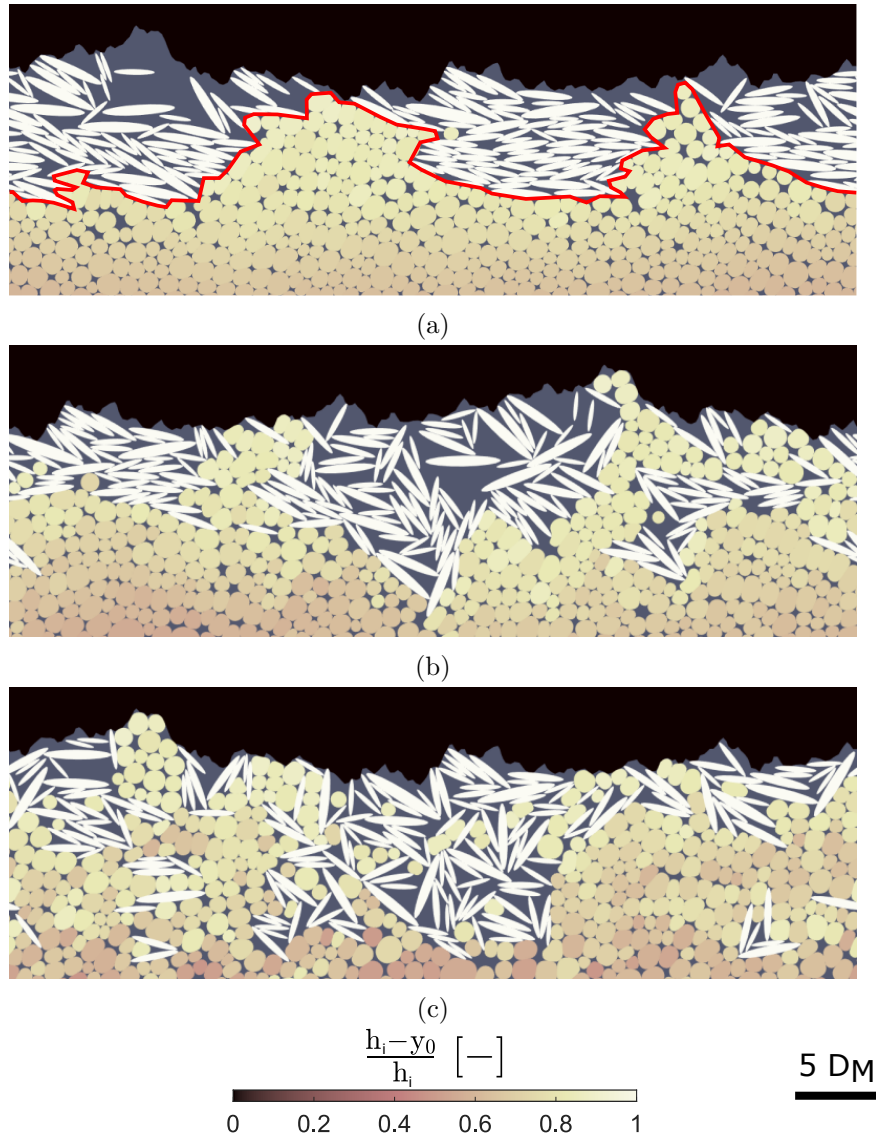


Figure 4.2: Different stages of the unsteady plowing mechanism<sup>#11</sup>; the color field corresponds only to the rubber particles, and the color of the minerals and the road-like surface is arbitrary;  $D_M$  corresponds to the mean equivalent diameter of the minerals,  $y_0$  to the initial depth of each centroid and  $h_i$  to the thickness of the interfacial layer (►)

The transition between the two previous mechanisms depends notably on the contact force between the minerals. Investigations were carried out by replacing the cohesive model between rubber and minerals by a friction law (with  $\mu_{rock}^{rubber} = 0.4$ ). The influence on intake of the coefficient of friction between rock-like materials ( $\mu_{rock}^{rock}$  for minerals and road-like surface) is

studied and presented in fig. 4.3. For a low  $\mu_{rock}^{rock}$  of 0.1, unsteady behavior is observed (fig. 4.3a). The strength of the agglomerate is low, and the rubber material fill the porosities. For a  $\mu_{rock}^{rock}$  equal to 0.2, a mineral drag begins to be observed (fig. 4.3b). However, the strength is too low and the drag remains at shallow depths. For a  $\mu_{rock}^{rock}$  of 0.3, results similar to the previous steady plowing mechanism are observed (fig. 4.3c). The mineral drag penetrates deep into the rubber and mineral agglomerates are incorporated until there are no minerals left on the surface. For a  $\mu_{rock}^{rock}$  greater than 0.4, agglomerate strength is too high and cannot be deformed (fig. 4.3d). In summary, the formation of a drag is the result of a mineral agglomerate that is strong enough to resist to mineral flow, and weak enough to allow internal reorganization. In practice, this may depend on parameters such as humidity.

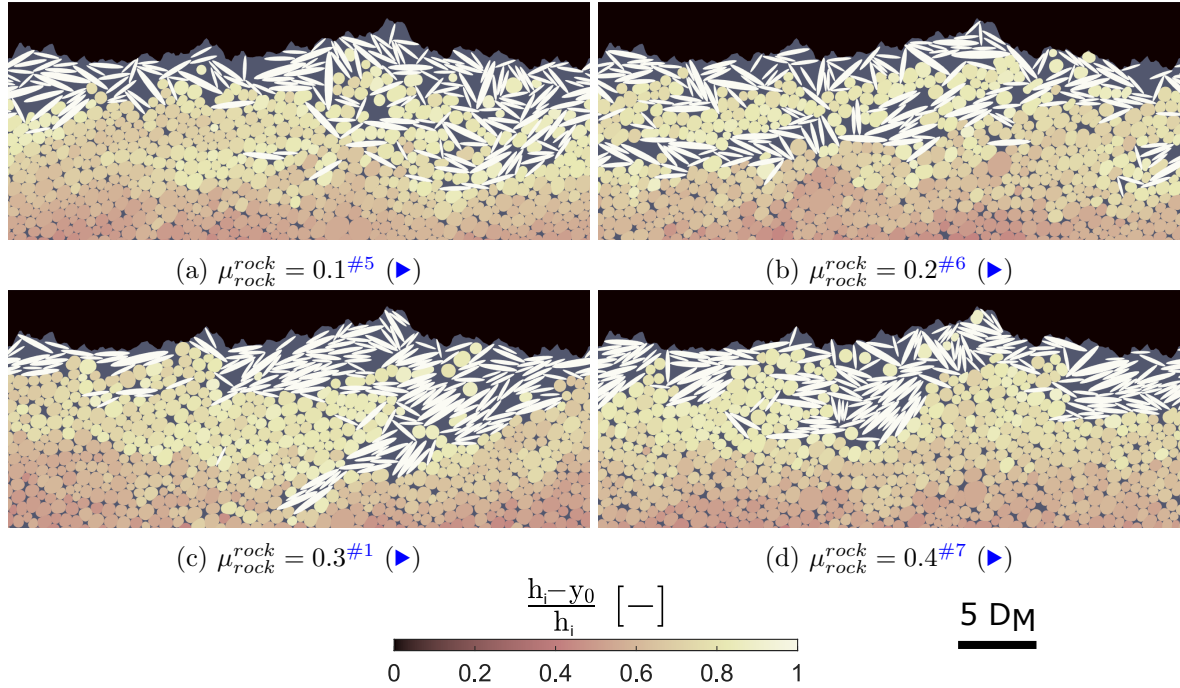


Figure 4.3: Intake according to  $\mu_{rock}^{rock}$  for a sliding distance of  $317 D_M$  and  $\mu_{rock}^{rubber} = 0.4$ ; the color corresponds only to the rubber particles, and the color of the minerals and the road-like surface is arbitrary;  $D_M$  corresponds to the mean equivalent diameter of the minerals,  $y_0$  to the initial depth of each centroid and  $h_i$  to the thickness of the interfacial layer

## 1.2 Abrasion

The plowing mechanism requires local reorganization of the mineral layer, which may not be possible if contact pressure is too high. It also requires a mineral layer that is strong enough to withstand shearing, but not too strong to allow deformation. If the above points are not respected, this results in an abrasion mechanism as shown in fig. 4.4. Due to a slight reorganization of the mineral layer, shear stress is transmitted by some minerals that have partially penetrated into the rubber material, as well as by the cohesive forces between rubber and minerals (fig. 4.4a). As the minerals are mainly oriented along the shear axis, they exert a significant localized shear force on the rubber material (fig. 4.4b). Finally, the friction force between minerals is lower than the transmitted shear force, and mineral agglomerates are incorporated as soon as the shear axis coincides with a mineral boundary (fig. 4.4c).



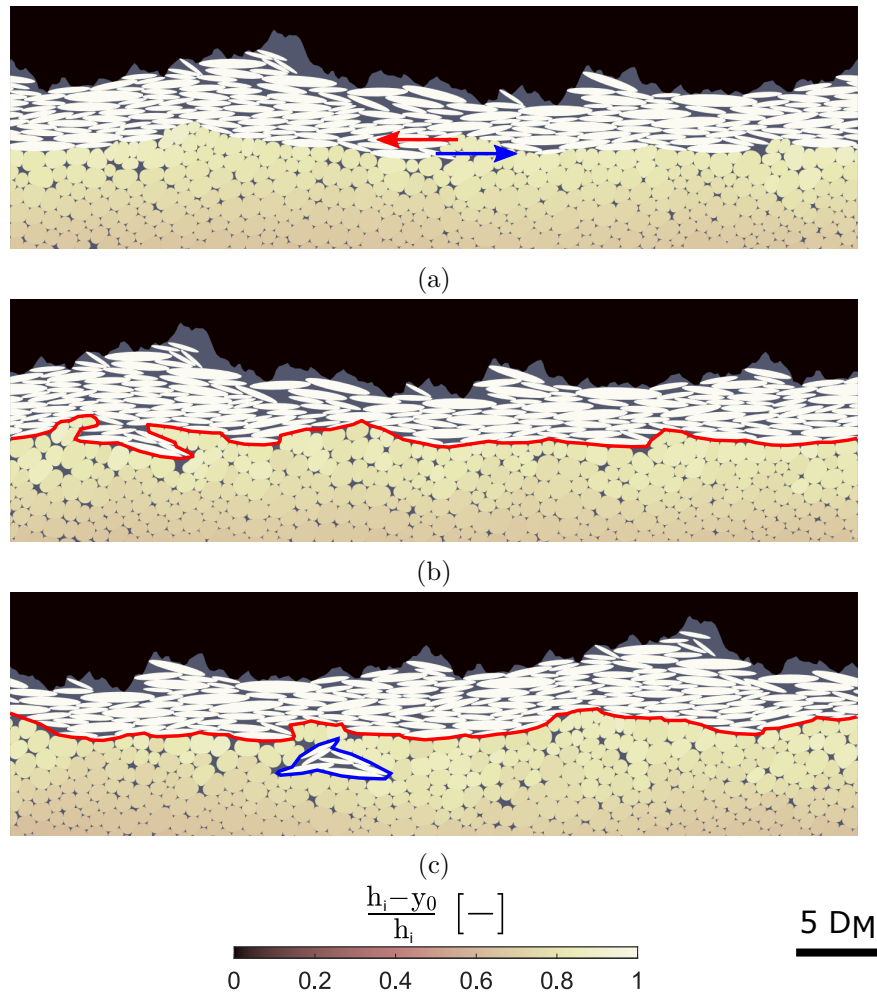


Figure 4.4: Different stages of the abrasion mechanism<sup>#26</sup>; the color field corresponds only to the rubber particles, and the color of the minerals and the road-like surface is arbitrary;  $D_M$  corresponds to the mean equivalent diameter of the minerals,  $y_0$  to the initial depth of each centroid and  $h_i$  to the thickness of the interfacial layer (►)

### 1.3 Fracture

The last mechanism is specific to highly cohesive rubber materials for a constant interfacial layer thickness. If cohesion is significant, it is more difficult for the rubber material to dissipate the energy induced by shear, leading to cyclic phenomena of energy storage and release. This is comparable to crack-opening as illustrated in fig. 4.5. Firstly, a reorganization of the mineral layer also occurs, but over very short times as the higher shear forces tend to dislocate it (fig. 4.5a). Energy can be stored until the stress exceeds the cohesion value. In this case, the link is removed and a crack opens (fig. 4.5b). This leads to a chain reaction due to the weakening of a shear band (fig. 4.5c). This process tends to generate significant intake and mixing of the material over much greater depths. It should be noted that these cracking mechanisms are mainly observed during intake, and to a much lesser extent during diffusion.

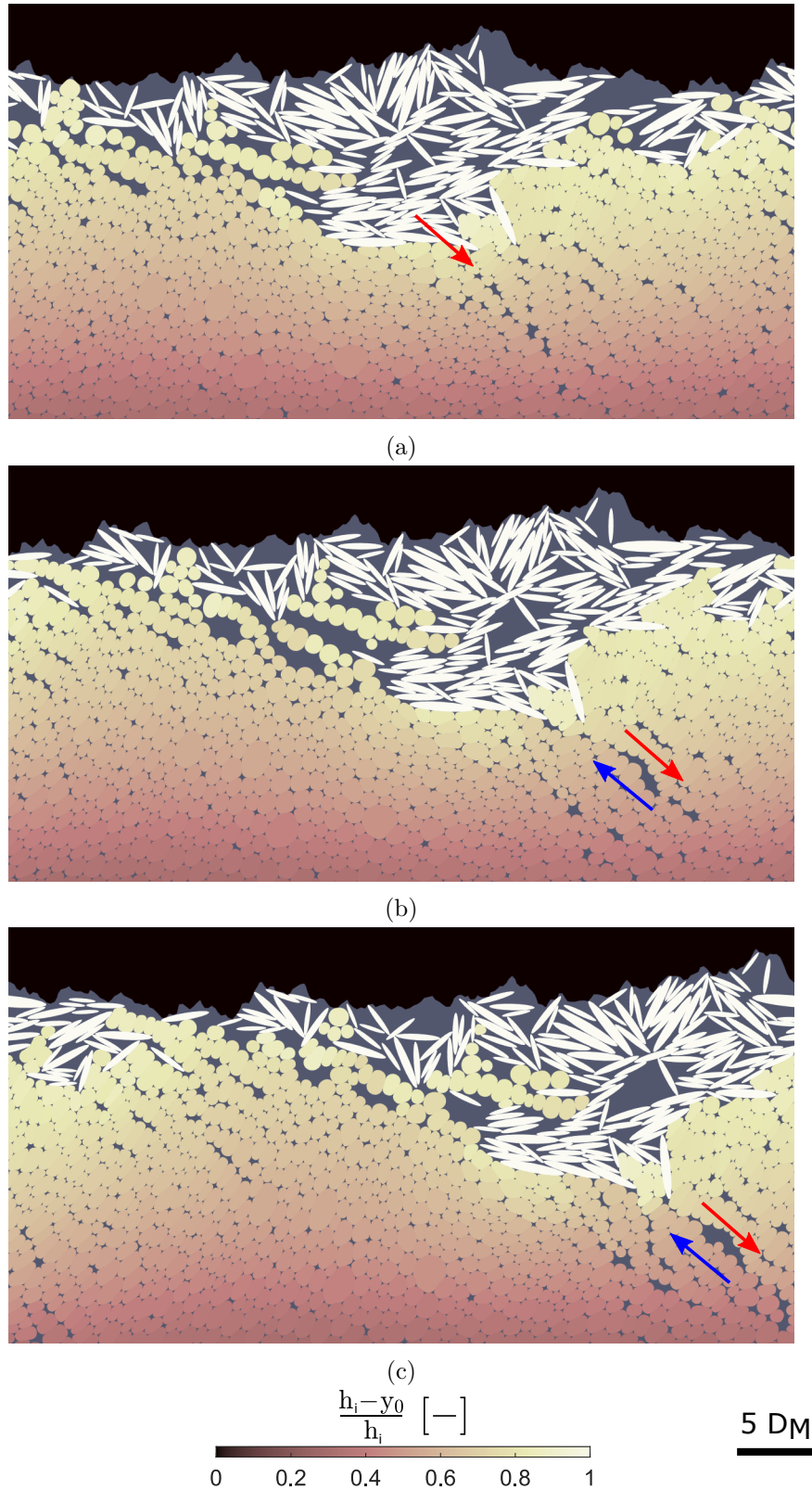


Figure 4.5: Different stages for the fracture mechanism<sup>#42</sup>; the color field corresponds only to the rubber particles, and the color of the minerals and the road-like surface is arbitrary;  $D_M$  corresponds to the mean equivalent diameter of the minerals,  $y_0$  to the initial depth of each centroid and  $h_i$  to the thickness of the interfacial layer (►)



### Highlights

- Several penetration modes are observed, depending on the configuration.
- Plowing is the most common mode, as it results from the higher shear strength of the initial mineral layer compared to the rubber one.
- An abrasion mode occurs if the reorganization within the mineral layer is restricted, thus limiting the formation of roughness on the rubber surface.
- A fracture mode appears in the case of a highly cohesive rubber, where elastic energy can be stored significantly until it is released, resulting in chain reaction due to the weakening of a shear band (similar to crack propagation).

## 2 Diffusion

### 2.1 Overview

When the minerals are sufficiently embedded in the interfacial layer, the underlying mechanisms are different from those observed previously during the intake. For the sake of simplicity, the example of one simulation<sup>#11</sup> (►) is taken, with the standard parameters already discussed in the description of the numerical model. Some of the main results concerning diffusion are presented in fig. 4.6.

First of all, the trajectory of a single mineral (fig. 4.6a) can be examined and reveals a highly erratic trajectory, with a position moving towards the road-like surface or away from it. It can also be noted that for a low sliding distance ( $< 200 D_M$ ), there is a fast and continuous decrease in position. This suggests a change in the mechanisms driving mineral migration. Now, if the trajectories of all the minerals are tracked (fig. 4.6b), it can be seen that they follow a certain tendency to go deeper into the rubber material. This leads to a homogenization of mineral fraction ( $\varphi$ ) in the interfacial layer as a function of time (fig. 4.6c). It may also be noted that, at the beginning, there is a kind of mineral reservoir effect, with a higher concentration near the surface, decreasing over longer times than the evolution of the front. This is attributed to intake mechanisms that differ from those occurring at greater depths. In addition, there is probably a maximum density of minerals, which requires sufficient front progression for the remaining minerals to begin diffusing. This density depends on several parameters and will be discussed later. The evolution of concentration along depth follows a Gaussian distribution that tends to flatten out with sliding distance (fig. 4.6d).

These results are very similar to those obtained with a random walk (fig. 2.8) or using the second law of Fick (fig. 2.9). Indeed, at first, the behavior appears to be stochastic at the scale of a single mineral, then turns out to be deterministic when looking at all the minerals. Moreover, a Gaussian distribution flattening over time is obtained. This reinforces the idea of using diffusion-related tools, even though there is no notion of chemical potential. In addition, it allows the model to be seen as evolving according to a law of Fick. A link can thus be made between diffusion and the gradient (in space and time) of the concentration.

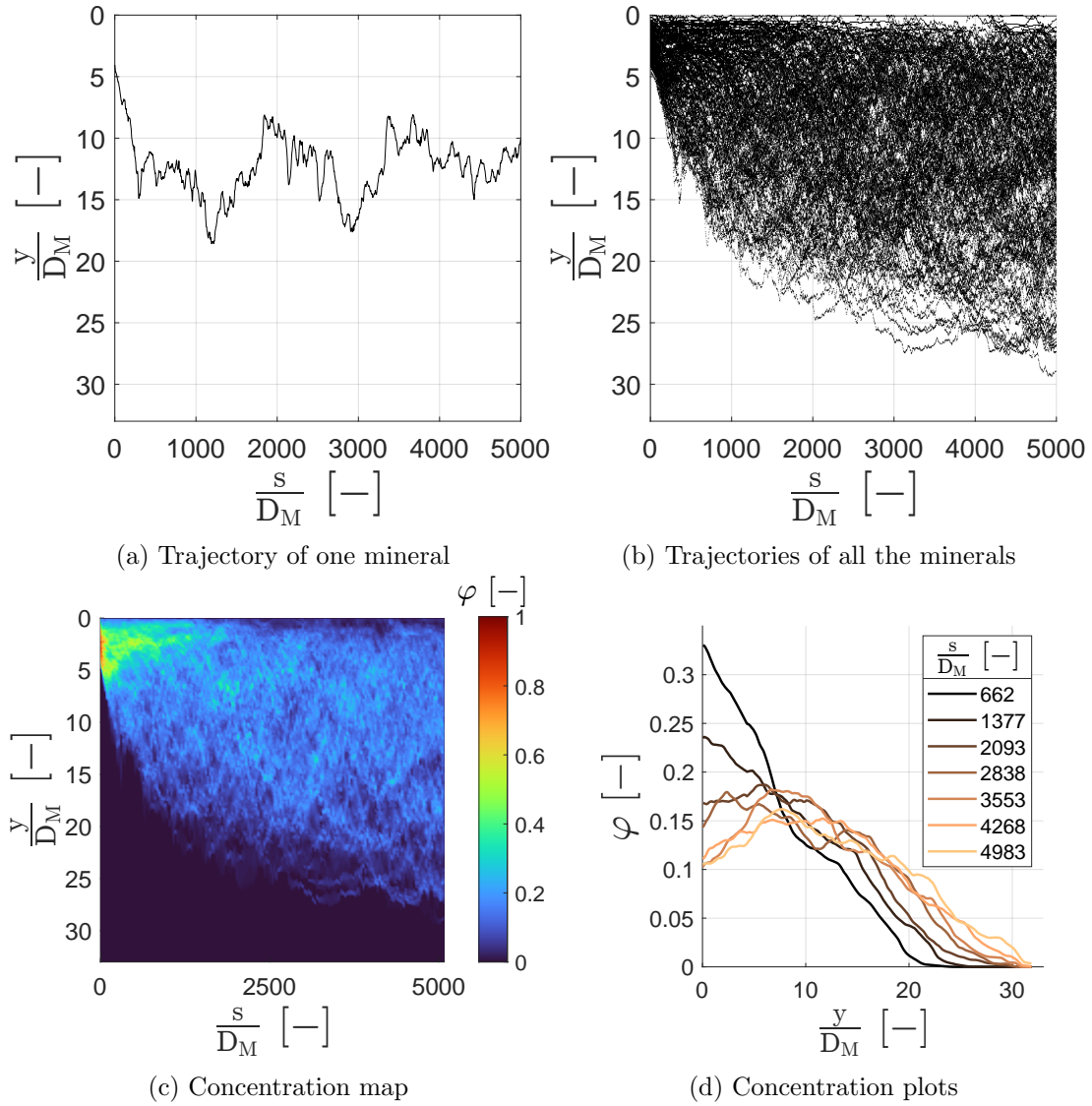


Figure 4.6: Main results about mineral diffusion;  $y$  is the depth (i.e. transverse coordinate) with 0 corresponding to the mean line of the road-like surface;  $D_M$  is the mean equivalent diameter of the minerals;  $s$  is the sliding distance and  $\varphi$  is the mineral fraction

## 2.2 Green-Kubo framework

As a reminder, the longitudinal velocity ( $V_L$ ) corresponds to the velocity projection in the sliding direction, and the transverse velocity ( $V_T$ ) corresponds to the velocity projection in the orthogonal direction to the sliding. Mineral diffusion (i.e. transverse displacement) is caused by transverse velocity which is displayed for the whole interfacial layer and for 6 successive steps in fig. 4.7.

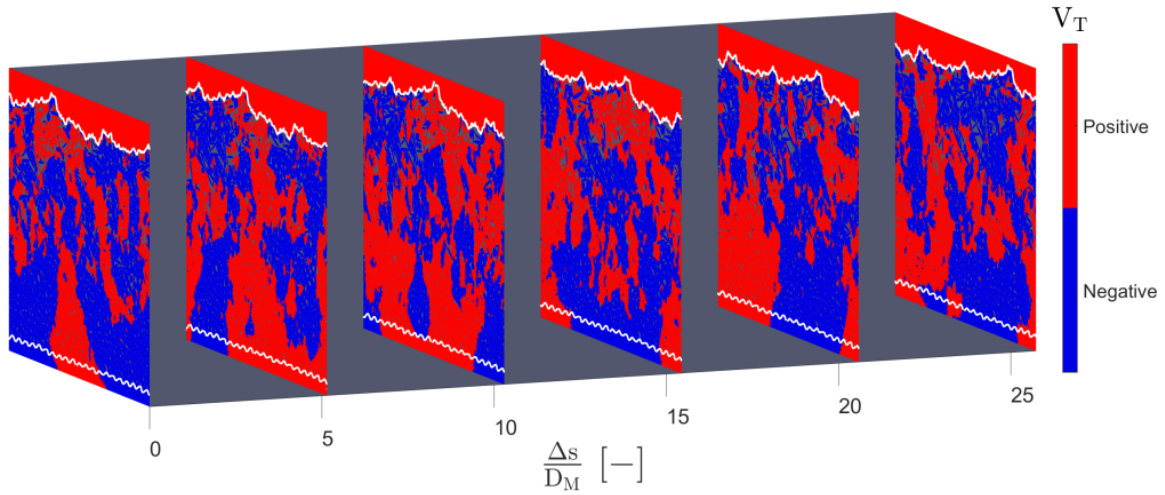


Figure 4.7: Transverse velocity during sliding (positive means towards the road-like surface and negative in the opposite direction)

The transverse velocity is highly inhomogeneous in both longitudinal and transverse directions. Moreover, this velocity is also short-lived, lasting only for a sliding distance of a few  $D_M$ . This clearly demonstrates the stochastic nature of mineral displacement, with erratic variations at a high frequency (compared to the scale of diffusion). Since the enclosed volume is constant, the average transverse velocity is zero. This means that a particle is shifted in one direction (positive or negative) if another particle is shifted in the opposite direction. The fact that transverse velocity fluctuates around 0 can be underlined by looking at the velocity of one mineral fig. 4.8.

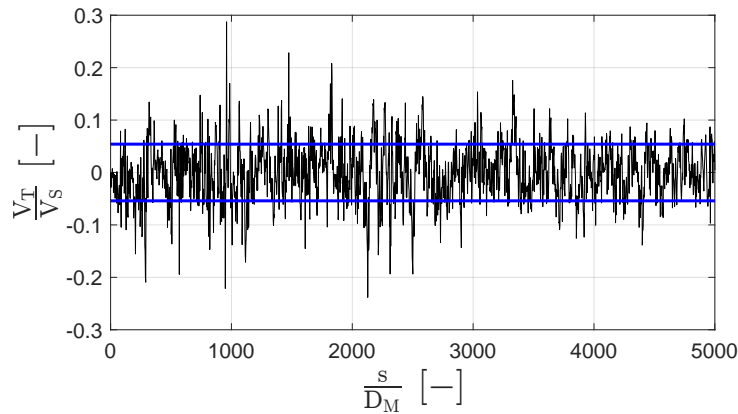


Figure 4.8: Transverse velocity of one mineral  $\pm$  one standard deviation

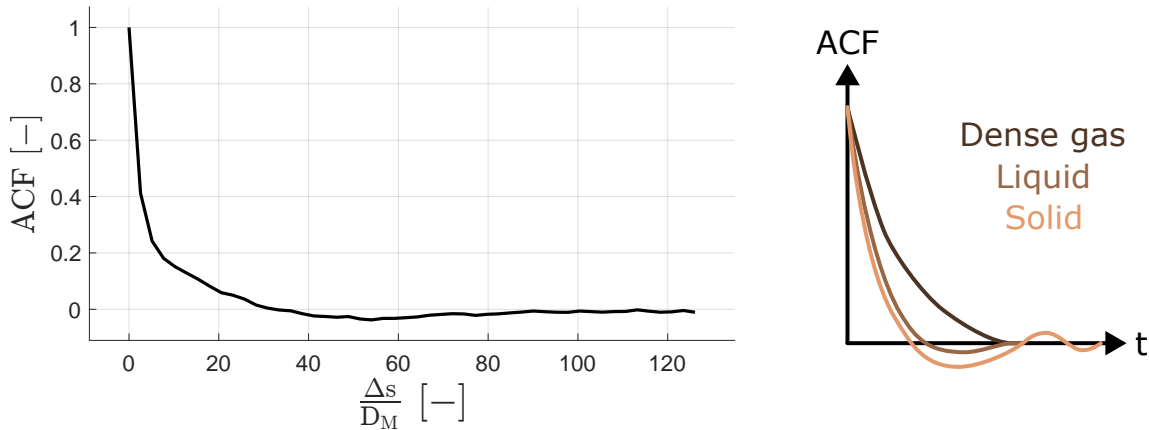
Like the position of a mineral, variations in transverse velocity are highly erratic and can be positive or negative. Moreover, the amplitude of these variations remains low compared to the sliding velocity (only a few %). The following method is based on the one proposed in [Macauley and Rognon, 2019]. Variations can be characterized by the standard deviation, which gives a velocity called velocity fluctuation ( $\Delta V_T$ ). It is computed over a certain time window discretized into  $N$  time steps, as specified in eq. (4.1).

$$\Delta V_T = \sqrt{\frac{\sum_{m=1}^M \sum_{i=1}^N \left( V_T^m(t^i) - \bar{V}_T \right)^2}{MN - 1}} \quad (4.1)$$

with  $\Delta V_T$  the velocity fluctuation,  $M$  the number of minerals,  $N$  the number of time steps,  $V_T^m$  the transverse velocity of a given mineral,  $t^i$  the corresponding time and  $\overline{V_T}$  the average transverse velocity (over time and minerals). In addition, the system drift is removed for this computation and the following (i.e. the average  $V_T$  over the minerals at each  $t^i$ ). If  $\Delta V_T$  were computed for the previous example (with one mineral), it would correspond to the blue lines in fig. 4.8. The computation can be performed for different time intervals, which will be specified in the corresponding sections. This velocity represents a characteristic velocity for each event, averaged over time and for all minerals. Note that as  $\overline{V_T}$  is close to 0, the standard deviation is close to the root mean square. To evaluate diffusion, which can to a lesser extent be reduced to a distance, this velocity must be associated with a holding time. This can be achieved using the autocorrelation function of the transverse velocity. It is computed as specified in eq. (4.2).

$$ACF(\Delta t) = \frac{1}{M} \sum_{m=1}^M \frac{\sum_{i=1}^N V_T^m(t_0^i) V_T^m(t_0^i + \Delta t)}{\sum_{i=1}^N V_T^m(t_0^i) V_T^m(t_0^i)} \quad (4.2)$$

with  $ACF$  the autocorrelation function of the transverse velocity,  $\Delta t$  the lag time,  $M$  the number of minerals,  $N$  the number of time steps,  $V_T^m$  the transverse velocity of a given mineral and  $t_0^i$  a reference time. In this work, time will most often be expressed as an absolute (s) or relative ( $\Delta s$ ) sliding distance. While  $\Delta V_T$  is a scalar,  $ACF$  depends on a lag time. It represents the correlation between velocity at a given  $t_0^i$  and velocity at  $t_0^i + \Delta t$ . For the simulation of this section, the  $ACF$  is shown in fig. 4.9a, complete with an illustration of the  $ACF$  for different states of matter in fig. 4.9b.



(a) For the interfacial layer

(b) For different states of matter

Figure 4.9: Autocorrelation function of the transverse velocity

This function generally shows an exponential decay. It provides information on the state of the interfacial layer. Indeed, a gas tends to give a positive  $ACF$  with a slow decay, a fluid gives a faster decay with a small oscillation around 0 and a solid gives an even faster decay with several oscillations around 0, as illustrated in fig. 4.9b [Ghosh and Krishnamurthy, 2018]. This tends to demonstrate that the interfacial layer remains closer to a fluid with a decay similar to a fluid, as shown in fig. 4.9a. Some parameters influence the  $ACF$ . For example, the more cohesion increases, the closer the interfacial layer is to a solid state. The  $ACF$  will not be discussed further, but can be found in appendix D for all simulations. The characteristic holding time of  $\Delta V_T$ , called the persistence ( $\Psi$ ), corresponds to the integral of the  $ACF$ , which can be computed for a finite time due to the exponential decay. Previously, it was shown that transverse velocity evolution corresponds to local events of short duration relative to the total duration of the

sliding (fig. 4.7). While velocity fluctuation describes the magnitude of these events, persistence describes their duration. It is computed as shown in eq. (4.3).

$$\Psi = \frac{\lambda}{V_S} = \int_0^\infty ACF d\Delta t \quad (4.3)$$

with  $\Psi$  the time persistence,  $\lambda$  the persistence brought to an equivalent sliding distance,  $V_S$  the sliding velocity,  $ACF$  the autocorrelation function of the transverse velocity and  $\Delta t$  the lag time. As  $\Delta V_T$ , this allows the results to be reduced to a single scalar. These two parameters can be linked to the diffusion coefficient using the Green-Kubo framework, as written in eq. (4.4).

$$D = \Delta V_T^2 \Psi \quad (4.4)$$

with  $D$  the diffusion coefficient,  $\Delta V_T$  the velocity fluctuation and  $\Psi$  the time persistence. The obtained diffusion coefficient is equivalent to what could be obtained using the framework of Einstein (eq. (4.4) can be derived from the formula of Einstein). A comparison of the diffusion coefficient obtained with these 2 methods is given in appendix A. The Green-Kubo framework gives much more information on mechanisms in the interfacial layer, but is more subject to statistical noise. The Green-Kubo framework will therefore be used if a steady state is found, otherwise, the Einstein framework will be preferred.

## 2.3 Mechanisms

A simplistic illustration of overtaking mechanisms is given in fig. 4.10.

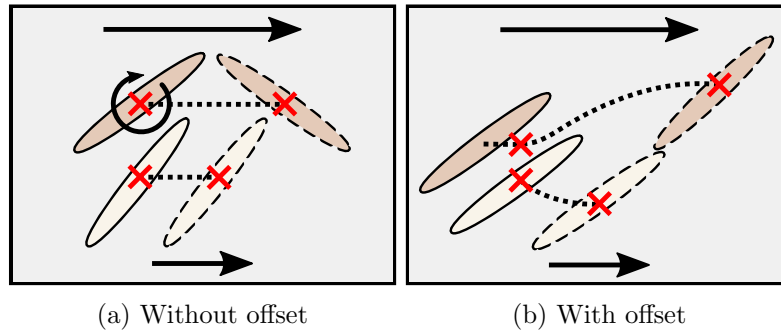


Figure 4.10: Illustration of overtaking mechanisms

Due to the shear rate, the minerals in the interfacial layer have a relative velocity between them, which will induce numerous contacts as the minerals must overtake (cf. fig. 2.10). Two overtaking modes have been observed. The first is due to the non-circular shape of the minerals. Indeed, the minerals are continuously rotating and can therefore cross each other without any offset (fig. 4.10a). This mode will be ignored as it has no influence on diffusion. The second mode is a more classical mechanism, as might be obtained with DEM, with a monotonic displacement of the two minerals (fig. 4.10b). Due to several effects (depending on the forces applied to the mineral), the offset may be greater than the mineral diameter. In addition, these two modes can be combined, resulting in a partial offset.

Each variation of  $V_T$  corresponds to a contact between 2 minerals (mineral agglomerates to be more specific) at a frequency determined by the shear rate. As previously mentioned, this velocity can be reduced to a velocity fluctuation ( $\Delta V_T$ ) and a persistence time ( $\Psi$ ). The aim is then to understand how parameters such as stiffness or cohesion influence  $\Delta V_T$ ,  $\Psi$ , and consequently  $D$ .

## 2.4 Orientation

The orientation of the minerals can be looked at, in particular to get a first idea of the anisotropy of the mixed layer. The distribution of orientations is shown fig. 4.11. Orientation corresponds to the angle between the major axis of a mineral and the sliding axis, and by considering a symmetry for a  $180^\circ$  rotation. It can be seen that the orientation is relatively evenly distributed (fig. 4.11a), with a preferred orientation along the sliding axis (fig. 4.11b). This is explained by the fact that the further the orientation is from 0, the greater the velocity differential exerted on a mineral (as the major axis projection along the sliding axis becomes greater), and therefore the more unstable the position becomes.

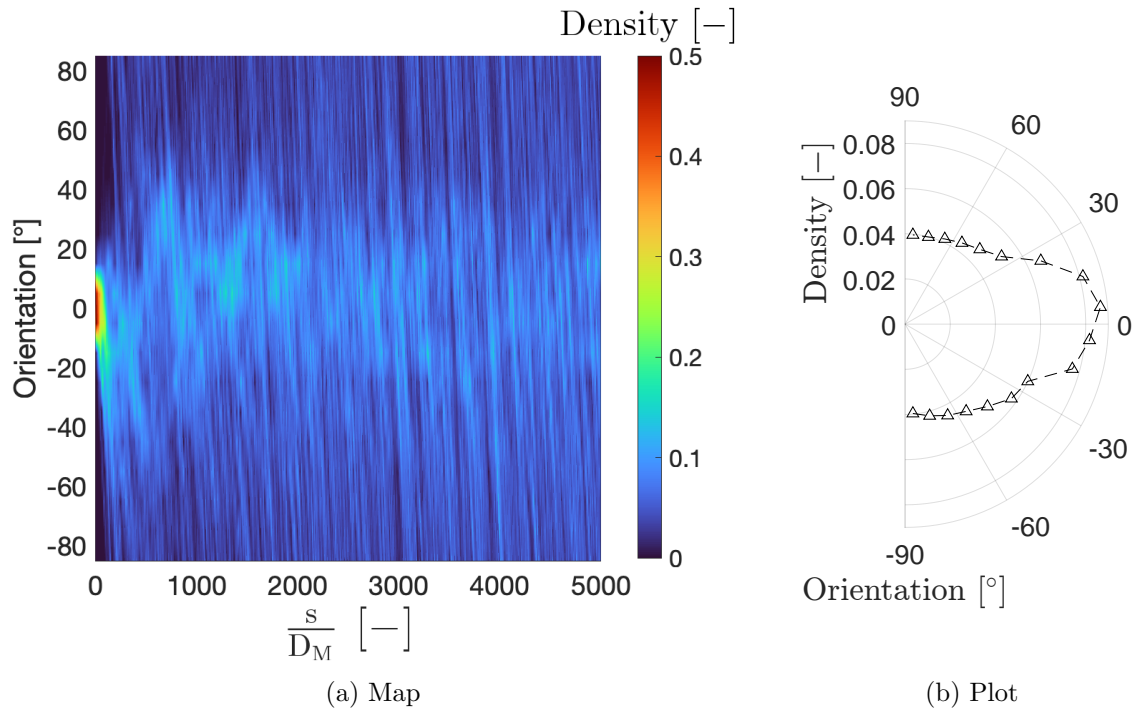


Figure 4.11: Orientation of minerals during sliding; the plot corresponds to the average orientation between a sliding distance of 2000 and 3000  $D_M$

### Highlights

- Mineral migration is similar to a stochastic and a diffusive process, due to repeated contacts between minerals.
- The velocity fluctuation ( $\Delta V_T$ ) corresponds to the standard deviation of the transverse velocity. It represents the velocity variation resulting from each contact.
- Persistence ( $\Psi$  or  $\lambda$  if expressed in terms of sliding distance) corresponds to the integral of the autocorrelation function of the transverse velocity. It represents a characteristic duration of each contact.
- A diffusion coefficient ( $D$ ) can be derived from velocity fluctuation and persistence.



### 3 Long time scales

This section will focus on the evolution of diffusion over long time scales. The notion of long time scales here refers to a duration greater than the duration of the steady state, as discussed below. It is indeed interesting to understand whether minerals are diffusing until they reach a homogeneous state throughout the whole interfacial layer. Some of the main results describing diffusion, including long time scales, are presented in fig. 4.12.

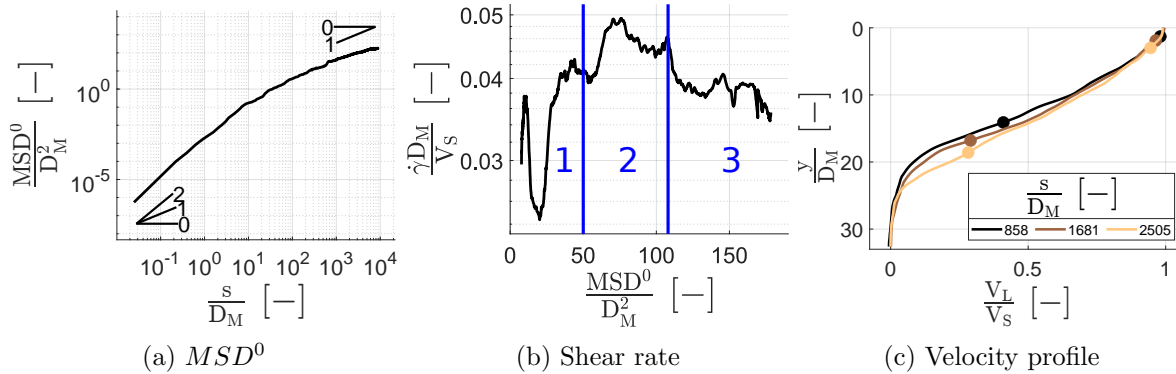


Figure 4.12: Diffusion for long sliding distance;  $MSD^0$  corresponds to the mean square displacement,  $V_L$  to the longitudinal velocity and the markers on the velocity profile to the mixed layer (respectively 90% and 10% of minerals below the corresponding depths)

The mixed layer corresponds to the layer containing rubber and minerals. It is delimited by the depths at which respectively 90% and 10% of the minerals are located below (and the layer therefore contains 80% of the minerals). This choice is made to limit the effect of the diffusion of a few minerals, not necessarily representative of the whole mixed layer. The shear rate  $\dot{\gamma}$  used hereafter corresponds to the shear rate of this layer. For long sliding distances, diffusion tends towards 0. Indeed, the instantaneous diffusion coefficient corresponds to the slope of the mean square displacement ( $MSD^0$ ). This slope becomes null for a long sliding distance, as shown in fig. 4.12a. This phenomenon can be assessed by looking at the shear rate in the mixed layer fig. 4.12b, which can be divided into 3 main stages.

1. At the beginning of sliding ( $MSD^0 \leq 50 D_M^2$ ), the minerals diffuse inside the layer with a non-zero velocity. This can be observed in fig. 4.12c (velocity profiles at the beginning of diffusion) where the mixed layer is progressively diffusing in this layer. The shear rate increases, as the minerals are first contained in a thin layer that can hardly undergo shearing.
2. The mixed layer has diffused sufficiently into the layer with a non-zero velocity to tend towards a constant shear rate (with some fluctuations). The shear rate of this layer and the mixed layer become close. This stage corresponds to what will be called the steady state.
3. The minerals reach the zone with a zero velocity. In a process similar to that observed during intake, they transmit a shear stress to the lower layer, leading to a progressive transmission of velocity at deeper depths. Consequently, the shear rate is also decreasing.

These different stages should also be observed in a more realistic case, with a greater quantity of minerals, a greater interfacial layer thickness and a greater sliding distance. Indeed, a greater quantity of minerals increases the thickness of the initial layer with non-zero velocity. As a result, the stage where minerals diffuse without any change in shear rate should also be observed over significant periods of time.



The slowdown in diffusion is initially linked to the decreasing shear rate. However, the fact that diffusion tends towards 0 is linked to a domain size effect (minerals reach the rubber bulk unable to incorporate minerals). The velocity fluctuation is also modified, as shown by fig. 4.13.

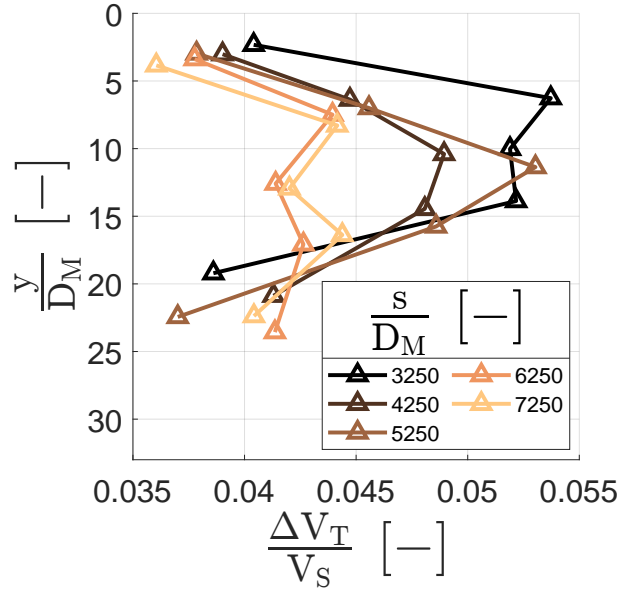


Figure 4.13: Velocity fluctuation for long sliding distance

The minerals are divided into 5 groups to determine  $\Delta V_T$  as a function of depth. Firstly, as the shear rate decreases,  $\Delta V_T$  also decreases, the 2 being linearly proportional [Kharel and Rognon, 2018]. It can also be seen that  $\Delta V_T$  is not constant along depth. This tends to show that the more minerals are localized in a thin layer, the more  $\Delta V_T$  increases. If the mixed layer is sufficiently scattered,  $\Delta V_T$  becomes constant along depth, except near the road-like surface. Over long time scales, this modification will also slow down diffusion.

The long time scale corresponds to the third stage (cf. fig. 4.12b) and will be ignored in the rest of this work for several reasons. Firstly, for computation time reasons, as this regime is reached for significant sliding distances. In addition, it requires a thick interfacial layer, without which the minerals reach the limits of the discrete medium. As the current model does not model rubber degradation, this effect of boundary conditions should be avoided. Moreover, increasing the thickness of this layer would further increase computation times. Finally, the shear rate is no longer constant during this stage, which makes the analysis more complex. Indeed, the various quantities extracted from the model cannot easily be averaged over time, and are therefore subject to significant statistical noise. In addition, this makes analysis for a given configuration difficult, as does comparison between several configurations. Indeed, this comparison requires a comparable state, which can hardly be defined in the case of a transient regime. However, a special case of transient regime will be studied below.

## Highlights

- Concerning the different stages of diffusion within a simulation, there is first a fast progression of the diffusion front and an increase in layer thickness with a non-zero velocity.
- Then, diffusion occurs within this layer, with a shear rate that varies around a mean value, and can therefore be considered constant (i.e. steady-state diffusion).
- Finally, once the minerals have diffused sufficiently, there is a slow evolution of the diffusion front, increasing the thickness of the layer with a non-zero velocity and thus decreasing the shear rate.

## 4 Transient diffusion

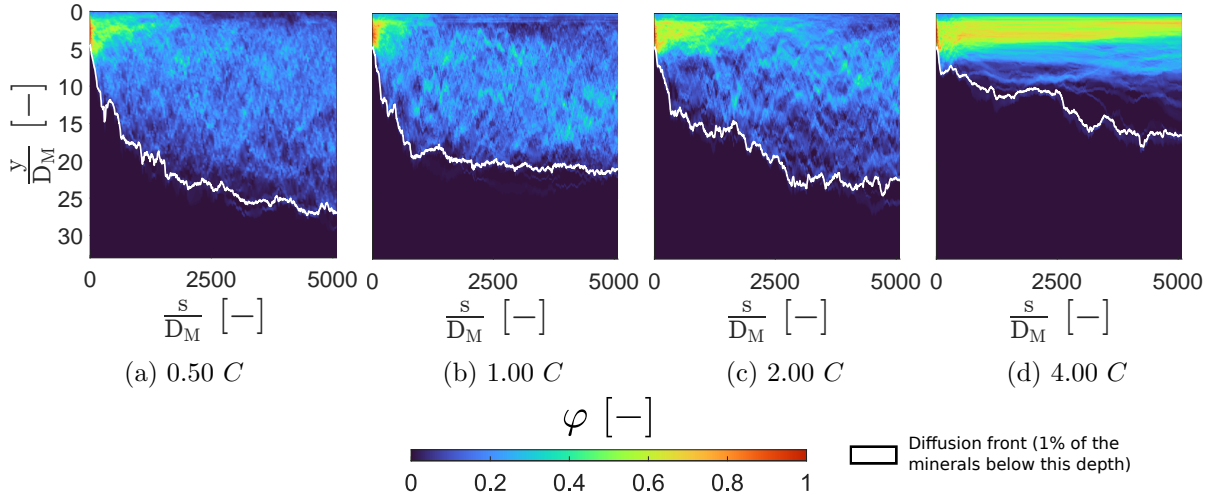
The value of contact forces between the different materials under study remains uncertain, and in practice depends on external conditions such as humidity. Depending on the chosen parameters, the shear rate may not exhibit a steady state as previously indicated (fig. 4.12b). Indeed, the shear rate can decrease locally in the interfacial layer, slowing down diffusion. This involves what will be referred to as jamming.

It is important to understand that for the subsequent investigations, the diffusion always exhibits a steady state. The particular study presented in this section, is a special case in which certain parameters have been modified, which lead to the loss of this steady state.

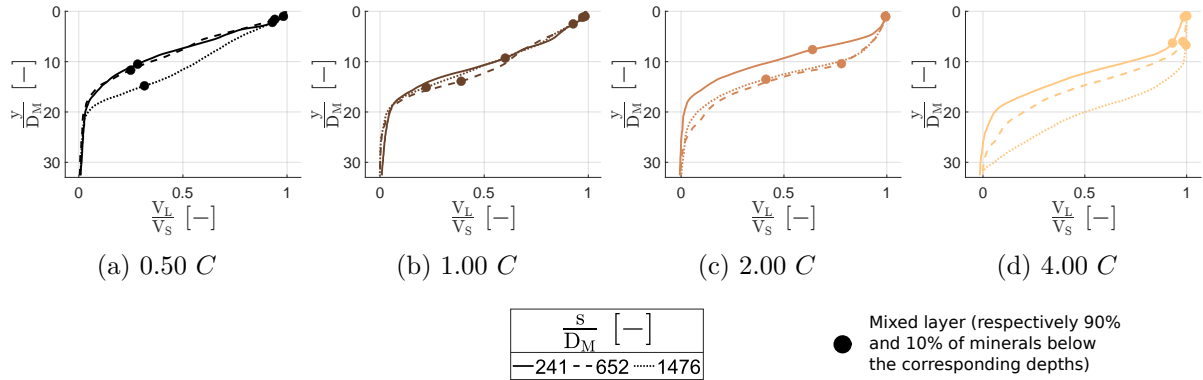
The Green-Kubo framework requires a sufficient number of data to be statistically significant. However, since the aim is to study transient states, averaging cannot be performed over a large time window to avoid hiding mechanisms. For this reason, all data in this section correspond to an average over a sliding distance of  $\pm 103 D_M$ , and the diffusion coefficient will be derived from the framework of Einstein. In addition, the data do not correspond to a relative sliding distance ( $\Delta s$ ) but to an absolute one ( $s$ ), as the steps are not equivalent to each other.

### 4.1 Direct jamming

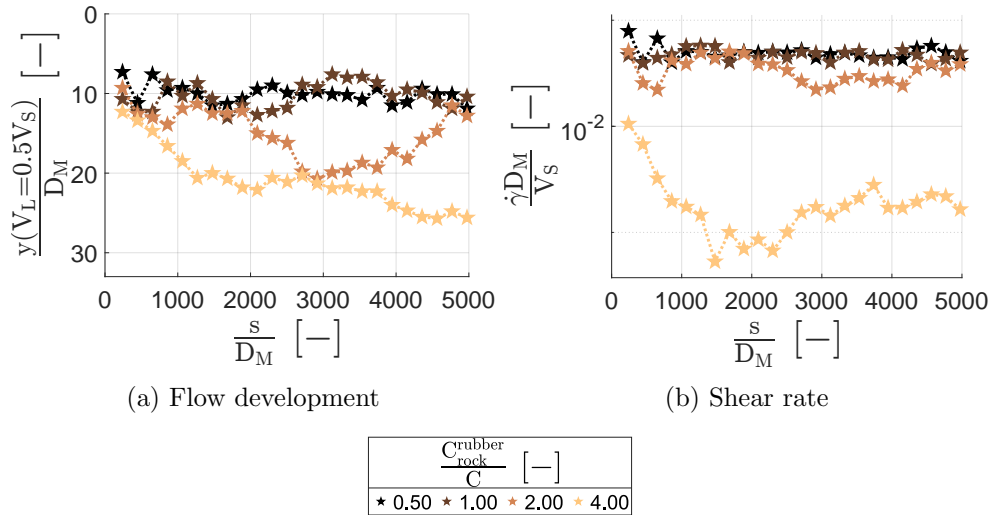
Between the minerals and the rubber material, a cohesive model is defined. This model is the same as the one used between rubber particles as already discussed in the chapter about indentation, but with a lower value ( $0.50 C$ ). The effect of this cohesion, called  $C_{rock}^{rubber}$ , is investigated for 4 different values (►):  $0.50^{#11}$  (►),  $1.00^{#12}$  (►),  $2.00^{#13}$  (►) and  $4.00^{#14}$  (►)  $C$ . mineral fraction maps are displayed in fig. 4.14.

Figure 4.14: Mineral fraction according to  $C_{rock}^{rubber}$ 

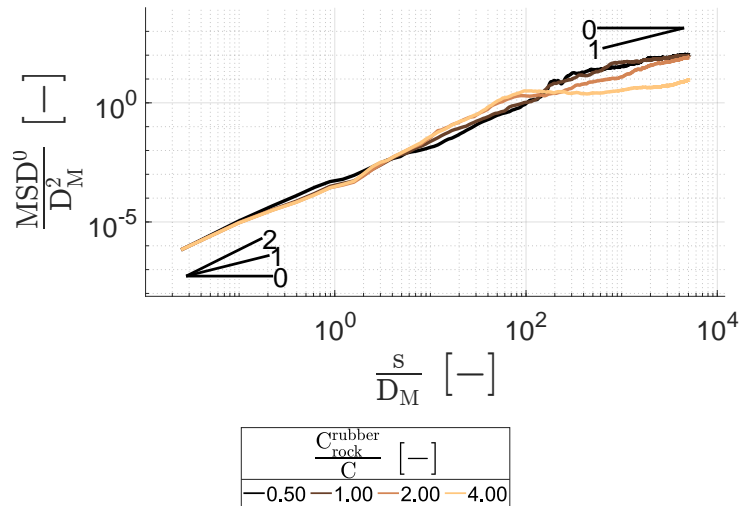
Concerning intake, the results are similar for cohesions of 0.50 and 1.00  $C$ , with relatively fast incorporation of the minerals into the rubber material (figs. 4.14a and 4.14b). For higher cohesions of 2.00 and 4.00  $C$ , a greater delay appears (figs. 4.14c and 4.14d). At the highest cohesion, some of the minerals seem to be entrapped close to the road-like surface. To better understand this phenomenon, velocity profiles are displayed fig. 4.15.

Figure 4.15: Velocity profile according to  $C_{rock}^{rubber}$ 

For cohesions of 0.50 and 1.00  $C$ , the velocity profiles are similar (figs. 4.15a and 4.15b). It reveals a stratified bi-layer flow, with a constant shear rate in the layer containing the minerals, followed by a shear-free layer. Note that for the lowest cohesion, a slight variation in profile can be observed, but this remains at low sliding scales ( $s \leq 652 D_M$ ) and will be attributed to shear initiation. For cohesions of 2.00 and 4.00  $C$ , a stratified tri-layer flow is observed (figs. 4.15c and 4.15d). The layer closest to the road-like surface has a variable or zero shear rate. Below this layer, a layer with a constant shear rate is formed. Finally, the deepest layer has a zero velocity, as for the lowest cohesions. It may be noted that velocity is transmitted at greater depths than for the 0.50 and 1.00  $C$  cohesions. Indeed, as the shear rate decreases in the upper layer, energy dissipation also decreases, requiring a greater thickness to dissipate the energy. These results seem to show a threshold effect for higher cohesions, which can be highlighted by looking at the median depth and shear rate fig. 4.16

Figure 4.16: Kinematics according to  $C_{rock}^{rubber}$ 

The depth corresponding to a longitudinal velocity ( $V_L$ ) of  $0.5 V_S$ , will hereafter be referred to as the median depth, for the sake of brevity. It gives an idea of the evolution of the flow over time. It can be seen in fig. 4.16a that for cohesion less than or equal to  $1.00 C$ , the median depth remains very similar over time with a value of  $10 D_M$  (also obtained for a cohesion of  $0.25 C$ ). For a cohesion of  $2.00 C$ , the median depth is similar until a transient regime is observed. Thereafter, it returns to a value close to  $10 D_M$ . For a cohesion of  $4.00 C$ , a progressive increase in median depth is first observed, followed by a plateau and then a slight increase. The shear rate in fig. 4.16b is similar for cohesions of  $0.05$ ,  $0.10$  and  $0.20 C$ , with a value around  $0.04 \frac{V_S}{D_M}$  for a sliding distance of  $5000 D_M$ . However, for a cohesion of  $4.00 C$ , the shear rate decreases and becomes around 20 times lower than for the other cohesions. The corresponding mean square displacements are shown in fig. 4.17.

Figure 4.17:  $MSD^0$  according to  $C_{rock}^{rubber}$ 

An important point is that, for a cohesion of  $4.00 C$ , although the shear rate progressively decreases until a sliding distance of  $1500 D_M$ , minerals do not diffuse significantly. Indeed, for  $s = 3530 D_M$ , the  $MSD^0$  is about 13 times lower for a cohesion of  $4.00 C$  than for the lowest cohesions. This state can therefore be considered as completely and directly jammed due to the lack of mobility in the mixed layer.

These results show that diffusion does not depend on  $C_{rock}^{rubber}$ . Indeed, no difference is observed in terms of kinematics or diffusion up to a value of 1.00  $C$ . However, even if there is not much experimental evidence, having a higher cohesion value between rock and rubber than between rubber and rubber seems unlikely. This also shows that a jamming state does not seem to be achievable with consistent cohesion values. The use of a cohesive model between mineral and rubber is somewhat arbitrary, again for lack of experimental evidence. For this reason, some investigations have been carried out using a Coulomb friction law between minerals and rubber.

## 4.2 Delayed jamming

The cohesive model between rubber and minerals is replaced by a Coulomb friction law with  $\mu_{rock}^{rubber} = 0.4$  (this also applies to the road-like surface). This value is chosen because it leads to a tangential stress close to 0.50  $C$  for the applied contact pressure. The value of  $\mu_{rock}^{rock}$  was lowered from 0.6 to 0.3 to remain below  $\mu_{rock}^{rubber}$ . The effect of these two coefficients will be examined later. Four interfacial layer thicknesses were tested (▶): 33<sup>#1</sup> (▶), 36<sup>#2</sup> (▶), 41<sup>#3</sup> (▶) and 45<sup>#4</sup> (▶)  $D_M$ . Mineral fraction maps are displayed in fig. 4.18.

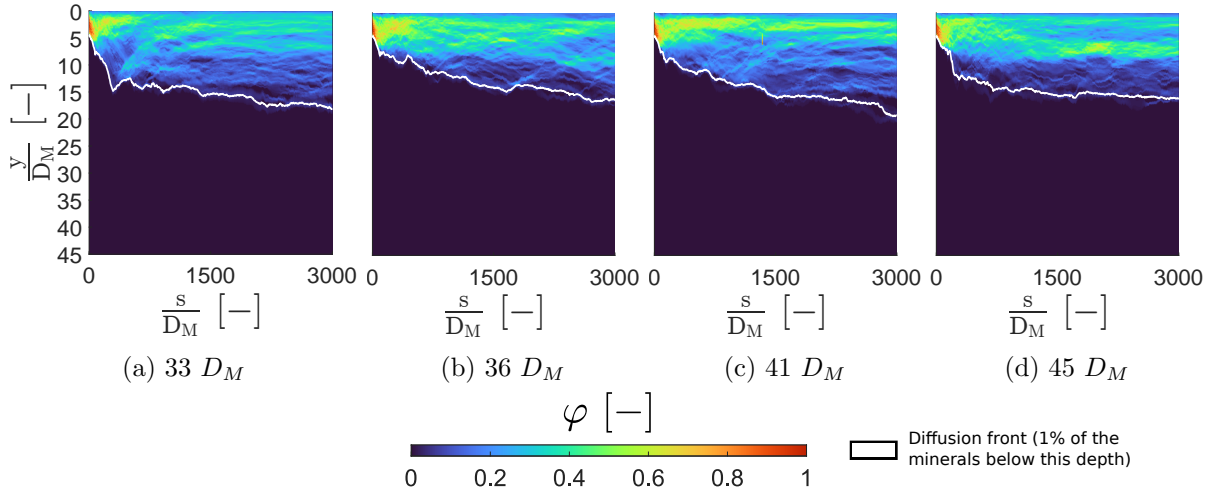
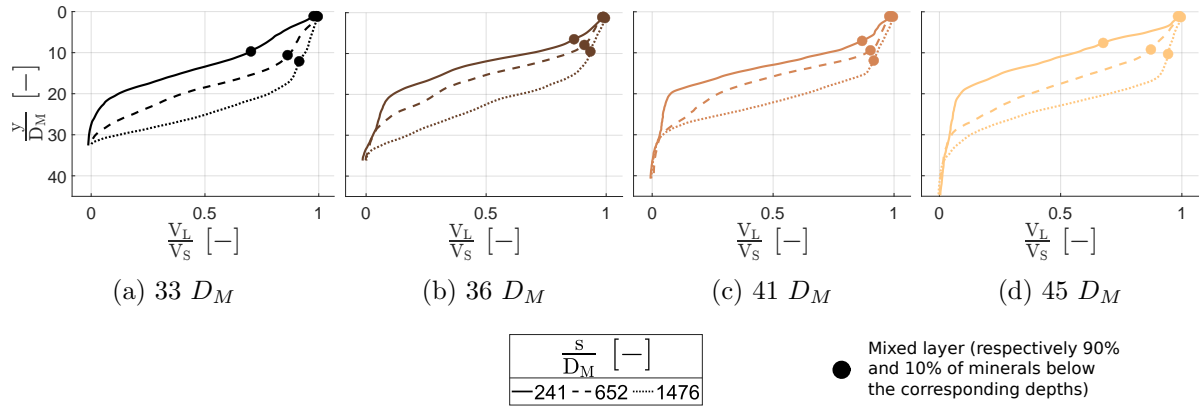


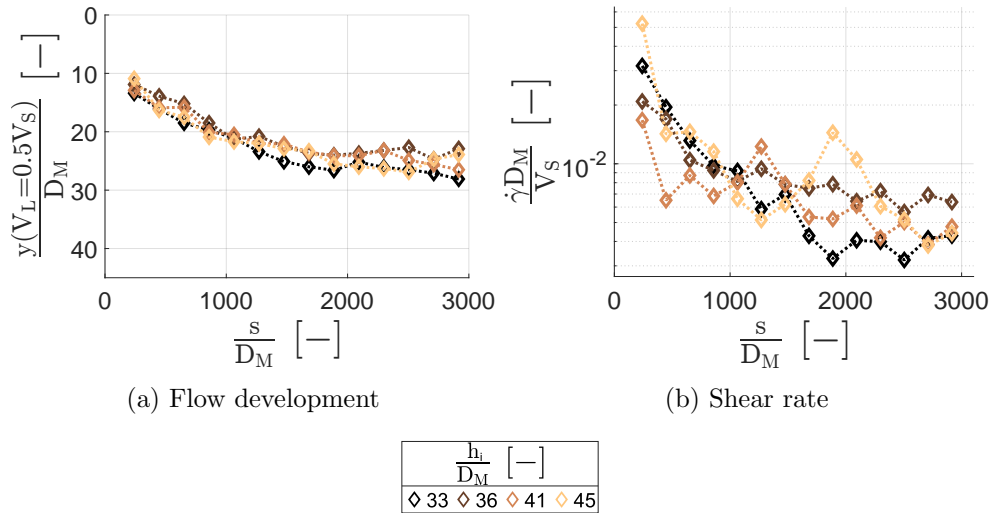
Figure 4.18: Mineral fraction according to  $h_i$  in a delayed jamming case

Regarding the intake, for all the thicknesses, it can be seen that a higher concentration, close to 0.5, is obtained near the road-like surface for a sliding distance of 3000  $D_M$ . In contrast, for the simulations using a cohesive model, the concentration almost systematically fell below 0.2 at 3000  $D_M$  (e.g. fig. 4.6c). Moreover, this higher concentration no longer evolves from 1000  $D_M$ , suggesting a jamming-like mechanism as obtained previously. Concerning the diffusion front, it does not seem to depend on thickness, with a depth close to 22  $D_M$  at 3000  $D_M$  for all thicknesses. To understand the higher concentration near the road-like surface, velocity profiles are displayed in fig. 4.19.

The resulting profiles correspond to a stratified tri-layer flow. The mixed layer with a constant shear rate, a sub-layer with a different but constant shear rate, and finally a third layer with a zero velocity. Although these results seem similar to those obtained in the previous section (for  $C_{rock}^{rubber}$  equal to 2.00 and 4.00  $C$ ), there are actually some significant differences. The first is that the shallowest layer has a constant shear rate and not a variable one, contrary to what could be observed for a  $C_{rock}^{rubber}$  of 2.00  $C$ . The second is that the shallowest layer corresponds to the mixed layer, whereas previously, the mixed layer was contained within the

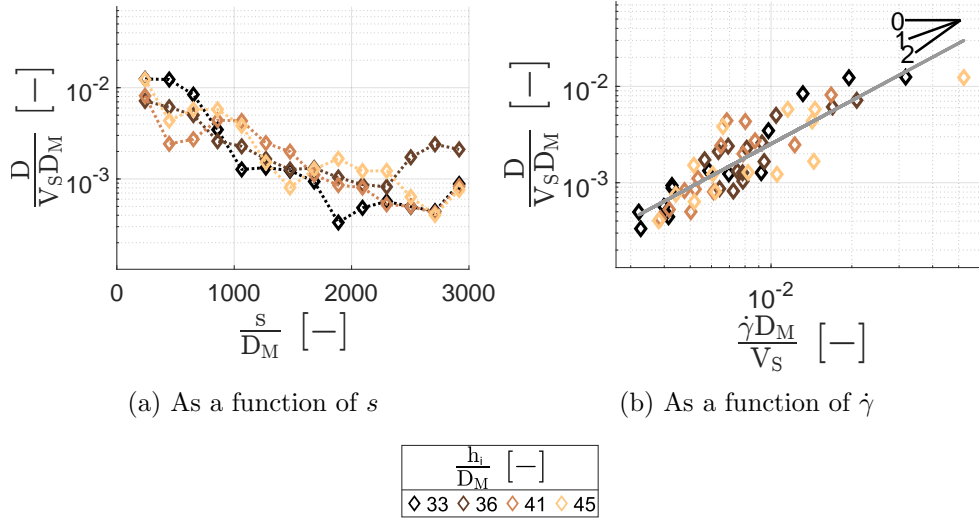
Figure 4.19: Velocity profile according to  $h_i$  in a delayed jamming case

whole domain. Finally, the evolution of the velocity profile as a function of sliding distance is more progressive, as shown in fig. 4.20.

Figure 4.20: Kinematics according to  $h_i$  in a delayed jamming case

The median depth decreases with sliding distance (fig. 4.20a), as suggested by the velocity profiles. This demonstrates an effect of minerals on kinematics. This decrease reaches a plateau from  $2000 D_M$ . Moreover, there is no significant effect of thickness on its value (close to  $25 D_M$ ). Shear rate also decreases (fig. 4.20b), with the same plateau at  $2000 D_M$ . As shear rate is closely related to diffusion, the latter also slows down, as shown in fig. 4.21.

The diffusion coefficient ( $D$ ) is continuously decreasing with sliding distance (fig. 4.21a). Between the first instants and stabilization, its value is divided by 10. In contrast, for steady-state diffusion, the diffusion coefficient easily exceeds  $1 \cdot 10^{-2} V_S D_M$  as it will be seen later. Therefore, a value close to  $1 \cdot 10^{-3} V_S D_M$  corresponds to an almost complete stop of diffusion. Furthermore, there is no significant effect of thickness on  $D$ . If the diffusion coefficient is compared with the shear rate (fig. 4.21b), the link between these 2 quantities becomes clear. A power law can be fitted from all the simulations, giving an exponent of 1.5. These results show that diffusion slows down as the shear rate decreases. On the other hand, they demonstrate that the notion of a global shear rate is meaningless. Indeed, if the shear rate is not constant in the whole interfacial layer, only the shear rate in the mixed layer seems to drive diffusion.

Figure 4.21: Diffusion according to  $h_i$  in a delayed jamming case

The reinforcing effect of minerals increases when mineral fraction decreases. Indeed, at the beginning of sliding, when the mineral fraction is high (above 0.7), the effect on shear rate is negligible. This is counter-intuitive to the studies about colloidal suspensions, where resistance to shear increases with solid fraction. This suggests that there is a non-monotonic relationship between this resistance and mineral fraction. This phenomenon was investigated in [Mollon, 2018a]. This study used rigid grains uniformly distributed in a packing of soft particles. It shows that beyond a certain fraction of rigid grains compared to soft particles, the resistance to shear becomes independent of this fraction. However, in the current study, there are two additional phenomena. First, the contact model between minerals is different from that between rubber particles. Consequently, there is a change in resistance due to the evolution of contact forces in the mixed layer. Then, the thickness of the mixed layer changes during diffusion. These phenomena act in parallel and the functional relationship is still unknown at this stage. The effect of  $\mu_{rock}^{rock}$  was studied for 4 different values ( $\blacktriangleright$ ), with a coefficient of 0.1<sup>#5</sup> ( $\blacktriangleright$ ), 0.2<sup>#6</sup> ( $\blacktriangleright$ ), 0.3<sup>#1</sup> ( $\blacktriangleright$ ) and 0.4<sup>#7</sup> ( $\blacktriangleright$ ). The effect of  $\mu_{rock}^{rubber}$  was also studied for 4 different values ( $\blacktriangleright$ ), with a coefficient of 0.3<sup>#8</sup> ( $\blacktriangleright$ ), 0.4<sup>#1</sup> ( $\blacktriangleright$ ), 0.5<sup>#9</sup> ( $\blacktriangleright$ ) and 0.6<sup>#10</sup> ( $\blacktriangleright$ ). The reinforcement was investigated through the shear rate in the mixed layer (for  $h_i = 33 D_M$ ). The results are presented in fig. 4.22.

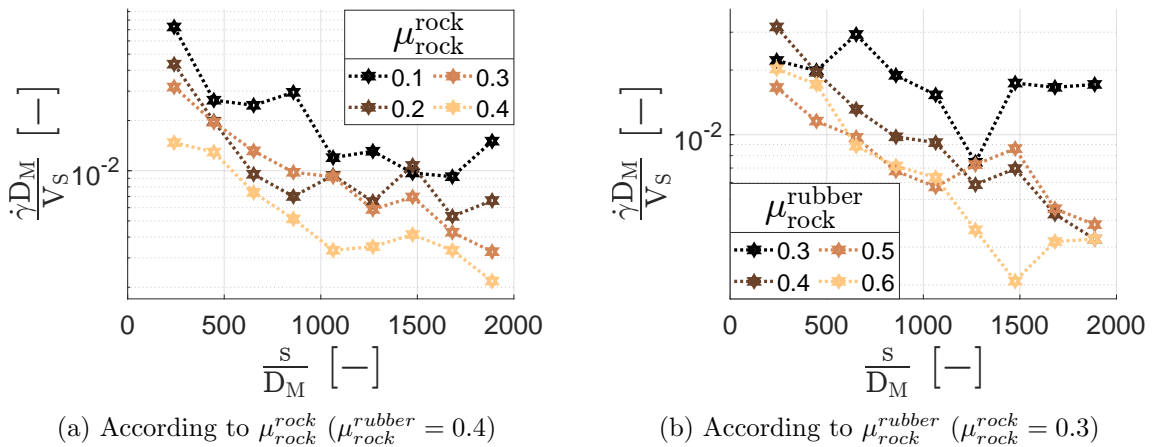


Figure 4.22: Effect of the friction coefficients



Firstly, it can be seen that whatever the value of  $\mu_{rock}^{rock}$  (fig. 4.22a) and  $\mu_{rock}^{rubber}$  (fig. 4.22b) (except  $\mu_{rock}^{rubber} = 0.3$ ), the shear rate tends towards 0 with sliding distance. It therefore seems that the observed transient behavior is a general effect of the use of a friction law between minerals and rubber, and not just due to a specific set of parameters. For  $\mu_{rock}^{rock}$ , a clear trend is observed with a decrease in shear rate as the coefficient increases. Moreover, the value of the coefficient does not seem to influence the rate at which the shear rate decreases. A plausible explanation is that, at the beginning, contacts between minerals are numerous, and the value of this coefficient is therefore significant. The higher the coefficient, the lower the shear rate, creating a delay in diffusion. Then, contacts between minerals become less numerous, and the value of the coefficient becomes less preponderant. However, the lag initiated at the beginning persists, and the evolution of the shear rate is therefore time-shifted.

Regarding  $\mu_{rock}^{rubber}$ , it is more difficult to identify a clear trend. However, it can be noted that for a value of 0.3, the shear rate is 5 times higher than the higher coefficients, and shows no particular downward trend. However, the velocity profile also corresponds to a stratified tri-layer flow, with a shear rate that is not constant in the whole interfacial layer. The result is therefore not equivalent to what could be obtained using a cohesive model.

### Highlights

- Depending on the chosen contact model between minerals and rubber, diffusion may not exhibit a steady state regime.
- If a Coulomb friction model is defined (contrary to the cohesive model used in the rest of the study), the shear rate is at the beginning maximum, then continuously tends towards zero. In this case, the shear rate is therefore not constant, and this will be referred to as transient diffusion.
- The decrease in the shear rate leads to a decrease in the diffusion coefficient, until diffusion has almost completely stopped.

## 5 Experimental observations

Several tests were carried out on a tribometer. These results have already been discussed in [Daigne et al., 2024]. The corresponding surfaces were observed (after testing) on a ThermoFisher QUANTA 600 environmental scanning electron microscope (ESEM), using a water vapor pressure of 350 Pa. A GAD (Gaseous Analytical Detector) with a cone was used. In the following SEM images (figs. 4.23 and 4.24), contrast corresponds to atomic number (Z). The lightest areas are corresponding to kaolinite, essentially alumina and silica. The darker areas are corresponding to rubber, mainly composed of carbon. For all images, the sliding direction is horizontal from left to right.

### 5.1 Surfaces

To study the evolution of a surface during sliding, 4 rubber specimens were observed for several sliding distances. Wear tests were carried out under a normal load of 377 N (0.2 MPa if applied to the apparent contact area) and a rotary speed of 32 RPM (0.10 m.s<sup>-1</sup> on the median radius). In fig. 4.23, several characteristic views of the state of the track at different sliding distances can be seen.

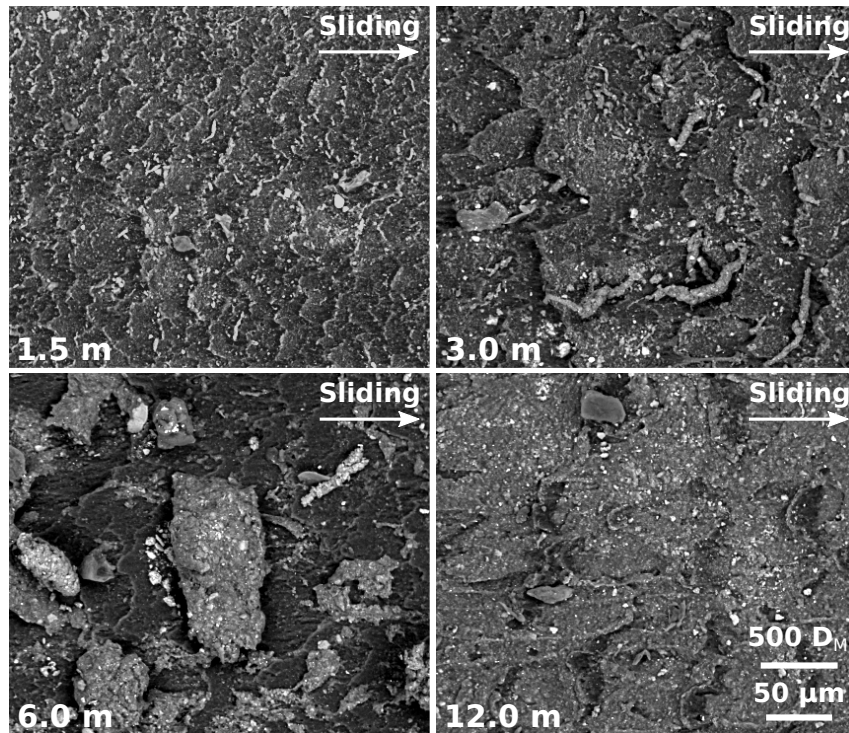


Figure 4.23: Z-contrast images of the surfaces for 4 sliding distances (1.5, 3.0, 6.0 and 12.0 *m*)

For a sliding distance of 1.5 *m*, numerous particles (light shading) composed of a mixture of rubber and minerals are visible. These particles are mainly located near surface asperities (i.e. surface wrinkles). For a distance of 3.0 *m*, roller-shaped particles are observed. There are areas of higher particle concentration, suggesting the formation of particle agglomerates. In addition, small particles remain on the surface, as can be seen for the 1.5 *m* sliding distance. One possible explanation is that, in parallel with the agglomeration of existing particles, new particles are still being generated as the quantity of minerals remains sufficient to do so. For a sliding distance of 6.0 *m*, particles are again larger and less numerous. Some particles appear to have been sheared and milled on the surface. The largest particle in the center of the image has an elongated shape in the orthogonal direction of friction with several mineral inclusions. It corresponds to the typical aspect of a tire wear particle [Kreider et al., 2010; Adachi and Tainosho, 2004; Morris and Kosyrev, 2018].

For a sliding distance of 12.0 *m*, only a few small particles are still visible. Two possibly coupled mechanisms could explain this observation. The first one is that, as no minerals are added during the experiment, all the minerals will be at some point ejected or incorporated. This leads to a change in particle generation. Another explanation is that as the particles on the surface become larger and larger, the shear stress may exceed their shear strength. This leads to the fragmentation of these agglomerates, as can be seen for the sliding distance of 6.0 *m*. Similar results regarding particle fragmentation were obtained numerically [Milanese et al., 2020].

## 5.2 Longitudinal section

A longitudinal section was obtained using a crosspolisher (Gatan, Ilion II). The section can be seen fig. 4.24. The wear test was carried out under a normal load of 1508 *N* (0.8 *MPa* if applied to the apparent contact area), a rotary speed of 32 *RPM* (0.10 *m.s*<sup>-1</sup> on the median radius) and for a sliding distance of 3.0 *m*.

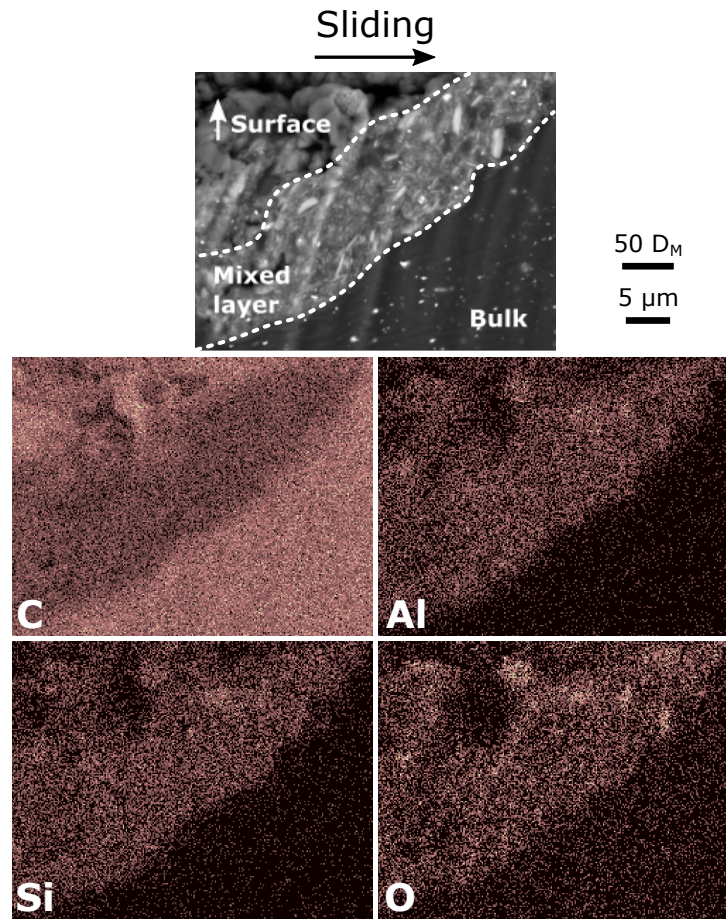


Figure 4.24: Z-contrast image of a cross-section view of the rubber sample and the corresponding EDX maps for carbon (C), aluminum (Al), silicon (Si) and oxygen (O)

It can be seen that minerals have been mixed with the rubber up to a distance of 10-12  $\mu\text{m}$ . A mixture of minerals and rubber mix is visible near the surface. This observation is confirmed by EDX analysis. Indeed, the mixed layer has a higher concentration of C, Al, Si and O, which is characteristic of kaolinite composition. In addition, there is no Al and Si in the material composition. Therefore, this can only be attributed to kaolinite. The minerals have the shape of thin platelets. Note that the white spots in the bulk area correspond to zinc oxide (ZnO), which is a vulcanizing agent.

There is a clear boundary between this layer with minerals and the bulk without minerals. This boundary is not horizontal (i.e. in the sliding direction), which can be explained by the fact that the mixed layer corresponds to a detachment of rubber material that does not follow this direction. This detachment is mixed with the minerals, forming the mixed layer, which is then sheared on the rubber bulk giving this non-horizontal boundary. The diffusion is linked to the concentration gradient. Consequently, it should tend towards a homogenized state in the whole space, as it leads to a zero gradient. Moreover, if diffusion is still in progress, which could justify the gradient, the concentration profile should be close to a smooth step (cf. fig. 4.6d and [Wei et al., 2019]).

Based on the above comments, three hypotheses can be proposed to explain this boundary. The first is that the view only concerns the early stage of diffusion, and it will continue due to the gradient near the boundary. However, this cannot fully explain such a concentration gradient. The second is that the material is not degraded enough below this boundary (which

modifies the plastic properties). Finally, the third is a difference in shear rate on either side of the boundary. Indeed, as previously discussed, the shear rate drives the diffusion process. This last hypothesis will be studied in detail, by investigating the links between kinematics and diffusion.

#### Highlights

- The particles formed on the surface of the wear specimen are roll-shaped, similar to tire wear particles. The size of these particles increases with the sliding distance, until they are milled onto the surface.
- A longitudinal section, combined with EDX analysis, shows that the minerals have begun to diffuse into the rubber specimen.

## Conclusion

The use of a soft rubber material implies several specificities compared to more standard discrete shear models. Firstly, a greater variety of intake mechanisms can be observed. Overall, 3 main types have been identified, namely plowing, abrasion and fracture. All these mechanisms lead to specific features (intake flow, generation of agglomerates, etc.) and the influence of several parameters on intake will be studied thereafter.

A particular attention has been paid to laying the foundations for the work that will follow. Indeed, shear-induced diffusion in a solid flow composed of a soft material does not seem to have been studied in the literature. It was therefore necessary to demonstrate that this was genuinely a diffusive process and not a more general class of mechanical mixing. To do so, certain well-known features of shear-induced diffusion had to be found for this particular class of flow.

It has been shown that even in the case of an interface composed of a soft material such as rubber, mineral displacement also exhibits a stochastic behavior. This result may be surprising, since in granular diffusion, the displacement is driven by the rigid grains, which explains the sudden variations in velocity. In the current model, this result is explained by the fact that these variations are due to contacts between rigid minerals. It has also been shown that, by considering all the minerals, a deterministic behavior is observed. In addition, the concentration shows a Gaussian pattern that flattens with time, similar to what can be obtained in more classical diffusion processes. These results seem to demonstrate that the process modeled in this study can be considered as a diffusive one.

Some key quantities have been introduced, notably the velocity fluctuation  $\Delta V_T$  and the time persistence  $\Psi$ . The velocity fluctuation corresponds to a characteristic transverse velocity of a mineral and the time persistence to the holding time of this velocity. A procedure has been carried out to show that the Green-Kubo framework is applicable to this type of flow, enabling a diffusion coefficient to be derived.

The effect of the contact model between minerals and between minerals and rubber was investigated. It was shown that in the case of a cohesive model between minerals and rubber, the results were independent of this cohesion within a consistent range of values. It was also shown that if this model was modified by a Coulomb friction law, the kinematics was affected. In this case, there is a continuous decrease in the shear rate, leading to a quick slowdown of diffusion. Subsequently, a cohesive model will be used, as it seems more appropriate at this



scale. There is, however, a lack of literature on this subject, and this point could be explored further.

Wear tests were carried out and the surfaces were observed using a scanning electron microscope. On the worn surfaces, the size of the agglomerates seems to increase with the sliding distance. However, above a certain distance, these agglomerates are milled. This suggests an effect of minerals on wear behavior, as the minerals are completely ejected through the wear particles at some point. By examining the longitudinal section, a clear boundary between the mixed layer and the layer without minerals was observed. Several hypotheses have been put forward, including one that assumes a difference in kinematics on either side of this boundary. This hypothesis suggests the importance of establishing a link between kinematics and diffusion.



## Chapter 5

# Steady-state diffusion

This chapter will focus on how diffusion is influenced by several parameters in the case of a constant shear rate (i.e. steady-state diffusion). For each parameter, a global analysis of intake and diffusion will be carried out. Then, kinematics and diffusion will be examined, trying to establish a link between these two closely related components. First, a study of the influence of arbitrarily chosen parameters is presented in section 1. Subsequently, parameters external to the tire, such as contact pressure, are studied in section 2. Finally, the influence of rubber properties will be investigated in section 3.

Several quantities will describe the overall steady-state regime (velocity profile, shear rate, velocity fluctuation, persistence and diffusion coefficient). To establish a link between kinematics and diffusion, similar states must be compared. To this end, for each simulation, the starting point of the steady-state is taken for a  $MSD^0$  of  $50 D_M^2$ . As a reminder,  $MSD^0$  corresponds to the mean square displacement of the minerals (taking the initial state as the reference configuration) and  $D_M$  to their equivalent mean diameter. If this is not possible (target sliding velocity not yet reached,  $MSD^0$  not high enough, etc.), the nearest step is taken. The data are then processed over a sliding distance of  $2058 D_M$ . The validity of this method has been checked in appendix A.

Many results will be normalized by  $D_M$ . Some quantities are linked to  $D_M$ , giving meaning to this normalization, but some are not. This is the case, for example, of time, which is expressed as a sliding distance normalized by  $D_M$ . However, this sliding distance should be normalized by the thickness of the layer with a non-zero velocity, which is equivalent to multiplying time by the shear rate. However, this thickness is unknown and varies according to the simulation. Consequently, for the sake of comparison,  $D_M$  will be used for the normalization of all the quantities.

For all the simulations of this chapter, snapshots can be found in appendix B, the mean square displacements in appendix C and the velocity autocorrelation functions in appendix D. Moreover, the corresponding numerical parameters can be found in table 2.1 by referring to the superscript # and available animations are indicated by a ►.

## 1 Numerical parameters

### 1.1 Sliding velocity

The first parameter to be studied is the sliding velocity. Although this parameter has a physical meaning, it is currently artificially increased for computation time reasons. The aim is therefore to determine whether this choice will influence the results. It will also give an initial



indication of how some quantities vary over wide ranges of shear rate. To this end, 4 sliding velocities ( $v_s$ ) were investigated around the one used hereafter ( $V_S$ ), equal to  $0.5^{#15}$  ( $\blacktriangleright$ ),  $1.0^{#11}$  ( $\blacktriangleright$ ),  $2.0^{#16}$  ( $\blacktriangleright$ ) and  $4.0^{#17}$  ( $\blacktriangleright$ )  $V_S$  respectively.

Depending on the input parameters, delay of intake can be significant, and some minerals may begin to diffuse while others have already reached the diffusion front. Understanding the intake is important for several reasons. Firstly, the current model does not take mineral ejection into account. However, it can be assumed that the longer a mineral remains on the surface, the greater the probability of it being ejected. In addition, the current model uses only a small quantity of minerals compared to the experimental set-up (about 100 times less if all the minerals were experimentally incorporated into the rubber material). With a larger amount, as it will be seen later, the instantaneous quantity of minerals embedded into the interfacial layer could modify the instantaneous kinematics, which is determined by the intake flow and wear flow. Because of the closed contact and the small quantity of minerals, the model is not intended to give a precise answer concerning intake, but rather to provide a first thought. Intake can be observed notably on mineral fraction maps, as shown in fig. 5.1.

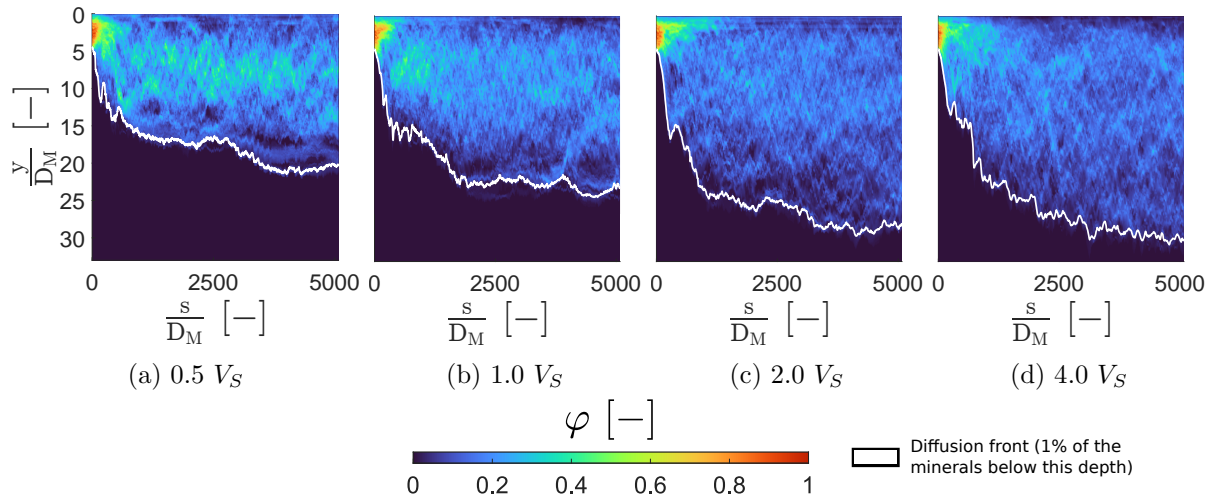
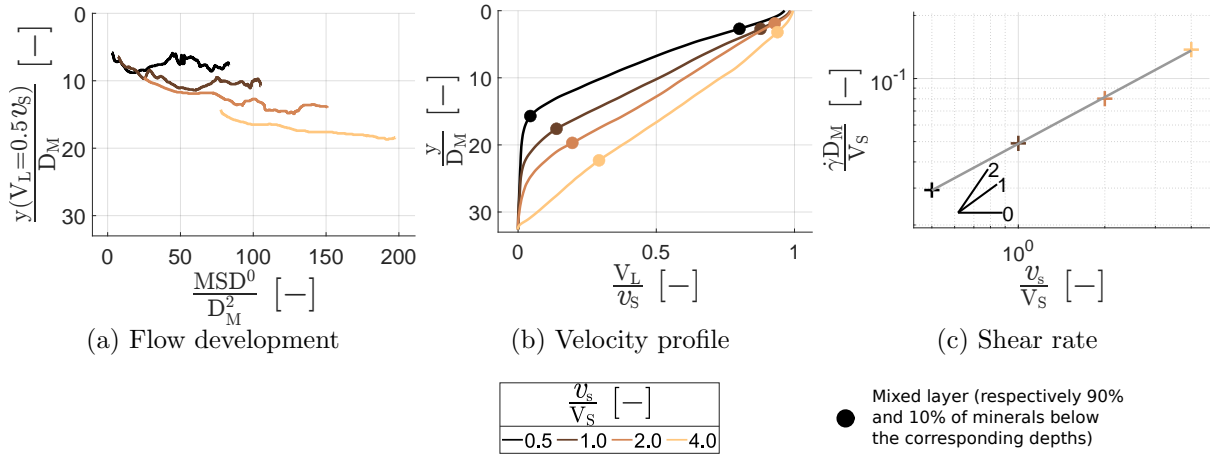


Figure 5.1: Mineral fraction according to  $v_S$

Acceleration at the beginning of sliding is identical and constant for all the simulations ( $v_S$  is reached at a sliding distance of  $137 \frac{v_S}{V_S} D_M$ ). For this reason, there is no apparent effect on intake, since it is performed at the same instantaneous velocity. Regarding the diffusion front, the higher the velocity, the deeper the mineral diffuses. For increasing  $v_S$  and a sliding distance of  $5000 D_M$ , the front reaches depths of 20, 23, 28 and  $30 D_M$  respectively.

A less homogeneous concentration can also be observed for a velocity of  $0.5 V_S$ , with agglomerates forming at a depth of  $8 D_M$ . This phenomenon begins to appear at a velocity of  $1.0 V_S$ , but quickly vanishes. This would indicate a characteristic mineral reorganization time. Indeed, if the velocity is too high, geometric interlocking prevents the minerals from forming agglomerates by increasing their contact surface (a kind of jamming at the mineral scale). It will be seen later that with a homogeneous mineral size distribution, the formation of agglomerates is much higher, confirming the existence of this characteristic reorganization time. The results concerning kinematics are given in fig. 5.2.

To study the influence of diffusion on the velocity profile, the median depth is plotted not as a function of  $s$  but as a function of  $MSD^0$ . To this end, a moving average of  $MSD^0$  and the velocity profile over a sliding distance of  $\pm 257 D_M$  is first performed. As the smoothed  $MSD^0$

Figure 5.2: Kinematics according to  $v_s$ 

is not necessarily monotonic, for the sake of uniqueness, only strictly increasing values of  $MSD^0$  are kept. A sliding distance is associated with each value of the smoothed  $MSD^0$ , allowing to find the corresponding smoothed velocity profile, and ultimately the median depth. The part under acceleration is removed from the analysis.

It can be seen in fig. 5.2a that median depth increases with velocity. Moreover, a plateau is observed for 0.5 and 1.0  $V_S$ . This plateau is delayed with velocity. As a reminder, the thickness of the interfacial layer is equal to 33  $D_M$ . For a velocity of 4.0  $V_S$ , the median depth thus becomes greater than half this thickness from a  $MSD^0$  of 120  $D_M^2$ .

Velocity profiles are displayed in fig. 5.2b. It can be seen that as  $v_s$  increases, more velocity is transmitted deeper. The origin of this phenomenon is not yet fully understood. The inertial effect of soft and cohesive bodies remains an open question (the inertial number being more appropriate for rigid and cohesionless bodies). At the scale of the interfacial layer, the tangential force does not depend on velocity, suggesting that this is not due to a global inertial or viscous effect.

A plausible explanation is that, locally, as the minerals are heavier and less cohesive than rubber, local inertial effects may occur. It was previously discussed that over longer time scales, kinematics was modified due to a velocity transmission from the diffusion front to the deepest layer (initially having a velocity of zero). Inertial effects at the front could increase this transmission, thus advancing this phenomenon over shorter times. This hypothesis is supported by the progressive evolution of the velocity profile at higher  $v_s$ . It should be noted that some quantities ( $\dot{\gamma}$ ,  $\Delta V_T$ ,  $\lambda$  and  $D$ ) will subsequently be normalized by  $V_S$  (and not  $v_s$ ), which has no influence on the slope in a logarithmic space compared to a non-normalized quantity.

The corresponding shear rate is displayed in fig. 5.2c and shows an increase with sliding velocity. The scaling of shear rate according to sliding velocity is given in eq. (5.1). The exponent is equal to 0.74 (and therefore lower than 1) because the shear rate increases linearly with the sliding velocity, but also decreases as the layer with a non-zero velocity is thicker.

$$\dot{\gamma} \propto v_s^{0.74} \quad (5.1)$$

As a reminder, it has been shown that the evolution of transverse velocity corresponds to local events of short duration relative to the total duration of sliding (fig. 4.7). Velocity fluctuation ( $\Delta V_T$ ) describes the magnitude of these events, while persistence ( $\Psi$ ) describes their durations.

Persistence is expressed in terms of an equivalent sliding distance ( $\lambda = \Psi V_S$ ). Finally, the diffusion coefficient ( $D$ ) describes the capacity of the minerals to diffuse more or less rapidly (which depends on material properties and several external parameters). An important point for subsequent analysis in this chapter is the dependence of  $\Delta V_T$ ,  $\lambda$  and  $D$  on  $\dot{\gamma}$ . Empirical scalings based on the physics of granular media as written in eqs. (5.2) to (5.4) are expected [Macaulay and Rognon, 2019]. It is worth remembering that  $\Delta V_T$  has a quadratic influence on  $D$  (cf. eq. (4.4)). Because of the linear increase in  $\Delta V_T$  and the linear decrease in  $\lambda$ ,  $D$  depends linearly on  $\dot{\gamma}$ .

$$\begin{cases} \Delta V_T \propto \dot{\gamma}^{1.00} & (5.2) \\ \lambda \propto \dot{\gamma}^{-1.00} & (5.3) \\ D \propto \dot{\gamma}^{1.00} & (5.4) \end{cases}$$

Results concerning diffusion are displayed in fig. 5.3.

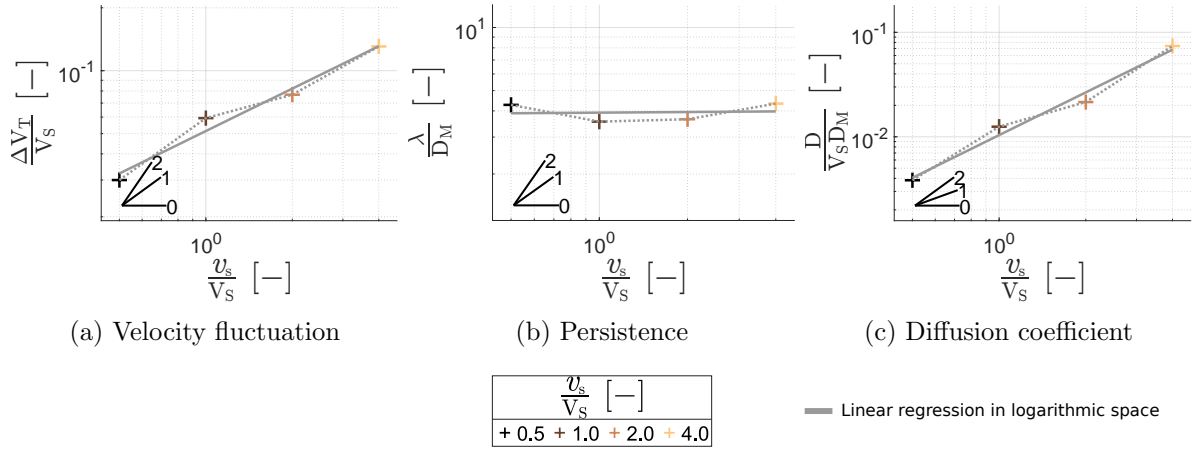


Figure 5.3: Diffusion according to  $v_S$

First, there is an increase in  $\Delta V_T$  with  $v_S$  of the same order of magnitude as the increase in shear rate, with an exponent close to 0.7 (fig. 5.3a and eq. (5.5)). It therefore seems that the two are linked, and that  $\Delta V_T$  no longer increases linearly with  $v_S$  for the same reasons as for  $\dot{\gamma}$ . A more surprising result concerns persistence. Persistence becomes independent of  $v_S$  and does not show the usual linear response to shear rate, the exponent being close to 0 instead of -1 (fig. 5.3b and eq. (5.6)). This would confirm a local inertial effect that helps the minerals to maintain their transverse velocity at each offset event. However, the link between this increase and the transmission of velocity at the front is still to be demonstrated. It may be noted that this point should be studied further, as it could be a good candidate for defining an inertial number in a cohesive soft-body mixture. The direct consequence of the increase in  $\lambda$  is a superlinear increase in  $D$  with  $v_S$  (fig. 5.3c and eq. (5.7)).

$$\begin{cases} \Delta V_T \propto v_S^{0.67} & (5.5) \\ \lambda \propto v_S^{0.01} & (5.6) \\ D \propto v_S^{1.36} & (5.7) \end{cases}$$

## Highlights

- The higher the sliding velocity, the deeper the velocity is transmitted, inducing a sub-linear dependence of shear rate on sliding velocity. This is attributed to local inertial effects of the minerals near the diffusion front.
- The change in shear rate induces a change in velocity fluctuation in the same proportion (i.e. both are linearly proportional). However, inertial effects significantly increase persistence, inducing a super-linear dependence of the diffusion coefficient on sliding velocity.

## 1.2 Interfacial layer thickness

The objective is now to evaluate the effect of interfacial layer thickness. As previously discussed, over a long time scale, minerals tend to diffuse into the whole layer. In this case, it is clear that thickness will play a role. However, it remains to investigate how this thickness can influence diffusion during the steady state. To this end, 4 interfacial layer thicknesses ( $h_i$ ) were investigated (▶), equal to  $33^{#11}$  (▶),  $36^{#18}$  (▶),  $41^{#19}$  (▶) and  $45^{#20}$  (▶)  $D_M$  respectively. Mineral fraction maps are shown in fig. 5.4.

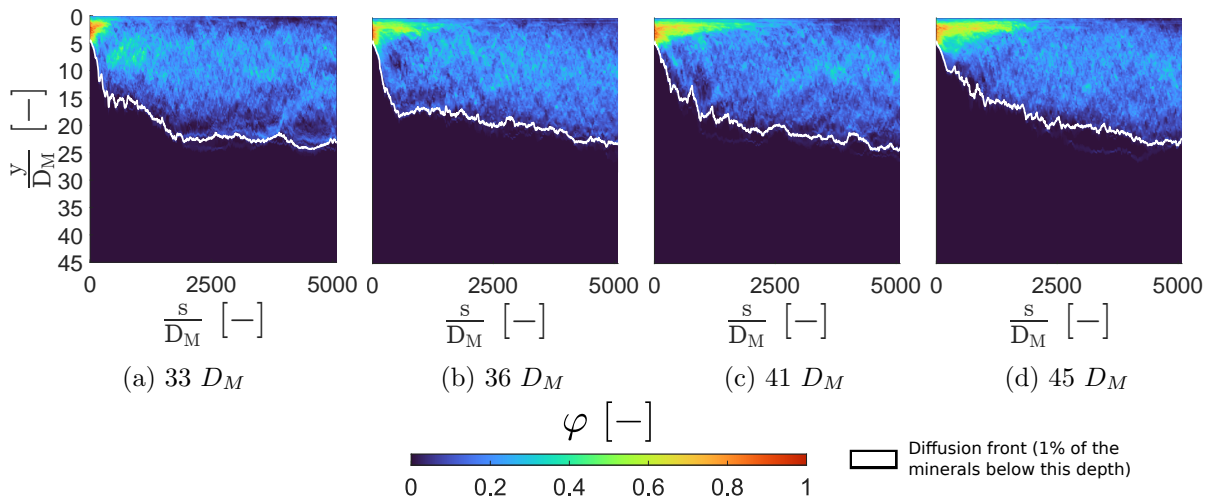
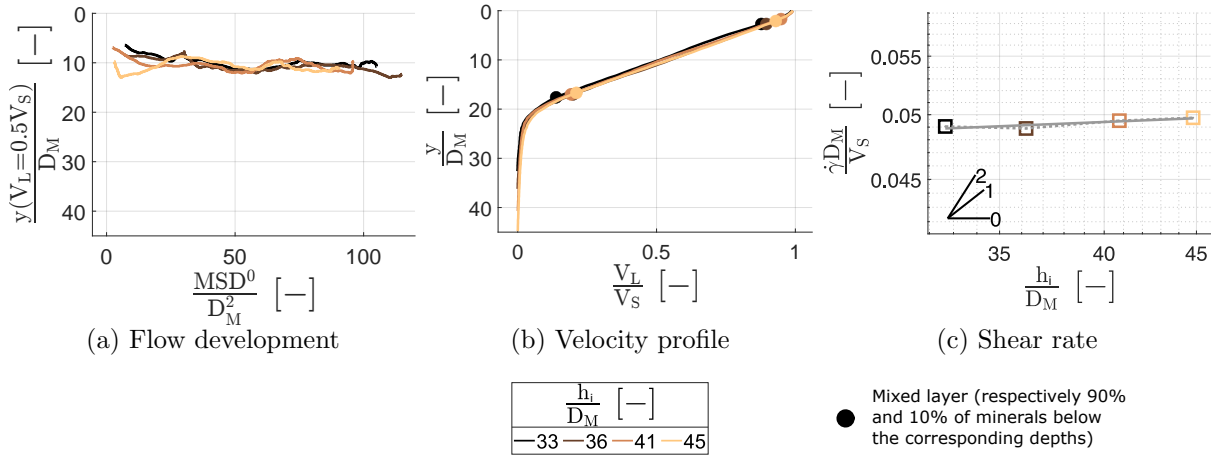


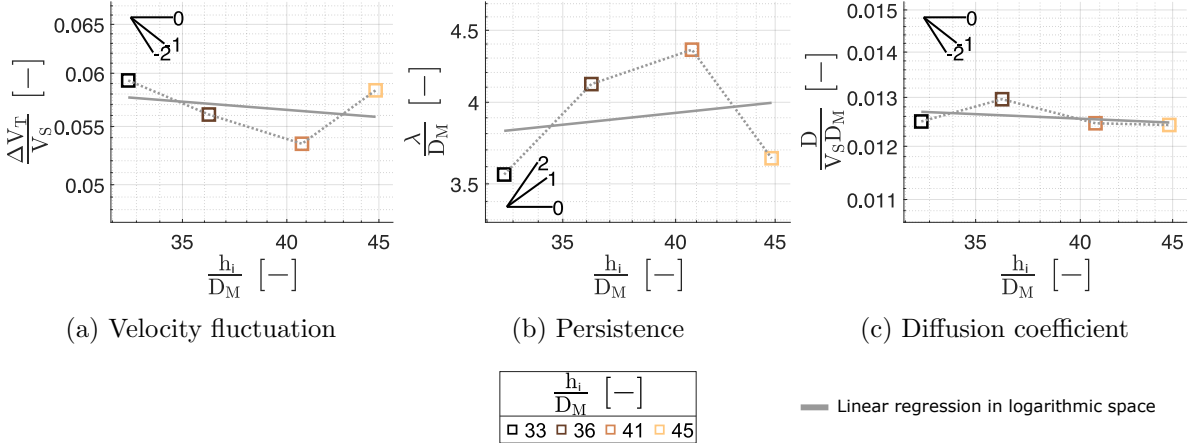
Figure 5.4: Mineral fraction according to  $h_i$

It seems that a lower  $h_i$  tends to increase mineral intake. Indeed, the concentration drops below 0.5 from a sliding distance of  $400 D_M$  for a  $h_i$  of  $33 D_M$ ,  $1300 D_M$  for a  $h_i$  of  $36 D_M$ , and close to  $2000 D_M$  for a  $h_i$  of  $41$  and  $45 D_M$ . There is however no trend in the diffusion front, with a depth at  $5000 D_M$  around  $23 D_M$  for all thicknesses. The results concerning kinematics are given in fig. 5.5.

Figure 5.5: Kinematics according to  $h_i$ 

Firstly, looking at the median depth in fig. 5.5a, there is no effect of thickness on this depth. For a  $MSD^0$  of  $80 D_M^2$ , this depth varies between 10 and  $12 D_M$ , which remains low compared to the variations of a given simulation. Moreover, this depth does not depend on mineral diffusion. The same applies to the velocity profiles in fig. 5.5b. Indeed, the velocity profiles are very similar in terms of slope and inflection point. As shown in fig. 5.5c, the corresponding shear rate does not depend on thickness. The slope in the linear space is equal to  $6.79 \cdot 10^{-5}$ . Note that for this study, the range of variation of  $h_i$  does not allow power laws to be extracted.

Results concerning diffusion are displayed in fig. 5.6.

Figure 5.6: Diffusion according to  $h_i$ 

Like the rheological results, thickness does not appear to influence velocity fluctuation (fig. 5.6a), persistence (fig. 5.6b) and diffusion coefficient (fig. 5.6c). The slopes in the linear space are respectively equal to  $-1.28 \cdot 10^{-4}$ ,  $1.16 \cdot 10^{-2}$  and  $-1.94 \cdot 10^{-5}$ . Assuming that the discrete medium represents the degraded rubber, these results mean that the thickness of the degraded rubber layer affects neither kinematics nor diffusion, as long as the minerals do not reach its boundary. In the current model, as this degradation is not simulated, the chosen thickness is a purely numerical parameter, and it is therefore convenient that the results are independent of this arbitrary choice.

## Highlights

- The shear rate does not depend on the thickness of the interfacial layer (which can be considered as the layer composed of degraded rubber). This is because, in the current configuration, the velocity is not transmitted through the whole layer.
- Velocity fluctuation, persistence and diffusion coefficient do not depend on the thickness of the interfacial layer.

### 1.3 Rubber particle size

In a more standard DEM approach, materials are assumed to be rigid (or at least very stiff). For this type of model, diffusion is directly controlled by particle size, as particles lead to a given spatial jump with a clear characteristic size (with a frequency that depends notably on shear rate). For a mono or polydisperse particle size distribution, particles can be reduced to a characteristic size (e.g. diameter). While a characteristic size may exist for minerals, it is less obvious for rubber soft particles. Moreover, although the term particle is used, the discrete medium defined in this model is a continuous medium (i.e. it corresponds to a pre-cut material). The aim of this section is to investigate whether the results depend on the size of the rubber particles (i.e. whether there is a characteristic rubber particle size). More generally, because of shorter computation time of DEM, it is often used as a first approximation, even in the case of non-negligible contact pressure compared to stiffness. This study will therefore also show whether this approximation works in the case of diffusion. To this end, 4 mean diameters ( $d_M^{rubber}$ ) were used (▶), equal to  $1.10^{#11}$  (▶),  $1.40^{#21}$  (▶),  $1.77^{#22}$  (▶) and  $2.09^{#23}$  (▶)  $D_M$  respectively. Mineral fraction maps are shown in fig. 5.7.

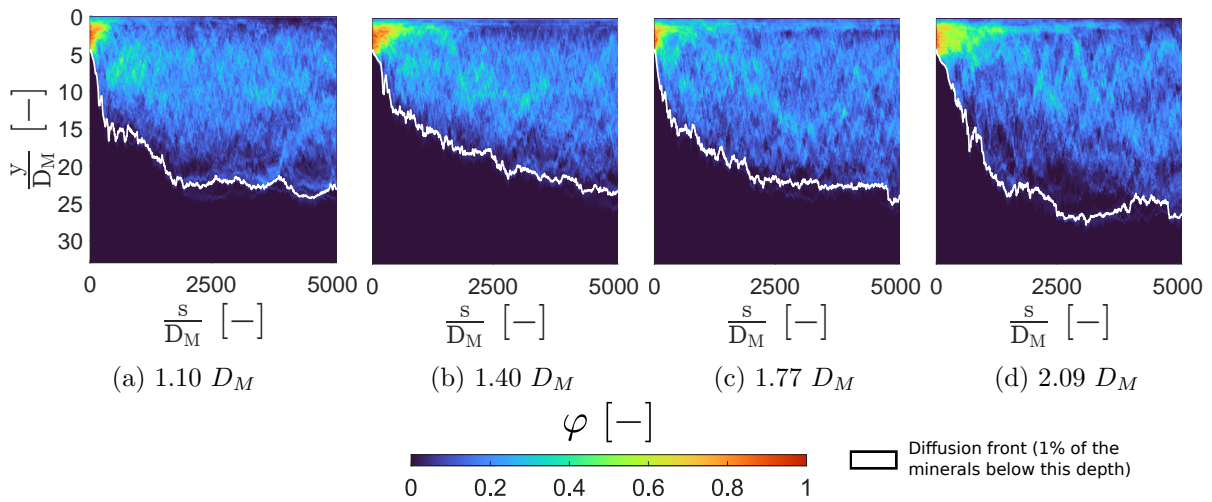
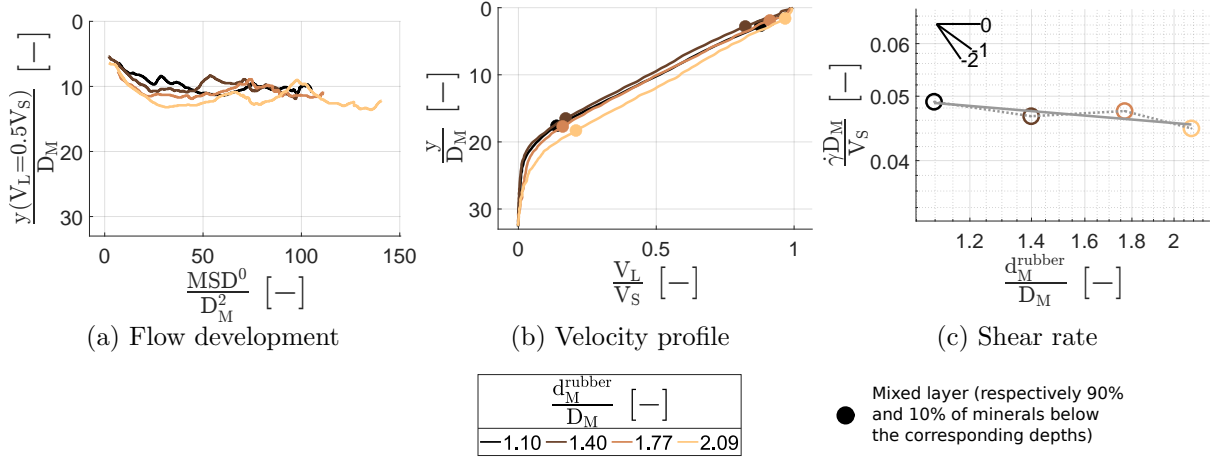


Figure 5.7: Mineral fraction according to  $d_M^{rubber}$

There is no overall significant trend on intake and diffusion front. A slightly slower intake can be observed for a  $d_M^{rubber}$  of  $2.09 D_M$ . This is due to the fact that large rubber particles tend to create large mineral agglomerates, making intake more difficult. Indeed, the early agglomerates from the mineral layer are broken up by the shearing action of the rubber particles. This shear requires the size of the rubber particles to be smaller than the size of the agglomerates, which is less and less the case as  $d_M^{rubber}$  increases. The results concerning kinematics are given in fig. 5.8.

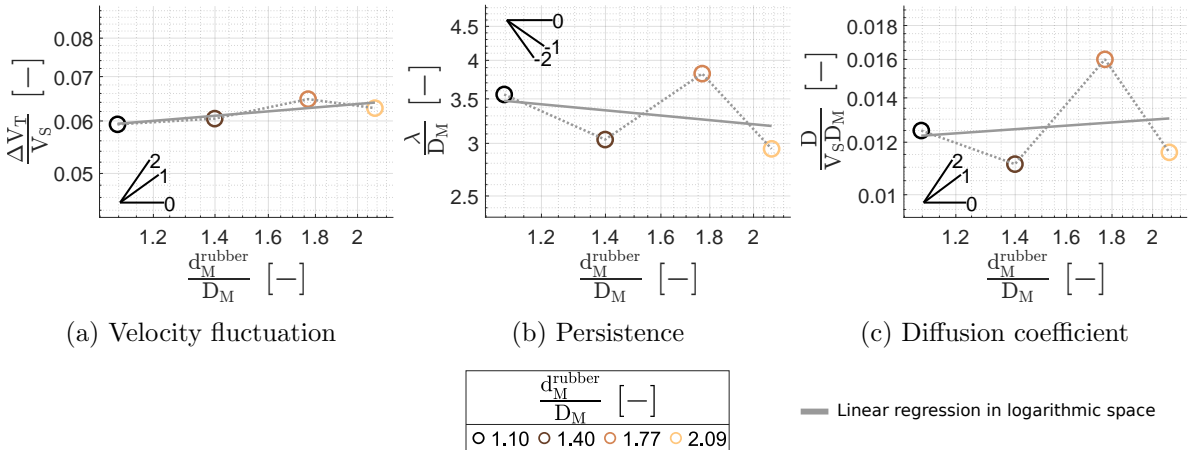


Figure 5.8: Kinematics according to  $d_M^{rubber}$ 

Firstly, with regard to the median depth in fig. 5.8a, there is a small trend for the median depth to increase with  $d_M^{rubber}$  up to a  $MSD^0$  of  $50 D_M^2$ . However, this trend then seems to disappear. For the steady state regime, velocity profiles in fig. 5.8b are similar, with a slightly deeper inflection point ( $+2 D_M$ ) for a diameter of  $2.09 D_M$ . However, these differences are small compared with the significant difference in size, which translates into an almost constant shear rate (fig. 5.8c) and therefore a relatively low exponent of  $-0.12$  (eq. (5.8)). It should be noted that, given the chaotic nature of such simulations, a parameter will only be considered as having an influence if the exponent is significantly different from zero and if a trend exists (e.g.  $\dot{\gamma}$  increases when the parameter under study increases). However, it is difficult to rigorously define a significance threshold for the exponent. Arbitrarily, an exponent of less than 0.15 will be considered non-significant if it is not associated with a clear trend.

$$\dot{\gamma} \propto d_M^{rubber^{-0.12}} \quad (5.8)$$

Results concerning diffusion are displayed in fig. 5.9.

Figure 5.9: Diffusion according to  $d_M^{rubber}$ 

The values for velocity fluctuation (fig. 5.9a), persistence (fig. 5.9b) and diffusion coefficient (fig. 5.9c) are also nearly constant. Indeed, the exponent lies around  $\pm 0.15$  (eqs. (5.9) to (5.11)), in the same order of magnitude as the shear rate. It can be considered negligible as it is not



supported by a clear trend (i.e.  $\Delta V_T$ ,  $\lambda$  and  $D$  do not evolve monotonically with  $d_M^{rubber}$ ). Three main comments can be made. The first is that while diffusion does not depend on the choice of rubber particle size, rubber material can however influence diffusion depending on its mechanical properties (e.g. cohesion). The second is that size non-dependency applies only to soft particles, and not to rigid ones (i.e. minerals), as discussed later. The third is that although a DEM model would drastically reduce computation times, it would induce an intrinsic definition of a rubber particle size, which is therefore questionable. This reinforces the idea that although the use of rigid bodies is still widely used even for soft materials compared to the corresponding stress, it is not always relevant in view of the new discrete methods considering deformation. These methods, like the one used in this study, are however computationally time-consuming, and further developments are needed for a more general adoption.

$$\begin{cases} \Delta V_T \propto d_M^{rubber^{0.11}} & (5.9) \\ \lambda \propto d_M^{rubber^{-0.14}} & (5.10) \\ D \propto d_M^{rubber^{0.09}} & (5.11) \end{cases}$$

### Highlights

- Shear rate, velocity fluctuation, persistence and diffusion coefficient do not depend on the size of the soft rubber particles.

## 2 External parameters

### 2.1 Contact pressure

The effect of contact pressure is investigated. To this end, the road-like surface was shifted in the transverse direction (and thus the compacity was also modified) for 4 different values (►). This corresponds to stabilized contact pressures over long sliding distance ( $\sigma_N$ ) of 0.075 (►), 0.110 (►), 0.192 (►) and 0.316 (►)  $E$ . The associated compacities (including minerals and rubber particles) are respectively equal to 0.84<sup>#24</sup>, 0.87<sup>#11</sup>, 0.90<sup>#25</sup> and 0.93<sup>#26</sup>. In some subsequent studies, the contact pressure will not be constant. This study will also provide a means of correcting and estimating certain parameters at equivalent contact pressure. Mineral fraction maps are shown in fig. 5.10.

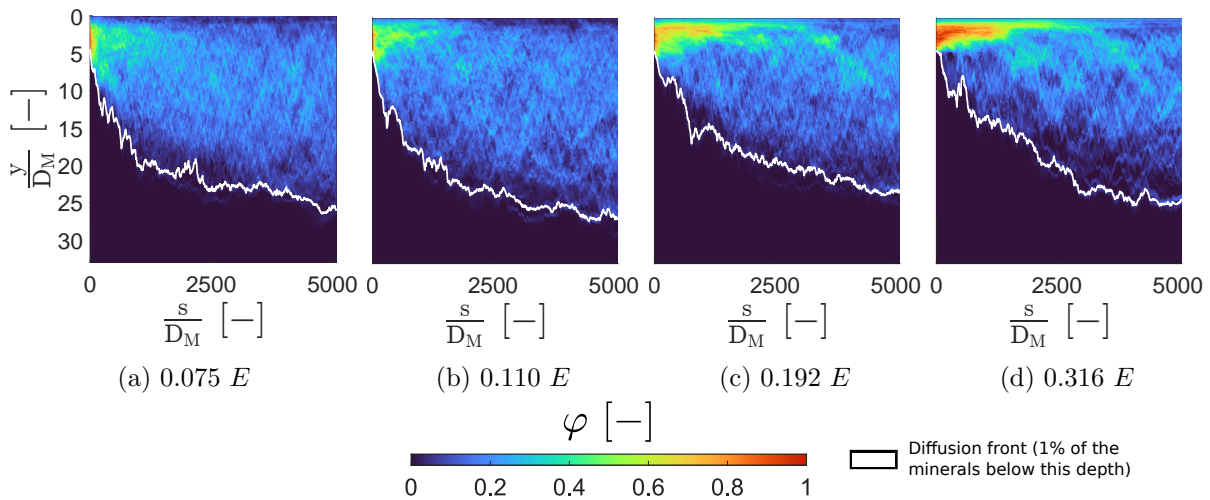


Figure 5.10: Mineral fraction according to  $\sigma_N$

First of all, the intake is slowed down as contact pressure increases. There are two main reasons for this. The first is that the higher the compacity, the more limited the reorganization of the mineral layer. Consequently, the minerals are mainly oriented in the sliding direction, leading to a decrease in shear stress (which is necessary for breaking up the initial mineral structure) due to a loss of grip. Indeed, the force transmission for higher contact pressure is mainly performed through the cohesive forces between the minerals and the rubber, and less through the punching of the minerals into the rubber material. The second is that a Coulomb friction law (tangential force increases with  $\sigma_N$ ) is used between the minerals, while a cohesive model (tangential force increases with contact area) is used between the rubber particles. For increasing contact pressure, the frictional force increases more than the cohesive one, so the strength of the mineral layer increases relative to that of the rubber layer. No trend is observed for the diffusion front. It is worth remembering that the front is not an indicator of the diffusion coefficient. Indeed, the front depends on the intake and not on the mineral distribution in the layer, in contrast to the diffusion coefficient. The results concerning kinematics are given in fig. 5.11.

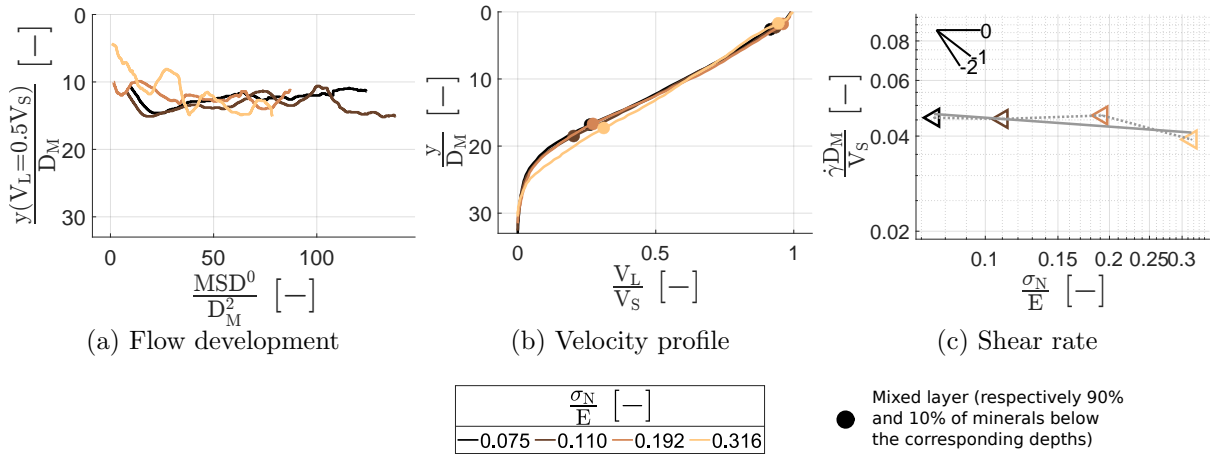


Figure 5.11: Kinematics according to  $\sigma_N$

First of all, it can be seen in fig. 5.11a that for a  $\sigma_N$  of  $0.316 E$ , the velocity in the interfacial layer seems to be stabilized from a  $MSD^0$  of  $40 D_M^2$ . This can be explained by the insufficient force transmission discussed above (lack of punching and reorganization of the mineral layer). At higher  $MSD^0$ , there is no effect of  $\sigma_N$  and mineral diffusion on the median depth. The velocity profiles displayed in fig. 5.11b are also very similar, with a slight deviation beyond a depth of  $11 D_M$  for a  $\sigma_N$  equal to  $0.316 E$ . This leads to an almost constant shear rate, as shown in fig. 5.11 with an exponent of  $-0.09$  (eq. (5.12)). The shear rate is decreasing from a  $\sigma_N$  of  $0.316 E$ , but more data are needed to confirm this trend.

$$\dot{\gamma} \propto \sigma_N^{-0.09} \quad (5.12)$$

Results concerning diffusion are displayed in fig. 5.12. A first interesting result in fig. 5.12a is that  $\Delta V_T$  varies while the shear rate is almost constant, whereas the two are closely linked. The exponent for  $\Delta V_T$  is equal to  $-0.29$  (eq. (5.13)), which since the effect of  $\Delta V_T$  is quadratic, is significant. Several scenarios can be put forward. The first is that the intake mode for higher pressures tends to generate less agglomerates (i.e. abrasion mechanism as shown in fig. 4.4). The effect of agglomerates will be investigated later. The second is the combination of overtaking mechanisms described previously. Indeed, at higher contact pressures, although the number of agglomerates decreases globally during sliding, there are several agglomerates creation/destruction cycles during diffusion. This leads to a coordinated rotation of minerals

(fig. 4.10a), with a non-zero offset (fig. 4.10b) after splitting. This results in a lower offset than if there had been no coordinated rotation.

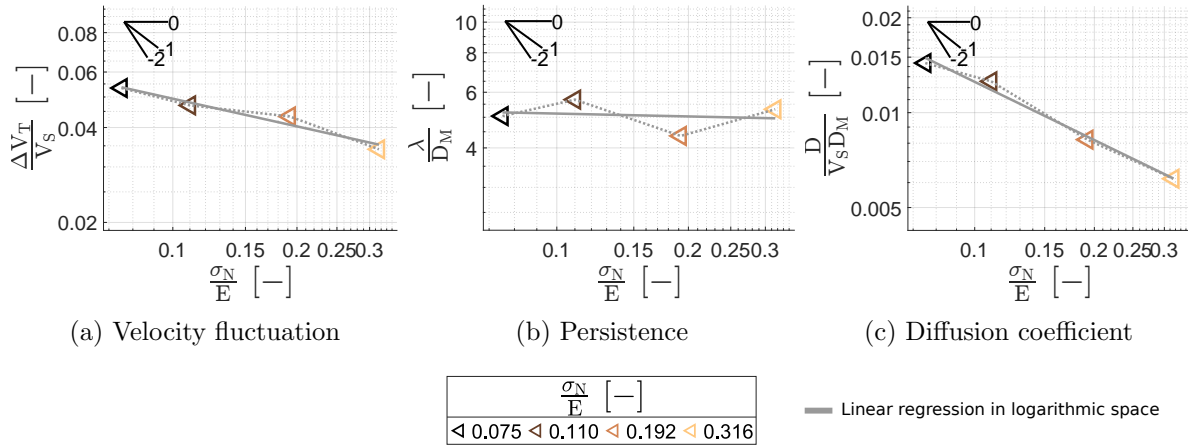


Figure 5.12: Diffusion according to  $\sigma_N$

Persistence does not depend on pressure (fig. 5.12b) with an exponent equal to -0.03 (eq. (5.14)). For persistence, it is useful to interpret the change in pressure solely as a change in compacity. This result shows that for a dense flow like this, there is no notion of a mean free path. Persistence is therefore due solely to deceleration, driven by the external forces applied on a mineral. In this case, these forces correspond to stiffness and cohesion, which will be studied in greater detail later. The decrease in  $\Delta V_T$  leads to a decrease in  $D$  (fig. 5.12c) with an exponent of -0.61 (eq. (5.14)). There is therefore a significant effect of pressure on diffusion.

$$\begin{cases} \Delta V_T \propto \sigma_N^{-0.29} & (5.13) \\ \lambda \propto \sigma_N^{-0.03} & (5.14) \\ D \propto \sigma_N^{-0.61} & (5.15) \end{cases}$$

### Highlights

- Shear rate does not depend on contact pressure.
- Velocity fluctuation and therefore diffusion coefficient decrease with increasing contact pressure.

## 2.2 Roughness

The aim of this study is to examine the influence of the road roughness. To this end, a high-pass filter was applied on the road-like surface (i.e. the asperities with the highest periods or lowest frequencies were filtered out). The 3 selected cut-off periods ( $\blacktriangleright$ ), called  $\lambda_c^{max}$ , are equal to 3.23<sup>#27</sup> ( $\blacktriangleright$ ), 10.33<sup>#28</sup> ( $\blacktriangleright$ ) and 51.46<sup>#11</sup> ( $\blacktriangleright$ )  $D_M$  respectively. The highest period corresponds to the width of the model. The generated surfaces are displayed in fig. 5.13. In the same way, a low-pass filter was applied (i.e. the asperities with the lowest periods or highest frequencies were filtered out). The 3 selected cut-off periods ( $\blacktriangleright$ ), called  $\lambda_c^{min}$ , are respectively equal to 0.44<sup>#11</sup> ( $\blacktriangleright$ ), 1.32<sup>#29</sup> ( $\blacktriangleright$ ) and 4.30<sup>#30</sup> ( $\blacktriangleright$ )  $D_M$ . The lowest period is close to the discretization step. The generated surfaces are displayed in fig. 5.14. Regardless of diffusion, this study also provides valuable results on how kinematics can be influenced by roughness using this type of model.

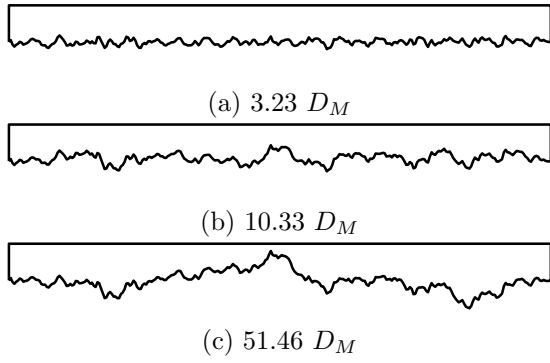


Figure 5.13: Road-like surface according to  $\lambda_c^{max}$

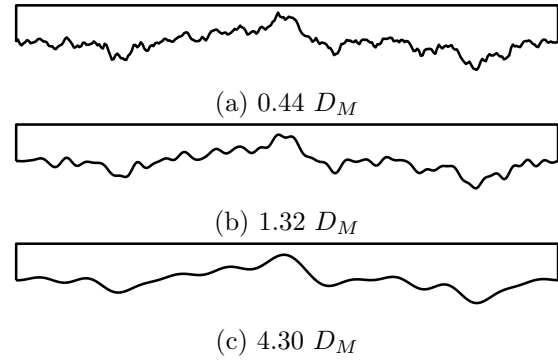


Figure 5.14: Road-like surface according to  $\lambda_c^{min}$

For both cases (high-pass and low-pass filters), no difference was observed in terms of kinematics (eqs. (5.16) and (5.20)), velocity fluctuation (eqs. (5.17) and (5.21)), persistence (eqs. (5.18) and (5.22)) and therefore diffusion coefficient (eqs. (5.19) and (5.23)). The only minor difference concerns the low-pass filter with  $\lambda_c^{min} = 4.30 D_M$ , for which after a  $MSD^0$  of  $50 D_M^2$ , there is a loss of traction at the interface of the road-like surface and the mixed layer. The transmission is completely lost from a  $MSD^0$  of  $87 D_M^2$ .

The effects of roughness are often linked to hysteresis [Emami et al., 2021], which can be characterized as a ratio between the viscous and elastic components of the visco-elastic material. However, this study focuses on a much smaller scale than that of real contact, and remains mainly plastic with irreversible displacement of the matter. It is therefore not surprising that the usual macroscopic trend is not found, and a larger scale should be required to study this type of effect. However, in some cases, stick-slip and therefore cyclic phenomena may occur. It is therefore possible that under particular conditions, notably with higher cohesion, a roughness effect may be observed.

$$\dot{\gamma} \propto \lambda_c^{max 0.01} \quad (5.16)$$

$$\dot{\gamma} \propto \lambda_c^{min 0.05} \quad (5.20)$$

$$\begin{cases} \Delta V_T \propto \lambda_c^{max -0.03} & (5.17) \\ \lambda \propto \lambda_c^{max 0.07} & (5.18) \\ D \propto \lambda_c^{max 0.01} & (5.19) \end{cases}$$

$$\begin{cases} \Delta V_T \propto \lambda_c^{min -0.02} & (5.21) \\ \lambda \propto \lambda_c^{min 0.06} & (5.22) \\ D \propto \lambda_c^{min 0.02} & (5.23) \end{cases}$$

### Highlights

- Shear rate, velocity fluctuation, persistence and diffusion coefficient do not depend on road-like surface roughness.

## 2.3 Mineral fraction

The effect of mineral quantity is investigated. In practice, the instantaneous concentration of minerals in the interfacial layer will depend on a balance between the diffusion rate and the wear rate (which is not considered in the current model). Thus, to obtain an idea of the influence of this instantaneous concentration, several mineral quantities will be used. To this end, the

amount of minerals is increased, while the amount of rubber is kept constant. Consequently, the thickness of the interfacial layer is increased to keep a compacity of 0.87. To obtain a parameter independent of this thickness, the mineral solid fraction ( $\phi^{mineral}$ ) is expressed as a function of the rubber solid fraction ( $\phi^{rubber}$ ). These fractions correspond to the sum of the areas of all the particles of a given material in relation to the area contained between the road-like surface and the rubber bulk. Respectively, 3 values of  $\frac{\phi^{mineral}}{\phi^{rubber}}$  were tested (►): 0.062<sup>#31</sup> (►), 0.123<sup>#11</sup> (►) and 0.247<sup>#32</sup> (►). Corresponding contact pressures are not constant and are equal to 0.08, 0.11 and 0.18  $E$ . Mineral fraction maps are shown in fig. 5.15.

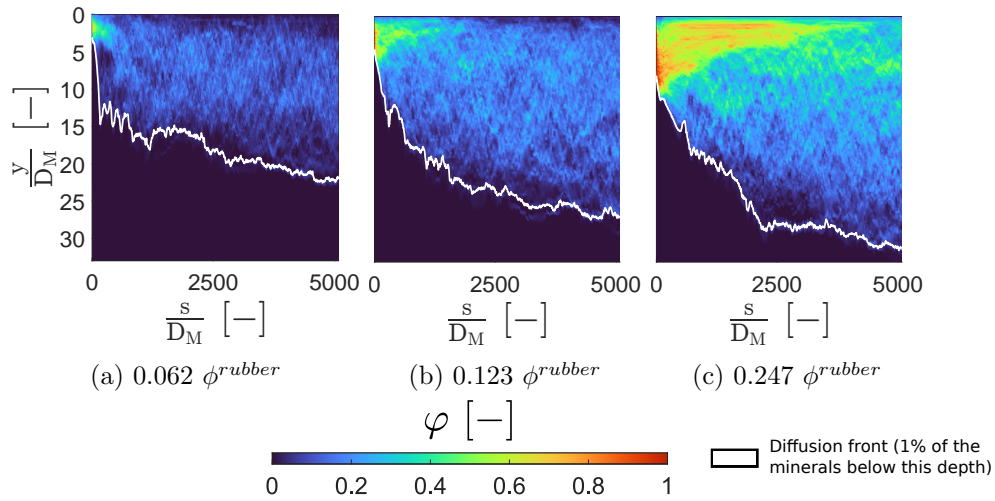


Figure 5.15: Mineral fraction according to  $\frac{\phi^{mineral}}{\phi^{rubber}}$

First of all, it should be noted that the reference ( $y = 0$  corresponding to the mean line of the road-like surface) has a real meaning for a long sliding distance, but is less clear at the beginning, especially with a thick initial mineral layer. Indeed, this layer has a mineral fraction greater than 0.7 and so the depth that can be considered as the surface of the mixed layer is difficult to identify. However, it seems that minerals close to the road-like surface are only inclined to diffuse if minerals at greater depths have diffused sufficiently. This suggests a critical mineral density that cannot be exceeded in a given configuration. Diffusion front is defined according to the 0.123  $\phi^{rubber}$  case (i.e. same mineral content below the front for all the cases). This front is deeper as the mineral fraction increases. The results concerning kinematics are given in fig. 5.16.

Concerning the median depth in fig. 5.16a, the duration (in the  $MSD$  sense) of the transient regime observed during shear initiation increases with the fraction. For the lowest fraction, it ends during the acceleration phase and is therefore not visible. For the 0.123  $\phi^{rubber}$  fraction, stabilization can be estimated at a  $MSD^0$  of 18  $D_M^2$  and 38  $D_M^2$  for the 0.247  $\phi^{rubber}$  fraction (i.e. double duration for double quantity). This should be confirmed by other simulations, but it suggests that the  $MSD^0$  required to reach a stable state is linearly proportional to the fraction. Once this regime has passed, the higher the fraction, the lower the median depth.

It should be noted that the starting point of the steady state regime for the highest fraction is taken at a  $MSD$  of 80  $D_M^2$ , due to the delay in intake. The velocity profiles show a constant shear rate in the mixed layer for a given fraction (fig. 5.16b) and this shear rate depends on the fraction (fig. 5.16c), with an exponent equal to -0.51 (eq. (5.24)). The shear rate is also expressed as a function of the mineral fraction in the mixed layer  $\phi_{ML}^{mineral}$  (i.e. mineral density). Indeed, even if a larger quantity of minerals is used, it is diluted in a thicker layer and therefore

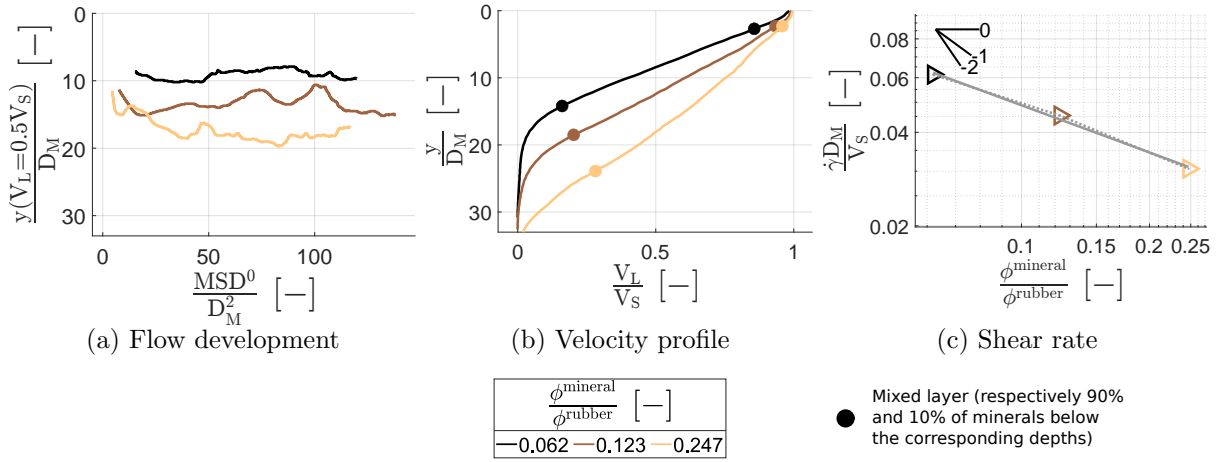


Figure 5.16: Kinematics according to  $\frac{\phi_{\text{mineral}}}{\phi_{\text{rubber}}}$

does not reflect the local state. Shear rate decreases as  $\phi_{ML}^{\text{mineral}}$  increases with an exponent of -0.98.

$$\dot{\gamma} \propto \left( \frac{\phi_{\text{mineral}}}{\phi_{\text{rubber}}} \right)^{-0.51} \propto (\phi_{ML}^{\text{mineral}})^{-0.98} \quad (5.24)$$

In a more realistic case, the quantity of minerals is higher and depends on the balance between diffusion flow, wear flow and, therefore, potentially on time. As the shear rate depends on this fraction, it could also be a function of time. Results concerning diffusion are displayed in fig. 5.17.

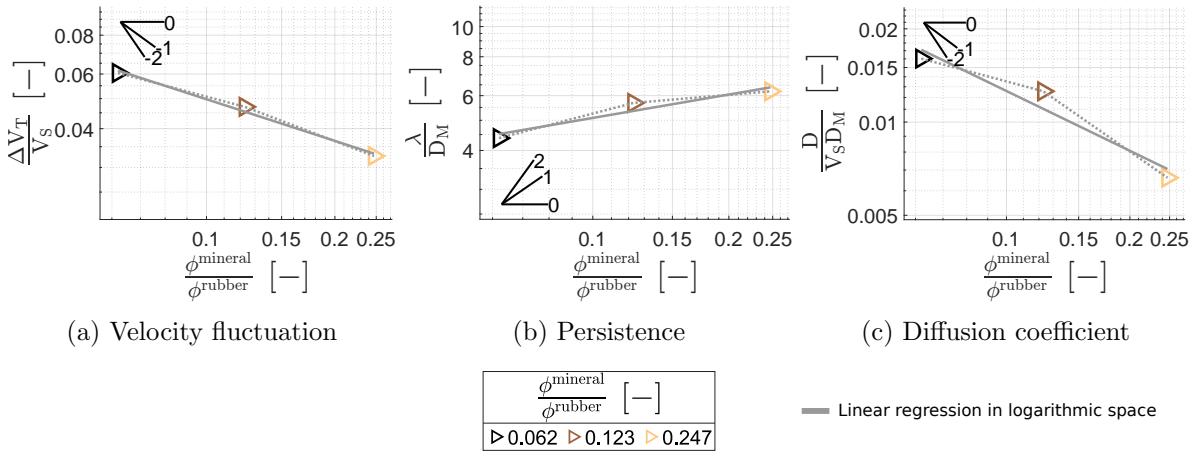


Figure 5.17: Diffusion according to  $\frac{\phi_{\text{mineral}}}{\phi_{\text{rubber}}}$

To compare the values without the  $\sigma_N$  effect, a correction based on the previous study of contact pressure is applied. It is assumed that proportionality can be written as the product of different empirical scalings. The values of  $\Delta V_T$  are then multiplied by  $(\frac{\sigma_{\text{real}}}{\sigma_{\text{ref}}})^{0.3}$  and the values of  $D$  by the same ratio with an exponent of 0.6. The  $\sigma_{\text{real}}$  corresponds to the real contact pressure, and the  $\sigma_{\text{ref}}$  can be any value from the study, since only the slope is considered. Furthermore, contact pressure has no significant influence on  $\dot{\gamma}$  and  $\lambda$ . The values shown on the graphs correspond to the uncorrected values. Concerning exponents, by taking the example of



velocity fluctuation, the uncorrected value will be named  $\Delta V_T(\sigma_N)$  and the corrected one  $\Delta V_T$ . The exponents given thereafter correspond to the corrected ones.

The value of velocity fluctuation decreases with the fraction (fig. 5.17a), with an exponent of -0.27 (eq. (5.28)). For persistence, it increases with the fraction (fig. 5.17b), with an exponent of 0.25 (eq. (5.29)). Consequently, the diffusion coefficient decreases with the fraction (fig. 5.17c), with an exponent of -0.30 (eq. (5.30)). The link between fraction or density and diffusion does not seem obvious, as the shear rate decreases more than the diffusion coefficient.

$$\left\{ \begin{array}{l} \Delta V_T(\sigma_N) \propto \left( \frac{\phi^{mineral}}{\phi^{rubber}} \right)^{-0.45} \\ \lambda(\sigma_N) \propto \left( \frac{\phi^{mineral}}{\phi^{rubber}} \right)^{0.25} \\ D(\sigma_N) \propto \left( \frac{\phi^{mineral}}{\phi^{rubber}} \right)^{-0.64} \end{array} \right. \quad (5.25) \quad (5.26) \quad (5.27)$$

$$\Delta V_T \propto \left( \frac{\phi^{mineral}}{\phi^{rubber}} \right)^{-0.27} \quad (5.28)$$

$$\lambda \propto \left( \frac{\phi^{mineral}}{\phi^{rubber}} \right)^{0.25} \quad (5.29)$$

$$D \propto \left( \frac{\phi^{mineral}}{\phi^{rubber}} \right)^{-0.30} \quad (5.30)$$

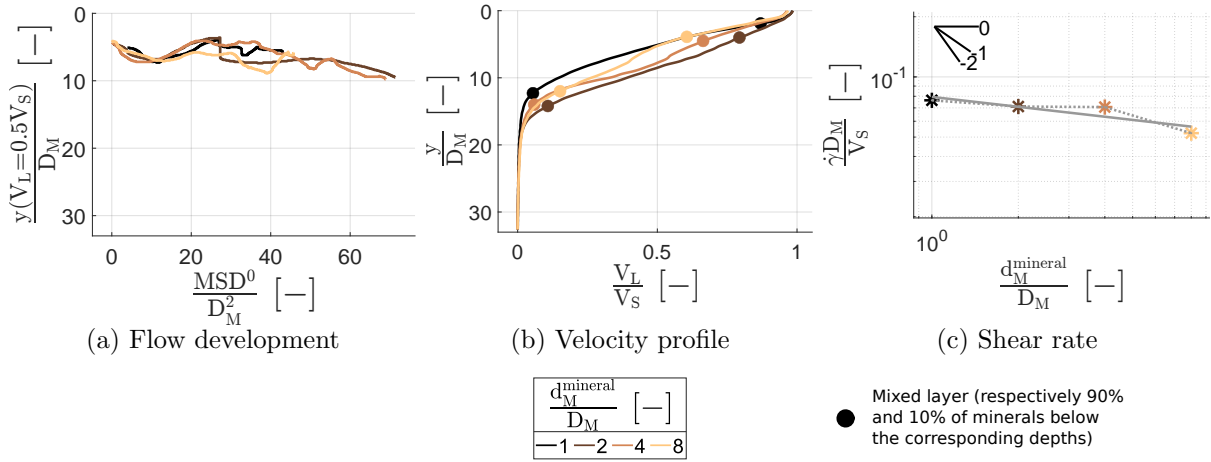
### Highlights

- The higher the mineral quantity, the deeper the velocity is transmitted and consequently the lower the shear rate.
- Kinematics depends only slightly on the distribution of minerals within the layer, but rather on the total embedded quantity, with a steady kinematics occurring rapidly compared to the diffusion scale.

## 2.4 Mineral size

It has been shown previously that rubber particle size does not play a role in the kinematics and diffusion of minerals. However, this could be different for mineral size. To investigate this effect, 4 homogeneous mineral size distributions were first studied (►), with a mean equivalent mineral diameter ( $d_M^{mineral}$ ) of 1<sup>#33</sup> (►), 2<sup>#34</sup> (►), 4<sup>#35</sup> (►) and 8<sup>#36</sup> (►)  $D_M$ . For the previous simulations, a log-normal distribution with a  $d_M^{mineral}$  of 1  $D_M$  was used. Using a homogeneous size distribution leads to inaccurate results. Indeed, for current material properties, the minerals form large agglomerates (all minerals are grouped into 3-4 agglomerates as shown in fig. B.12), which is not fully consistent with what is observed experimentally (agglomerates are also observed but in lesser proportions). The most plausible scenario is that a homogeneous distribution reduces geometric jamming, increasing contact between minerals and thus contact forces. This phenomenon is very similar to the increase in the number of agglomerates as sliding velocity decreases, as previously discussed. Indeed, the lower the velocity, the more minerals have time to reorganize, increasing contact between minerals and thus contact forces. A diffusive regime is nevertheless obtained and this study is interesting to understand the role of mineral size. The results concerning kinematics are given in fig. 5.18.

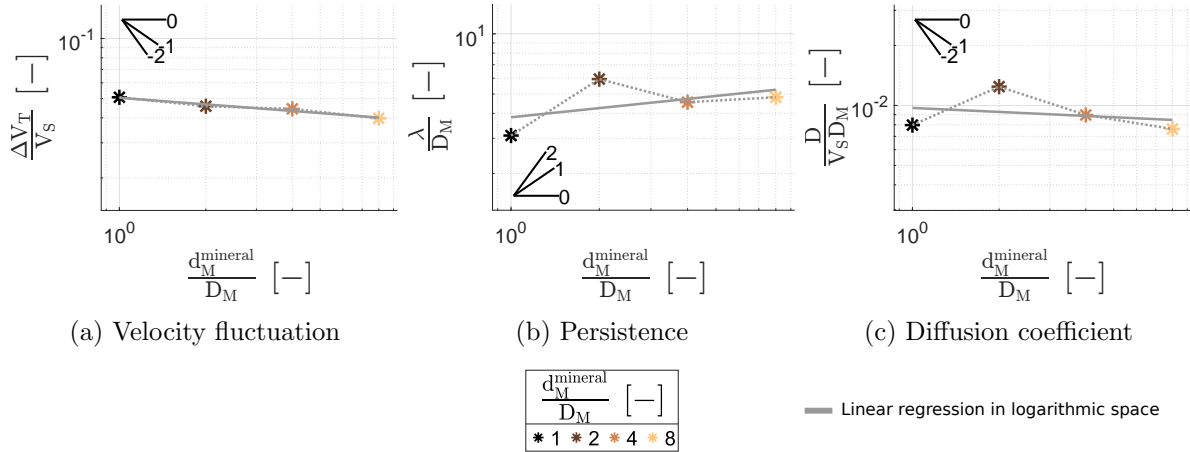


Figure 5.18: Kinematics according to  $d_M^{\text{mineral}}$ 

Firstly, it can be seen by looking at the median depth (fig. 5.18a) that the velocity is transmitted in a thinner layer than in the previous cases, with a value close to  $7 D_M$  for a  $MSD^0$  of  $40 D_M^2$  (compared to a depth close to  $13 D_M$  for a more standard case). This is attributed to a reinforcing effect of the minerals due to the large size of the agglomerates. There is no obvious trend between mineral sizes. Furthermore, for the 1 and 2  $D_M$  cases, the median depth decreases from a  $MSD^0$  of  $40 D_M^2$ . Regarding velocity profiles (fig. 5.18b), they remain relatively close and linear, although more disturbed than previously observed. Finally, the shear rate is only slightly dependent on mineral size (fig. 5.18c), with an exponent of -0.16 (eq. (5.31)).

$$\dot{\gamma} \propto d_M^{\text{mineral}-0.16} \quad (5.31)$$

Results concerning diffusion are displayed in fig. 5.19.

Figure 5.19: Diffusion according to  $d_M^{\text{mineral}}$ 

As for the study of the rubber particle size, small variations of the velocity fluctuation (fig. 5.19a), persistence (fig. 5.19b) and diffusion coefficient (fig. 5.19c) is observed. These variations are of the same order of magnitude of the shear rate (around  $\pm 0.15$ ), as written in eqs. (5.32) to (5.34).

$$\begin{cases} \Delta V_T \propto d_M^{mineral-0.11} & (5.32) \\ \lambda \propto d_M^{mineral0.15} & (5.33) \\ D \propto d_M^{mineral-0.07} & (5.34) \end{cases}$$

Interestingly, even though very different mineral sizes are used (a ratio of 8 between the smallest and largest), similar results are obtained. In particular, for a granular medium, the value of  $\Delta V_T$  is directly related to particle size. Actually, this result can be explained by the fact that, with the formation of agglomerates, the size of a given mineral no longer plays a role. The similarity of the results is due to the close size of the agglomerates.

To emphasize this point, the corresponding agglomerate sizes are now examined for all the simulations. Identifying a characteristic size for an agglomerate is challenging, as there are numerous configurations that can lead to many physical differences (aspect ratio, strength, etc.). A relatively simple agglomerate detection algorithm is used. A given mineral is considered to belong to another agglomerate if the closest distance between its center and the agglomerate contour is less than  $1 D_M$ . The process is then repeated for each mineral. Finally, only the length corresponding to the agglomerate surface projection on the transverse plane is considered, as it is this distance that is responsible of the transverse displacement. This value is then averaged over all agglomerates, and then over all steady-state time steps, giving  $d_T^{agg}$ . An illustration of  $d_T^{agg}$  is shown in fig. 5.20.

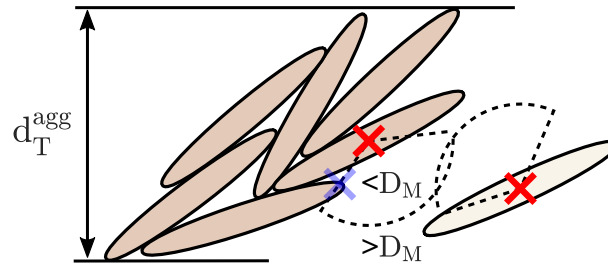


Figure 5.20: Illustration of  $d_T^{agg}$  for one agglomerate ( $D_M$  is magnified for clarity)

It is assumed that after contact between 2 agglomerates, the two are on average respectively shifted by half their diameters. The duration of this process is linked to the shear rate, giving the ratio  $\frac{\dot{\gamma} d_T^{agg}}{2V_S}$ , which will be compared to  $\frac{\Delta V_T}{V_S}$ . Results are displayed in fig. 5.21.

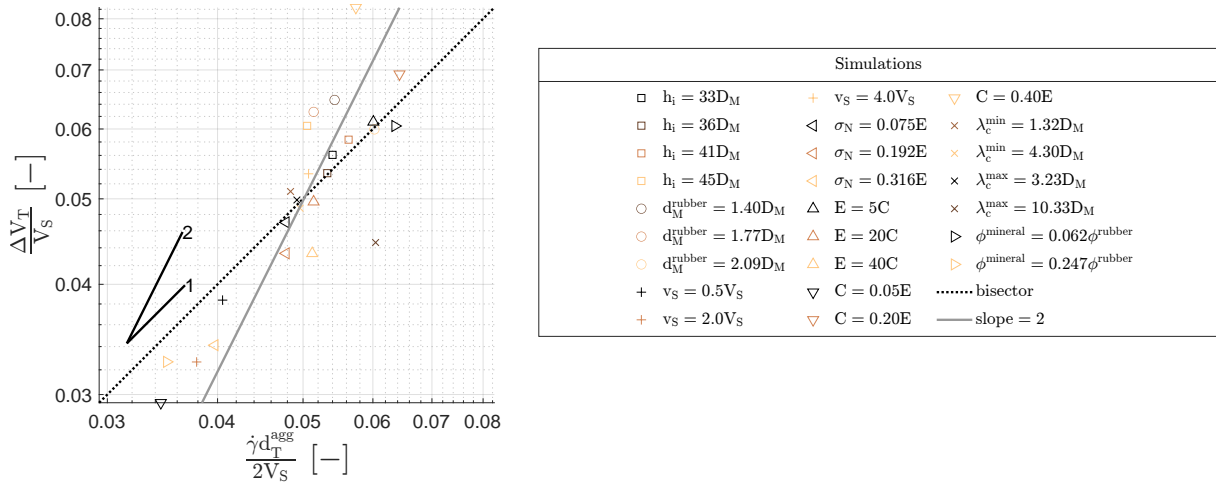


Figure 5.21: Comparison between the particle jump and the transverse velocity

The evolution of  $\Delta V_T$  seems to follow the one of  $\dot{\gamma} \frac{d_T^{\text{agg}}}{2}$ . More importantly, the values are close to the bisector, showing that in absolute terms (and not just a scaling), the characteristic size of the transverse displacement seems to correspond to the half of  $d_T^{\text{agg}}$ . This relationship is highly instructive with regard to the diffusion mechanism. Indeed, this tends to confirm that diffusion is due to repeated contacts between agglomerates. It should be noted that using  $D_M$  or even the equivalent diameter of the agglomerate would lead to a significant mean deviation and high dispersion. If a power law is fitted, an exponent of 1.28 is found.

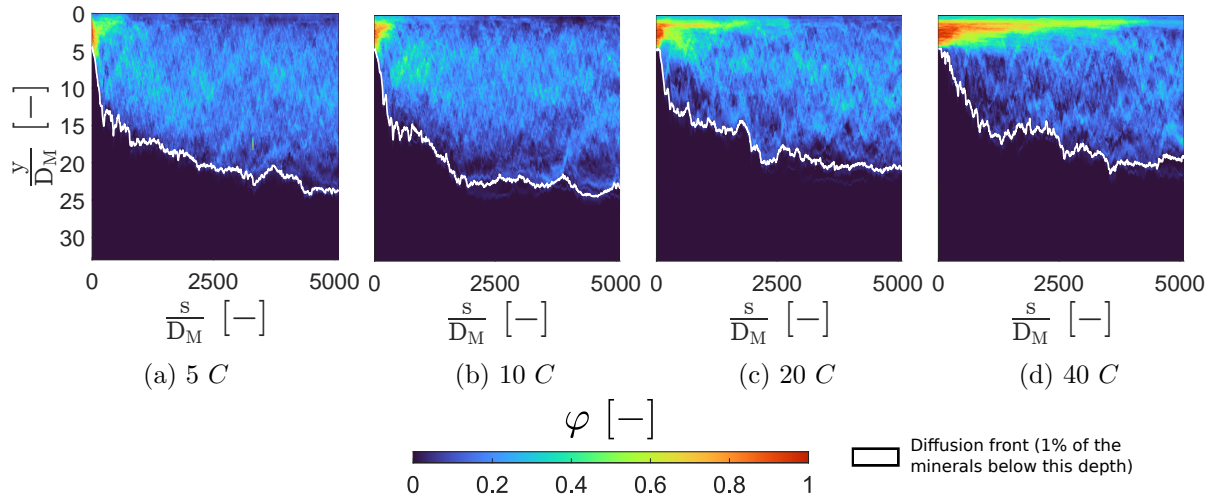
### Highlights

- The individual size of each mineral has no effect on shear rate and diffusion, and only the size of mineral agglomerates should be considered.
- This size corresponds to the mean transverse projection of the surface of the mineral agglomerates.
- Velocity fluctuation is close to the  $\dot{\gamma} \frac{d_T^{\text{agg}}}{2}$  ratio, reinforcing the idea that diffusion is due to repeated contacts between mineral agglomerates.

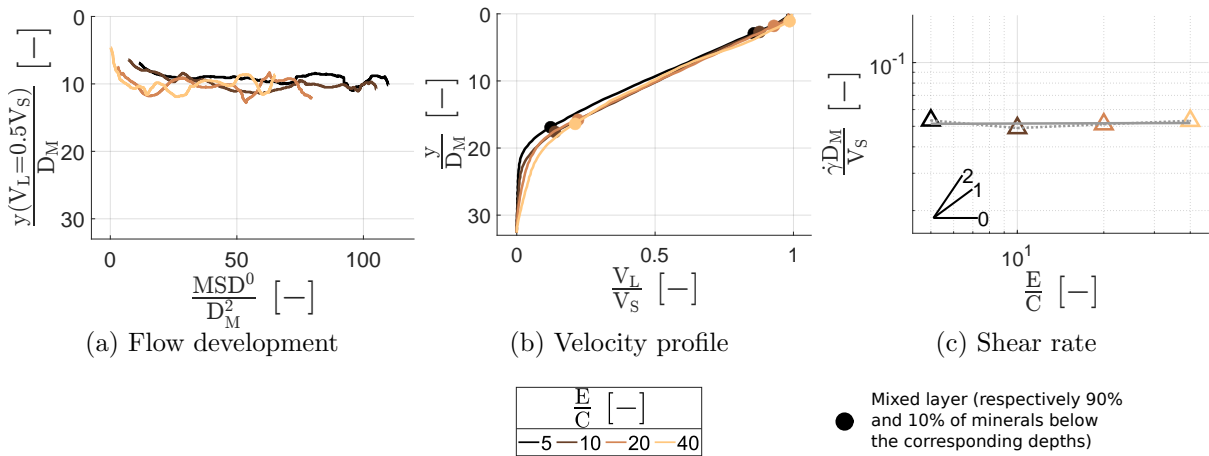
## 3 Rubber properties

### 3.1 Rubber stiffness

In this work, rubber properties are studied through 2 main components: stiffness and cohesion. One of the fundamental characteristics of a rubber-like material is its low stiffness. To understand this effect, 4 stiffnesses ( $E$ ) were used (►), with respective values of 5<sup>#37</sup> (►), 10<sup>#11</sup> (►), 20<sup>#38</sup> (►) and 40<sup>#39</sup> (►)  $C$ . Corresponding contact pressures are not constant and are equal to 0.79, 0.95, 1.76 and 2.56  $C$ . Unlike the contact pressure study, the compacity is constant (the material being quasi-incompressible). However, the fraction varies locally. One notable difference, if stiffness increases, is that the solid fraction decreases in areas of high rubber concentration, and increases in areas of high mineral fraction (cf. fig. B.13). This results in higher contact surfaces, and therefore higher contact forces between minerals. The direct consequence is that minerals tend to form more agglomerates. Mineral fraction maps are shown in fig. 5.22.

Figure 5.22: Mineral fraction according to  $E$ 

It can be seen that intake is delayed as stiffness increases. This is firstly due to an absolute increase in contact pressure, but the delay is significant and cannot be explained solely by the change in contact pressure. Indeed, in comparison, the contact pressure for the highest stiffness is equal to 0.8 times the highest contact pressure in the previous study, whereas the delay here is higher. The main reason is that for a softer material, the minerals can more easily punch the rubber material, creating significant stress localization and thus initiating diffusion more rapidly. For a stiffer rubber material, the material is less deformed and the minerals tend to slide across the rubber surface. This leads to a mechanism very similar to abrasion. The depth of the diffusion front depends mainly on how the intake is delayed, with a depth at 5000  $D_M$  of 24  $D_M$  for the lowest stiffness and 19  $D_M$  for the highest one. The results concerning kinematics are given in fig. 5.23.

Figure 5.23: Kinematics according to  $E$ 

The median depth depends neither on mineral diffusion nor on stiffness (fig. 5.23a), with an average value of 10  $D_M$ . An interesting point is that despite a significant difference in delay, whatever the stiffness, the median depth stabilizes for a  $MSD^0$  around 15  $D_M^2$ . This clearly shows that this transient regime depends on the minerals and is not just an effect of shear initiation. The velocity profiles are also very similar (fig. 5.23b). It may be noted that as stiffness increases, velocity increases in the mineral-free sublayer (beyond a depth of 20  $D_M$ ).

As a reminder, over long time scales, there is a slow evolution of the velocity profile due to the progressive transmission of velocity by the minerals at the front. This transmission can be compared to what is observed during intake. Knowing that intake is strongly dependent on stiffness, it would be interesting to study the effect of stiffness on the progression of the front over long periods of time, as a difference can already be observed here. However, during the steady-state stage, the shear rate can be considered constant (fig. 5.23c) with an exponent of 0.00 (eq. (5.35)).

$$\dot{\gamma} \propto E^{0.00} \quad (5.35)$$

Results concerning diffusion are displayed in fig. 5.24.

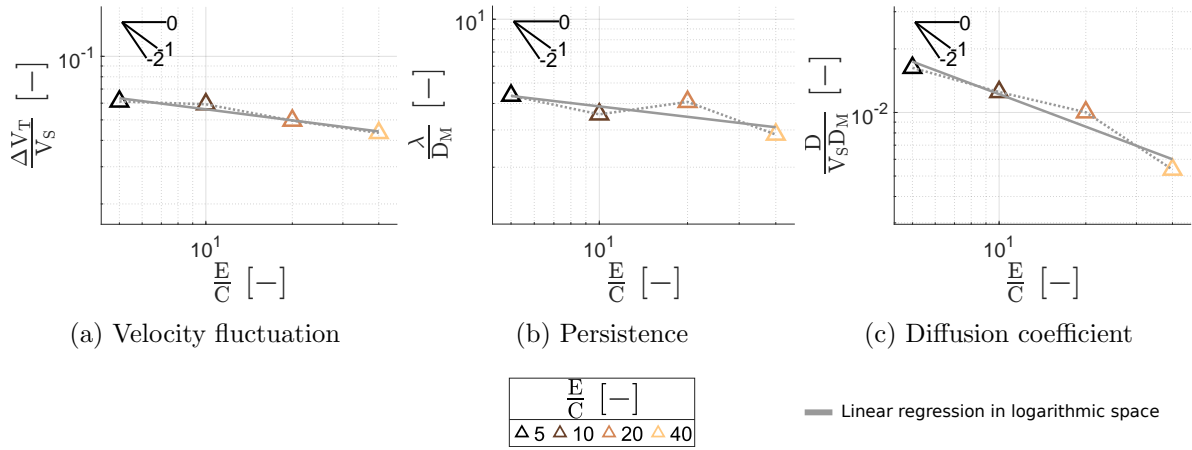


Figure 5.24: Diffusion according to  $E$

The exponents given below correspond to values for which the contact pressure is corrected. Firstly, the velocity fluctuation decreases with  $E$  due to an increase in contact pressure (fig. 5.24a). Indeed, after correction, the exponent is equal to 0.01 (eq. (5.39)). There is a slight decrease in persistence with stiffness (fig. 5.24b), with an exponent of -0.16 (eq. (5.40)). Although low, this decrease is consistent with an increase in the elastic forces exerted on the minerals for increasing stiffness, resulting in higher deceleration. The increase in persistence therefore leads to an increase in the diffusion coefficient (fig. 5.24c). As far as material properties are concerned, it is difficult to describe an increase as small, since depending on the conditions, these properties can vary over several orders of magnitude. Assuming that the glass transition is sufficiently far away (in terms of frequency and temperature), the dependence of diffusion on stiffness can be qualified as low, with an exponent of -0.15 (eq. (5.41)).

$$\begin{cases} \Delta V_T(\sigma_N) \propto E^{-0.17} & (5.36) \\ \lambda(\sigma_N) \propto E^{-0.16} & (5.37) \\ D(\sigma_N) \propto E^{-0.51} & (5.38) \end{cases}$$

$$\begin{cases} \Delta V_T \propto E^{0.01} & (5.39) \\ \lambda \propto E^{-0.16} & (5.40) \\ D \propto E^{-0.15} & (5.41) \end{cases}$$

### Highlights

- Shear rate, velocity fluctuation, persistence and diffusion coefficient do not depend on rubber stiffness.

### 3.2 Rubber cohesion

The second parameter studied with regard to rubber properties is cohesion. As mentioned in the chapter on indentation, cohesion corresponds to the stress bonding the rubber particles together. For indentation, this can easily be related to a yield stress. However, its meaning for a shear interface is less straightforward. First, the notion of viscosity on such shear rate is unknown. One of the assumptions made previously was that, since the relaxation time was much higher than the time ranges under study, this viscosity could be seen as a time-independent plastic dissipation, modeled by cohesion. However, this view is not entirely satisfactory. For example, at high cohesion, crack propagation phenomena appear (fig. 4.5), which do not seem to be related to material viscosity. For these reasons, the precise interpretation that can be made of this widely-used parameter remains an open question. In the present case, it could be likened to a dynamic viscosity.

To study the effect of cohesion ( $C$ ), 4 different cohesions were used ( $\blacktriangleright$ ), with respective values of  $0.05^{#40}$  ( $\blacktriangleright$ ),  $0.10^{#11}$  ( $\blacktriangleright$ ),  $0.20^{#41}$  ( $\blacktriangleright$ ) and  $0.40^{#42}$  ( $\blacktriangleright$ )  $E$ . The contact pressure is not constant and is equal to  $0.095$ ,  $0.110$ ,  $0.164$  and  $0.250 E$ . Mineral fraction maps are shown in fig. 5.25.

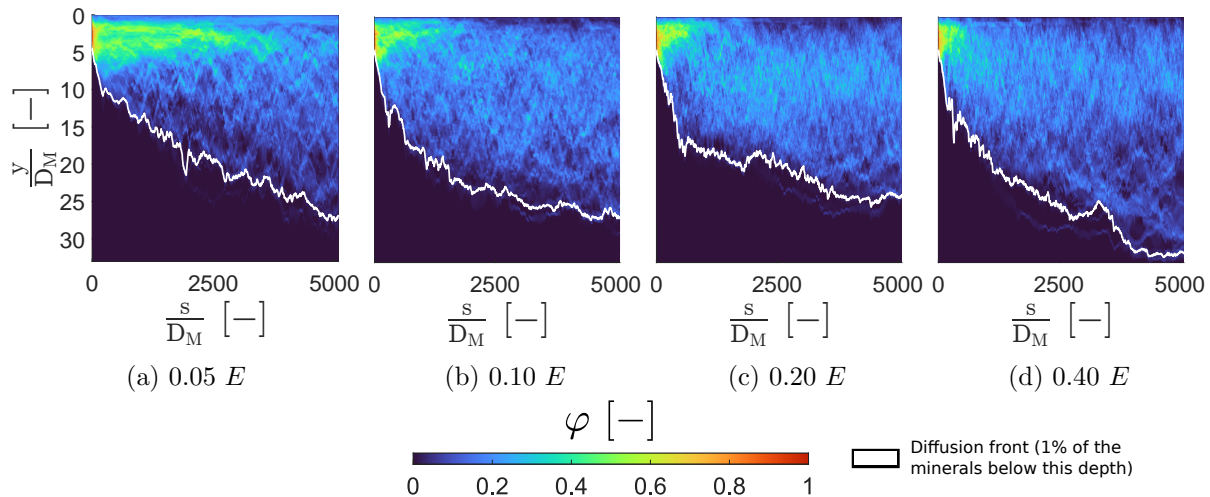


Figure 5.25: Mineral fraction according to  $C$

A surprising result at first sight is that the higher the cohesion, the faster the intake. The reason is similar to the one given for stiffness. Intake is facilitated by the punching of the mineral on the rubber, creating stress localizations. However, at low cohesion values, the link between rubber particles is broken before significant deformation is reached. As a result, sliding occurs close to the mineral-rubber interface (i.e. creation of a shear band in the rubber material), reducing the stress required for minerals to be embedded and form a mixed layer. Another way of interpreting this phenomenon is that, as rubber particle reorganization is easier, it tends to reduce stress. Generally speaking, intake is facilitated by significant deformation of the rubber material. This deformation requires a low stiffness in relation to the contact pressure and a high cohesion to reduce effects similar to a plastic softening phenomenon.

For a sliding distance of  $5000 D_M$  and increasing cohesion, the depth of the front is equal to  $27$ ,  $27$ ,  $24$  and  $32 D_M$  respectively. There is a threshold effect for a cohesion of  $0.4 E$ . For this cohesion value, crack openings are significant during intake (less during diffusion), and cracks even reach the bulk of the rubber. This leads to a front that evolves more deeply, but a lower concentration of minerals is observed at depths ranging from  $15$  to  $23 D_M$ . This results in a



diffusion coefficient that is actually not higher, as discussed below. This non-monotonic behavior can be highlighted in the results about kinematics (fig. 5.26).

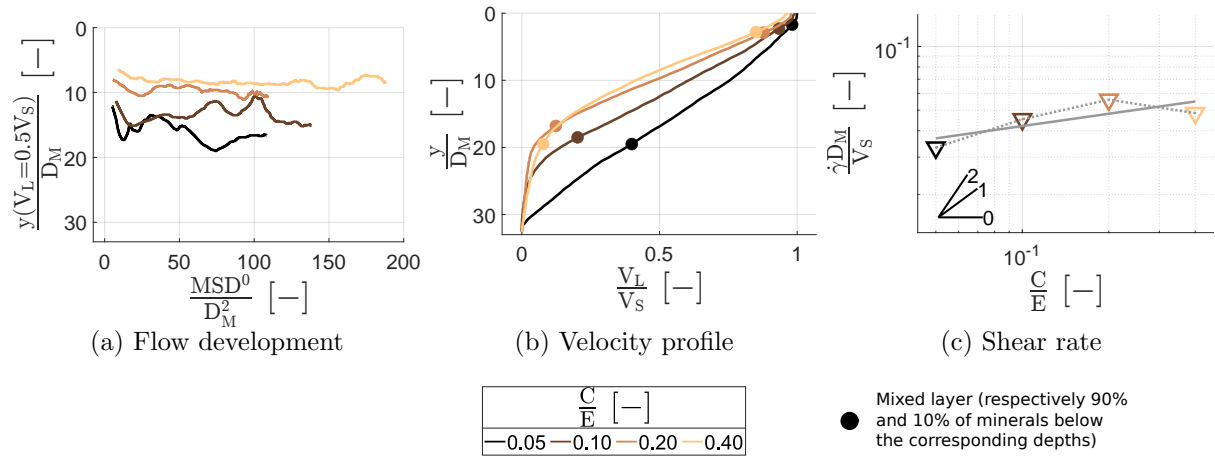


Figure 5.26: Kinematics according to  $C$

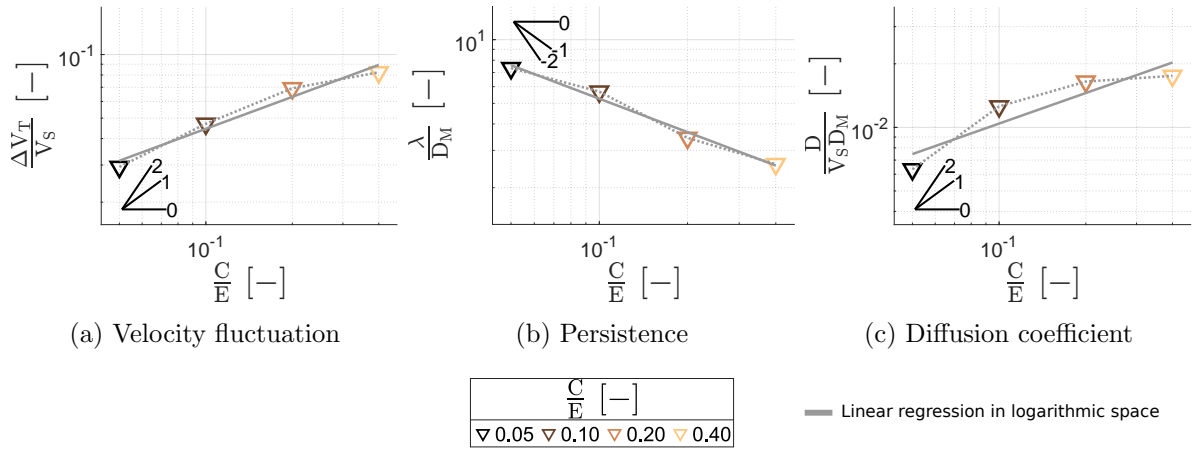
Firstly, as cohesion increases, median depth decreases (fig. 5.26a). This is because higher cohesion values allow the same amount of energy to be dissipated in a thinner layer. In addition, the median depth does not depend on diffusion. The dependence of median depth on cohesion can be observed by examining velocity profiles (fig. 5.26b). Regardless of the cohesion value, the shear rate is constant in the mixed layer. For a cohesion of  $0.05 E$ , the velocity is transmitted through the whole interfacial layer. The non-monotonic behavior is also reflected in the velocity profiles, where the profile no longer evolves from a cohesion of  $0.20 E$ . This can be highlighted by examining the shear rate (fig. 5.27c). It can be seen that the shear rate increases with cohesion up to a value of  $0.2 E$ , and then decreases. If the cohesion of  $0.4 E$  is taken into account, the exponent is equal to  $0.19$  (eq. (5.42)), and otherwise it is equal to  $0.38$  (eq. (5.43)).

$$\begin{cases} \dot{\gamma} \propto C^{0.19} & (5.42) \\ \dot{\gamma} \propto C^{0.38} \text{ for } C \leq 0.2E & (5.43) \end{cases}$$

It is difficult to give a definitive answer to this non-monotonic behavior. A first possibility is that a minimum period of time is required for the reorganization of the minerals in the mixed layer, and the shear rate cannot exceed a certain value, resulting in a minimum thickness. If this time is exceeded, the layer is jammed, as a rigid mineral cannot be sheared. This phenomenon is similar to the jamming observed in granular media. A second possibility is the existence of a ratio between the crack opening velocity and the relaxation velocity of each rubber particle. Results concerning diffusion are displayed in fig. 5.27.

The exponents given below correspond to values for which the contact pressure is corrected and excluding the  $0.4 E$  cohesion. It should also be noted that contact pressure has no influence on kinematics and non-monotonic results are present even after pressure correction. The higher the cohesion, the higher the velocity fluctuation (fig. 5.27a), with an exponent equal to  $0.74$  (eq. (5.50)). Indeed, there is first an effect of the increasing shear rate. Moreover, the increase in cohesion leads to a storage of elastic energy which is then released in the form of kinetic energy, and thus to an increase in velocity fluctuation. It is particularly important to put this point in perspective with the boundary conditions. Indeed, the thickness of the interfacial layer ( $h_i$ ) is constant. If the road-like surface were controlled according to a given contact pressure, it is highly likely that an increase in  $h_i$  would be observed, with much less crack propagation phenomena.



Figure 5.27: Diffusion according to  $C$ 

Persistence decreases with cohesion (fig. 5.27c), with an exponent of -0.55 (eq. (5.51)). There is also an effect of increasing shear rate. In addition, as cohesion increases, rubber is less able to reorganize itself, and therefore the effect of stress softening decreases. This leads to higher stresses on the mineral, and therefore greater deceleration. Consequently, the diffusion coefficient increases with cohesion (fig. 5.27c), with an exponent of 0.93 (eq. (5.52)).

It is interesting to compare the results for stiffness and cohesion. Indeed, stiffness has very little effect compared with cohesion, with an exponent for the diffusion coefficient of -0.15 versus 0.93 for cohesion. This suggests that diffusion is driven by dissipative phenomena.

$$\begin{cases} \Delta V_T(\sigma_N) \propto C^{0.50} & (5.44) \\ \lambda(\sigma_N) \propto C^{-0.52} & (5.45) \\ D(\sigma_N) \propto C^{0.48} & (5.46) \end{cases}$$

$$\begin{cases} \Delta V_T \propto C^{0.65} & (5.47) \\ \lambda \propto C^{-0.52} & (5.48) \\ D \propto C^{0.77} & (5.49) \end{cases}$$

$$\text{For } C \leq 0.2 E \begin{cases} \Delta V_T \propto C^{0.74} & (5.50) \\ \lambda \propto C^{-0.55} & (5.51) \\ D \propto C^{0.93} & (5.52) \end{cases}$$

### Highlights

- The lower the cohesion of the rubber, the deeper the velocity is transmitted and, consequently, the lower the shear rate. Indeed, as cohesion decreases, a greater thickness is required to dissipate the energy introduced into the system.
- Velocity fluctuation and persistence are strongly dependent on cohesion. As a result, the diffusion coefficient is almost linearly proportional to cohesion. Firstly, this is due to the change in shear rate. Secondly, higher cohesion leads to higher storage and release of elastic energy, which increases velocity fluctuation.

## Conclusion

This study showed how kinematics and diffusion depend on several parameters. These changes were then linked to mechanisms within the interfacial layer. A summary of the results with the main (hypothetical) associated explanation is given table 5.1.

Preliminary analyses have laid the groundwork for diffusion in solid flows. It has been shown, for example, that velocity fluctuations are linked to the size of mineral agglomerates. This shows that, despite a different medium compared with a granular one (the medium most closely related to the scope of this work), the underlying mechanism is the same, with particles that have to overtake each other due to the relative velocity. It can also be noted that even a medium without minerals (i.e. only deformable particles) exhibits diffusion. However, this point has not been addressed because of its specificity.

Some parameters showed interesting effects for further studies. In particular, the effect of mineral quantity confirmed an initial transient state of kinematics, followed by a steady state. Furthermore, the shear rate reached during the steady state is directly related to the quantity of minerals. Consequently, if any model needs to integrate wear mechanisms, it must be able to take into account this dependence of shear rate on mineral quantity.

Rubber shows a mineral diffusion that can be explained by two specific characteristics. The first is a low stiffness. It has been shown that low stiffness allows minerals to be punched into the rubber material, resulting in much faster intake. It can be assumed that the faster this intake takes place, the less the minerals are ejected from the contact and therefore the more penetrate the rubber. This low stiffness must be coupled with a high enough cohesion, otherwise the stress softening will not enable sufficient strain to be reached. During steady-state diffusion, high cohesion increases both shear rate and velocity fluctuation. This dual effect significantly increases the diffusion coefficient. In summary, diffusion is facilitated by low stiffness and high cohesion, which seems to be consistent with a material such as rubber.

Highlights

	Kinematics	Diffusion
$\triangle$ Sliding velocity	$\dot{\gamma} \propto v_S^{0.74}$ Velocity is transmitted to deeper depths due to mineral inertial effects, reducing the shear rate	$D \propto v_S^{1.36}$ Inertia increases persistence and therefore $D$
Interfacial layer thickness	No significant effect	No significant effect
Rubber particle size	$\dot{\gamma} \propto d_M^{rubber-0.12}$ No significant effect	$D \propto d_M^{rubber0.09}$ No significant effect
$\triangle$ Contact pressure	$\dot{\gamma} \propto \sigma_N^{-0.09}$ No significant effect	$D \propto \sigma_N^{-0.61}$ Modification of overtaking mechanisms, leading to a decrease in velocity fluctuation and therefore in $D$
Roughness (high-pass filter)	$\dot{\gamma} \propto \lambda_c^{max0.01}$ No significant effect	$D \propto \lambda_c^{max0.01}$ No significant effect
Roughness (low-pass filter)	$\dot{\gamma} \propto \lambda_c^{min0.05}$ No significant effect	$D \propto \lambda_c^{min0.02}$ No significant effect
$\triangle$ Mineral fraction	$\dot{\gamma} \propto \frac{\phi^{mineral}}{\phi^{rubber}}^{-0.51}$ Increased reinforcing effect of minerals, resulting in transmission to deeper depths and therefore a decrease in $\dot{\gamma}$	$D \propto \frac{\phi^{mineral}}{\phi^{rubber}}^{-0.30}$ Change in shear rate
Stiffness	$\dot{\gamma} \propto E^{0.00}$ No significant effect	$D \propto E^{-0.15}$ No significant effect
$\triangle$ Cohesion	$\dot{\gamma} \propto C^{0.38}$ Higher cohesion allows energy to be dissipated in a thinner layer and therefore an increase in $\dot{\gamma}$	$D \propto C^{0.93}$ Storage and release of elastic energy increases velocity fluctuations, which, coupled with an increase in $\dot{\gamma}$ , increases $D$

Table 5.1: Summary of the effect of several parameters under steady-state regime



# General conclusion

Tire wear particles are composed of a mixture of rubber from the tire tread and minerals from the road. However, the mechanisms occurring prior to particle generation are not fully understood. In particular, it has been observed that minerals tend to migrate deeply into the tire tread. To study this phenomenon, a numerical model of a rubber-like material sliding on a road-like surface was developed. This model is based on an experimental reference configuration. The main question of this work is how and why minerals are migrating within the rubber-like material? A particular focus was placed on the flow kinematics, which is closely related to this migration. It was first necessary to characterize the rubber-like material in order to define the inputs of the numerical model. This was followed by a global analysis of the results from the numerical model, in order to understand what type of physics was involved behind this migration. Finally, an in-depth study of the influence of several parameters was carried out.

To successfully study diffusion, it was first necessary to develop a characterization method adapted to soft particles. This was achieved by reverse analysis of a characterization technique that had to meet 3 key requirements: elastic deformation, plastic flow and unicity of the solution. To this end, indentation tests were carried out. A method has been proposed to identify two numerical parameters, namely the stiffness and cohesion of the rubber material. Whereas indentation models on a material composed of discrete bodies were mainly intended for irreversible processes (e.g. fracture), it is possible with this method to obtain a significant elastic recovery during unloading.

Flow kinematics during indentation has been investigated and the result is similar to that obtained experimentally. For example, plastic flow is observed in the tangential direction to the indentation axis. This shows that, although the material is composed of elastic particles, their irreversible displacements produce the same kinematics, and therefore a physically consistent result. Important work has also been carried out on the unicity of the solution. Indeed, if this point is not respected, the reverse analysis cannot be performed. This limits the number of characterization techniques that can be used. It has been shown that for a constant normalized cohesion ( $\frac{C}{E}$ ), stiffness only influences the hardness. Consequently, as the cohesion modifies the residual depth, it is possible to identify the unique set of numerical parameters which provides a given hardness and residual depth. This method could thus be used in further studies involving soft particles.

Regarding the diffusion model, a key benefit of using soft particles is the diversity of intake mechanisms. Three main mechanisms have been observed: plowing, abrasion and fracture. These have a direct effect on the rate of penetration of the minerals into the rubber material. Since the mineral layer is more resistant than the rubber layer for the tested configurations, plowing is the one that occurs most of the time. It has been shown that fast intake is directly linked to the ability of the minerals to punch the rubber material. This ability depends on several parameters. For example, the rubber material needs to be relatively soft in order to reach higher strain. It also needs to be resistant enough to avoid a stress softening effect, similar

to what could be obtained by reducing cohesion for an indentation. Other parameters, such as contact pressure, also play a role.

Indentation model has shown that modeling the material as a collection of soft particles gives results similar to those of a continuous material with an elasto-plastic constitutive model. However, this equivalence is much less obvious for diffusion. It was first necessary to determine what kind of process leads to mineral displacement. It was shown that this process was similar to a stochastic process, with an erratic evolution of the position of a mineral. However, if all the minerals are considered collectively, the behavior becomes deterministic and the concentration follows a Gaussian distribution, spreading out over time. This suggests a diffusive process. This diffusion is driven by brief local variations in transverse velocity. The amplitude of these variations is characterized by the standard deviation and the duration by the persistence (integral of the velocity autocorrelation function). This makes it possible to determine a diffusion coefficient according to the framework of Green-Kubo, which has been compared to the conventional framework of Einstein, giving very close results. The mechanisms governing diffusion are different from those of the intake described above. Indeed, the main mechanism for diffusion is the overtaking of minerals, which have a relative velocity due to the shear rate. This is supported by the fact that velocity fluctuations are directly related to shear rate and mineral agglomerate size.

The effect of the interfacial layer can be described in terms of two main characteristics. Firstly, from a kinematic point of view, it is the medium driving the longitudinal displacement of minerals. Secondly, this layer is applying a resisting force on the minerals, which modifies the diffusion process. Indeed, diffusion at mineral scale is a dynamic process. This can be seen, for example, in the effect of cohesion. As cohesion increases, elastic energy is increasingly stored and released, resulting in significant velocity fluctuations. Moreover, as the interfacial layer is responsible for the forces exerted on a mineral, it is also responsible for the persistence of these velocity fluctuations. The results show little dependence on rubber stiffness and a high dependence on cohesion. This shows that diffusion in the current model is primarily a plastic process through irreversible local deformation of rubber material.

The results are also highly dependent on the contact model between the minerals and the rubber. Indeed, if a cohesive model is used, then a steady state regime is observed, where the shear rate is constant. If the cohesive model is replaced by a Coulomb friction law, then the shear rate is no longer constant and decreases with diffusion, giving a transient regime. It is difficult to demonstrate rigorously which type of contact model is the most appropriate. However, this transient study clearly shows that diffusion is linked to shear rate. Indeed, the diffusion coefficient decreases with shear rate, until diffusion has almost completely stopped.

Whatever the input parameters, the interfacial layer exhibits a stratified flow. Indeed, there is a significant difference between the kinematics of the mixed layer and the mineral-free layer. A clear boundary between the mixed layer and the bulk of the rubber material could be seen on the longitudinal section of the wear sample. This experimentally observed limit can have several origins, one of which is kinematics. Indeed, the mineral concentration gradient near this boundary is significant, which could be explained by a zero shear rate in the mineral-free layer. However, other hypotheses have also been put forward, such as the non-degradation of rubber in the mineral-free layer.

Over longer time scales, the diffusion front progresses and the velocity becomes non-zero in an increasingly thick layer. This leads to a decrease in the shear rate, and hence in diffusion. This long-term diffusion is also corresponding to a homogenization of velocity fluctuations in the layer. For the tested configurations with a steady state regime, a complete stop of diffusion over long time scales has never been observed.

# Perspectives

This study has revealed several important aspects that require further investigations. Firstly, it showed that diffusion for the tested configurations is an irreversible process governed by the cohesion of the material and not its stiffness. However, there may also be an effect of the viscous component of the rubber. The effect of this parameter is not yet well understood. In the present study, this was not investigated for computation time reasons. It would be interesting to see if, and how, a change in the viscosity affects the forces exerted on the minerals and therefore diffusion. However, the notion of viscosity on these time and space scales is still poorly understood. Moreover, part of the dissipation is due to large-scale deformation of the rubber. This global dissipation may have a local effect on diffusion. Nevertheless, such a scale is not accessible at reasonable computation times. A first interesting option, however, is the use of SDEM (soft discrete element method) [Mollon, 2021], which is less costly (by reducing the number of degrees of freedom) and therefore opens up more possibilities. In particular, it would allow the study of diffusion on longer time scales, and with larger quantities of minerals.

Another interesting point for further studies is the effect of road-like surface boundary conditions. The surface currently has a zero transverse displacement. However, if a constant contact pressure were applied, it could significantly influence kinematics, and therefore diffusion. In particular, vortex formation is strongly linked to the transverse displacement of the road-like surface. Indeed, a high enough compacity is initially required to give the interfacial layer its initial velocity. To form vortices, a decrease in compacity is then necessary, otherwise the vortices are sheared and milled. This can lead to different conclusions. For example, the current study shows that persistence decreases with cohesion, which is consistent with an increase in forces exerted on the minerals. However, for a constant contact pressure, an increase in cohesion increases the interfacial layer thickness, which notably increases persistence for a granular medium [Macaulay and Rognon, 2019]. More generally, it would be interesting to understand how to take more accurately into account the transverse displacement of the road-like surface.

An important point raised by this study is the importance of considering mineral ejection flow. Indeed, it was first shown that intake can be strongly delayed depending on the input parameters. For example, for the highest stiffness, a considerable quantity of minerals begin to diffuse for times equivalent to the duration of the steady state in other simulations. However, if these minerals could be ejected, then this could potentially drastically change the amount of minerals embedded within the layer. In addition, this could partly explain why diffusion is observed particularly in rubber and not in other materials. This point, however, requires a 3D model, which is currently out of reach for computation time reasons. One way of getting an initial idea would be to define a 3D semi-analytical model. The minerals would be modeled in a discrete way and the road-like surface and rubber in a continuous way. The minerals would be incorporated into the rubber (i.e. removed from contact) according to a law of Fick (or a more appropriate penetration law). This would give the mineral quantity ejected compared with the mineral quantity incorporated, without taking into account the diffusive processes occurring within the rubber.



The previous point is seen through the intake point of view, but will also have a more complex effect on mineral diffusion. Indeed, as previously seen by modifying the quantity of minerals, the shear rate depends directly on the mineral quantity embedded into the rubber material. This quantity is directly linked to the balance between diffusion rate and wear rate. In longitudinal sections, minerals can be observed in the rubber material. On the one hand, this means that the diffusion rate was at a given time, higher than the wear rate. This is not surprising, since diffusion evolves according to  $\sqrt{t}$ . It would be interesting to find that transition where the wear rate exceeds the diffusion rate. On the other hand, since experimentally the quantity of minerals decreases continuously (may be different in a real case where there is a continuous supply in minerals), the shear rate should not be constant over time. This time dependency therefore remains to be determined by further studies.

Concerning wear tests carried out for several sliding distances, a very distinct change in surface aspect is observed for the longest distance (fig. 4.23). This is probably linked to the fact that, after a certain time, all the minerals are ejected from the contact and rubber specimen. The objective is therefore to understand how minerals can affect the mechanical properties when they are still embedded in the material. A first result concerns the orientation of minerals in the layer, which gives information on the anisotropy of its mechanical properties. A second result is the change in shear rate when the quantity of minerals changes, reflecting an increase in shear strength. However, as can be seen from the images of the wear tests, the presence of minerals tends to form a fine powder (fig. 1.41). It is difficult to explain the formation of a powder by a reduction in the shear rate due to the presence of minerals. It is therefore possible that the current model is unable to model the physical process behind this transition. One hypothesis is that the change in properties is due to rubber degradation and not directly to the presence of minerals. An approach would be to establish a link between local variations in velocity (fluctuations and persistence) and a degradation model.

Initial attempts have been made to model wear. A simplified method is to model wear with a plane-strain kinematics. An important parameter is how to consider the experimental configuration, as shown in fig. 5.28.

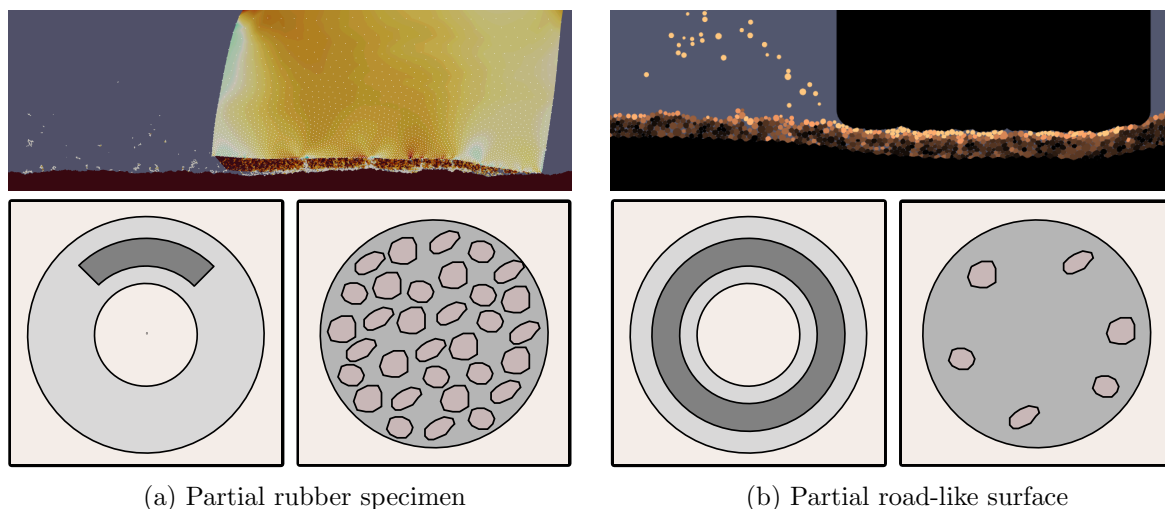


Figure 5.28: Examples of wear models with plane-strain kinematics; the color of the discrete particles represents the degree of damage

Each of these methods has its advantages and disadvantages. The first (fig. 5.28a) consists in modeling a rubber sample (upper body) sliding on a continuous road-like surface (lower

body). This method is less costly in terms of computation time, but less accurate in terms of contact loss between the rubber and each aggregate. This loss may generate a larger deformation (and dissipation) than the potential stick-slip observed by this model. The second (fig. 5.28b) involves modeling an aggregate (upper body) sliding on a continuous rubber sample (lower body). This method is more costly, but provides a more accurate representation of large-scale material deformation, with deformation cycles (and therefore hysteresis) depending on the position of the aggregate. In both cases, this would make it possible to study phenomena at the inlet and outlet of the contact, such as particle agglomeration.

A key parameter of a wear model is the consideration of kinematics. At this scale, minerals cannot be modeled explicitly, and a semi-analytical model is required. One way of proceeding would be to modify the contact models between discrete bodies according to the target kinematics. A first step would be to start with an identical contact model for each body in the mixed layer (i.e. mineral diffusion is immobilized), and a different model for all the other bodies. The aim is to see how the shear rate evolves as bodies from the mixed layer are ejected. A second step would be to have a time-dependent contact model for a constant diffusion coefficient. This would model the effect of diffusion on kinematics, and ultimately on wear. Finally, a last step would be to use a contact model with a diffusion coefficient that depends on the shear rate, and therefore on diffusion and wear. To this end, it is possible to incorporate the different scalings found previously into these contact models.



# Appendices



## Appendix A

# Green-Kubo validation

The results obtained by the Green-Kubo framework depend on the selected time window for a given simulation. This window is defined by a starting point and a width. The starting point must be sufficiently far from intake, as the mechanisms are different from those of diffusion. This starting point is defined when a minimum value of  $MSD^0$  is reached, giving an initial sliding distance  $s_{initial}$ . Width is defined as the sliding distance covered between  $s_{initial}$  and  $s_{max}$ . It must be chosen with care. A narrow width means small mineral displacement and therefore noisy results. To decorrelate the effect of width from the size of the data set, the analysis will be carried out for 3 different sizes. The example of one simulation is taken with the standard parameters already discussed in the description of the numerical model. Results are compared with the mean value (indicated by a bar) and are shown in figs. A.1 to A.3.

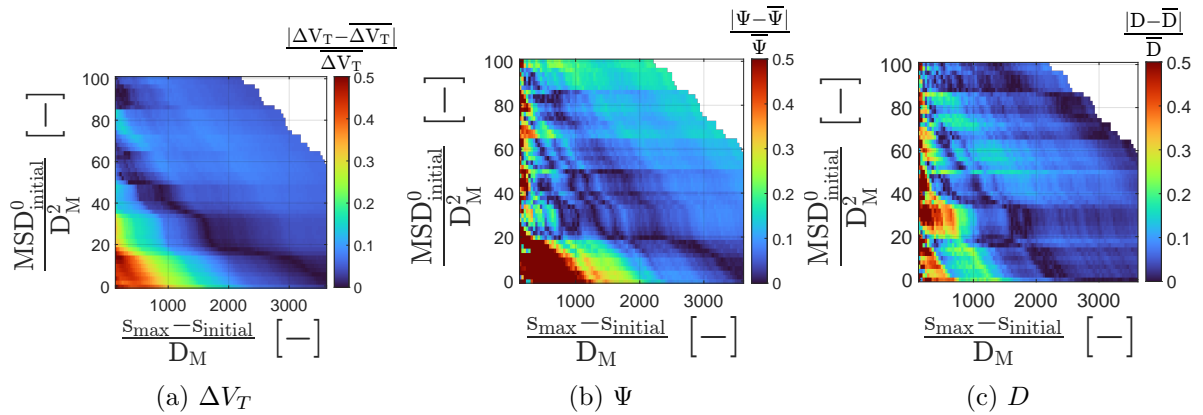
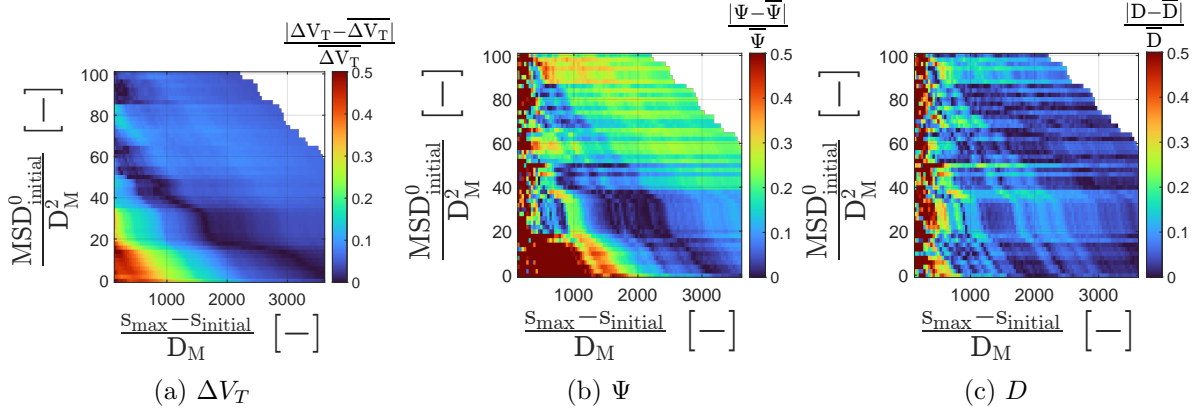
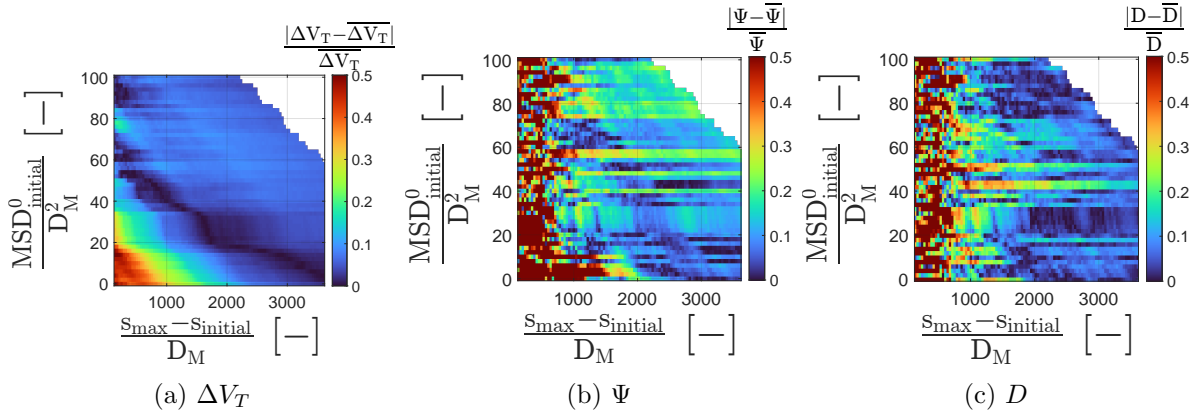


Figure A.1: Results for a dataset generated every  $2.6 D_M$  of sliding

Figure A.2: Results for a dataset generated every  $5.1 D_M$  of slidingFigure A.3: Results for a dataset generated every  $10.3 D_M$  of sliding

A difference in the diagonal typically indicates a true change (i.e. not due to statistical error) in the state of a given model. This can be seen, for example, in the value of  $\Delta V_T$  at low  $MSD^0$ , which corresponds to the beginning of sliding. The value of  $\Delta V_T$  is almost independent of the size of the data set, demonstrating that the results are statistically significant and homogeneous. The  $\Psi$  results, however, are much more dependent on the size of the data set, with non-homogeneous results if the data are extracted beyond a step of  $2.6 D_M$ . This is due to the velocity autocorrelation function, as the velocity jump events are very short compared to the scale of the diffusion. The ACF for several data generation steps is shown in fig. A.4.



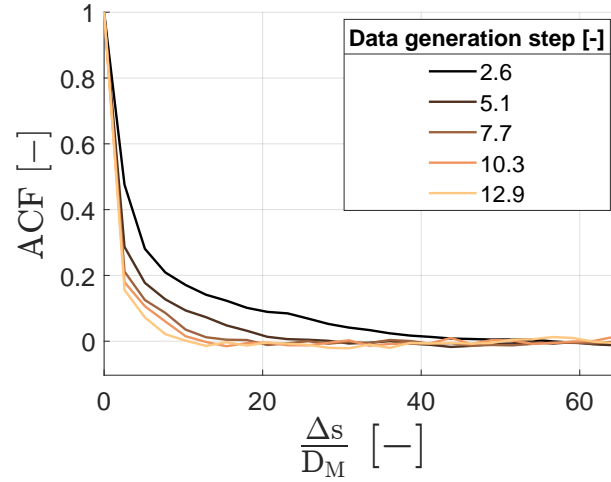


Figure A.4: Results for  $MSD_{initial}^0 = 50 D_M^2$  and a width of  $2058 D_M$

If the step value is too high, the ACF tends to be underestimated. In practice, there is a more complex relationship between step size and data set size. The dependence of  $\Psi$  on the data generation step is linearly transmitted to  $D$ . The direct consequence is that the method is only appropriate in cases where a significant data set size can be obtained (i.e. under steady-state conditions with a constant shear rate). In this case and for the smallest step size, the results can be considered homogeneous and, consequently, a point can be selected sufficiently far from the initial state to be considered as representative of the overall state. A comparison between the diffusion coefficient derived from the Einstein ( $D_E$ ) and Green-Kubo ( $D_{GK}$ ) frameworks is presented in fig. A.5.

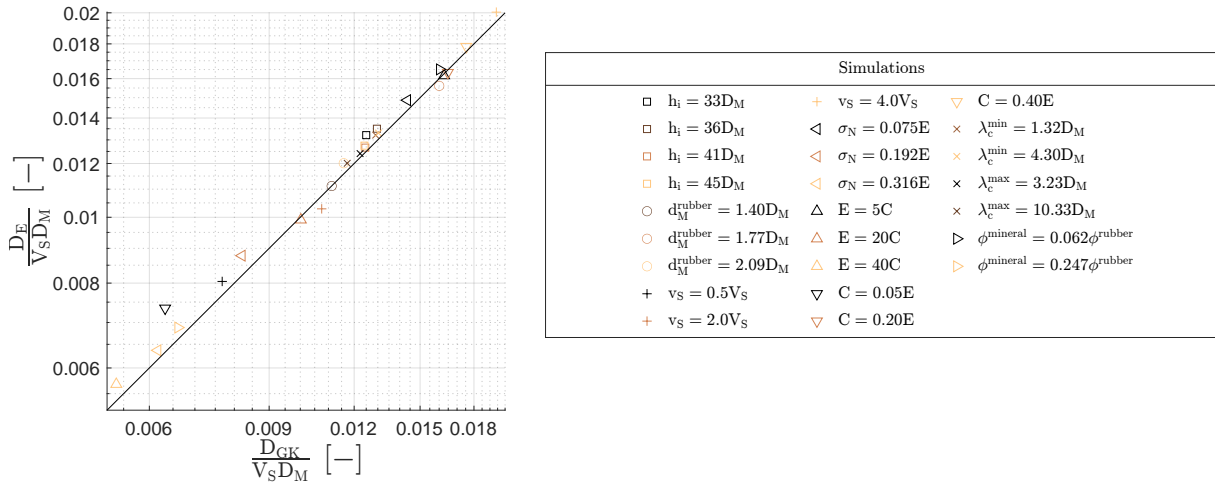


Figure A.5: Comparison of diffusion coefficients derived from Einstein and Green-Kubo frameworks

The diffusion coefficient from the framework of Einstein can be considered as a reference, as it directly links time to mineral displacement. The Green-Kubo method shows very good accuracy, with an average relative deviation of 3.3% and a maximum deviation of 13.9%. This deviation tends to increase when diffusion slows down (e.g. homogeneous mineral size, jamming of the mineral layer, etc.). This can be seen on fig. A.5 where the deviation increases for low values of  $D$ .



# Appendix B

## Snapshots

### 1 Direct jamming

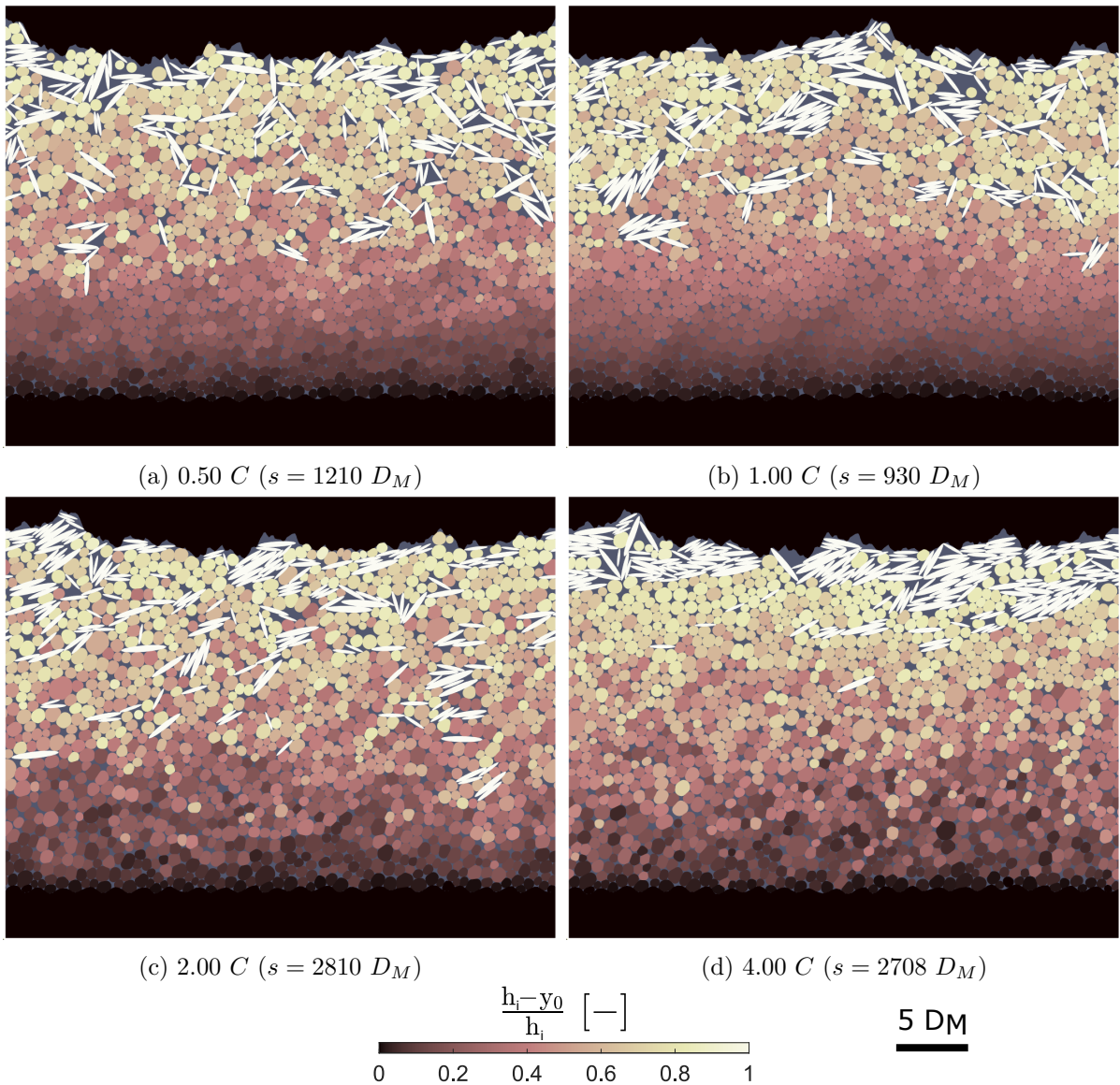


Figure B.1: Snapshots according to  $C_{rock}^{rubber}$ ;  $MSD^0 = 50 D_M^2$  for figs. B.1a to B.1c and  $MSD^0 = 5 D_M^2$  for fig. B.1d

## 2 Delayed jamming

### 2.1 Interfacial layer thickness in a delayed jamming case

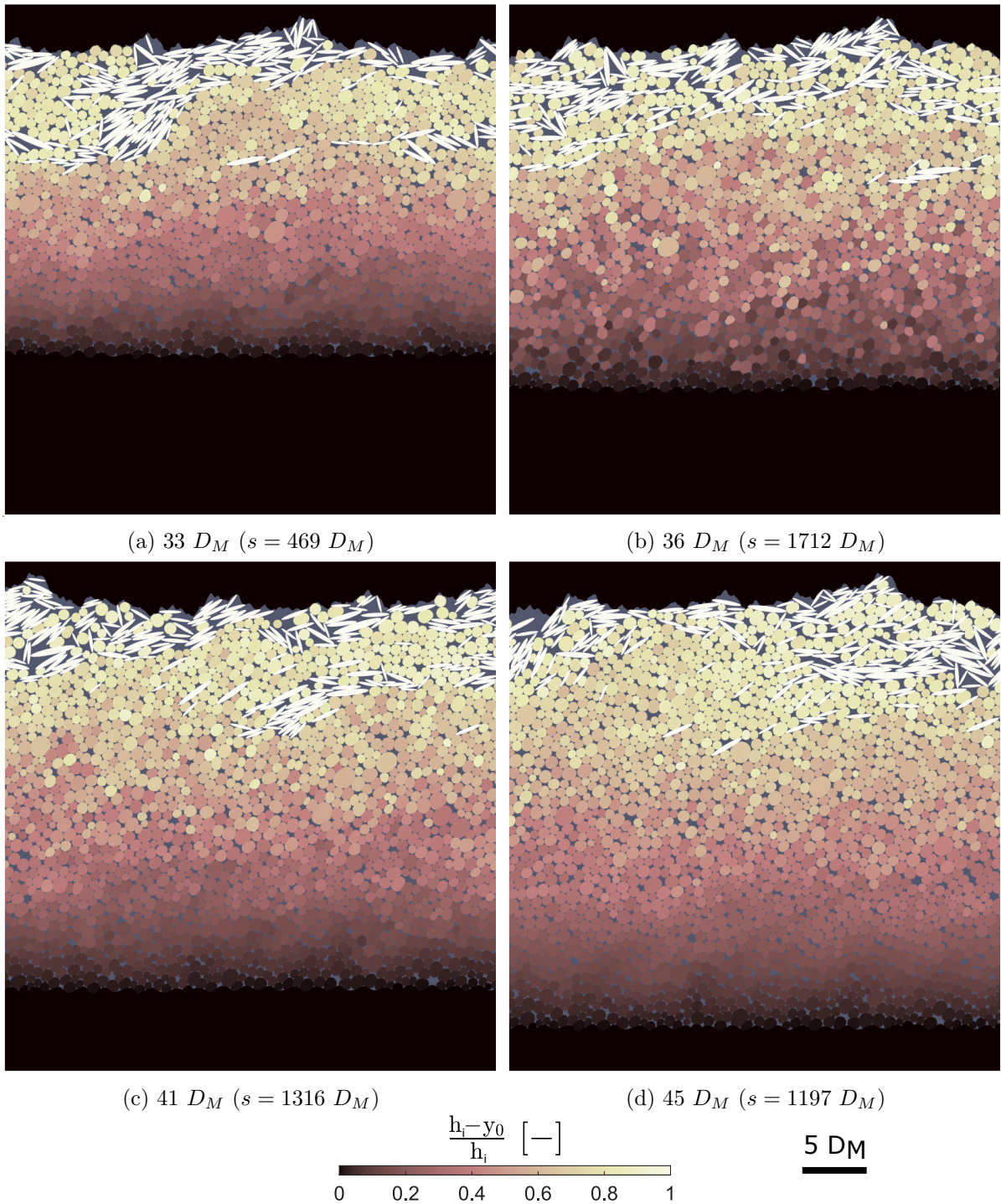


Figure B.2: Snapshots according to  $h_i$  in a delayed jamming case and for  $MSD^0 = 19 D_M^2$

## 2.2 Friction between rocky materials

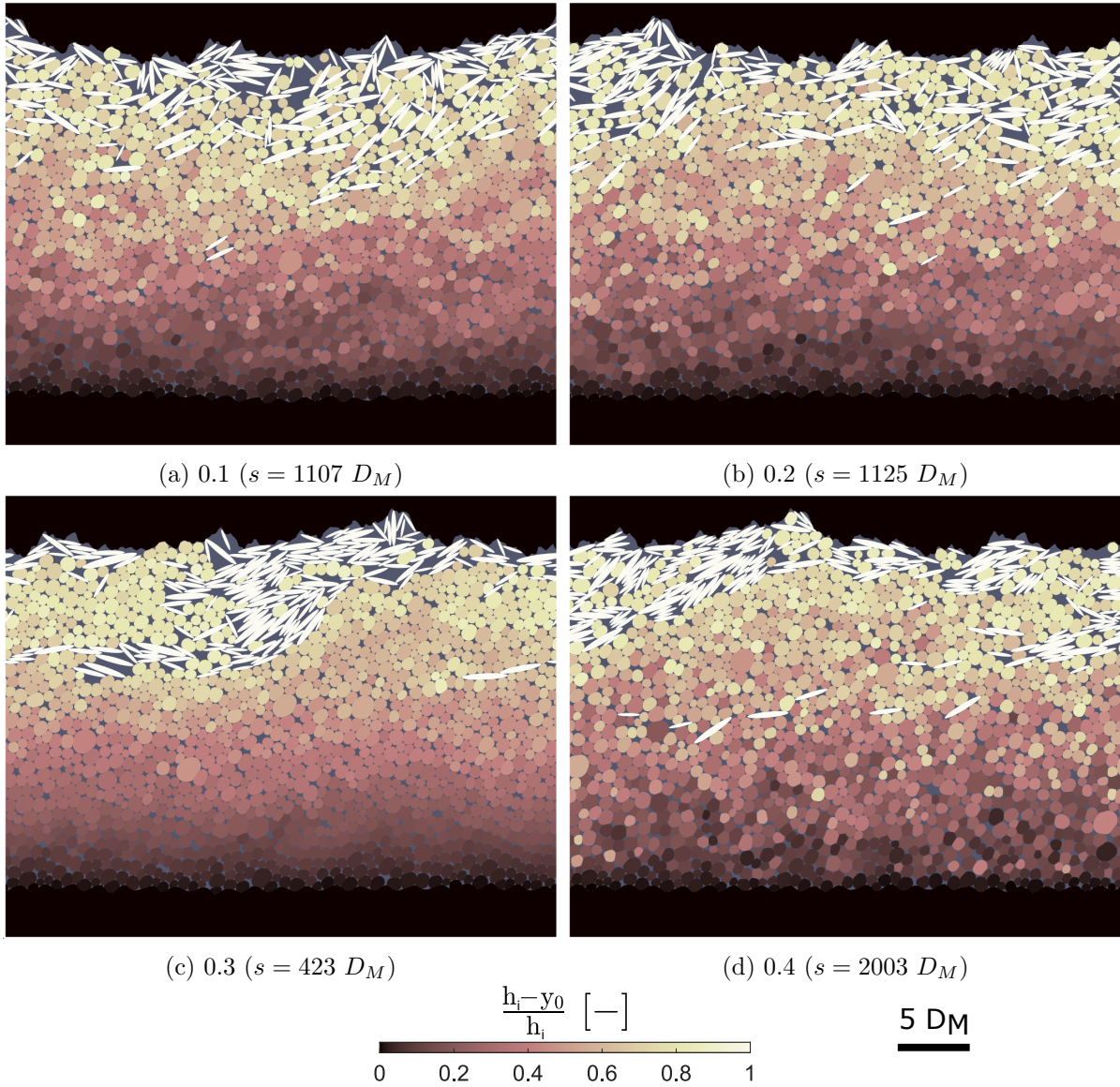
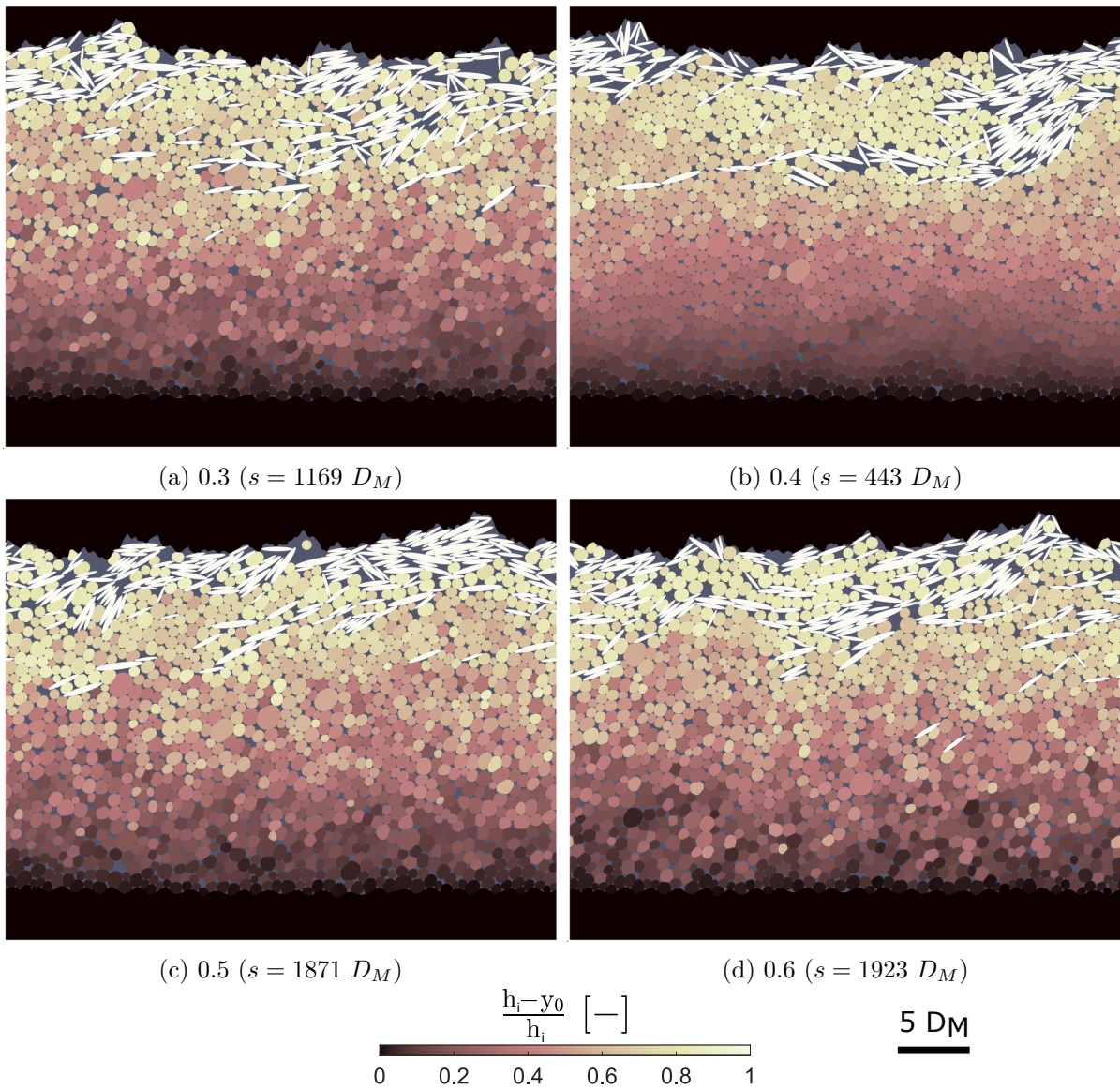


Figure B.3: Snapshots according to  $\mu_{rock}^{rock}$  and for  $MSD^0 = 17 D_M^2$



## 2.3 Friction between rock and rubber materials

Figure B.4: Snapshots according to  $\mu_{rock}^{rubber}$  and for  $MSD^0 = 18 D_M^2$

### 3 Steady-state diffusion

#### 3.1 Numerical parameters

##### 3.1.1 Sliding velocity

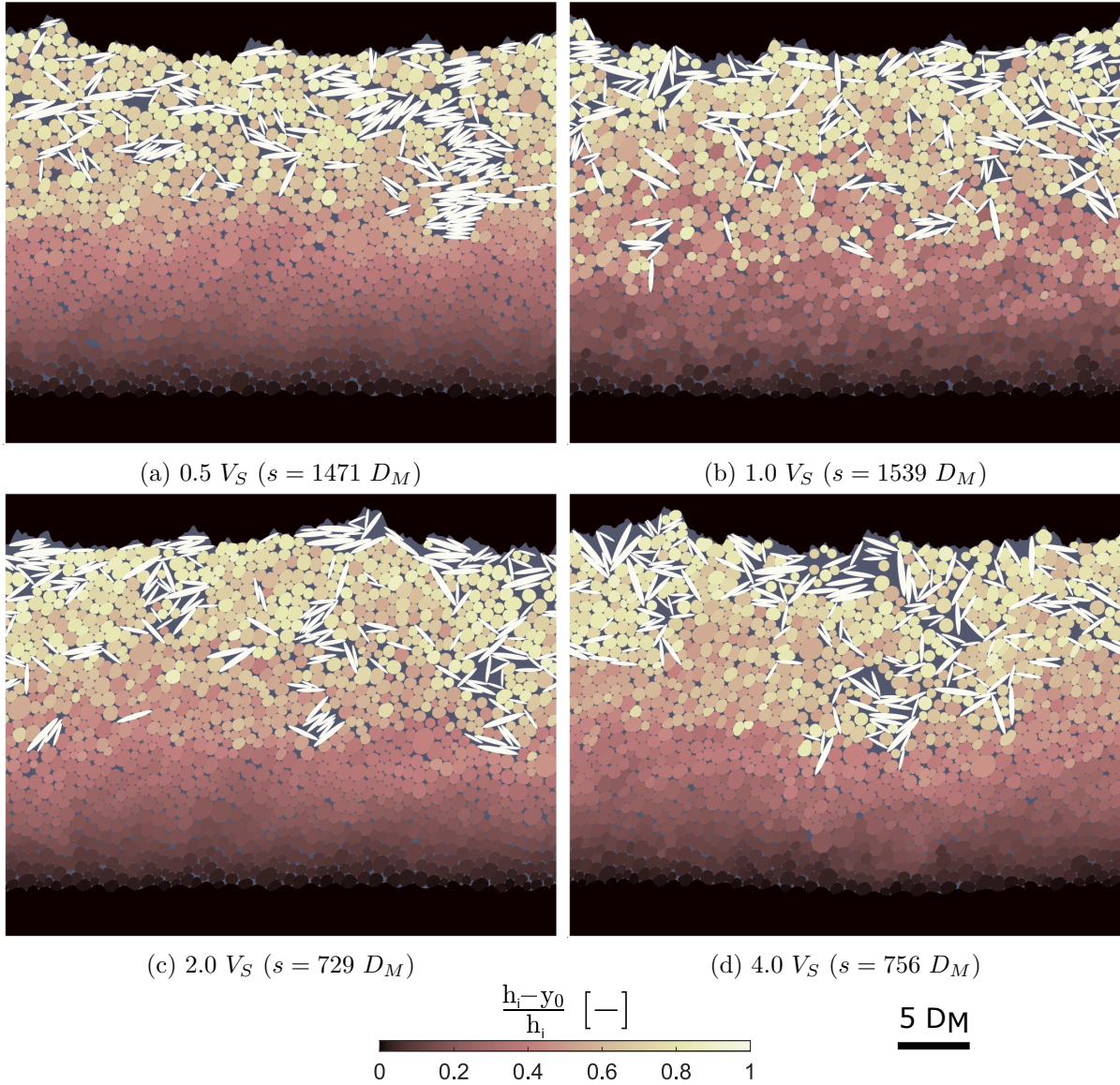
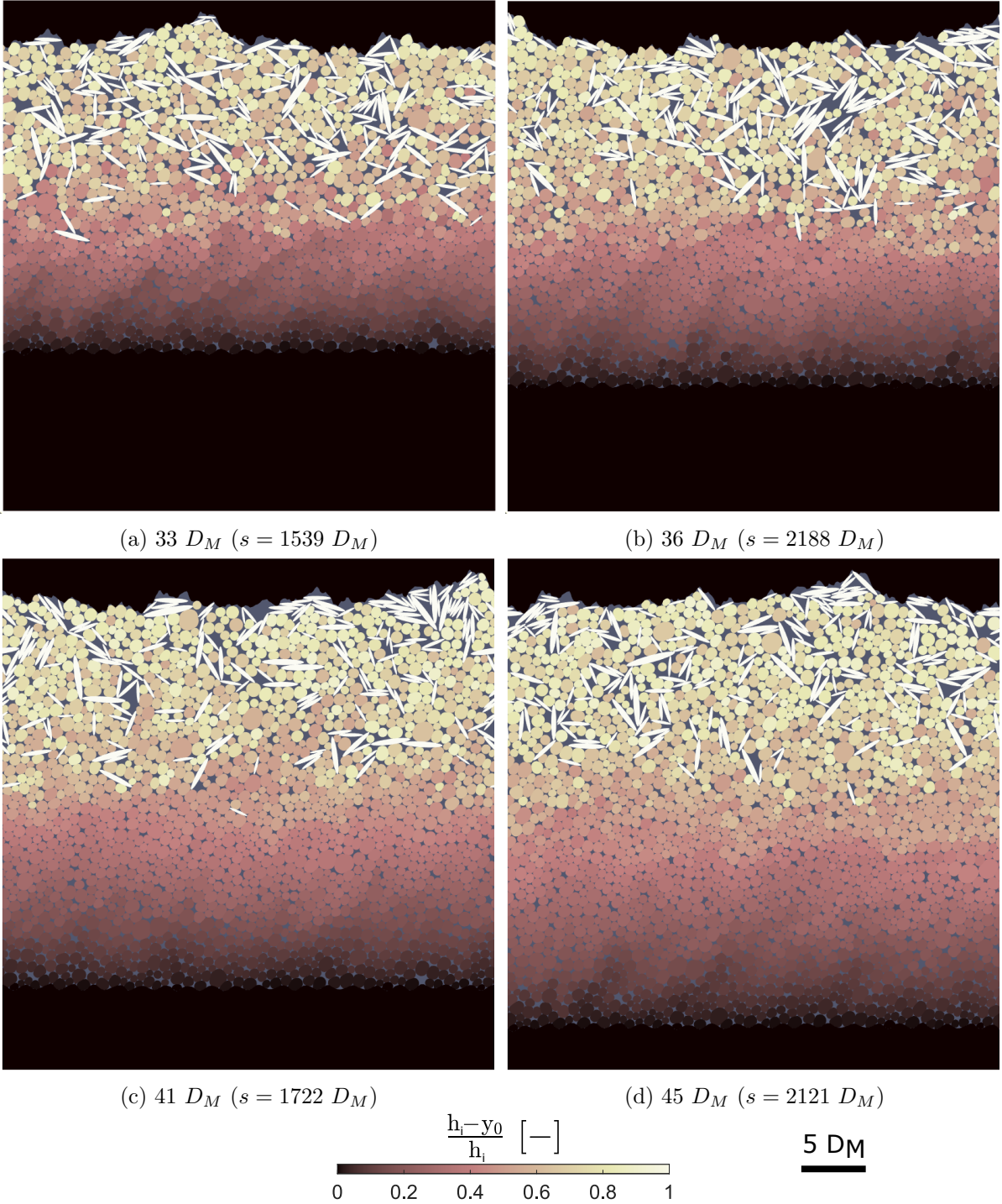


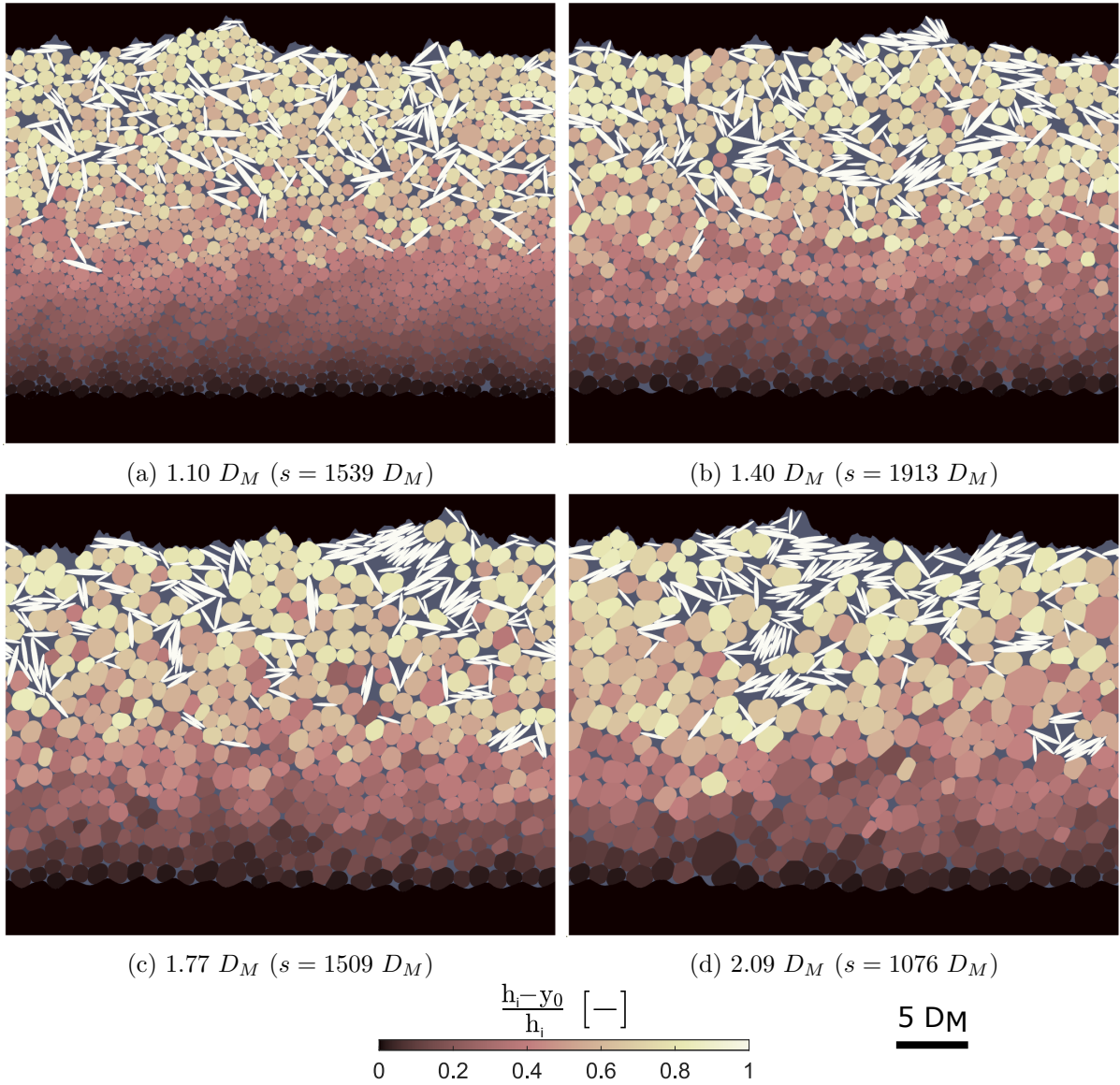
Figure B.5: Snapshots according to  $v_S$  and for  $MSD^0 = 50 D_M^2$



## 3.1.2 Interfacial layer thickness

Figure B.6: Snapshots according to  $h_i$  and for  $MSD^0 = 50 D_M^2$

## 3.1.3 Rubber particle size

Figure B.7: Snapshots according to  $d_M^{rubber}$  and for  $MSD^0 = 50 D_M^2$

## 3.2 External parameters

### 3.2.1 Contact pressure

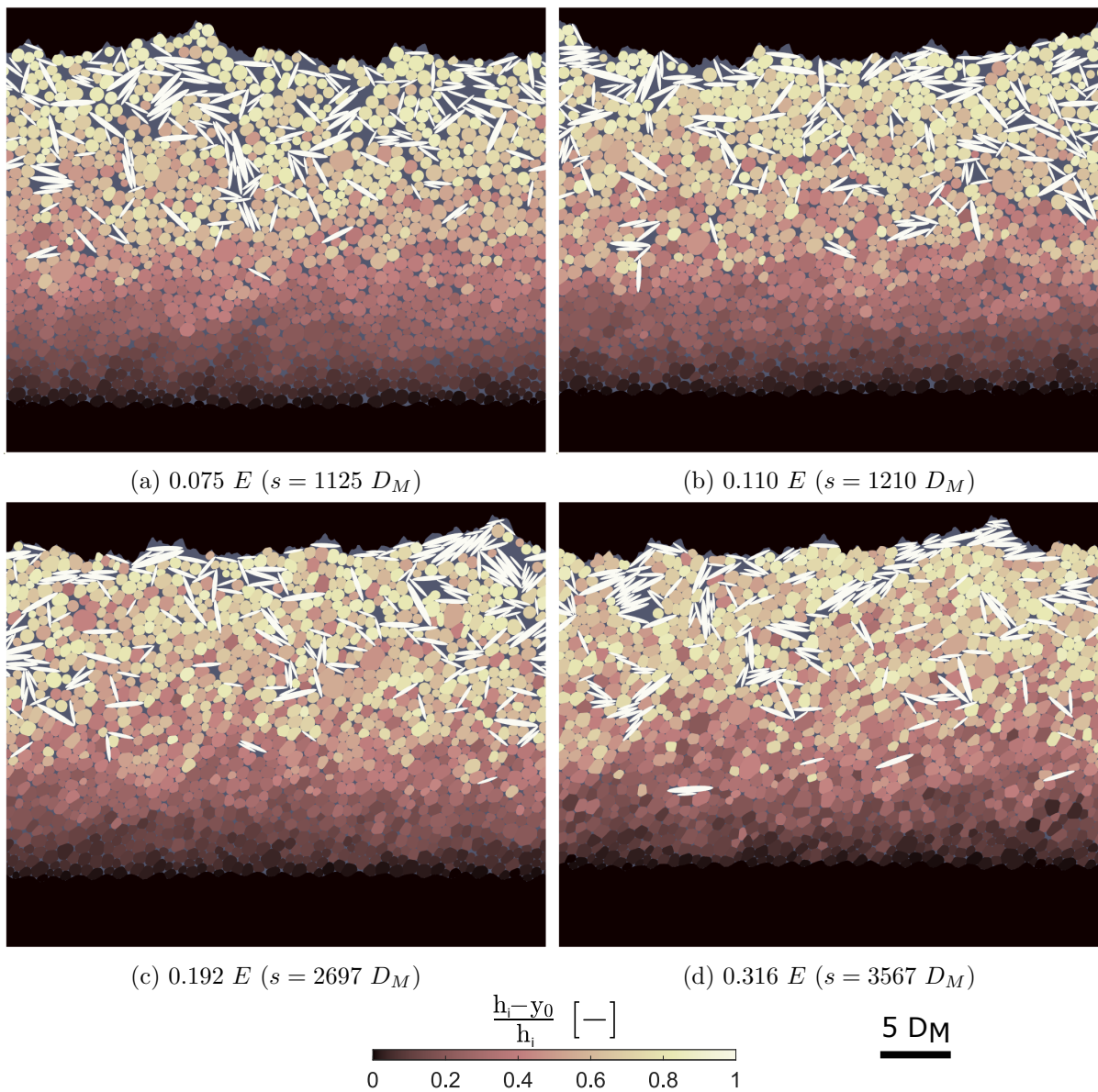
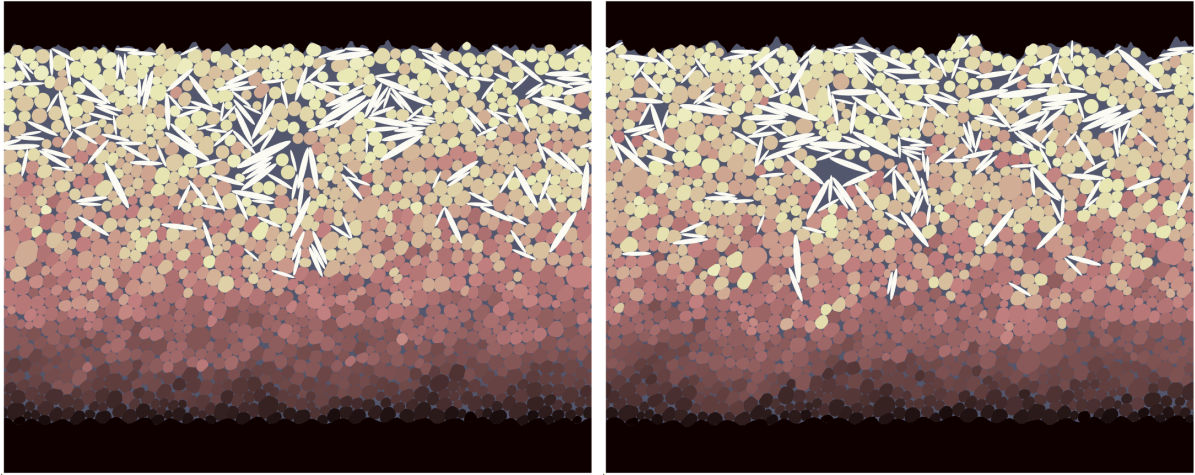
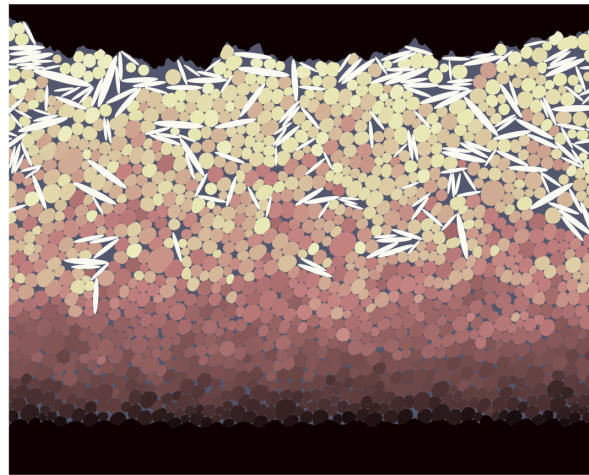
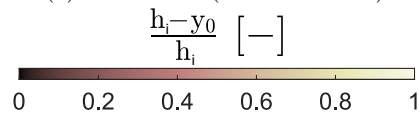


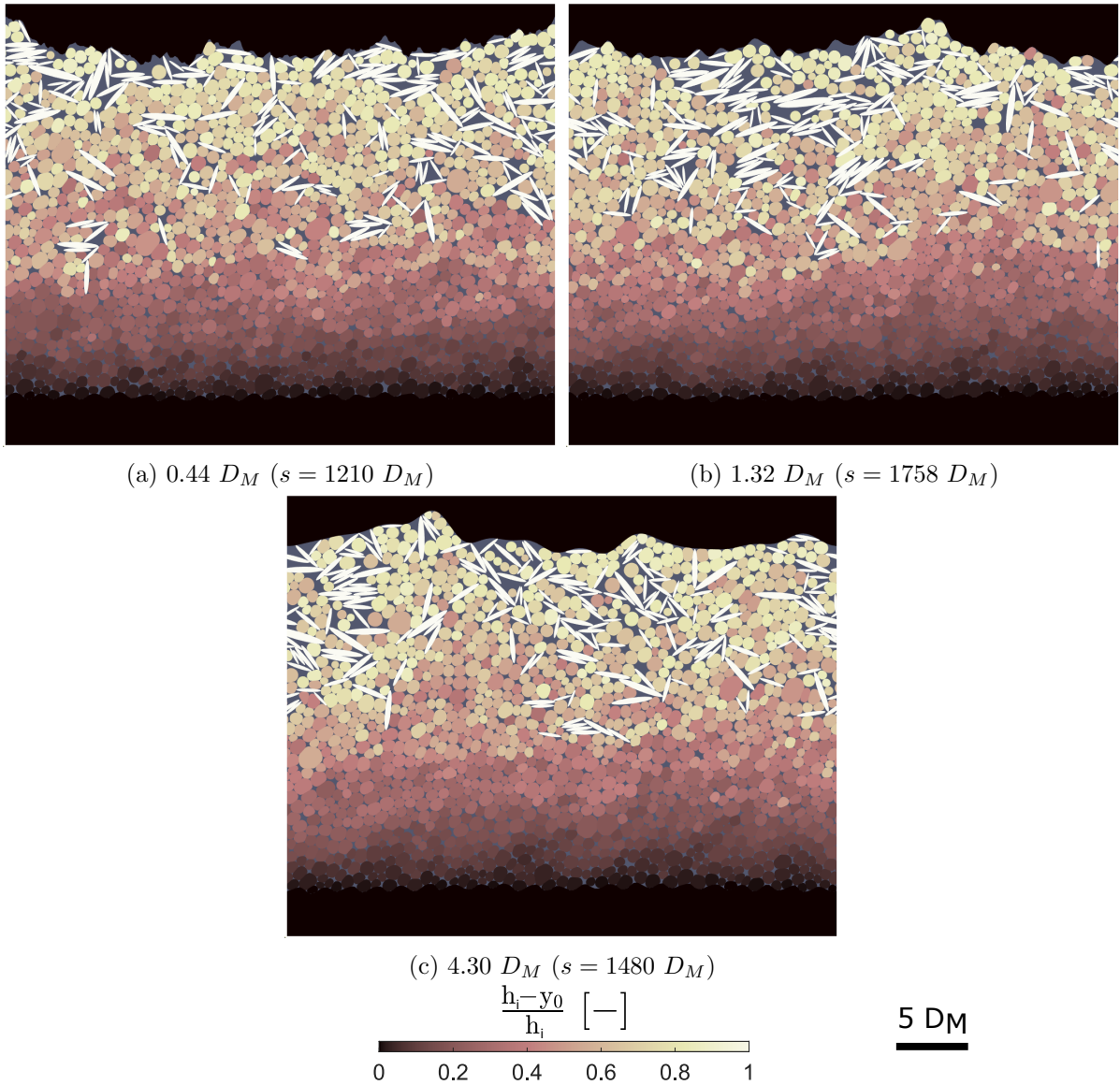
Figure B.8: Snapshots according to  $\sigma_N$  and for  $MSD^0 = 50 D_M^2$



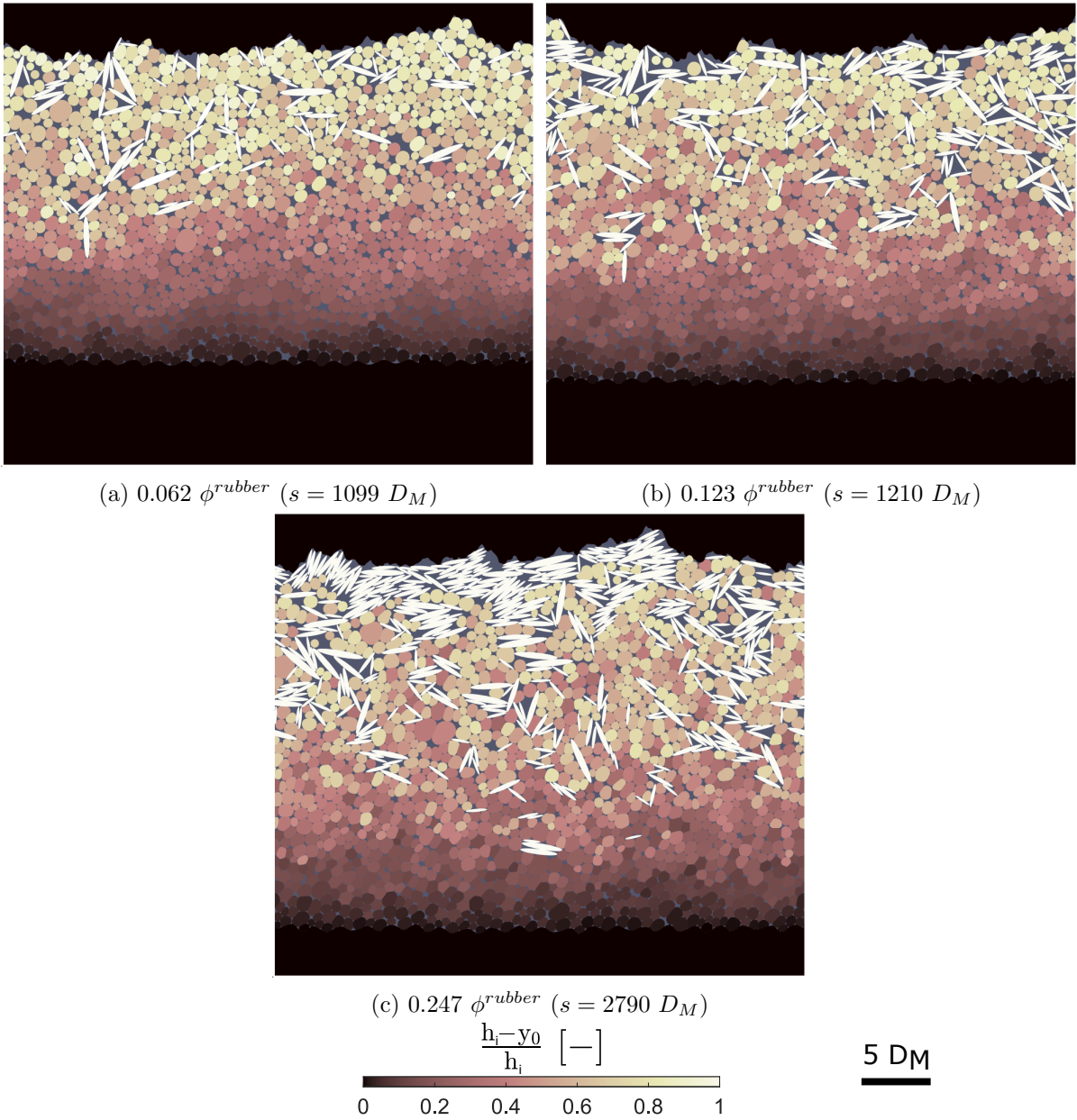
## 3.2.2 Roughness (high-pass filter)

(a)  $3.23 D_M$  ( $s = 1617 D_M$ )(b)  $10.33 D_M$  ( $s = 2013 D_M$ )(c)  $51.46 D_M$  ( $s = 1210 D_M$ )5  $D_M$ Figure B.9: Snapshots according to  $\lambda_c^{max}$  and for  $MSD^0 = 50 D_M^2$

## 3.2.3 Roughness (low-pass filter)

Figure B.10: Snapshots according to  $\lambda_c^{min}$  and for  $MSD^0 = 50 D_M^2$

## 3.2.4 Mineral fraction

Figure B.11: Snapshots according to  $\frac{\phi^{mineral}}{\phi^{rubber}}$  and for  $MSD^0 = 50 D_M^2$

## 3.2.5 Mineral size

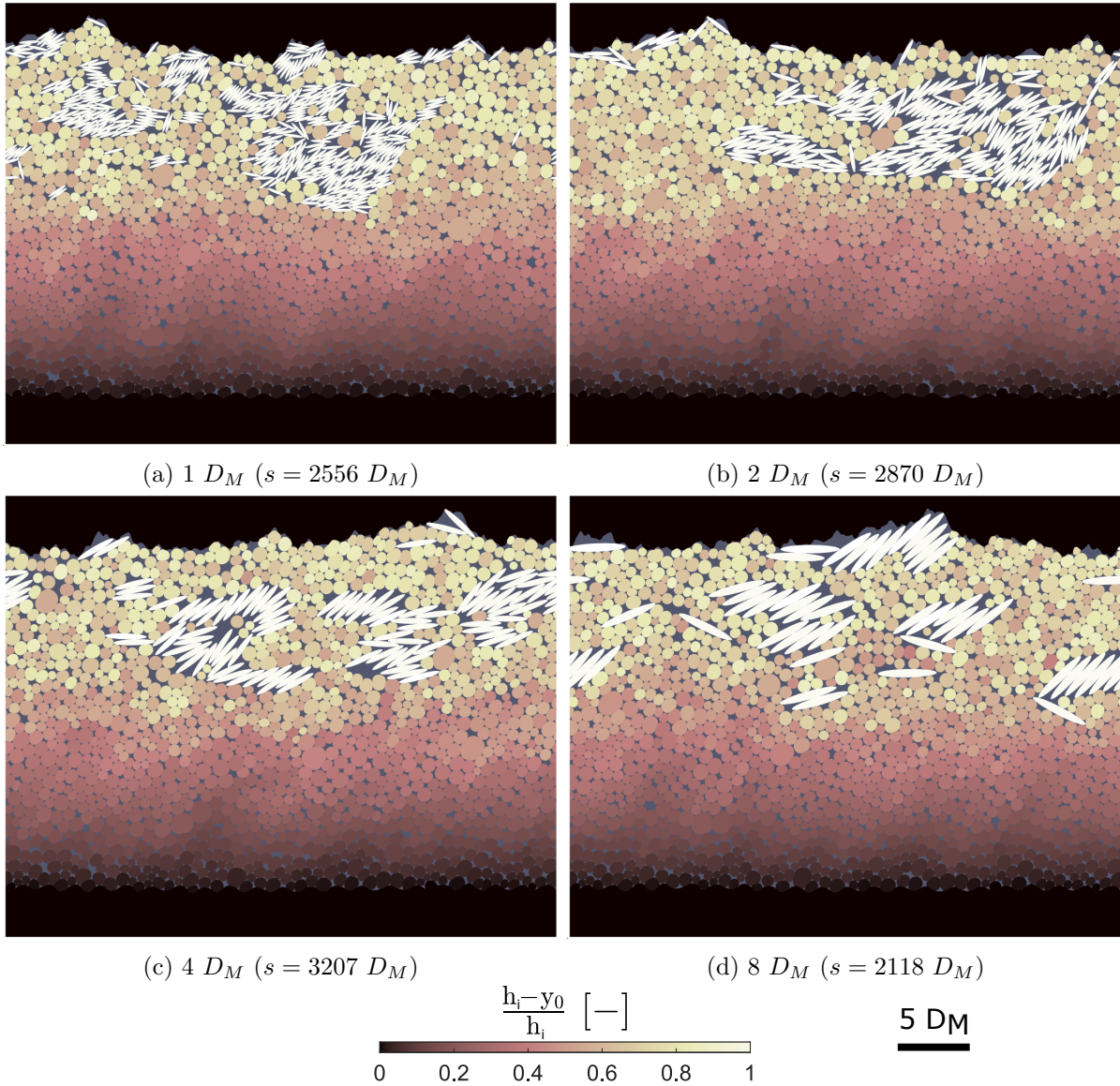


Figure B.12: Snapshots according to  $d_M^{mineral}$  and for  $MSD^0 = 40 D_M^2$



### 3.3 Material parameters

#### 3.3.1 Rubber stiffness

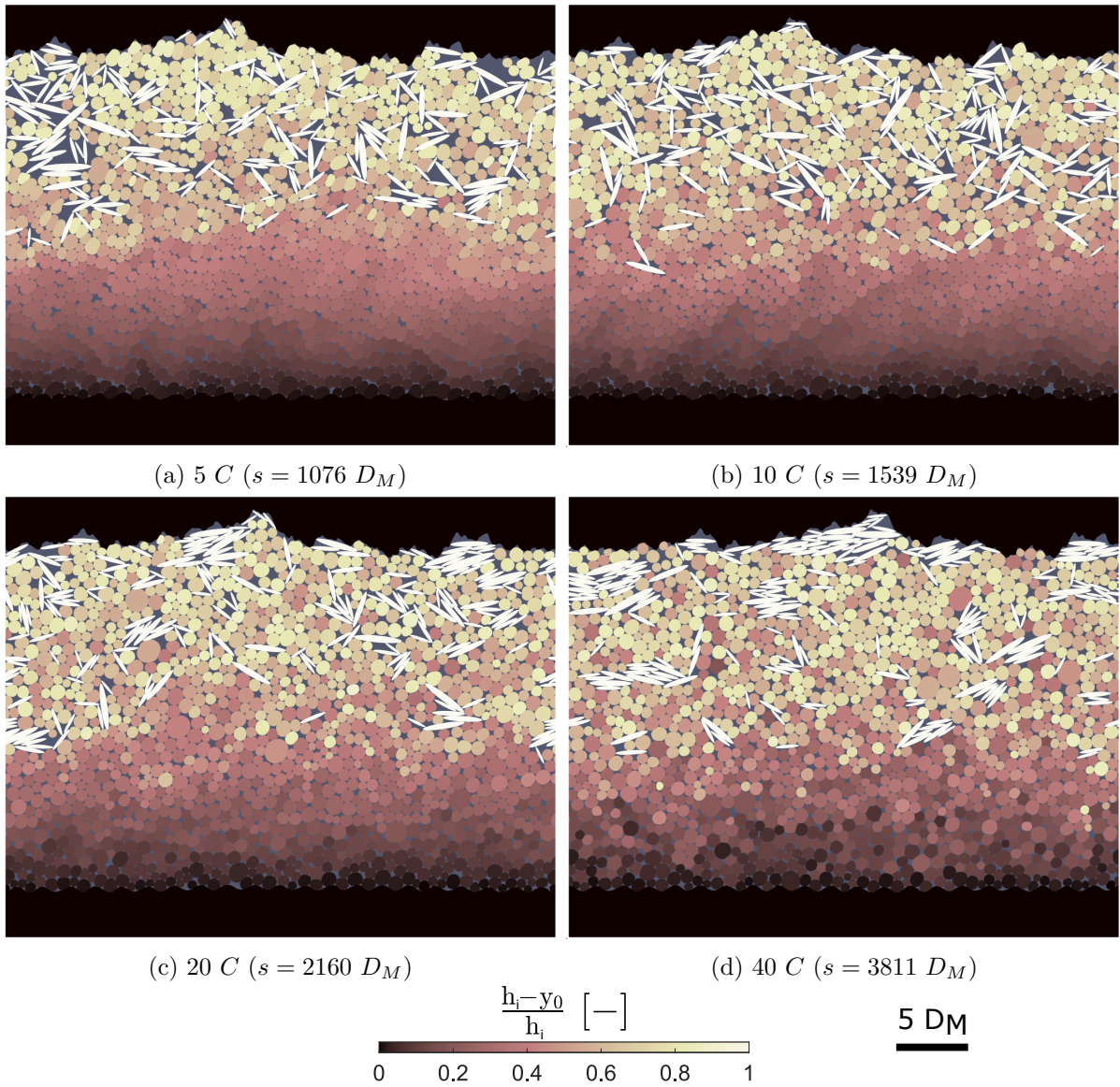
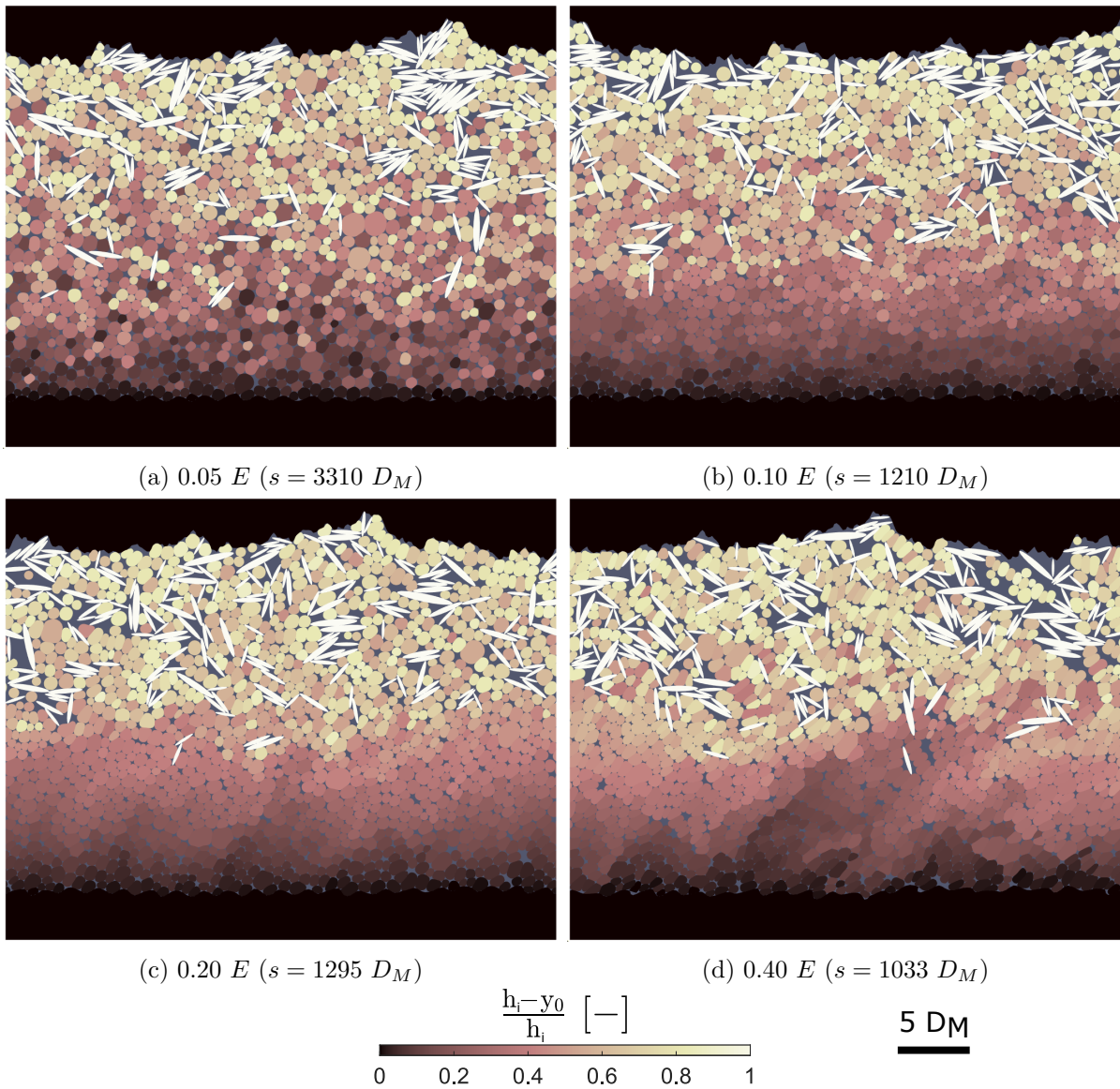


Figure B.13: Snapshots according to  $E$  and for  $MSD^0 = 50 D_M^2$

## 3.3.2 Rubber cohesion

Figure B.14: Snapshots according to  $C$  and for  $MSD^0 = 50 D_M^2$

## Appendix C

# Mean square displacement

### 1 Direct jamming

### 2 Delayed jamming

#### 2.1 Interfacial layer thickness in a delayed jamming case

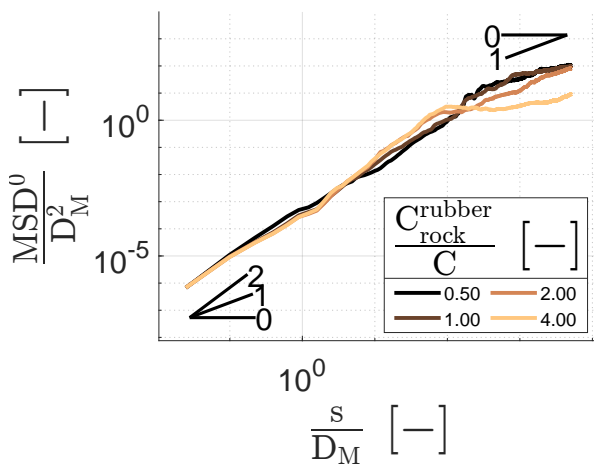


Figure C.1: Mean square displacement according to  $C_{rock}^{rubber}$

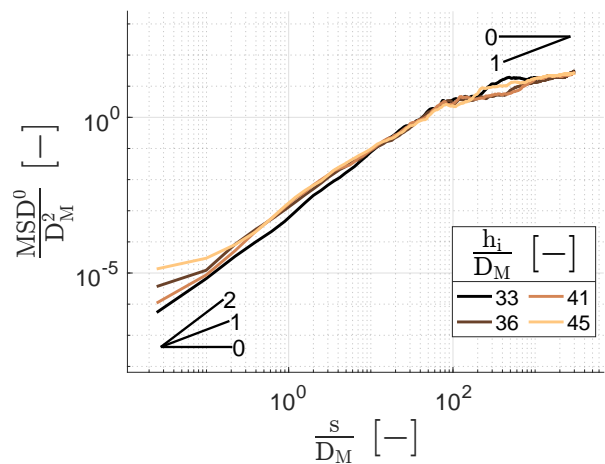


Figure C.2: Mean square displacement according to  $h_i$  in a delayed jamming case

## 2.2 Friction between rocky materials

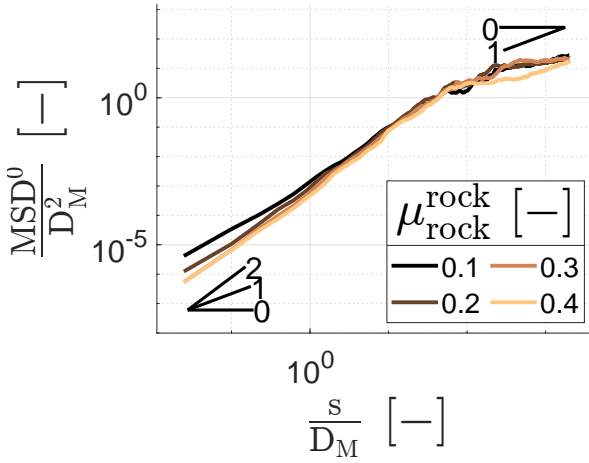


Figure C.3: Mean square displacement according to  $\mu_{rock}^{rock}$

## 2.3 Friction between rock and rubber materials

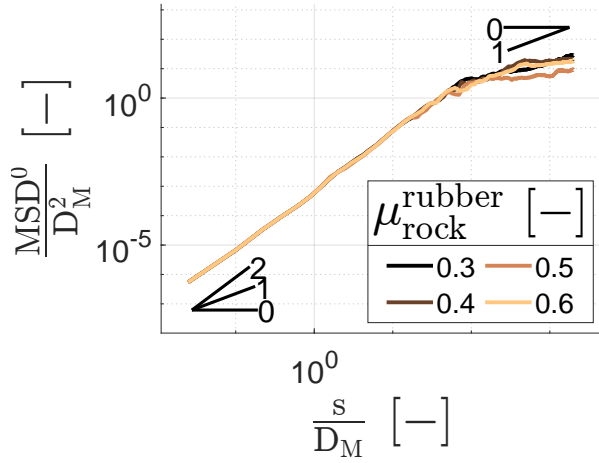


Figure C.4: Mean square displacement according to  $\mu_{rock}^{rubber}$

## 3 Steady-state diffusion

### 3.1 Numerical parameters

#### 3.1.1 Sliding velocity

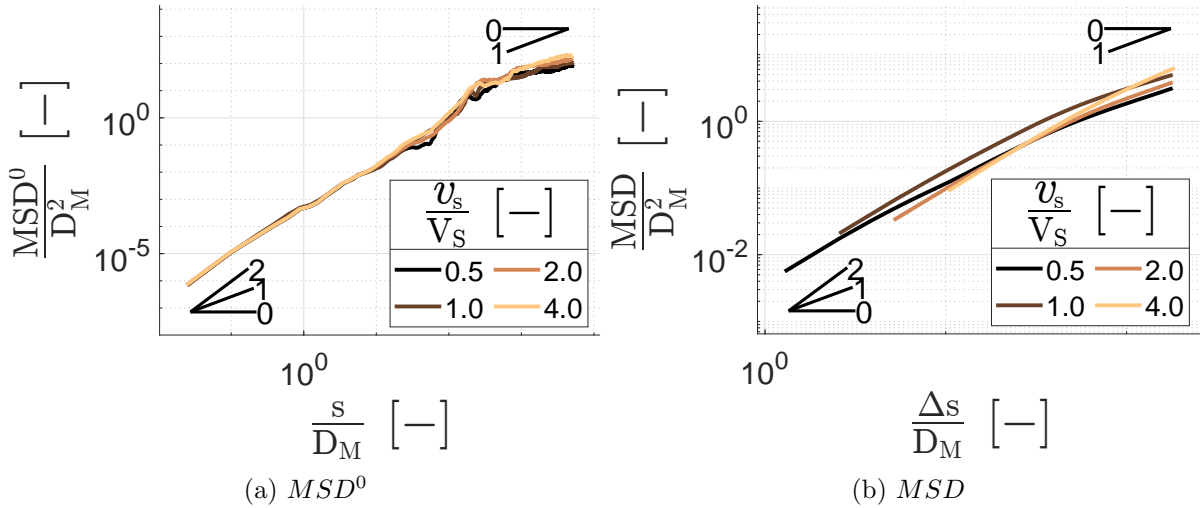


Figure C.5: Mean square displacement according to  $v_s$

### 3.1.2 Interfacial layer thickness

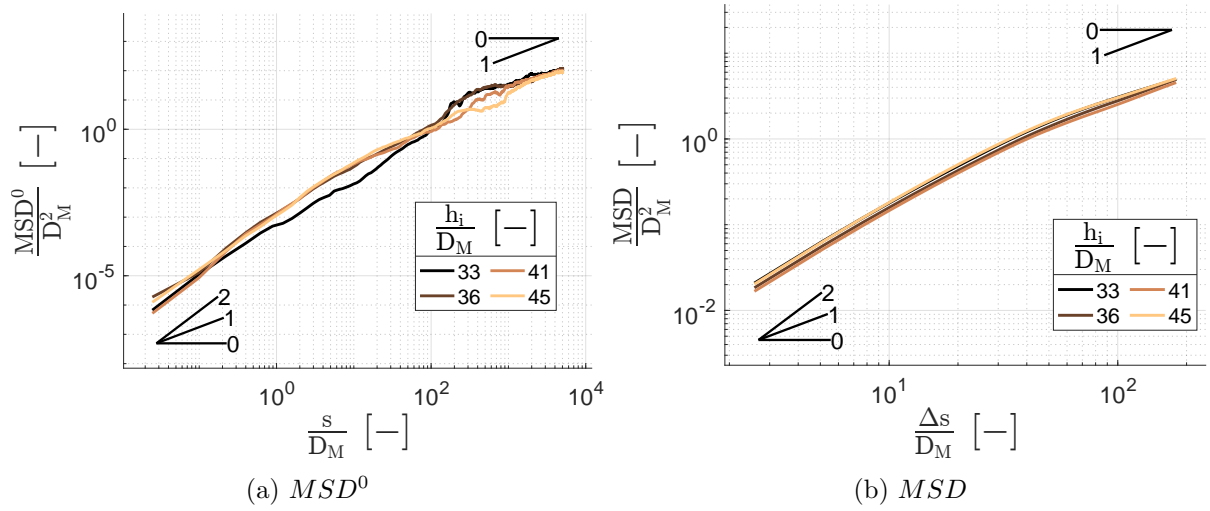


Figure C.6: Mean square displacement according to  $h_i$

### 3.1.3 Rubber particle size

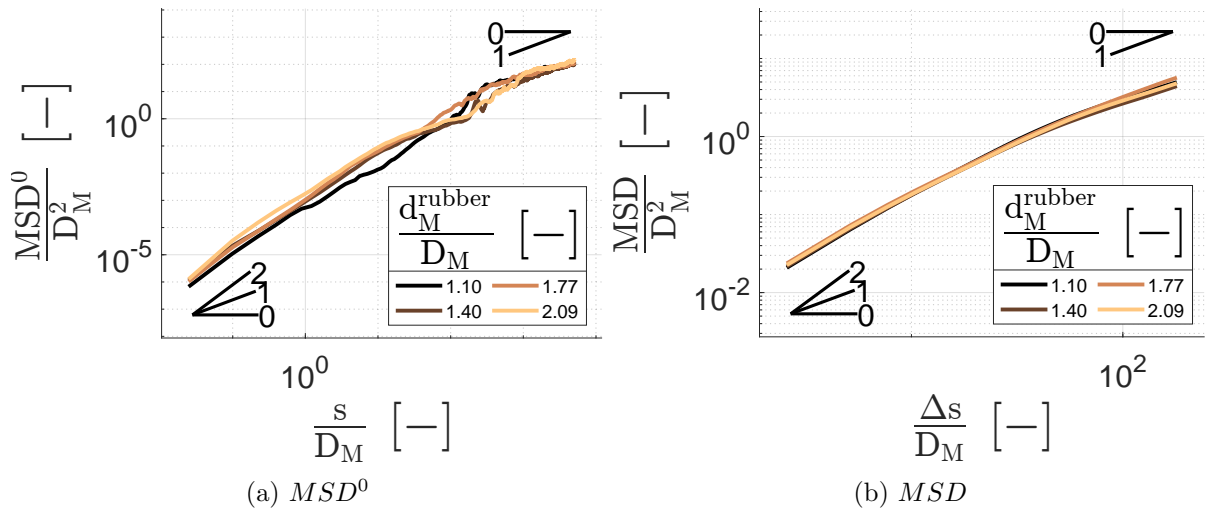


Figure C.7: Mean square displacement according to  $d_M^{rubber}$

### 3.2 External parameters

#### 3.2.1 Contact pressure

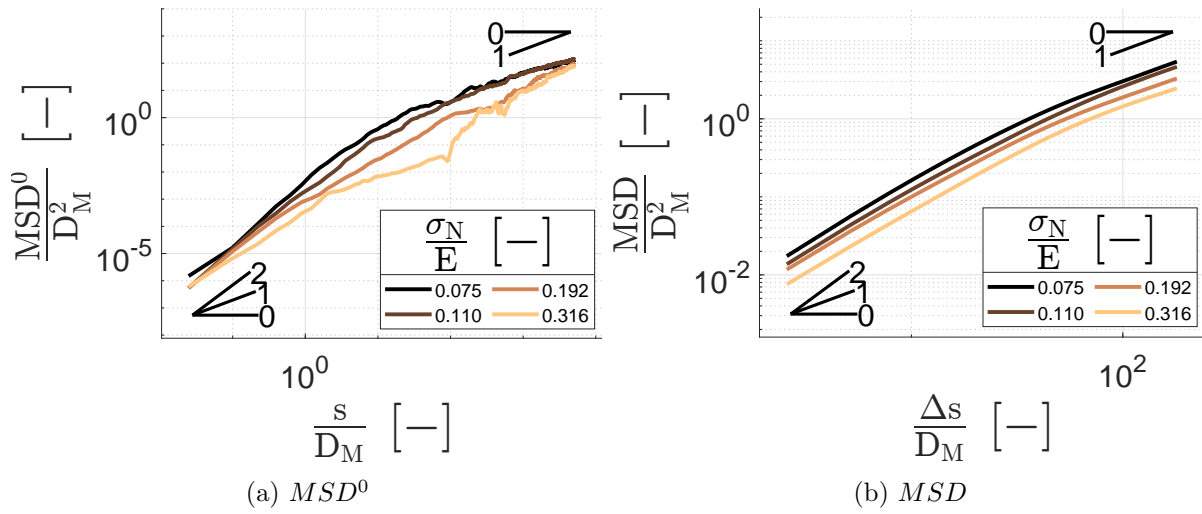


Figure C.8: Mean square displacement according to  $\sigma_N$

#### 3.2.2 Roughness (high-pass filter)

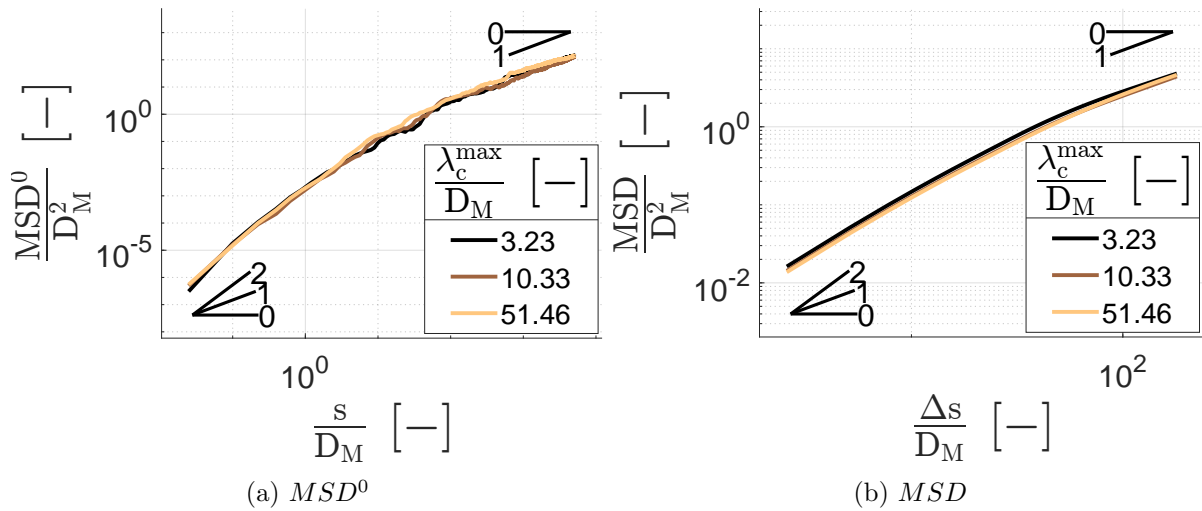


Figure C.9: Mean square displacement according to  $\lambda_c^{max}$



### 3.2.3 Roughness (low-pass filter)

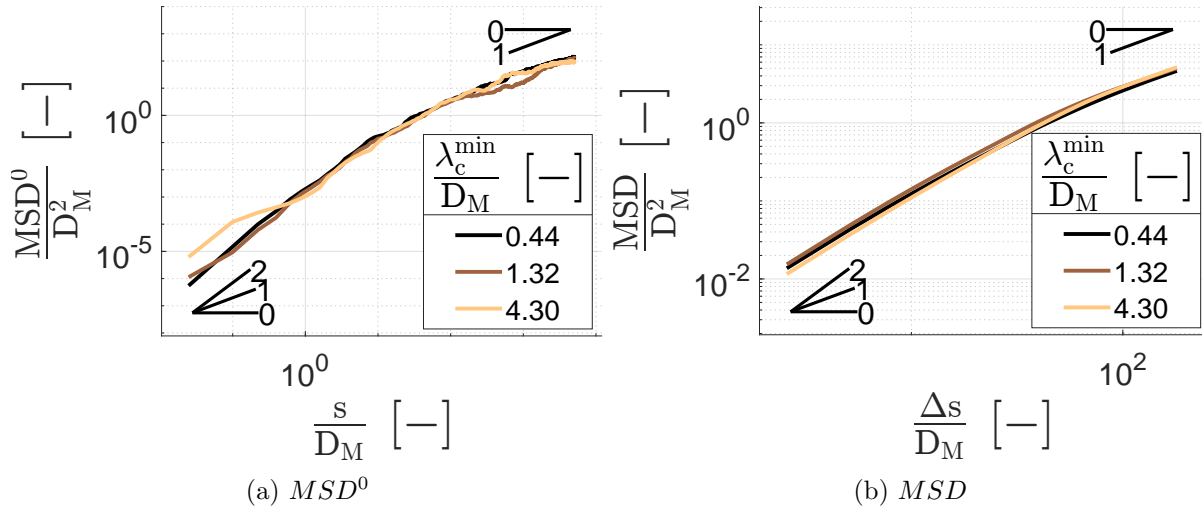


Figure C.10: Mean square displacement according to  $\lambda_c^{min}$

### 3.2.4 Mineral fraction

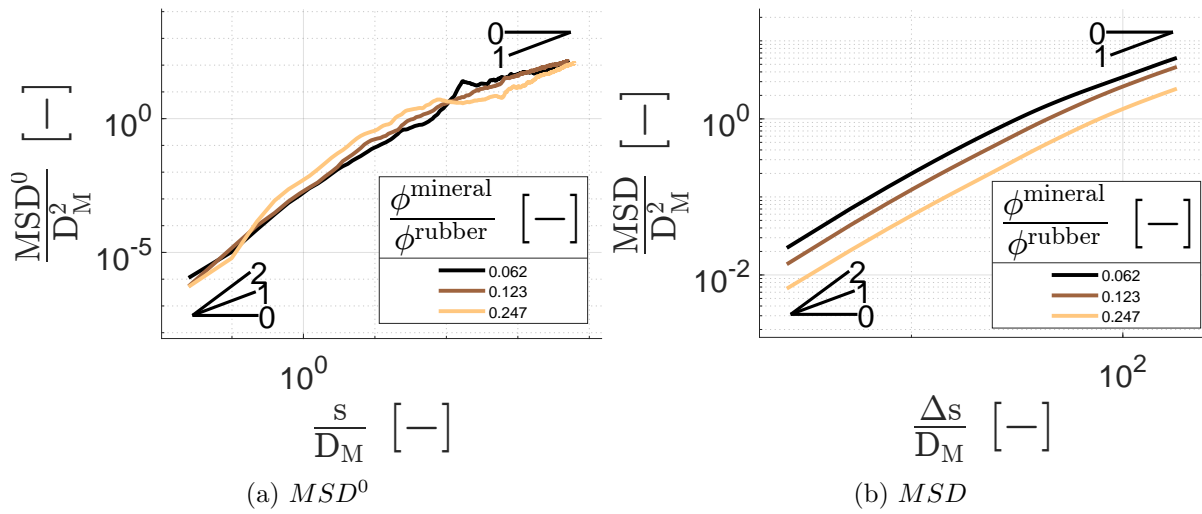


Figure C.11: Mean square displacement according to  $\frac{\phi^{mineral}}{\phi^{rubber}}$

### 3.2.5 Mineral size

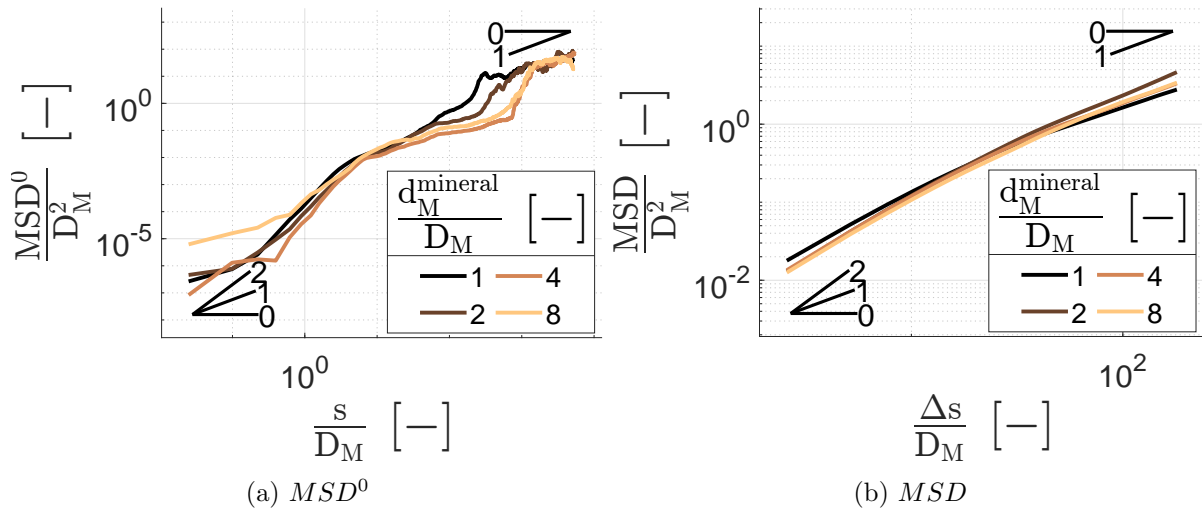


Figure C.12: Mean square displacement according to  $d_M^{mineral}$

### 3.3 Material parameters

#### 3.3.1 Rubber stiffness

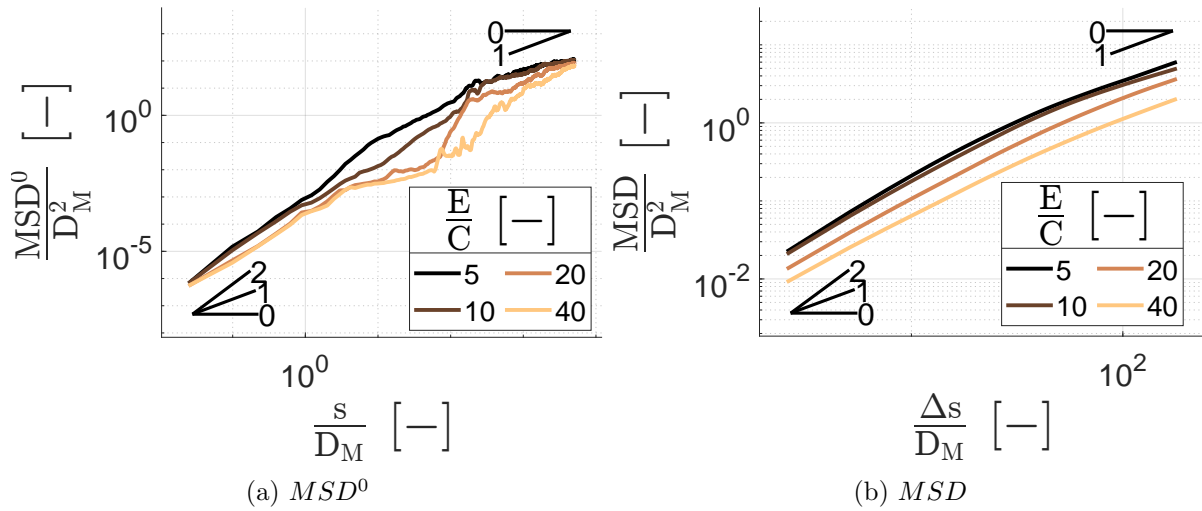


Figure C.13: Mean square displacement according to  $E$

### 3.3.2 Rubber cohesion

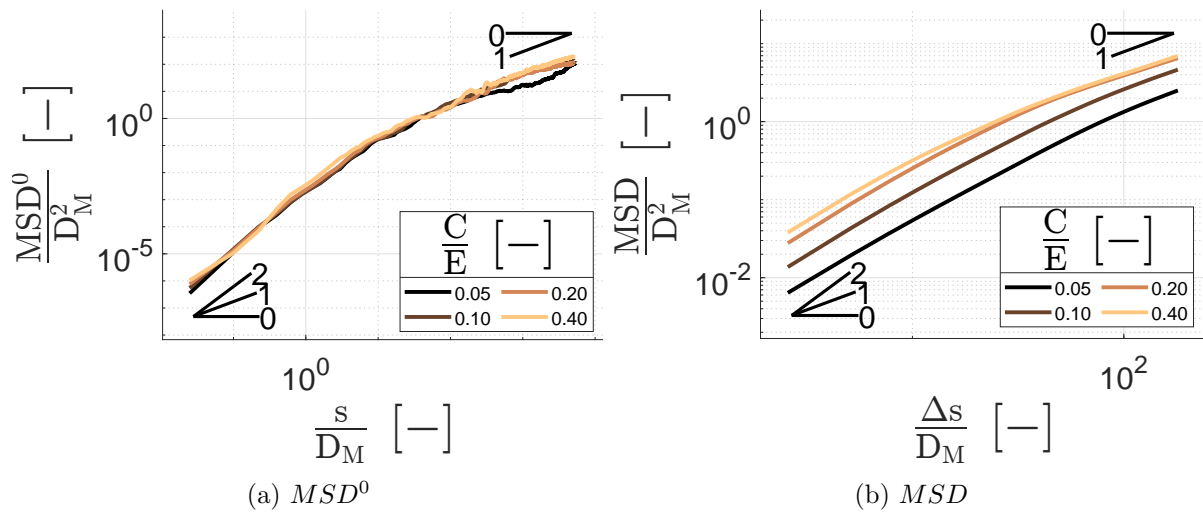


Figure C.14: Mean square displacement according to  $C$



## Appendix D

# Velocity autocorrelation function

### 1 Numerical parameters

### 1.2 Interfacial layer thickness

#### 1.1 Sliding velocity

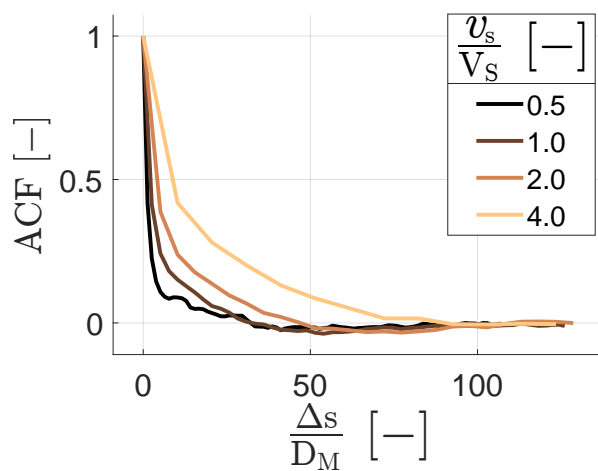


Figure D.1: Velocity autocorrelation function according to  $v_s$

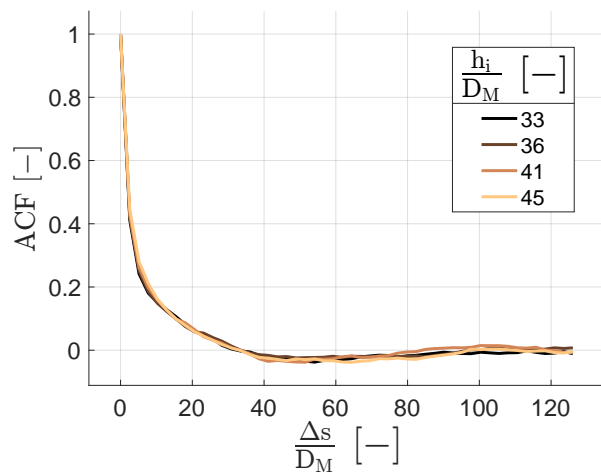


Figure D.2: Velocity autocorrelation function according to  $h_i$

### 1.3 Rubber particle size

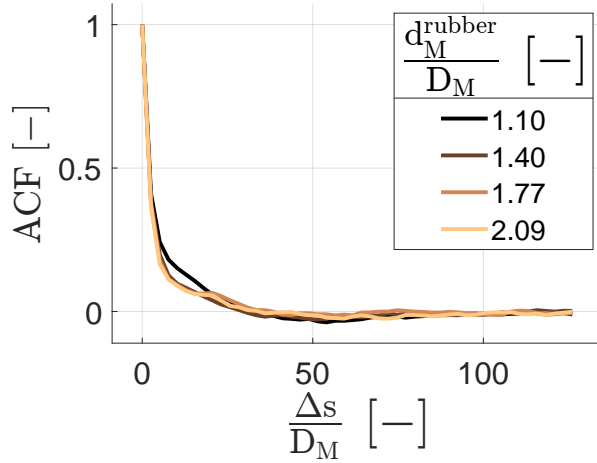


Figure D.3: Velocity autocorrelation function according to  $d_M^{rubber}$

### 2.2 Roughness (high-pass filter)

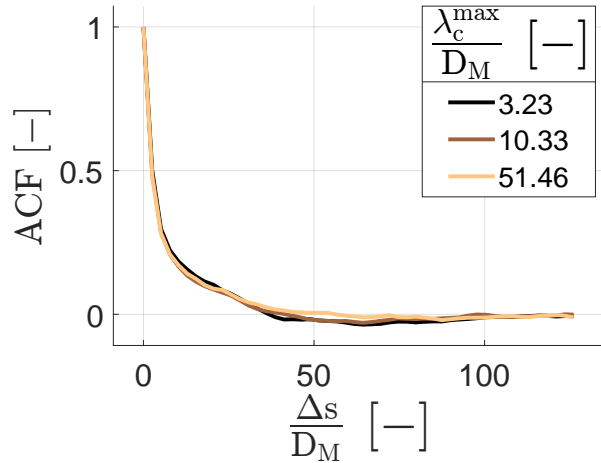


Figure D.5: Velocity autocorrelation function according to  $\lambda_c^{max}$

## 2 External parameters

### 2.1 Contact pressure

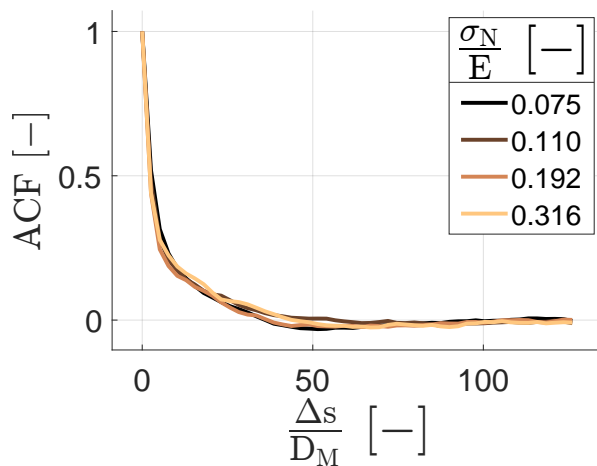


Figure D.4: Velocity autocorrelation function according to  $\sigma_N$

### 2.3 Roughness (low-pass filter)

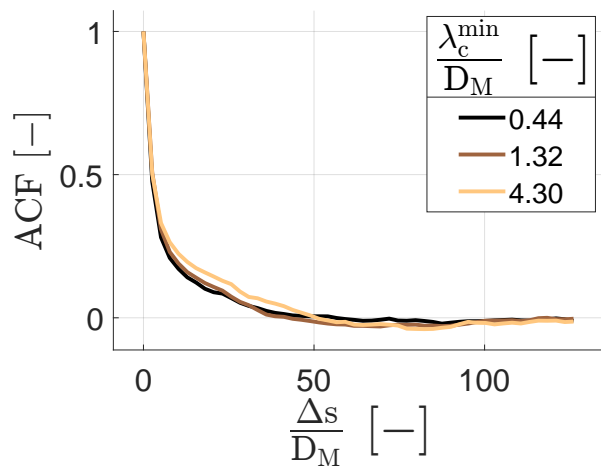


Figure D.6: Velocity autocorrelation function according to  $\lambda_c^{min}$



## 2.4 Mineral fraction

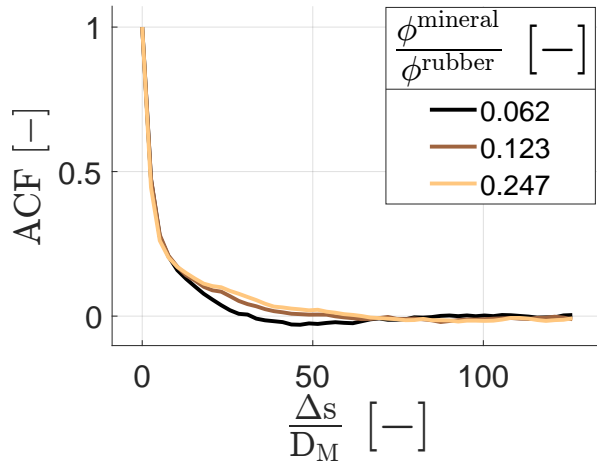


Figure D.7: Velocity autocorrelation function according to  $\frac{\phi_{\text{mineral}}}{\phi_{\text{rubber}}}$

## 3 Material parameters

### 3.1 Rubber stiffness

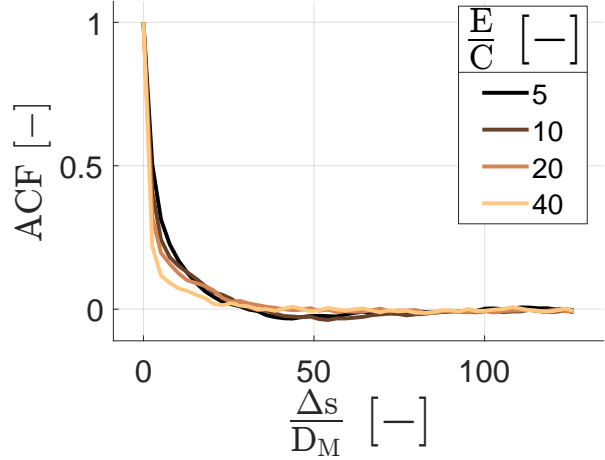


Figure D.9: Velocity autocorrelation function according to  $E$

## 2.5 Mineral size

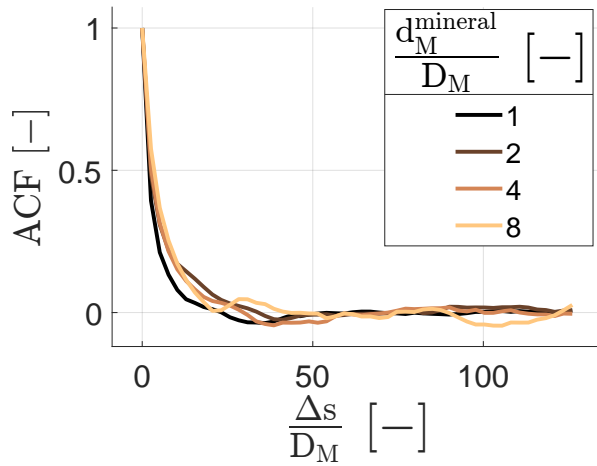


Figure D.8: Velocity autocorrelation function according to  $d_M^{\text{mineral}}$

### 3.2 Rubber cohesion

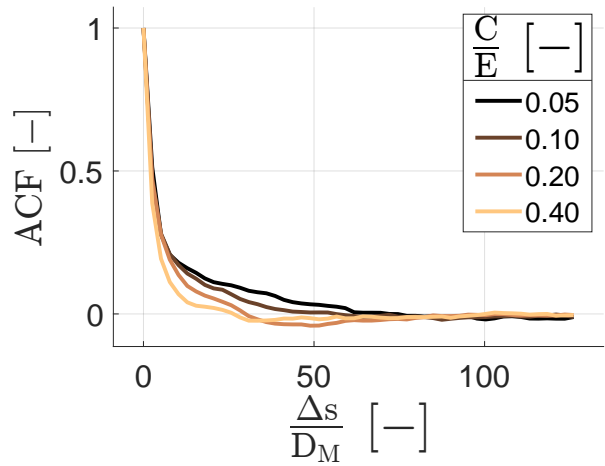


Figure D.10: Velocity autocorrelation function according to  $C$



# Bibliography

- Adachi, K. and Tainosho, Y. (2004). Characterization of heavy metal particles embedded in tire dust. *Environment International*, 30(8):1009–1017. [16](#), [48](#), [152](#)
- Aghababaei, R., Warner, D. H., and Molinari, J.-F. (2016). Critical length scale controls adhesive wear mechanisms. *Nature Communications*, 7(1):11816. Bandiera\_abtest: a Cc.license\_type: cc\_by Cg\_type: Nature Research Journals Number: 1 Primary\_atype: Research Publisher: Nature Publishing Group Subject\_term: Applied physics;Mechanical properties Subject\_term\_id: applied-physics;mechanical-properties. [64](#)
- Alfano, G. and Crisfield, M. A. (2001). Finite element interface models for the delamination analysis of laminated composites: mechanical and computational issues. *International Journal for Numerical Methods in Engineering*, 50(7):1701–1736. \_eprint: <https://onlinelibrary.wiley.com/doi/pdf/10.1002/nme.93>. [67](#)
- Aloui, S. and El Yaagoubi, M. (2021). Determining the Compression-Equivalent Deformation of SBR-Based Rubber Material Measured in Tensile Mode Using the Finite Element Method. *Applied Mechanics*, 2(1):195–208. Number: 1 Publisher: Multidisciplinary Digital Publishing Institute. [96](#)
- Altenhofen da Silva, M., Adeodato Vieira, M. G., Gomes Maçumoto, A. C., and Beppu, M. M. (2011). Polyvinylchloride (PVC) and natural rubber films plasticized with a natural polymeric plasticizer obtained through polyesterification of rice fatty acid. *Polymer Testing*, 30(5):478–484. [34](#)
- Andablo-Reyes, E., Hidalgo-Álvarez, R., and Vicente, J. d. (2011). Controlling friction using magnetic nanofluids. *Soft Matter*, 7(3):880–883. Publisher: The Royal Society of Chemistry. [50](#)
- Archard, J. F. (1953). Contact and Rubbing of Flat Surfaces. *Journal of Applied Physics*, 24(8):981–988. [65](#)
- Artoni, R., Richard, P., Larcher, M., and Jenkins, J. T. (2022). Self-diffusion in inhomogeneous granular shearing flows. *Physical Review E*, 106(3):L032901. Publisher: American Physical Society. [81](#)
- Bachelier, L. (1900). Théorie de la spéculation. *Annales scientifiques de l'École Normale Supérieure*, 17:21–86. [77](#)
- Baensch-Baltruschat, B., Kocher, B., Stock, F., and Reifferscheid, G. (2020). Tyre and road wear particles (TRWP) - A review of generation, properties, emissions, human health risk, ecotoxicity, and fate in the environment. *Science of The Total Environment*, 733:137823. [47](#), [48](#), [236](#)
- Barquins, M. (1985). Sliding friction of rubber and Schallamach waves — A review. *Materials Science and Engineering*, 73:45–63. [43](#), [44](#), [45](#), [236](#)

- Belytschko, T., Lu, Y. Y., and Gu, L. (1994). Element-free Galerkin methods. *International Journal for Numerical Methods in Engineering*, 37(2):229–256. [\\_eprint: https://onlinelibrary.wiley.com/doi/pdf/10.1002/nme.1620370205](https://onlinelibrary.wiley.com/doi/pdf/10.1002/nme.1620370205). 86
- Bolshakov, A. and Pharr, G. M. (1998). Influences of pileup on the measurement of mechanical properties by load and depth sensing indentation techniques. *Journal of Materials Research*, 13(4):1049–1058. Publisher: Cambridge University Press. 111
- Boochathum, P. and Prajudtake, W. (2001). Vulcanization of cis- and trans-polyisoprene and their blends: cure characteristics and crosslink distribution. *European Polymer Journal*, 37(3):417–427. 36, 68
- Bouillanne, O., Mollon, G., Saulot, A., Descartes, S., Serres, N., Demmou, K., and Chassaing, G. (2021). Detecting vorticity in cohesive deformable granular material. *EPJ Web of Conferences*, 249:08005. Publisher: EDP Sciences. 53, 58, 236
- Bui, H. D. and Chaillat, S. (2009). On a nonlinear inverse problem in viscoelasticity. *Vietnam Journal of Mechanics*, 31(3-4):211–219. Number: 3-4. 41
- Buradi, A., Morab, S., and Mahalingam, A. (2019). Effect of stenosis severity on shear-induced diffusion of red blood cells in coronary arteries. *Journal of Mechanics in Medicine and Biology*, 19(05):1950034. Publisher: World Scientific Publishing Co. 80
- Cadle, S. and Williams, R. (1978). Gas and Particle Emissions from Automobile Tires in Laboratory and Field Studies. *Journal of the Air Pollution Control Association*, 28(5):502–507. Publisher: Taylor & Francis [\\_eprint: https://doi.org/10.1080/00022470.1978.10470623](https://doi.org/10.1080/00022470.1978.10470623). 47
- Cai, R., Xiao, H., Zheng, J., and Zhao, Y. (2019). Diffusion of size bidisperse spheres in dense granular shear flow. *Physical Review E*, 99(3):032902. Publisher: American Physical Society. 81
- Campbell, C. S. and Brennen, C. E. (1983). Computer Simulation of Shear Flows of Granular Material. In Jenkins, J. T. and Satake, M., editors, *Studies in Applied Mechanics*, volume 7 of *Mechanics of Granular Materials*, pages 313–326. Elsevier. 61
- Candela, T., Renard, F., Klinger, Y., Mair, K., Schmittbuhl, J., and Brodsky, E. E. (2012). Roughness of fault surfaces over nine decades of length scales. *Journal of Geophysical Research: Solid Earth*, 117(B8). 76
- Cantor, D., Cárdenas-Barrantes, M., Preechawuttipong, I., Renouf, M., and Azéma, E. (2020). Compaction Model for Highly Deformable Particle Assemblies. *Physical Review Letters*, 124(20):208003. Publisher: American Physical Society. 62
- Carter, F. W. (1926). On the action of a locomotive driving wheel. *Proceedings of the Royal Society of London. Series A, Containing Papers of a Mathematical and Physical Character*, 112(760):151–157. Publisher: Royal Society. 55
- Casas, N. (2022). *Insights on the behavior of fault gouges during seismic sliding : A numerical investigation from granular rheology to friction laws*. These de doctorat, Lyon. 81
- Charbouillot, T., Janet, D. C., Schaal, P., Beynier, I., Boulat, J.-M., Grandchamp, A., and Biesse, F. (2023). Methodology for the direct measurement of tire emission factors. *Science of The Total Environment*, 863:160853. 47

- Chen, Z., Diebels, S., Peter, N. J., and Schneider, A. S. (2013). Identification of finite viscoelasticity and adhesion effects in nanoindentation of a soft polymer by inverse method. *Computational Materials Science*, 72:127–139. 110
- Cheng, Y.-T., Ni, W., and Cheng, C.-M. (2005). Determining the instantaneous modulus of viscoelastic solids using instrumented indentation measurements. *Journal of Materials Research*, 20(11):3061–3071. 125
- Chialvo, S., Sun, J., and Sundaresan, S. (2012). Bridging the rheology of granular flows in three regimes. *Physical Review E*, 85(2):021305. Publisher: American Physical Society. 61
- Cifuentes, S. C., Frutos, E., Benavente, R., González-Carrasco, J. L., and Lorenzo, V. (2014). Strain rate effect on semi-crystalline PLLA mechanical properties measured by instrumented indentation tests. *European Polymer Journal*, 59:239–246. 126
- Coran, A. Y. (2003). Chemistry of the vulcanization and protection of elastomers: A review of the achievements. *Journal of Applied Polymer Science*, 87(1):24–30. eprint: <https://onlinelibrary.wiley.com/doi/pdf/10.1002/app.11659>. 37, 92, 235
- Coulomb, C. A. -. A. d. t. (1821). *Théorie des machines simples (Nouv. éd.) / , en ayant égard au frottement de leurs parties et à la roideur des cordages, par C.-A. Coulomb, ... Nouvelle édition...* 50
- Cundall, P. A. and Strack, O. D. L. (1979). A discrete numerical model for granular assemblies. *Géotechnique*, 29(1):47–65. Publisher: ICE Publishing. 60
- Czichos, H., Becker, S., and Lexow, J. (1987). Multilaboratory tribotesting: Results from the Versailles Advanced Materials and Standards programme on wear test methods. *Wear*, 114(1):109–130. 50, 236
- Dahl, P. R. (1968). A Solid Friction Model:. Fort Belvoir, VA. Defense Technical Information Center. 57
- Daigne, K., Mollon, G., Descartes, S., Fillot, N., Jeanneret-Dit-Grosjean, R., Biesse, F., and Perriot, A. (2024). The tire–road contact: A mechanical mixing seen as a shear-induced diffusive process. *Wear*, 546-547:205339. 151
- Dall’Osto, M., Beddows, D. C. S., Gietl, J. K., Olatunbosun, O. A., Yang, X., and Harrison, R. M. (2014). Characteristics of tyre dust in polluted air: Studies by single particle mass spectrometry (ATOFMS). *Atmospheric Environment*, 94:224–230. 48
- Dao, M., Chollacoop, N., Van Vliet, K. J., Venkatesh, T. A., and Suresh, S. (2001). Computational modeling of the forward and reverse problems in instrumented sharp indentation. *Acta Materialia*, 49(19):3899–3918. 112
- de Wit, C. C., Olsson, H., Åström, K. J., and Lischinsky, P. (1995). A New Model for Control of Systems with Friction. *IEEE Transactions on Automatic Control*, 40(3). 57
- Dean, J. and Clyne, B. (2016). Extraction of Plasticity Parameters from a Single Test using a Spherical Indenter and FEM Modelling. *Mechanics of Materials*, 105. 120
- Decote, M., Fillot, N., Mahéo, Y., and Morales-Espejel, G. E. (2024). An Original Methodology to Model Stationary and Transient Starvation in Elastohydrodynamic Lubrication Contact. *Journal of Tribology*, 146(054102). 50
- Denny, D. F. (1953). The Influence of Load and Surface Roughness on the Friction of Rubber-Like Materials. *Proceedings of the Physical Society. Section B*, 66(9):721. 56

- Derjaguin, B. V., Muller, V. M., and Toporov, Y. P. (1975). Effect of contact deformations on the adhesion of particles. *Journal of Colloid and Interface Science*, 53(2):314–326. [53](#), [111](#)
- Descartes, S. and Berthier, Y. (2002). Rheology and flows of solid third bodies: background and application to an MoS<sub>1.6</sub> coating. *Wear*, 252(7):546–556. [51](#)
- Diani, J., Fayolle, B., and Gilormini, P. (2009). A review on the Mullins effect. *European Polymer Journal*, 45(3):601–612. [40](#), [236](#)
- Done, V., Kesavan, D., Krishna R, M., Chaise, T., and Nelias, D. (2017). Semi analytical fretting wear simulation including wear debris. *Tribology International*, 109:1–9. [66](#)
- Dowson, D. (1998). *History of Tribology, 2nd Edition*. [49](#), [236](#)
- Duriez, J. and Bonelli, S. (2021). Precision and computational costs of Level Set-Discrete Element Method (LS-DEM) with respect to DEM. *Computers and Geotechnics*, 134:104033. [62](#)
- Dvorak, S. D., Wahl, K. J., and Singer, I. L. (2007). In Situ Analysis of Third Body Contributions to Sliding Friction of a Pb–Mo–S Coating in Dry and Humid Air. *Tribology Letters*, 28(3):263–274. [51](#)
- Ebenstein, D. M. and Wahl, K. J. (2006). A comparison of JKR-based methods to analyze quasi-static and dynamic indentation force curves. *Journal of Colloid and Interface Science*, 298(2):652–662. [111](#)
- Edwards, D. C. (1990). Polymer-filler interactions in rubber reinforcement. *Journal of Materials Science*, 25(10):4175–4185. [34](#)
- Edwards, S. F. (1965). The statistical mechanics of polymers with excluded volume. *Proceedings of the Physical Society*, 85(4):613. [39](#)
- Einstein, A. (1906). Zur Theorie der Brownschen Bewegung. *Annalen der Physik*, 324(2):371–381. [79](#)
- Emami, A., Khaleghian, S., and Taheri, S. (2021). Asperity-based modification on theory of contact mechanics and rubber friction for self-affine fractal surfaces. *Friction*, 9(6):1707–1725. [46](#), [168](#)
- Fan, X., Xu, H., Wu, C., Song, Y., and Zheng, Q. (2020). Influences of chemical crosslinking, physical associating, and filler filling on nonlinear rheological responses of polyisoprene. *Journal of Rheology*, 64(4):775–784. [36](#)
- Fan, Y., Umbanhowar, P. B., Ottino, J. M., and Lueptow, R. M. (2015). Shear-Rate-Independent Diffusion in Granular Flows. *Physical Review Letters*, 115(8):088001. Publisher: American Physical Society. [81](#)
- Ferrellec, J.-F. and McDowell, G. R. (2010). A method to model realistic particle shape and inertia in DEM. *Granular Matter*, 12(5):459–467. [62](#)
- Feynman, R. (1962). The Feynman Lectures on Physics Vol. I Ch. 41: The Brownian Movement. [77](#)
- Fillot, N. (2004). *Etude mécanique de l'usure : Modélisation par Eléments Discrets des débits de troisième corps solide*. These de doctorat, Lyon, INSA. [58](#), [61](#), [67](#), [68](#), [236](#), [237](#)

- Fillot, N., Iordanoff, I., and Berthier, Y. (2007). Modelling third body flows with a discrete element method—a tool for understanding wear with adhesive particles. *Tribology International*, 40(6):973–981. 52
- Finkin, E. F. (1979). Adhesive wear: a general review of the state of experimental knowledge and theory. *International Journal of Materials in Engineering Applications*, 1(3):154–161. 65
- Fry, A. M., Umbanhowar, P. B., Ottino, J. M., and Lueptow, R. M. (2019). Diffusion, mixing, and segregation in confined granular flows. *AIChE Journal*, 65(3):875–881. eprint: <https://onlinelibrary.wiley.com/doi/pdf/10.1002/aic.16494>. 79
- Fujikawa, M., Maeda, N., Yamabe, J., Kodama, Y., and Koishi, M. (2014). Determining Stress–Strain in Rubber with In-Plane Biaxial Tensile Tester. *Experimental Mechanics*, 54(9):1639–1649. 96
- Furlong, O. J., Manzi, S. J., Pereyra, V. D., Bustos, V., and Tysoe, W. T. (2009). Kinetic Monte Carlo theory of sliding friction. *Physical Review B*, 80(15):153408. Publisher: American Physical Society. 64
- Garcin, S., Fouvry, S., and Heredia, S. (2015). A FEM fretting map modeling: Effect of surface wear on crack nucleation. *Wear*, 330-331:145–159. 66
- Geyer, R., Jambeck, J. R., and Law, K. L. (2017). Production, use, and fate of all plastics ever made. *Science Advances*, 3(7):e1700782. 47
- Ghosh, K. and Krishnamurthy, C. V. (2018). Structural behavior of supercritical fluids under confinement. *Physical Review E*, 97(1):012131. Publisher: American Physical Society. 140
- Gingold, R. A. and Monaghan, J. J. (1977). Smoothed particle hydrodynamics: theory and application to non-spherical stars. *Monthly Notices of the Royal Astronomical Society*, 181(3):375–389. 64
- Godet, M. (1984). The third-body approach: A mechanical view of wear. *Wear*, 100(1):437–452. 51
- Gorenflo, R., Mainardi, F., Moretti, D., Pagnini, G., and Paradisi, P. (2002). Discrete random walk models for space–time fractional diffusion. *Chemical Physics*, 284(1):521–541. 77
- Grosch, K. A. (2007). Goodyear Medalist Lecture. Rubber Friction and its Relation to Tire Traction. *Rubber Chemistry and Technology*, 80(3):379–411. 46, 236
- Grosch, K. A. and Bowden, F. P. (1997). The relation between the friction and visco-elastic properties of rubber. *Proceedings of the Royal Society of London. Series A. Mathematical and Physical Sciences*, 274(1356):21–39. Publisher: Royal Society. 38
- Grunlan, J. C., Xia, X., Rowenhorst, D., and Gerberich, W. W. (2001). Preparation and evaluation of tungsten tips relative to diamond for nanoindentation of soft materials. *Review of Scientific Instruments*, 72(6):2804. Publisher: American Institute of PhysicsAIP. 111
- Guan, J., Zhou, X., Liu, L., and Ran, M. (2023). Measurement of Tire-Pavement Contact Tri-Axial Stress Distribution Based on Sensor Array. *Coatings*, 13(2):416. Number: 2 Publisher: Multidisciplinary Digital Publishing Institute. 43, 236
- Haessig, Jr., D. A. and Friedland, B. (1991). On the Modeling and Simulation of Friction. *Journal of Dynamic Systems, Measurement, and Control*, 113(3):354–362. 56



- Hanson, D. E., Hawley, M., Houlton, R., Chitanvis, K., Rae, P., Orler, E. B., and Wroblewski, D. A. (2005). Stress softening experiments in silica-filled polydimethylsiloxane provide insight into a mechanism for the Mullins effect. *Polymer*, 46(24):10989–10995. [40](#)
- Hansson, T., Oostenbrink, C., and van Gunsteren, W. (2002). Molecular dynamics simulations. *Current Opinion in Structural Biology*, 12(2):190–196. [64](#)
- Harwood, J. a. C., Mullins, L., and Payne, A. R. (1965). Stress softening in natural rubber vulcanizates. Part II. Stress softening effects in pure gum and filler loaded rubbers. *Journal of Applied Polymer Science*, 9(9):3011–3021. \_eprint: <https://onlinelibrary.wiley.com/doi/pdf/10.1002/app.1965.070090907>. [40](#)
- Hegadekatte, V., Huber, N., and Kraft, O. (2004). Finite element based simulation of dry sliding wear. *Modelling and Simulation in Materials Science and Engineering*, 13(1):57. [66](#)
- Hemette, S. (2019). *Rubber-ice friction : a multi-scale and multi-physical approach*. phdthesis, Université de Lyon. [46](#), [236](#)
- Hermange, C. (2017). *Numerical simulation of the fluid-structure interactions inside the aquaplaning problem*. phdthesis, École centrale de Nantes. [64](#)
- Hertz, H. (1882). Ueber die Berührung fester elastischer Körper. *Journal für die reine und angewandte Mathematik*, 92:156–171. [50](#), [53](#)
- Hofstetter, K., Grohs, C., Eberhardsteiner, J., and Mang, H. A. (2006). Sliding behaviour of simplified tire tread patterns investigated by means of FEM. *Computers & Structures*, 84(17):1151–1163. [60](#)
- Hosler, D., Burkett, S. L., and Tarkanian, M. J. (1999). Prehistoric Polymers: Rubber Processing in Ancient Mesoamerica. *Science*, 284(5422):1988–1991. Publisher: American Association for the Advancement of Science. [32](#)
- Huang, M., Guibert, M., Thévenet, J., Fayolle, C., Chaussée, T., Guy, L., Vanel, L., Loubet, J. L., and Sotta, P. (2018). A new test method to simulate low-severity wear conditions experienced by rubber tire materials. *Wear*, 410-411:72–82. [51](#)
- Húlan, T. and Štubňa, I. (2020). Young’s modulus of kaolinite-illite mixtures during firing. *Applied Clay Science*, 190:105584. [96](#)
- Iordanoff, I. and Berthier, Y. (1999). First steps for a rheological model for the solid third body. In Dowson, D., Priest, M., Taylor, C. M., Ehret, P., Childs, T. H. C., Dalmaz, G., Berthier, Y., Flamand, L., Georges, J. M., and Lubrecht, A. A., editors, *Tribology Series*, volume 36 of *Lubrication at the Frontier*, pages 551–559. Elsevier. [61](#)
- Iurian, C., Ikhouane, F., Rodellar, J., and Griñó, R. (2005). Identification of a system with dry friction. [57](#), [236](#)
- Jean, M. (1999). The non-smooth contact dynamics method. *Computer Methods in Applied Mechanics and Engineering*, 177(3):235–257. [62](#)
- Johnson, K. L. (1987). *Contact Mechanics*. Cambridge University Press. Google-Books-ID: Do6WQIUwbpkC. [53](#)
- Johnson, K. L., Kendall, K., Roberts, A. D., and Tabor, D. (1971). Surface energy and the contact of elastic solids. *Proceedings of the Royal Society of London. A. Mathematical and Physical Sciences*, 324(1558):301–313. Publisher: Royal Society. [53](#), [111](#)

- Kalker, J. J. (1990). *Three-Dimensional Elastic Bodies in Rolling Contact*, volume 2 of *Solid Mechanics and Its Applications*. Springer Netherlands, Dordrecht. 55
- Kawahara, S., Nishioka, H., Yamano, M., and Yamamoto, Y. (2022). Synthetic Rubber with the Tensile Strength of Natural Rubber. *ACS Applied Polymer Materials*, 4(4):2323–2328. Publisher: American Chemical Society. 39
- Keoke, E. D. and Porterfield, K. M. (2002). *Encyclopedia of American Indian contributions to the world: 15,000 years of inventions and innovations*. Facts on File library of American history. Facts on File, New York, NY. 31
- Kermouche, G., Loubet, J. L., and Bergheau, J. M. (2006). A new index to estimate the strain rate sensitivity of glassy polymers using conical/pyramidal indentation. *Philosophical Magazine*, 86(33-35):5667–5677. Publisher: Taylor & Francis \_eprint: <https://doi.org/10.1080/14786430600778682>. 125
- Kharel, P. and Rognon, P. (2018). Shear-induced diffusion in non-local granular flows. *Europhysics Letters*, 124(2):24002. Publisher: EDP Sciences, IOP Publishing and Società Italiana di Fisica. 144
- Khodja, A. B. (2022). *Numerical and experimental methodologies for understanding and predicting the hydroplaning phenomenon of tires by numerical coupled SPH-Finite Elements simulations and PIV measurements*. phdthesis, École centrale de Nantes. 64
- Kim, S. and Kamrin, K. (2020). Power-Law Scaling in Granular Rheology across Flow Geometries. *Physical Review Letters*, 125(8):088002. Publisher: American Physical Society. 61
- Klapperich, C., Komvopoulos, K., and Pruitt, L. (2000). Nanomechanical Properties of Polymers Determined From Nanoindentation Experiments. *Journal of Tribology*, 123(3):624–631. 110
- Kole, P. J., Löhr, A. J., Van Belleghem, F. G. A. J., and Ragas, A. M. J. (2017). Wear and Tear of Tyres: A Stealthy Source of Microplastics in the Environment. *International Journal of Environmental Research and Public Health*, 14(10):1265. 47
- Kraus, G., Childers, C. W., and Rollmann, K. W. (1966). Stress softening in carbon black-reinforced vulcanizates. Strain rate and temperature effects. *Journal of Applied Polymer Science*, 10(2):229–244. \_eprint: <https://onlinelibrary.wiley.com/doi/pdf/10.1002/app.1966.070100205>. 40
- Kreider, M. L., Panko, J. M., McAtee, B. L., Sweet, L. I., and Finley, B. L. (2010). Physical and chemical characterization of tire-related particles: Comparison of particles generated using different methodologies. *Science of The Total Environment*, 408(3):652–659. 13, 16, 48, 49, 68, 152, 236
- Kummer, H. W. (1966). Unified Theory of Rubber and Tire Friction. Technical Report PB184487, Pennsylvania State Univ., University Park. Coll. of Engineering. Num Pages: 152. 46
- Lee, J., Lee, C., and Kim, B. (2009). Reverse analysis of nano-indentation using different representative strains and residual indentation profiles. *Materials & Design*, 30(9):3395–3404. 112
- Lichinchi, M., Lenardi, C., Haupt, J., and Vitali, R. (1998). Simulation of Berkovich nanoindentation experiments on thin films using finite element method. *Thin Solid Films*, 312(1):240–248. 117

- Limido, J., Espinosa, C., Salaün, M., and Lacombe, J. L. (2007). SPH method applied to high speed cutting modelling. *International Journal of Mechanical Sciences*, 49(7):898–908. [64](#)
- Liu, K., VanLandingham, M. R., and Ovaert, T. C. (2009). Mechanical characterization of soft viscoelastic gels via indentation and optimization-based inverse finite element analysis. *Journal of the Mechanical Behavior of Biomedical Materials*, 2(4):355–363. [112](#)
- Loadman, M. J. R. (2005). The glass transition temperature of natural rubber. *Journal of Thermal Analysis and Calorimetry*, 30(4):929–941. Publisher: Akadémiai Kiadó, co-published with Springer Science+Business Media B.V., Formerly Kluwer Academic Publishers B.V. Section: Journal of Thermal Analysis and Calorimetry. [38](#)
- Lorenz, B., Persson, B. N. J., Dieluweit, S., and Tada, T. (2011). Rubber friction: Comparison of theory with experiment. *The European Physical Journal E*, 34(12):129. [47](#)
- Macaulay, M. and Rognon, P. (2019). Shear-induced diffusion in cohesive granular flows: effect of enduring clusters. *Journal of Fluid Mechanics*, 858:R2. Publisher: Cambridge University Press. [25](#), [139](#), [160](#), [185](#)
- Manyo, E. Y. (2019). *Modélisation avancée du contact pneu-chaussée pour l'étude des dégradations des chaussées en surface*. phdthesis, Université de Limoges. [54](#), [236](#)
- Martínez, F. J., Canales, M., Izquierdo, S., Jiménez, M. A., and Martínez, M. A. (2012). Finite element implementation and validation of wear modelling in sliding polymer–metal contacts. *Wear*, 284-285:52–64. [66](#)
- Mashadi, B., Ebrahimi-Nejad, S., and Abbaspour, M. (2019). A rolling resistance estimate using nonlinear finite element numerical analysis of a full three-dimensional tyre model. *Proceedings of the Institution of Mechanical Engineers, Part D: Journal of Automobile Engineering*, 233(1):147–160. Publisher: IMECHE. [58](#), [236](#)
- McKee, C. T., Last, J. A., Russell, P., and Murphy, C. J. (2011). Indentation Versus Tensile Measurements of Young's Modulus for Soft Biological Tissues. *Tissue Engineering. Part B, Reviews*, 17(3):155–164. [110](#)
- Mekicha, M. A., de Rooij, M. B., Mishra, T., Matthews, D. T. A., Jacobs, L., and Schipper, D. J. (2021). Study of wear particles formation at single asperity contact: An experimental and numerical approach. *Wear*, 470-471:203644. [64](#)
- Milanese, E., Brink, T., Aghababaei, R., and Molinari, J.-F. (2020). Role of interfacial adhesion on minimum wear particle size and roughness evolution. *Physical Review E*, 102(4):043001. Publisher: American Physical Society. [16](#), [58](#), [152](#), [236](#)
- Molinari, J., Ortiz, M., Radovitzky, R., and Repetto, E. (2001). Finite-element modeling of dry sliding wear in metals. *Engineering Computations*, 18(3/4):592–610. Publisher: MCB UP Ltd. [66](#)
- Mollon, G. (2016). A multibody meshfree strategy for the simulation of highly deformable granular materials. *International Journal for Numerical Methods in Engineering*, 108(12):1477–1497. eprint: <https://onlinelibrary.wiley.com/doi/pdf/10.1002/nme.5258>. [15](#), [62](#), [81](#), [86](#), [237](#)
- Mollon, G. (2018a). Mixtures of hard and soft grains: micromechanical behavior at large strains. *Granular Matter*, 20(3):39. [150](#)
- Mollon, G. (2018b). A unified numerical framework for rigid and compliant granular materials. *Computational Particle Mechanics*, 5(4):517–527. [85](#), [90](#), [91](#), [237](#)

- Mollon, G. (2019). Solid Flow Regimes Within Dry Sliding Contacts. *Tribology Letters*, 67(4):120. [63](#), [82](#), [84](#), [109](#), [236](#), [237](#)
- Mollon, G. (2021). The soft discrete element method. *Granular Matter*, 24(1):11. [62](#), [185](#)
- Mollon, G., Aubry, J., and Schubnel, A. (2023). Laboratory Earthquakes Simulations—Typical Events, Fault Damage, and Gouge Production. *Journal of Geophysical Research: Solid Earth*, 128(2):e2022JB025429. \_eprint: <https://agupubs.onlinelibrary.wiley.com/doi/pdf/10.1029/2022JB025429>. [82](#), [237](#)
- Mollon, G. and Zhao, J. (2013). Generating realistic 3D sand particles using Fourier descriptors. *Granular Matter*, 15(1):95–108. [62](#)
- Moradkhani, A., Panahizadeh, V., and Hoseinpour, M. (2023). Indentation fracture resistance of brittle materials using irregular cracks: A review. *Heliyon*, 9(9):e19361. [110](#)
- Morris, M. D. and Kossyrev, P. A. (2018). INFLUENCE OF TIRE DEBRIS ON TIRE PERFORMANCE. *Rubber Chemistry and Technology*, 91(2):339–356. [16](#), [47](#), [51](#), [68](#), [152](#)
- Mullins, L. (1969). Softening of Rubber by Deformation. *Rubber Chemistry and Technology*, 42(1):339–362. [40](#)
- Ngan, A. H. W., Wang, H. T., Tang, B., and Sze, K. Y. (2005). Correcting power-law viscoelastic effects in elastic modulus measurement using depth-sensing indentation. *International Journal of Solids and Structures*, 42(5):1831–1846. [112](#)
- Ogden, R. W. and Roxburgh, D. G. (1999). A pseudo-elastic model for the Mullins effect in filled rubber. *Proceedings of the Royal Society of London. Series A: Mathematical, Physical and Engineering Sciences*, 455(1988):2861–2877. Publisher: Royal Society. [41](#)
- Oliver, W. and Pharr, G. (1992). An improved technique for determining hardness and elastic modulus using load and displacement sensing indentation experiments. *Journal of Materials Research*, 7(06):1564–1583. Publisher: Cambridge University Press (CUP). [111](#)
- Oliver, W. C. and Pharr, G. M. (2004). Measurement of hardness and elastic modulus by instrumented indentation: Advances in understanding and refinements to methodology. *Journal of Materials Research*, 19(1):3–20. Publisher: Cambridge University Press. [110](#)
- Oyen, M. L. and Cook, R. F. (2003). Load–displacement behavior during sharp indentation of viscous–elastic–plastic materials. *Journal of Materials Research*, 18(1):139–150. Publisher: Cambridge University Press. [110](#)
- Panko, J. M., Chu, J., Kreider, M. L., and Unice, K. M. (2013). Measurement of airborne concentrations of tire and road wear particles in urban and rural areas of France, Japan, and the United States. *Atmospheric Environment*, 72:192–199. [47](#)
- Payne, A. R. (1962). The dynamic properties of carbon black-loaded natural rubber vulcanizates. Part I. *Journal of Applied Polymer Science*, 6(19):57–63. \_eprint: <https://onlinelibrary.wiley.com/doi/pdf/10.1002/app.1962.070061906>. [39](#), [40](#), [68](#), [236](#)
- Persson, B. N. J. (1998). On the theory of rubber friction. *Surface Science*, 401(3):445–454. [46](#)
- Persson, B. N. J., Albohr, O., Tartaglino, U., Volokitin, A. I., and Tosatti, E. (2004). On the nature of surface roughness with application to contact mechanics, sealing, rubber friction and adhesion. *Journal of Physics: Condensed Matter*, 17(1):R1. [47](#)
- Petit, G. and Barquins, M. (2008). *Matériaux caoutchouteux - Gilles Petit, Michel Barquins*. Presses Polytechniques et Universitaires Romandes (PPUR). [32](#), [35](#)

- Piatkowski, T. (2014). Dahl and LuGre dynamic friction models — The analysis of selected properties. *Mechanism and Machine Theory*, 73:91–100. [57](#), [236](#)
- Pérez-Moral, N. and Mayes, A. G. (2004). Comparative study of imprinted polymer particles prepared by different polymerisation methods. *Analytica Chimica Acta*, 504(1):15–21. [34](#)
- Pödra, P. and Andersson, S. (1999). Simulating sliding wear with finite element method. *Tribology International*, 32(2):71–81. [66](#)
- Quacquarelli, A., Mollon, G., Commeau, T., and Fillot, N. (2023). Combining discrete and continuum mechanics to investigate local wear processes induced by an abrasive particle flow. *Tribology International*, 179:108126. [67](#)
- Reynolds, O. (1886). IV. On the theory of lubrication and its application to Mr. Beauchamp tower's experiments, including an experimental determination of the viscosity of olive oil. *Philosophical Transactions of the Royal Society of London*, 177:157–234. Publisher: Royal Society. [50](#)
- Riabokon, E., Poplygin, V., Turbakov, M., Kozhevnikov, E., Kobiakov, D., Guzev, M., and Wiercigroch, M. (2021). Nonlinear Young's Modulus of New Red Sandstone: Experimental Studies. *Acta Mechanica Solida Sinica*, 34(6):989–999. [96](#)
- Rodríguez, N., Masen, M., and Schipper, D.-J. (2013). Tribologically modified surfaces on elastomeric materials. *Proceedings of the Institution of Mechanical Engineers, Part J: Journal of Engineering Tribology*, 227(5):398–405. Publisher: IMECHE. [92](#)
- Rogge, W. F., Hildemann, L. M., Mazurek, M. A., Cass, G. R., and Simoneit, B. R. T. (1993). Sources of fine organic aerosol. 3. Road dust, tire debris, and organometallic brake lining dust: roads as sources and sinks. *Environmental Science & Technology*, 27(9):1892–1904. Publisher: American Chemical Society. [47](#)
- Rognon, P. and Macaulay, M. (2021). Shear-induced diffusion in dense granular fluids. *Soft Matter*, 17(21):5271–5277. Publisher: The Royal Society of Chemistry. [81](#)
- Roshan, H., Masoumi, H., and Regenauer-Lieb, K. (2017). Frictional behaviour of sandstone: A sample-size dependent triaxial investigation. *Journal of Structural Geology*, 94:154–165. [97](#)
- Sakharova, N. A., Fernandes, J. V., Antunes, J. M., and Oliveira, M. C. (2009). Comparison between Berkovich, Vickers and conical indentation tests: A three-dimensional numerical simulation study. *International Journal of Solids and Structures*, 46(5):1095–1104. [120](#)
- Savkoor, A. R. (1965). On the friction of rubber. *Wear*, 8(3):222–237. [46](#)
- Sawyer, W. G. and Tichy, J. A. (2000). Lubrication With Granular Flow: Continuum Theory, Particle Simulations, Comparison With Experiment. *Journal of Tribology*, 123(4):777–784. [61](#)
- Schallamach, A. (1953). The Velocity and Temperature Dependence of Rubber Friction. *Proceedings of the Physical Society. Section B*, 66(5):386. [56](#)
- Schallamach, A. (1971). How does rubber slide? *Wear*, 17(4):301–312. [42](#), [43](#), [45](#)
- Serier, J.-B. (1987). Avant le pneumatique. *Revue Générale du Caoutchouc et des Plastiques*. [33](#)
- Serier, J.-B. (1988). Importance et symbolisme du caoutchouc chez les précolombiens de l'aire mésoaméricaine. *Revue Générale du Caoutchouc et des Plastiques*. [31](#)
- Serier, J.-B. (1993). *Histoire du caoutchouc*. Desjonquières. [33](#)



- Shamim, N., Koh, Y. P., Simon, S. L., and McKenna, G. B. (2014). Glass transition temperature of thin polycarbonate films measured by flash differential scanning calorimetry. *Journal of Polymer Science Part B: Polymer Physics*, 52(22):1462–1468. eprint: <https://onlinelibrary.wiley.com/doi/pdf/10.1002/polb.23583>. 38
- Shi, X., Sun, S., Zhao, A., Zhang, H., Zuo, M., Song, Y., and Zheng, Q. (2021). Influence of carbon black on the Payne effect of filled natural rubber compounds. *Composites Science and Technology*, 203:108586. 39
- Shim, S., Oliver, W. C., and Pharr, G. M. (2007). A comparison of 3D finite element simulations for Berkovich and conical indentation of fused silica. *International Journal of Surface Science and Engineering*. Publisher: Inderscience Publishers. 117
- Shimamoto, T. and Logan, J. M. (1981). Effects of simulated clay gouges on the sliding behavior of Tennessee sandston. *Tectonophysics*, 75(3):243–255. 97
- Smith, R. W. and Veith, A. G. (1982). Electron Microscopical Examination of Worn Tire Treads and Tread Debris. *Rubber Chemistry and Technology*, 55(2):469–482. 68, 92, 112
- Sneddon, I. N. (1965). The relation between load and penetration in the axisymmetric boussinesq problem for a punch of arbitrary profile. *International Journal of Engineering Science*, 3(1):47–57. 111
- Sobczyk, K., Chmielewski, R., Kruszka, L., and Rekucki, R. (2022). Strength Characterization of Soils' Properties at High Strain Rates Using the Hopkinson Technique—A Review of Experimental Testing. *Materials*, 15(1):274. Number: 1 Publisher: Multidisciplinary Digital Publishing Institute. 125
- Stribeck, R. (1903). *Die wesentlichen Eigenschaften der Gleit- und Rollenlager*. Springer, Berlin. OCLC: 258709700. 50
- Suresh, S., Nieh, T. G., and Choi, B. W. (1999). Nano-indentation of copper thin films on silicon substrates. *Scripta Materialia*, 41(9):951–957. 110
- Tabor, D. (1977). Surface forces and surface interactions. *Journal of Colloid and Interface Science*, 58(1):2–13. 111
- Tabor, D. (2000). *The Hardness of Metals*. Oxford Classic Texts in the Physical Sciences. Oxford University Press, Oxford, New York. 118
- Taljat, B. and Pharr, G. M. (2004). Development of pile-up during spherical indentation of elastic–plastic solids. *International Journal of Solids and Structures*, 41(14):3891–3904. 20, 120
- Tallian, T. E. (1992). Simplified Contact Fatigue Life Prediction Model—Part I: Review of Published Models. *Journal of Tribology*, 114(2):207–213. 52
- Taylor, C. M., Childs, P. R. N., Berthier, Y., Flamand, L., Dalmaz, G., Dowson, D., Lubrecht, A. A., and Georges, J. M. (1996). *The Third Body Concept: Interpretation of Tribological Phenomena*. Elsevier. Google-Books-ID: .K3ZR0WiLBIC. 51
- Teoh, S. H., Chan, W. H., and Thampuran, R. (2002). An elasto-plastic finite element model for polyethylene wear in total hip arthroplasty. *Journal of Biomechanics*, 35(3):323–330. 65
- Tho, K. K., Swaddiwudhipong, S., Liu, Z. S., Zeng, K., and Hua, J. (2004). Uniqueness of reverse analysis from conical indentation tests. *Journal of Materials Research*, 19(8):2498–2502. 112

- Tiwari, A., Miyashita, N., and Persson, B. N. J. (2021). Rubber Wear and the Role of Transfer Films on Rubber Friction on Hard Rough Substrates. *Tribology Letters*, 69(2):42. 51
- Tsimpanogiannis, I. N., Moulton, O. A., Franco, L. F. M., Spera, M. B. d. M., Erdős, M., and Economou, I. G. (2019). Self-diffusion coefficient of bulk and confined water: a critical review of classical molecular simulation studies. *Molecular Simulation*, 45(4-5):425–453. Publisher: Taylor & Francis \_eprint: <https://doi.org/10.1080/08927022.2018.1511903>. 80
- Tsuneyuki, S., Tsukada, M., Aoki, H., and Matsui, Y. (1988). First-Principles Interatomic Potential of Silica Applied to Molecular Dynamics. *Physical Review Letters*, 61(7):869–872. Publisher: American Physical Society. 64
- Udupa, A., Sundaram, N., Sugihara, T., and Chandrasekar, S. (2019). Direct *In Situ* Observation of Deformation Modes in Wedge Indentation of Metals. *Materials Transactions*, 60(8):1442–1449. 120
- Unice, K. M., Weeber, M. P., Abramson, M. M., Reid, R. C. D., van Gils, J. a. G., Markus, A. A., Vethaak, A. D., and Panko, J. M. (2019). Characterizing export of land-based microplastics to the estuary - Part I: Application of integrated geospatial microplastic transport models to assess tire and road wear particles in the Seine watershed. *The Science of the Total Environment*, 646:1639–1649. 47
- Urzhumtsev, Y. S. (1975). Time-temperature superposition. Review. *Polymer Mechanics*, 11(1):57–72. 38, 68
- VanLandingham, M. R., Villarrubia, J. S., Guthrie, W. F., and Meyers, G. F. (2001). Nanoindentation of polymers: an overview. *Macromolecular Symposia*, 167(1):15–44. \_eprint: <https://onlinelibrary.wiley.com/doi/pdf/10.1002/1521-3900%28200103%29167%3A1%3C15%3A%3AAID-MASY15%3E3.0.CO%3B2-T>. 110
- Vignali, V., Mazzotta, F., Sangiorgi, C., Simone, A., Lantieri, C., and Dondi, G. (2016). Incorporation of Rubber Powder as Filler in a New Dry-Hybrid Technology: Rheological and 3D DEM Mastic Performances Evaluation. *Materials*, 9(10):842. Number: 10 Publisher: Multidisciplinary Digital Publishing Institute. 61
- Vouaillat, G., Noyel, J.-P., Ville, F., Kleber, X., and Rathery, S. (2019). From Hertzian contact to spur gears: analyses of stresses and rolling contact fatigue. *Mechanics & Industry*, 20(6):626. Number: 6 Publisher: EDP Sciences. 53
- Wallace, E. R. (2022). *On the rolling contact between multi-layered bodies, application to tire-pavement modelling*. phdthesis, Université de Lyon. 55, 236
- Wang, L., Gao, Y., Xue, Q., Liu, H., and Xu, T. (2005). Microstructure and tribological properties of electrodeposited Ni–Co alloy deposits. *Applied Surface Science*, 242(3):326–332. 65
- Wang, M.-J. (1999). The Role of Filler Networking in Dynamic Properties of Filled Rubber. *Rubber Chemistry and Technology*, 72(2):430–448. 39
- Wang, W., Liu, Y., Zhu, G., and Liu, K. (2014). Using FEM–DEM coupling method to study three-body friction behavior. *Wear*, 318(1):114–123. 62
- Warren, A. W. and Guo, Y. B. (2006). Machined surface properties determined by nanoindentation: Experimental and FEA studies on the effects of surface integrity and tip geometry. *Surface and Coatings Technology*, 201(1):423–433. 118



- Wei, X.-F., Linde, E., and Hedenqvist, M. S. (2019). Plasticiser loss from plastic or rubber products through diffusion and evaporation. *npj Materials Degradation*, 3(1):1–8. Number: 1 Publisher: Nature Publishing Group. 153
- Williams, M. L., Landel, R. F., and Ferry, J. D. (1955). The Temperature Dependence of Relaxation Mechanisms in Amorphous Polymers and Other Glass-forming Liquids. *Journal of the American Chemical Society*, 77(14):3701–3707. Publisher: American Chemical Society. 38
- Won, Y.-Y. and Ramkrishna, D. (2019). Revised Formulation of Fick’s, Fourier’s, and Newton’s Laws for Spatially Varying Linear Transport Coefficients. *ACS Omega*, 4(6):11215–11222. Publisher: American Chemical Society. 80
- Woodcock, C. L. and Bahr, D. F. (2000). Plastic zone evolution around small scale indentations. *Scripta Materialia*, 43(9):783–788. 110
- Yan, W., Pun, C. L., and Simon, G. P. (2012). Conditions of applying Oliver–Pharr method to the nanoindentation of particles in composites. *Composites Science and Technology*, 72(10):1147–1152. 111
- Yang, E., Bui, H. H., Nguyen, G. D., Choi, C. E., Ng, C. W. W., De Sterck, H., and Bouazza, A. (2021). Numerical investigation of the mechanism of granular flow impact on rigid control structures. *Acta Geotechnica*, 16(8):2505–2527. 58, 64, 236
- Yoon, M. and Kang, G.-H. (2023). Effect of dynamic friction and static friction in finite element analysis of carbon fiber preform. *Polymer Composites*, 44(4):2396–2404. eprint: <https://4spepublications.onlinelibrary.wiley.com/doi/pdf/10.1002/pc.27251>. 59
- Zeng, E. Y., Tran, K., and Young, D. (2004). Evaluation of Potential Molecular Markers for Urban Stormwater Runoff. *Environmental Monitoring and Assessment*, 90(1):23–43. 47
- Zhang, F., An, M., Zhang, L., Fang, Y., and Elsworth, D. (2019). The Role of Mineral Composition on the Frictional and Stability Properties of Powdered Reservoir Rocks. *Journal of Geophysical Research: Solid Earth*, 124(2):1480–1497. eprint: <https://onlinelibrary.wiley.com/doi/pdf/10.1029/2018JB016174>. 97
- Álvarez Vázquez, A., Fernández-Canteli, A., Castillo Ron, E., Fernández Fernández, P., Muñoz-Calvente, M., and Lamela Rey, M. J. (2020). A Novel Approach to Describe the Time–Temperature Conversion among Relaxation Curves of Viscoelastic Materials. *Materials*, 13(8):1809. Number: 8 Publisher: Multidisciplinary Digital Publishing Institute. 38
- Škec, L., Alfano, G., and Jelenić, G. (2018). On  $G_c$ ,  $J_c$  and the characterisation of the mode-I fracture resistance in delamination or adhesive debonding. *International Journal of Solids and Structures*, 144-145:100–122. 67, 236



# List of Figures

1	Image MEB (microscope électronique à balayage) avec un contraste correspondant au numéro atomique (Z-contrast) pour une coupe longitudinale d'une éprouvette après un essai d'usure; la direction de glissement est horizontale . . . . .	13
2	Illustration du mécanisme étudié . . . . .	14
3	Illustration du tribomètre et des deux corps en contact . . . . .	15
4	Images MEB avec un contraste correspondant au numéro atomique (Z-contrast) pour 4 distances glissées (1,5, 3,0, 6,0 et 12,0 m) . . . . .	16
5	Image MEB avec un contraste correspondant au numéro atomique (Z-contrast) et cartes EDX correspondantes pour le carbone (C), l'aluminium (Al), le silicium (Si) et l'oxygène (O); la section longitudinale est obtenue par une coupe à la guillotine suivie d'un polissage ionique (Gatan, Ilion II); la charge normale est de 1508 N (0,8 MPa rapporté à l'aire de contact apparente), la vitesse de rotation de 32 RPM (0,10 m.s <sup>-1</sup> sur le rayon médian) et la longueur glissée de 3,0 m . . . . .	17
6	Illustration du modèle numérique d'indentation . . . . .	18
7	Cinématique selon la cohésion normalisée ( $E = 5 \text{ MPa}$ ); le fond correspond au champ de déplacement résiduel ( $U_r$ ) normalisé par la profondeur maximale d'indentation ( $h_{max}$ ); $U_r$ est égal à la norme du déplacement de chaque centroïde entre l'état initial et l'état final; les lignes correspondent aux différentes positions des centroïdes au cours de l'indentation et la couleur au temps ( $t$ ) normalisé par le temps auquel l'indenteur est revenu à sa position initiale ( $t_{max}$ ) . . . . .	19
8	Méthode d'identification de $E$ et $C$ à partir d'une analyse inverse; les rapports obtenus numériquement sont mis en évidence en bleu et les valeurs qui peuvent être extraites des mesures en rouge . . . . .	21
9	Illustration du modèle numérique de diffusion . . . . .	22
10	Principaux résultats concernant la diffusion . . . . .	24
11	Illustration des mécanismes de chevauchement . . . . .	25
1.1	Monument 171 from Tonina showing a Maya ball game (from D. Stuart) . . . . .	31
1.2	Worker removing a tire from an industrial oven used for vulcanization and molding in 1943 (from Flickr, BiblioArchives/LibraryArchives) . . . . .	32
1.3	Pedestrian hobbyhorse, 1819 (from National Cycle Museum, Wales) . . . . .	33
1.4	Isoprene . . . . .	34
1.5	Polyisoprene (from Roland Chem) . . . . .	34
1.6	Granules and powders used in the mixing process . . . . .	35
1.7	Rubber mixture after the mixing process (from indiamart) . . . . .	35
1.8	Vulcanization of polyisoprene . . . . .	36
1.9	Illustration of the loss angle . . . . .	36
1.10	Properties as a function of crosslink density (from [Coran, 2003]) . . . . .	37
1.11	Modulus as a function of temperature . . . . .	37
1.12	Extrapolation using the WLF method . . . . .	39

1.13	Modulus of a natural rubber as a function of the dynamic tensile strain amplitude and for different amounts of carbon black fillers given as a percentage of total volume (from [Payne, 1962]) . . . . .	40
1.14	Stress-strain curves for a 50 phr carbon-black filled SBR under a simple and a cyclic uniaxial tension test (from [Diani et al., 2009]) . . . . .	40
1.15	Rheological models describing rubber-like materials . . . . .	41
1.16	Structure of a radial tire . . . . .	42
1.17	Sliding of a hemispherical glass slider on a transparent rubber plate in a stationary state . . . . .	43
1.18	Load per unit area (from [Guan et al., 2023]) . . . . .	43
1.19	Sliding (from left to right) of a hemispherical glass slider on a transparent rubber plate in a non-stationary state (from [Barquins, 1985]) . . . . .	44
1.20	Schallamach waves observed for the sliding (from left to right) of a hemispherical glass slider on a transparent rubber plate in a non-stationary state (from [Barquins, 1985]) . . . . .	45
1.21	Friction test for nitrile butadiene rubber (NBR), styrene butadiene rubber (SBR), natural rubber (NR) and butadiene rubber (BR), with two counter surfaces and for several sliding velocity ( $V_g$ ); frequencies ( $f$ ) are obtained using an equivalent wavelength and are multiplied by the translation factor ( $\alpha_T$ ) (from [Grosch, 2007; Hemente, 2019]) . . . . .	46
1.22	Main TRWP transport modes and the associated risks (from [Baensch-Baltrusch et al., 2020]) . . . . .	48
1.23	SEM images of a TWP for different magnifications (from [Kreider et al., 2010]) . . . . .	49
1.24	Tomb of Tehuti-Hetep, El-Bersheh, 1880 BC (adapted from [Dowson, 1998]) . . . . .	49
1.25	Results of the VAMAS experiment; each bar represents the amplitude of the friction coefficient for a given laboratory; horizontal lines correspond to the mean value $\pm$ the standard deviation over all laboratories (results from [Czichos et al., 1987] and graphic adapted from CETIM magazine) . . . . .	50
1.26	Illustration of the tribological circuit with $Q_I$ the internal flow, $Q_R$ the recirculation flow, $Q_S$ the source flow, $Q_E$ the external flow and $Q_W$ the wear flow . . . . .	52
1.27	Different contact geometries covered by Hertzian theory (cylinder/plane, sphere/plane) (from [Bouillanne et al., 2021]) . . . . .	53
1.28	Illustration of the differences between the JKR, Hertzian and DMT theories; the red line represents the Hertzian contact area; the blue line represents the contact area due to adhesion forces . . . . .	54
1.29	Illustration of a rolling contact (from [Manyo, 2019]) . . . . .	54
1.30	Illustration of the theory of Carter with $x$ the spatial dimension and $q_x$ the friction force per unit area (from [Wallace, 2022]) . . . . .	55
1.31	Illustration of the bristle model (from [Iurian et al., 2005]) . . . . .	57
1.32	Illustration of two physics-based models (adapted from [Piatkowski, 2014]) . . . . .	57
1.33	Illustration of different methods related to dry friction (simulation images from [Milanese et al., 2020; Fillot, 2004; Yang et al., 2021; Mashadi et al., 2019]) . . . . .	58
1.34	Illustration of a model at the scale of the first bodies . . . . .	59
1.35	Illustration of two rigid grains in contact . . . . .	61
1.36	Illustration of two soft grains in contact . . . . .	63
1.37	Simulations using the same grain contact model with high and low grain stiffness (from [Mollon, 2019]) . . . . .	63
1.38	Illustration of the mesh before and after particle removal . . . . .	66
1.39	Illustration of the CZM (from [Škec et al., 2018]) . . . . .	67

1.40	Wear model using DEM for which particles can be ejected from the contact; yellow and green particles represent first bodies and purple particles represent particles detached from first bodies (from [Fillot, 2004]) . . . . .	68
1.41	Photos of the worn specimens . . . . .	69
1.42	SEM image of a particle on the surface of a worn specimen (color representing Z-contrast) . . . . .	69
1.43	SEM image of a longitudinal section of a wear specimen (color representing the Z-contrast); sliding direction is horizontal . . . . .	70
1.44	Illustration of the main features required by the model . . . . .	71
2.1	Illustration of the tribometer and the two bodies in contact . . . . .	73
2.2	Cutting plan of the longitudinal sections . . . . .	74
2.3	Mineral size distribution obtained from segmentation analysis; the equivalent diameter corresponds to the diameter of the circle to obtain the same area . . . . .	75
2.4	Fitting from mineral segmentation . . . . .	75
2.5	Surface topography measured by interferometry . . . . .	76
2.6	Power spectral density as a function of spatial frequency; the markers correspond to the 1D PSD matrix and the dotted lines to the fittings . . . . .	76
2.7	Illustration of a diffusive process between two chemical species . . . . .	77
2.8	Random walk algorithm for 10000 particles and 10000 iterations (i.e. time steps); at each time step, a particle is randomly (without defining a probability distribution) shifted by -1, 0 or 1; $y_{max} = 392$ , $t_{max} = 10000$ and the bin width is equal to $0.05 y_{max}$ for the histogram . . . . .	78
2.9	Concentration according to the second law of Fick for arbitrary parameters ( $y_{max} = 1 m$ , $t_{max} = 1 s$ , $D = 4.10^{-2} m^2.s^{-1}$ , $\varphi = 1$ for $y \in [-0.025, 0.025] \times y_{max}$ and $t = 0 s$ ) . . . . .	79
2.10	Illustration of a particle jump due to a collision with another particle . . . . .	80
2.11	Compression of a brittle material under several confining stresses (from [Mollon et al., 2023]) . . . . .	82
2.12	Friction coefficients of a sliding interface model using soft bodies (from [Mollon, 2019]) . . . . .	82
2.13	Snapshots (particle color is arbitrary) for a given viscosity and for several stiffnesses and cohesions (from [Mollon, 2019]) . . . . .	84
2.14	Illustration of pre-cut materials with $F$ a tensile force and $V_s$ a sliding velocity . . . . .	85
2.15	Comparison of soft and rigid bodies (from [Mollon, 2018b]) . . . . .	85
2.16	Discretization nodes of a soft body (from [Mollon, 2016]) . . . . .	86
2.17	Proximity detection stages (from [Mollon, 2018b]) . . . . .	90
2.18	Computation of the interpenetration distance of nodes from body B in body A (from [Mollon, 2018b]) . . . . .	91
2.19	Illustration of the diffusion model . . . . .	93
2.20	Generated 2D profile for the road-like surface . . . . .	94
2.21	Minerals after a compaction stage for several quantities; masses are expressed in terms of contact area equivalence between the experimental set-up and the numerical model . . . . .	95
2.22	Typical thickness variation for an imposed contact pressure, for several sliding velocities $v_S$ and as a function of the sliding distance; $h_i^0$ corresponds to the thickness at the initial state . . . . .	96
2.23	Main stages of a given simulation . . . . .	98
2.24	Example of MSD for a given simulation . . . . .	99
2.25	Illustration of the mineral fraction computation for a rough description of mineral size distribution . . . . .	100
2.26	Illustration of the velocity profile computation . . . . .	101

2.27	Illustration of the shear rate computation . . . . .	102
3.1	Illustration of non-unicity for arbitrary parameters; the specified parameters could refer to any parameters, such as $\sigma$ a stress, $\mu$ a friction coefficient, $E$ the Young's modulus and $C$ the cohesion.; if the reverse analysis is performed based on $\mu$ , it might give the wrong set of input parameters and a wrong value of $\sigma$ . . . . .	110
3.2	Illustration of pile-up and sink-in phenomena . . . . .	111
3.3	Illustration of a load-displacement curve of an indentation test . . . . .	112
3.4	Surface topography measured by interferometry . . . . .	114
3.5	Configurations used for the indentations . . . . .	115
3.6	Illustration of the indentation model; $h_{max}$ corresponds to the maximum indentation depth ( $1 \mu m$ ) . . . . .	115
3.7	Preliminary study to determine the semicircular radius . . . . .	116
3.8	Preliminary study to determine the size of the discrete domain . . . . .	116
3.9	Main preliminary stages . . . . .	117
3.10	Kinematics according to normalized cohesion ( $E = 5 MPa$ ); the background corresponds to the residual displacement field ( $U_r$ ) normalized by the maximum indentation depth ( $h_{max}$ ); $U_r$ is equal to the centroid displacement norm between the initial and final states; the lines correspond to various centroid positions during indentation and the color to time ( $t$ ) normalized by the time at which the tip has returned to its initial position ( $t_{max}$ ) (►) . . . . .	119
3.11	Load-depth curves according to the stiffness (1, 5 and 10 MPa) and for several normalized cohesions (0.05, 0.10, 0.20 and 0.40) . . . . .	121
3.12	Method for identifying $C$ and $E$ from reverse analysis; ratios obtained numerically are highlighted in blue and values that can be extracted from measurements in red	123
3.13	Experimental results for several strain rates (0.01, 0.02, 0.03, 0.04, 0.05, 0.06, 0.10, 0.20 and $0.50 s^{-1}$ ) . . . . .	125
3.14	Results according to indentation depth from CSM tests . . . . .	126
3.15	Reverse analysis procedure; ratios obtained numerically are highlighted in blue and values that can be extracted from measurements in red . . . . .	127
3.16	Results from the reverse analysis for $E = E_0 = 18 MPa$ . . . . .	128
4.1	Different stages of the steady plowing mechanism <sup>#32</sup> ; the color field corresponds only to the rubber particles, and the color of the minerals and the road-like surface is arbitrary; $D_M$ corresponds to the mean equivalent diameter of the minerals, $y_0$ to the initial depth of each centroid and $h_i$ to the thickness of the interfacial layer (►) . . . . .	132
4.2	Different stages of the unsteady plowing mechanism <sup>#11</sup> ; the color field corresponds only to the rubber particles, and the color of the minerals and the road-like surface is arbitrary; $D_M$ corresponds to the mean equivalent diameter of the minerals, $y_0$ to the initial depth of each centroid and $h_i$ to the thickness of the interfacial layer (►) . . . . .	133
4.3	Intake according to $\mu_{rock}^{rock}$ for a sliding distance of $317 D_M$ and $\mu_{rock}^{rubber} = 0.4$ ; the color field corresponds only to the rubber particles, and the color of the minerals and the road-like surface is arbitrary; $D_M$ corresponds to the mean equivalent diameter of the minerals, $y_0$ to the initial depth of each centroid and $h_i$ to the thickness of the interfacial layer (►) . . . . .	134
4.4	Different stages of the abrasion mechanism <sup>#26</sup> ; the color field corresponds only to the rubber particles, and the color of the minerals and the road-like surface is arbitrary; $D_M$ corresponds to the mean equivalent diameter of the minerals, $y_0$ to the initial depth of each centroid and $h_i$ to the thickness of the interfacial layer (►) . . . . .	135



4.5	Different stages for the fracture mechanism <sup>#42</sup> ; the color field corresponds only to the rubber particles, and the color of the minerals and the road-like surface is arbitrary; $D_M$ corresponds to the mean equivalent diameter of the minerals, $y_0$ to the initial depth of each centroid and $h_i$ to the thickness of the interfacial layer (►) . . . . .	136
4.6	Main results about mineral diffusion; $y$ is the depth (i.e. transverse coordinate) with 0 corresponding to the mean line of the road-like surface; $D_M$ is the mean equivalent diameter of the minerals; $s$ is the sliding distance and $\varphi$ is the mineral fraction . . . . .	138
4.7	Transverse velocity during sliding (positive means towards the road-like surface and negative in the opposite direction) . . . . .	139
4.8	Transverse velocity of one mineral $\pm$ one standard deviation . . . . .	139
4.9	Autocorrelation function of the transverse velocity . . . . .	140
4.10	Illustration of overtaking mechanisms . . . . .	141
4.11	Orientation of minerals during sliding; the plot corresponds to the average orientation between a sliding distance of 2000 and 3000 $D_M$ . . . . .	142
4.12	Diffusion for long sliding distance; $MSD^0$ corresponds to the mean square displacement, $V_L$ to the longitudinal velocity and the markers on the velocity profile to the mixed layer (respectively 90% and 10% of minerals below the corresponding depths) . . . . .	143
4.13	Velocity fluctuation for long sliding distance . . . . .	144
4.14	Mineral fraction according to $C_{rock}^{rubber}$ . . . . .	146
4.15	Velocity profile according to $C_{rock}^{rubber}$ . . . . .	146
4.16	Kinematics according to $C_{rock}^{rubber}$ . . . . .	147
4.17	$MSD^0$ according to $C_{rock}^{rubber}$ . . . . .	147
4.18	Mineral fraction according to $h_i$ in a delayed jamming case . . . . .	148
4.19	Velocity profile according to $h_i$ in a delayed jamming case . . . . .	149
4.20	Kinematics according to $h_i$ in a delayed jamming case . . . . .	149
4.21	Diffusion according to $h_i$ in a delayed jamming case . . . . .	150
4.22	Effect of the friction coefficients . . . . .	150
4.23	Z-contrast images of the surfaces for 4 sliding distances (1.5, 3.0, 6.0 and 12.0 $m$ ) . . . . .	152
4.24	Z-contrast image of a cross-section view of the rubber sample and the corresponding EDX maps for carbon (C), aluminum (Al), silicon (Si) and oxygen (O) . . . . .	153
5.1	Mineral fraction according to $v_S$ . . . . .	158
5.2	Kinematics according to $v_S$ . . . . .	159
5.3	Diffusion according to $v_S$ . . . . .	160
5.4	Mineral fraction according to $h_i$ . . . . .	161
5.5	Kinematics according to $h_i$ . . . . .	162
5.6	Diffusion according to $h_i$ . . . . .	162
5.7	Mineral fraction according to $d_M^{rubber}$ . . . . .	163
5.8	Kinematics according to $d_M^{rubber}$ . . . . .	164
5.9	Diffusion according to $d_M^{rubber}$ . . . . .	164
5.10	Mineral fraction according to $\sigma_N$ . . . . .	165
5.11	Kinematics according to $\sigma_N$ . . . . .	166
5.12	Diffusion according to $\sigma_N$ . . . . .	167
5.13	Road-like surface according to $\lambda_c^{max}$ . . . . .	168
5.14	Road-like surface according to $\lambda_c^{min}$ . . . . .	168
5.15	Mineral fraction according to $\frac{\phi^{mineral}}{\phi^{rubber}}$ . . . . .	169
5.16	Kinematics according to $\frac{\phi^{mineral}}{\phi^{rubber}}$ . . . . .	170
5.17	Diffusion according to $\frac{\phi^{mineral}}{\phi^{rubber}}$ . . . . .	170

5.18	Kinematics according to $d_M^{mineral}$	172
5.19	Diffusion according to $d_M^{mineral}$	172
5.20	Illustration of $d_T^{agg}$ for one agglomerate ( $D_M$ is magnified for clarity)	173
5.21	Comparison between the particle jump and the transverse velocity	174
5.22	Mineral fraction according to $E$	175
5.23	Kinematics according to $E$	175
5.24	Diffusion according to $E$	176
5.25	Mineral fraction according to $C$	177
5.26	Kinematics according to $C$	178
5.27	Diffusion according to $C$	179
5.28	Examples of wear models with plane-strain kinematics; the color of the discrete particles represents the degree of damage	186
A.1	Results for a dataset generated every 2.6 $D_M$ of sliding	191
A.2	Results for a dataset generated every 5.1 $D_M$ of sliding	192
A.3	Results for a dataset generated every 10.3 $D_M$ of sliding	192
A.4	Results for $MSD_{initial}^0 = 50 D_M^2$ and a width of 2058 $D_M$	193
A.5	Comparison of diffusion coefficients derived from Einstein and Green-Kubo frameworks	193
B.1	Snapshots according to $C_{rock}^{rubber}$ ; $MSD^0 = 50 D_M^2$ for figs. B.1a to B.1c and $MSD^0 = 5 D_M^2$ for fig. B.1d	195
B.2	Snapshots according to $h_i$ in a delayed jamming case and for $MSD^0 = 19 D_M^2$	196
B.3	Snapshots according to $\mu_{rock}^{rock}$ and for $MSD^0 = 17 D_M^2$	197
B.4	Snapshots according to $\mu_{rock}^{rubber}$ and for $MSD^0 = 18 D_M^2$	198
B.5	Snapshots according to $v_S$ and for $MSD^0 = 50 D_M^2$	199
B.6	Snapshots according to $h_i$ and for $MSD^0 = 50 D_M^2$	200
B.7	Snapshots according to $d_M^{rubber}$ and for $MSD^0 = 50 D_M^2$	201
B.8	Snapshots according to $\sigma_N$ and for $MSD^0 = 50 D_M^2$	202
B.9	Snapshots according to $\lambda_c^{max}$ and for $MSD^0 = 50 D_M^2$	203
B.10	Snapshots according to $\lambda_c^{min}$ and for $MSD^0 = 50 D_M^2$	204
B.11	Snapshots according to $\frac{\phi^{mineral}}{\phi^{rubber}}$ and for $MSD^0 = 50 D_M^2$	205
B.12	Snapshots according to $d_M^{mineral}$ and for $MSD^0 = 40 D_M^2$	206
B.13	Snapshots according to $E$ and for $MSD^0 = 50 D_M^2$	207
B.14	Snapshots according to $C$ and for $MSD^0 = 50 D_M^2$	208
C.1	Mean square displacement according to $C_{rock}^{rubber}$	209
C.2	Mean square displacement according to $h_i$ in a delayed jamming case	209
C.3	Mean square displacement according to $\mu_{rock}^{rock}$	210
C.4	Mean square displacement according to $\mu_{rock}^{rubber}$	210
C.5	Mean square displacement according to $v_S$	210
C.6	Mean square displacement according to $h_i$	211
C.7	Mean square displacement according to $d_M^{rubber}$	211
C.8	Mean square displacement according to $\sigma_N$	212
C.9	Mean square displacement according to $\lambda_c^{max}$	212
C.10	Mean square displacement according to $\lambda_c^{min}$	213
C.11	Mean square displacement according to $\frac{\phi^{mineral}}{\phi^{rubber}}$	213
C.12	Mean square displacement according to $d_M^{mineral}$	214
C.13	Mean square displacement according to $E$	214
C.14	Mean square displacement according to $C$	215
D.1	Velocity autocorrelation function according to $v_S$	217

D.2	Velocity autocorrelation function according to $h_i$	217
D.3	Velocity autocorrelation function according to $d_M^{rubber}$	218
D.4	Velocity autocorrelation function according to $\sigma_N$	218
D.5	Velocity autocorrelation function according to $\lambda_c^{max}$	218
D.6	Velocity autocorrelation function according to $\lambda_c^{min}$	218
D.7	Velocity autocorrelation function according to $\frac{\phi^{mineral}}{\phi^{rubber}}$	219
D.8	Velocity autocorrelation function according to $d_M^{mineral}$	219
D.9	Velocity autocorrelation function according to $E$	219
D.10	Velocity autocorrelation function according to $C$	219



# List of Tables

2.1	List of the simulations and their associated numerical parameters . . . . .	107
5.1	Summary of the effect of several parameters under steady-state regime . . . . .	181



# List of Algorithms

1	Reverse analysis procedure	124
---	----------------------------	-----







## FOLIO ADMINISTRATIF

### THESE DE L'INSA LYON, MEMBRE DE L'UNIVERSITE DE LYON

NOM : **DAIGNE**

DATE de SOUTENANCE : **24/05/2024**

Prénoms : **Kévin, Jason**

TITRE : **Shear-induced diffusion of road minerals within the tire tread: a solid flow modeling using a soft multibody approach**

NATURE : **Doctorat**

Numéro d'ordre : **2024ISAL0046**

École Doctorale : **Mécanique, Énergétique, Génie Civil et Acoustique (MÉGA)**

Spécialité : **Génie Mécanique**

#### RÉSUMÉ :

Il peut être observé par des coupes longitudinales d'une bande de roulement que les minéraux de la route pénètrent à l'intérieur du pneumatique. L'objectif de ce travail est, pour une configuration expérimentale de référence, d'étudier expérimentalement et numériquement le processus menant à cette pénétration. Ce travail s'est articulé autour de trois grands axes. Le premier a été de proposer une méthode de caractérisation du matériau composé de caoutchouc, adaptée au modèle numérique utilisé par la suite. Pour ce faire, une analyse inverse d'un essai d'indentation a été réalisée. Le modèle numérique considère le matériau comme étant composé d'une multitude de corps discrets et déformables. Les paramètres à identifier sont la rigidité et la cohésion entre chaque corps discret. L'étude a montré que la cinématique obtenue est proche de ce qui est mesuré expérimentalement. Un critère de convergence pour l'analyse inverse a été défini, qui se base sur la dureté et la profondeur résiduelle mesurée. Il a été montré que pour un ratio de cohésion sur rigidité constant, la rigidité modifie uniquement la dureté. Par conséquent, comme cette cohésion modifie la profondeur résiduelle, la solution obtenue est unique. Un modèle numérique pour étudier la pénétration des minéraux a ensuite été réalisé. Il consiste à cisailier une couche de minéraux déposée sur la surface d'un matériau composé de caoutchouc, modélisé comme un ensemble de corps discrets et déformables. Il a tout d'abord été montré que les phénomènes initiaux de pénétration des minéraux dans la matière, sont différents de ceux observés à plus long terme. Notamment, trois modes de pénétration ont pu être définis, que sont le labourage, l'abrasion et la fracturation. Ces modes modifient la vitesse à laquelle les minéraux pénètrent à l'intérieur du matériau. Lorsque les minéraux sont suffisamment incorporés au matériau, ils forment ce qui sera appelé une couche mixée. Les minéraux migrent de plus en plus profondément, du fait de contacts répétés entre agglomérats de minéraux, causés par leurs vitesses relatives (pilotées par le taux de cisaillement). Il est notamment montré que ces contacts conduisent à une évolution stochastique de la position d'un minéral. Si l'ensemble des minéraux est considéré, le comportement devient déterministe et suit une évolution proche de ce qui est attendu pour un processus diffusif. Ce dernier point permet ainsi d'utiliser les outils de la diffusion, notamment d'évaluer un coefficient de diffusion via la fluctuation de vitesse transverse et sa persistance. Il est ainsi montré que ces deux paramètres dépendent fortement de phénomènes plastiques locaux, qui dans le modèle actuel sont pilotés par la cohésion.

MOTS-CLÉS : **Frottement sec ; Pneumatique ; Diffusion ; Écoulement ; Troisième corps ; Tribologie**

Laboratoire de recherche : **Laboratoire de mécanique des Contacts et des Structures (LaMCoS)**

Directeur de thèse : **Pr. Nicolas Fillot**

Président du Jury : **Emilien AZEMA**

Composition du Jury : **Emilien AZEMA, Julie DIANI, Vincent MAGNIER, Nicolas FILLOT, Guilhem MOLLON**